

Quantifying forearc deformation patterns using coastal geomorphic markers

**A comprehensive study of marine terraces along the 2010 Maule earthquake
(M8.8) rupture zone**

Dissertation von Julius Jara Muñoz

Geboren am 12.12.1979 in Santiago, Chile

Dissertation zur Auszeichnung des akademischen Grades Doktor der
Naturwissenschaften (Dr. rer. nat.) in der Wissenschaftsdisziplin Geologie.

Eingereicht am Institut für Erd- und Umweltwissenschaften der Mathematisch-Naturwissenschaftlichen
Fakultät der Universität Potsdam

Potsdam, August 2016



Quantifying forearc deformation patterns using coastal geomorphic markers

**A comprehensive study of marine terraces along the 2010 Maule earthquake
(M8.8) rupture zone**



Julius Jara Muñoz

Dissertation zur Auszeichnung des akademischen Grades Doktor der Naturwissenschaften

(**Dr. rer. nat.**) in der Wissenschaftsdisziplin Geologie

Eingereicht am Institut für Erd- und Umweltwissenschaften der Mathematisch-Naturwissenschaftlichen
Fakultät der Universität Potsdam

Potsdam, August 2016

This work is licensed under a Creative Commons License:
Attribution 4.0 International
To view a copy of this license visit
<http://creativecommons.org/licenses/by/4.0/>

Advisor:
Prof. Dr. Manfred Strecker

Date of final exam: 20.12.2016

Published online at the
Institutional Repository of the University of Potsdam:
URN [urn:nbn:de:kobv:517-opus4-102652](http://nbn-resolving.de/urn:nbn:de:kobv:517-opus4-102652)
<http://nbn-resolving.de/urn:nbn:de:kobv:517-opus4-102652>

El discurso científico y el humorístico poseen la misma estructura: ambos intentan asociar dos ideas que nunca antes se habían combinado (Koestler,1964).

Scientific and humoristic discourse share a common pattern, a blending of elements drawn from two previously unrelated ideas (Koestler,1964).

Wissenschaftlicher und humoristischer Diskurs haben ein gemeinsames Muster, eine Mischung von Elementen gezogen aus zwei bisher unabhängigen Ideen (Koestler,1964).

*Dedicado a Violeta y Silke ...
Dedicated to Violeta and Silke ...
Gewidmet an Violeta und Silke ...*

Allgemeine Zusammenfassung

Die stärksten Erdbeben, die auf der Welt instrumental registriert wurden, haben sich in Subduktionszonen ereignet. Diese tektonisch aktiven Regionen sind durch die Konvergenz zwischen kontinentalen und ozeanischen Platten gekennzeichnet. Erdbeben entlang von Brüchen entstehen durch das Verschieben zweier Platten und die damit sofortige Freisetzung elastischer Verformung, die sich seit mehr als 10 bis 100 Jahren akkumuliert hat. Dieser wiederkehrende Prozess der Anhäufung und der Freisetzung der Deformation definiert den Erdbebenzyklus. Nach mehreren Erdbebenzyklen werden, theoretisch, Teile der elastischen Deformation, die während des Erdbebens nicht freigesetzt wurde, in der Kruste als permanente Deformation gespeichert. Sie zeigen sich als tektonische Höhen und Tiefen.

Küstengebiete, die in der Nähe von Subduktionszonen liegen speichern fossile Beweise/Spuren ehemaliger Meeresspiegelpositionen. Sie zeigen so wie die ehemalige Küstenlinien oder Meeresterrassen, die heutzutage im Landensinnern oder höher gelegen sind, im Bezug zu der aktuellen Position des Meeresspiegels liegen. Das Auftreten dieser Landformen wird meist mit den aktiven tektonischen Erhöhungen in Verbindung gebracht, diese sind für die Entstehung des Küstenreliefs seit tausenden oder millionen von Jahren verantwortlich. Anhand fossiler Meeresspiegelmarkierungen kann die Magnitude der Deformationen, welche durch mehrere Erdbebenzyklen entstanden sind, sowie auch das Ausmaß der wiederkehrenden Erbeben entlang der Bruchzonen bestimmt werden.

Es ist allerdings nicht einfach Belege der vergangenen Meeresspiegelhöhen über einen tausendjährigen Zeitraum mit Erdbebenzyklen über einen kürzeren Zeitraum miteinander in Verbindung zu bringen. Hierzu benötigt es die Entwicklung von spezifischen Methoden, die es erlauben beide Aspekte zu untersuchen: Die Entwicklung der Küstenlandschaften und die Deformation, während der verschiedenen Phasen der Erdbebenzyklen.

In dieser Arbeit wird die 500 km lange Bruchzone des M8.8 Maule Erdbeben, das sich im Jahr 2010 ereignet hat untersucht. Aus historischen Aufzeichnungen ist zu entnehmen, dass dieses Küstengebiet von wiederkehrenden Megaerdbeben betroffen ist und war. Neue Methoden um die tektonisch aktiven Küstengebiete zu untersuchen wurden entwickelt um Meeresspiegelmarker, anhand hochauflösender Topographie und quantitativer Geomorphologie zu finden. Die Aufzeichnung der Höhenveränderungen an Land, sowie mathematische Modelle, Aufzeichnungen der Megathrust-Deformation während der Erdbebenzyklen, werden mit dem permanenten Deformationsmuster, welches auf Meeresterrassenaufzeichnungen basiert, verglichen. Dieser Vergleich ermöglicht es, den Mechanismus zu verstehen, der für die Akkumulation dieser Deformationen verantwortlich war und dessen Einfluss auf die Segmentation der Megathrust-Erdbeben in dieser Gegend zu erklären.

Die Ergebnisse dieser Arbeit zeigen neuartige und fundamentale Information zu adäquaten Risikountersuchungen entlang der Küste sowie die Erwartung bezüglich realistischer Erdbeben und Tsunami Szenarien.

Abstract

Rapidly uplifting coastlines are frequently associated with convergent tectonic boundaries, like subduction zones, which are repeatedly breached by giant megathrust earthquakes. The coastal relief along tectonically active realms is shaped by the effect of sea-level variations and heterogeneous patterns of permanent tectonic deformation, which are accumulated through several cycles of megathrust earthquakes. However, the correlation between earthquake deformation patterns and the sustained long-term segmentation of forearcs, particularly in Chile, remains poorly understood. Furthermore, the methods used to estimate permanent deformation from geomorphic markers, like marine terraces, have remained qualitative and are based on unrepeatable methods. This contrasts with the increasing resolution of digital elevation models, such as Light Detection and Ranging (LiDAR) and high-resolution bathymetric surveys.

Throughout this thesis I study permanent deformation in a holistic manner: from the methods to assess deformation rates, to the processes involved in its accumulation. My research focuses particularly on two aspects: Developing methodologies to assess permanent deformation using marine terraces, and comparing permanent deformation with seismic cycle deformation patterns under different spatial scales along the M8.8 Maule earthquake (2010) rupture zone. Two methods are developed to determine deformation rates from wave-built and wave-cut terraces respectively. I selected an archetypal example of a wave-built terrace at Santa Maria Island studying its stratigraphy and recognizing sequences of reoccupation events tied with eleven radiocarbon sample ages (^{14}C ages). I developed a method to link patterns of reoccupation with sea-level proxies by iterating relative sea level curves for a range of uplift rates. I find the best fit between relative sea-level and the stratigraphic patterns for an uplift rate of 1.5 ± 0.3 m/ka.

A Graphical User Interface named TerraceM® was developed in Matlab®. This novel software tool determines shoreline angles in wave-cut terraces under different geomorphic scenarios. To validate the methods, I select test sites in areas of available high-resolution LiDAR topography along the Maule earthquake rupture zone and in California, USA. The software allows determining the 3D location of the shoreline angle, which is a proxy for the estimation of permanent deformation rates. The method is based on linear interpolations to define the paleo platform and cliff on swath profiles. The shoreline angle is then located by intersecting these interpolations. The accuracy and precision of TerraceM® was tested by comparing its results with previous assessments, and through an experiment with students in a computer lab setting at the University of Potsdam.

I combined the methods developed to analyze wave-built and wave-cut terraces to assess regional patterns of permanent deformation along the (2010) Maule earthquake rupture. Wave-built terraces are tied using 12 Infra Red Stimulated luminescence ages (IRSL ages) and shoreline angles in wave-cut terraces are estimated from 170 aligned swath profiles. The comparison of coseismic slip, interseismic coupling, and permanent deformation, leads to three areas of high permanent uplift, terrace warping, and sharp fault offsets. These three areas correlate with regions of high slip and low coupling, as well as with the spatial limit of at least eight historical megathrust ruptures (M8-9.5). I propose that the zones of upwarping at Arauco and Topocalma reflect changes in frictional properties of the megathrust, which result in discrete boundaries for the propagation of mega earthquakes.

To explore the application of geomorphic markers and quantitative morphology in offshore areas I performed a local study of patterns of permanent deformation inferred from hitherto unrecognized drowned shorelines at the Arauco Bay, at the southern part of the (2010) Maule earthquake rupture zone. A multidisciplinary approach, including morphometry, sedimentology, paleontology, 3D morphoscopy, and a landscape Evolution Model is used to recognize, map, and assess local rates and patterns of permanent deformation in submarine environments. Permanent deformation patterns are then reproduced using elastic models to assess deformation rates of an active submarine splay fault defined as Santa Maria Fault System. The best fit suggests a reverse structure with a slip rate of 3.7 m/ka for the last 30 ka. The register of land level changes during the earthquake cycle at Santa Maria Island suggest that most of the deformation may be accrued through splay fault reactivation during mega earthquakes, like the (2010) Maule event. Considering a recurrence time of 150 to 200 years, as determined from historical and geological observations, slip between 0.3 and 0.7 m per event would be required to account for the 3.7 m/ka millennial slip rate. However, if the SMFS slips only every ~ 1000 years, representing a few megathrust earthquakes, then a slip of ~ 3.5 m per event would be required to account for the long-term rate. Such event would be equivalent to a magnitude ~ 6.7 earthquake capable to generate a local tsunami.

The results of this thesis provide novel and fundamental information regarding the amount of permanent deformation accrued in the crust, and the mechanisms responsible for this accumulation at millennial time-scales along the M8.8 Maule earthquake (2010) rupture zone. Furthermore, the results of this thesis highlight the application of quantitative geomorphology and the use of repeatable methods to determine permanent deformation, improve the accuracy of marine terrace assessments, and estimates of vertical deformation rates in tectonically active coastal areas. This is vital information for adequate coastal-hazard assessments and to anticipate realistic earthquake and tsunami scenarios.

Zusammenfassung

Küstenregionen, die von schnellen Hebungsraten gekennzeichnet sind, werden häufig mit konvergierenden Plattengrenzen assoziiert, beispielsweise mit Subduktionszonen, die wiederholt von Mega-Erdbeben betroffen sind. Das Küstenrelief tektonisch aktiver Gebiete formt sich durch die Effekte von Meeresspiegelschwankungen und die heterogenen Muster der permanenten tektonischen Deformation, die im Zuge von mehreren Erdbebenzyklen entstand. Jedoch die Korrelation zwischen den Deformationsmustern von Erdbeben und der langfristig anhaltenden Segmentation der ‚Forearcs‘ ist noch wenig erforscht, insbesondere in Chile. Darüber hinaus sind die Methoden zur Schätzung der permanenten Deformation geomorphologischer Marker, wie beispielsweise mariner Terrassen, lediglich qualitativ oder basieren nicht auf wiederholbaren Messungen. Dies steht im Kontrast zu der mittlerweile höheren Auflösung verfügbarer digitaler Geländemodelle, die z.B. mit LiDAR (Light Detection and Ranging) oder durch hochauflösende bathymetrische Studien gewonnen werden.

Im Rahmen dieser Dissertation wird die permanente Deformation einer ganzheitlichen Betrachtung unterzogen, die von den zu Grunde liegenden Methoden zur Bestimmung der Deformationsraten bis hin zu den involvierten Prozessen bei deren Akkumulation reicht. Besonderes Augenmerk wird dabei auf zwei Aspekte gerichtet: Einerseits die Entwicklung von Methoden zur Messung permanenter Deformation anhand von marinen Terrassen, und andererseits der Vergleich zwischen permanenter Deformation und Deformationsmustern des seismischen Zyklus anhand unterschiedlicher räumlicher Ausmaße entlang der Bruchzone des M8.8 Maule (2010) Erdbebens entstanden. Es werden zwei Methoden zur Bestimmung der Deformationsraten von ‚wave-built‘ und ‚wave-cut‘ Terrassen entwickelt.

Ein archetypischer Beispiel einer ‚wave-built‘ Terrasse wird auf der Insel Santa Maria untersucht. Durch die detaillierte Studie der Sedimentabfolge, werden wiederkehrende Ereignisse der Reaktivierung der Terrasse identifiziert, die anhand von Messungen an Kohlenstoffisotopen (C^{14} -Datierung) von 11 Proben zeitlich eingegrenzt werden. Es wird eine Methode entwickelt, um solche Reaktivierungsmuster mit Meeresspiegelindikatoren in Verbindung zu bringen, wobei die relativen Meeresspiegelkurven mit einer Reihe von Hebungsraten korreliert werden. Die beste Korrelation zwischen Meeresspiegelschwankungen und dem stratigrafischen Muster wird unter Berücksichtigung einer Hebungsrate von 1.5 ± 0.3 m/ka erreicht.

Unter Verwendung der Software Matlab® wird die grafische Benutzeroberfläche TerraceM® entwickelt. Diese neue Methode erlaubt die Bestimmung von Küstenwinkels in ‚wave-cut‘ Terrassen in verschiedenen geomorphischen Szenarien. Zur Validierung der Methoden werden Regionen entlang der Bruchzone des Maule-Erdbebens und in Kalifornien ausgewählt, für die hochauflösende LiDAR-Daten der Topografie zur Verfügung stehen. Die Software ermöglicht es, den 3D Standort des Küstenwinkels zu bestimmen, der als Proxy für die Schätzung permanenter Deformationsraten fungiert. Dabei nutzt die Methode lineare Interpolation um die Paleo Plattform und die Klippen mit Swath Profilen zu definieren. Im Anschluss wird der Küstenwinkel durch die Überschneidung dieser Interpolationen lokalisiert. Die Genauigkeit und Robustheit von „TerraceM“ wird durch den Vergleich der Ergebnisse mit denen vorangegangener Untersuchungen überprüft.

Um regionale Muster permanenter Deformationen entlang der (2010) Maule Bruchzone zu untersuchen werden die Methoden für die ‚wave-built‘ und ‚wave-cut‘ Terrassen kombiniert.

‘Wave-built’ Terrassen werden mittels 12 Infrarot-Optisch-Stimulierten Lumineszenz (IRSL) Proben datiert, während die Küstenwinkel der ‘wave-cut’ Terrassen anhand von 170 abgestimmten SWATH-Profilen geschätzt wurden. Durch den Vergleich von co-seismischem Versatz, interseismischer Kopplung und permanenter Deformation ergaben sich drei Gebiete mit hoher permanenter Erhebung, Terrassenkrümmung und abruptem, störungsbedingtem Versatz. Diese drei Gebiete korrelieren mit Regionen von hohem Versatz und niedriger Kopplung, sowie mit der räumlichen Begrenzung der Bruchzonen von mindestens acht historischen Mega-Erdbeben. Es wird argumentiert, dass die ansteigenden Zonen bei Arauco und Topocalma Änderungen der Reibungseigenschaften von Mega-Erdbeben widerspiegeln, was diskrete Grenzen für die Ausbreitung von Mega-Erdbeben zur Folge hat.

Ein weiterer Beitrag dieser Dissertation ist die lokale Untersuchung permanenter Deformationsmuster von bislang unbekannt überflutete Küstenlinien in der Arauco-Bucht bei der Santa Maria Insel, die ebenfalls vom Maule Erdbeben betroffen wurde. Ein multidisziplinärer Ansatz wird verwendet, um lokale Muster permanenter Deformation in submarinen Umgebungen zu erkennen, abzubilden und zu untersuchen. Dabei kommen Morphometrie, Sedimentologie, Paläontologie, 3D Morphoskopie und ein Landschafts-Entwicklungs-Model zum Einsatz.

Permanente Deformationsmuster werden anhand eines elastischen Modells nachgebildet und bestimmen die Deformationsraten einer aktiven, submarinen Aussenstörung (‘splay fault’), die als Santa Maria Störungszone definiert wird und durch eine Versatzrate von 3.7 m/ka für die letzten 30 ka charakterisiert ist. Die Aufzeichnungen zu Veränderungen der Elevation der Erdoberfläche während des Santa Maria Erdbebenzyklus deuten darauf hin, dass der wesentliche Teil der Deformation auf die Reaktivierung einer ‘Splay Fault’ während Mega-Erdbeben (wie z.B. das Maule (2010) Erdbeben) zurückzuführen ist. Allerdings die Sismizität in geringer Tiefe, die während der letzten zehn Jahre vor dem Maule-Erdbeben registriert wurde, deutet auf vorübergehende Störungsaktivität in der interseismischen Phase hin.

Die Ergebnisse dieser Dissertation liefern neuartige und fundamentale Daten bezüglich der Menge und Mechanismen der Akkumulation permanenter Deformation in der Erdkruste über mehrere tausend Jahre hinweg in der Region des M8.8 Maule Erdbebens (2010). Die in dieser Dissertation präsentierten neuen Methoden zur Charakterisierung permanenter Deformation mithilfe von geomorphologischen Küstenmarkern bieten einen breiteren quantitativen Ansatz zur Interpretation aktiver Deformation dar und können somit zu einem besseren Verständnis der Geologie in tektonisch aktiven Küstengebieten beitragen.

Resumen

Las regiones costeras tectónicamente activas están generalmente asociadas con zonas de subducción, las cuales son recurrentemente afectadas por megaterremotos de gran magnitud. El relieve costero es modelado por el efecto combinado de variaciones eustáticas y patrones de alzamiento tectónico heterogéneos, los cuales son acumulados luego de varios ciclos de megaterremotos. Sin embargo, la correlación entre los patrones de deformación asociados a megaterremotos y la persistente segmentación de las zonas de antearco, especialmente en Chile, no han sido aún entendidos del todo. Por otra parte, los métodos normalmente usados para estimar deformación permanente y basados en marcadores geomorfológicos, como las terrazas marinas, han permanecido basados en aproximaciones cualitativas y no repetibles. Esta situación es contrastante con el rápido avance de modelos de elevación digital de alta resolución como Light Detection and Ranging (LiDAR) y batimetrías de última generación.

A lo largo de esta tesis me enfoco en estudiar la deformación permanente desde un punto de vista holístico: Desde los métodos usados para medir deformación permanente, hasta el estudio de los procesos responsables de su acumulación en la corteza. Mi investigación se enfoca específicamente en dos aspectos: Desarrollar nuevos métodos para medir deformación permanente usando terrazas marinas y comparar la magnitud de la deformación permanente con diferentes escalas temporales de deformación registrada durante las distintas fases del ciclo sísmico a lo largo de la zona de ruptura del (M8.8) Terremoto Maule 2010. En esta tesis he desarrollado dos métodos para determinar tasas de deformación en terrazas marinas del tipo wave-built y wave-cut. Para el primero, me enfoco en estudiar un ejemplo arquetípico de terraza marina tipo wave-built en Isla Santa María, mapeando su estratigrafía en detalle y reconociendo patrones de eventos de reocupación datados mediante once edades de radiocarbono (^{14}C). He desarrollado un método para vincular los patrones de reocupación con variaciones del nivel del mar mediante la iteración de curvas relativas del nivel del mar para un rango de tasas de alzamiento. El mejor ajuste entre nivel del mar relativo y los patrones estratigráficos señala una tasa de alzamiento de 1.5 ± 0.3 m/ka.

El segundo método es un software de interfaz gráfica llamado TerraceM® y desarrollado usando Matlab®. Esta novedosa herramienta permite determinar el shoreline-angle en terrazas del tipo wave-cut para diferentes escenarios geomorfológicos. Para validar estos métodos he seleccionado zonas de prueba con disponibilidad de topografía LiDAR a lo largo de la zona de ruptura del Terremoto Maule (2010), en Chile, y en California, USA. TerraceM permite determinar la ubicación tridimensional del shoreline-angle, el cual es usado para calcular tasas de deformación permanente. El shoreline-angle es localizado mediante la intersección de interpolaciones lineales, las que son usadas para definir la paleo plataforma y el paleo acantilado en perfiles topográficos swath. La precisión y exactitud de las mediciones con TerraceM es testada comprando los resultados con mapeos previos y mediante un experimento de respetabilidad con estudiantes en el laboratorio de computación de la Universidad de Potsdam.

He combinado los métodos creados anteriormente, para analizar terrazas del tipo wave-cut y wave-built, con el objetivo de medir la deformación permanente acumulada a lo largo de la zona de ruptura del Terremoto Maule (2010). Las terrazas tipo wave-built fueron datadas usando doce edades de Luminiscencia Estimulada por Luz Infrarroja (IRSL), las terrazas wave-cut fueron estudiadas utilizando 170 perfiles swaths alineados. Mediante la comparación de deslizamiento co-

sísmico, acople intersísmico y tasas de deformación permanente he detectado tres áreas de alto alzamiento tectónico, plegamiento de terrazas marinas y zonas desplazadas por fallas activas. Estas tres áreas coinciden con zonas de alto deslizamiento cosísmico y acople, y con el límite espacial de al menos ocho megaterremotos históricos (M8-9.5). Propongo que las zonas de plegamiento de terrazas marinas en Arauco y Topocalma reflejan cambios en fricción de la zona de interplaca, que da como resultado la formación de barreras discretas para la propagación de megaterremotos.

Con el objetivo de explorar la aplicación de geomorfología cuantitativa y marcadores geomorfológicos en ambientes submarinos, he desarrollado un estudio local de para determinar tasas de alzamiento tectónico utilizando líneas de costa sumergidas en el Golfo de Arauco, en la parte sur de la zona de ruptura del Terremoto Maule (2010). Utilizo una metodología multidisciplinaria que incluye: morfometría, sedimentología, paleontología, morfoscopia 3D y un modelo de evolución del relieve, con el objetivo de reconocer, cartografiar, y medir tasas y patrones de deformación permanente en ambientes submarinos. Luego, se utilizó un modelo elástico para reproducir los patrones de deformación permanente de una falla ramificada (splay-fault) definida como Sistema de Falla Santa María. El mejor modelo sugiere una estructura inversa con una tasa de deslizamiento de 3.7 m/ka durante los últimos ~30 ka. El registro de cambios del nivel del terreno durante el ciclo sísmico en Isla Santa María sugiere que la mayor parte de la deformación es acumulada a través de la reactivación de fallas ramificadas durante megaterremotos como el Maule (2010). Si consideramos 150 a 200 años como tiempo de recurrencia de estos mega eventos, un deslizamiento de entre 0.3 y 0.7 metros por evento sería necesario para equilibrar la tasa de deslizamiento de 3.7 m/ka. Sin embargo, si la falla se deslizara cada ~1000 años, sugiriendo que solo algunos terremotos podrían reactivarla, un deslizamiento de ~3.5 metros por evento serían necesarios para equilibrar la tasa de deslizamiento. Tal evento sería equivalente a un terremoto magnitud ~6.7 que sería capaz de producir un tsunami local.

Los resultados de esta tesis entregan información nueva y fundamental acerca de la cantidad de deformación permanente y los posibles mecanismos asociados a esta deformación a escala de miles de años a lo largo de la zona de ruptura del M8.8 Terremoto Maule (2010). Además, los resultados de esta tesis destacan la aplicación de métodos de geomorfología cuantitativa, incluyendo nuevas herramientas computacionales como TerraceM®, el cual ayudará a expandir el uso de la geomorfología cuantitativa y métodos repetibles, además de mejorar la precisión y exactitud de estimaciones de deformación permanente en zonas costeras. Esta información es imprescindible para una adecuada ponderación de riesgos geológicos en zonas costeras y para anticipar escenarios de terremotos y tsunamis realísticos.

Acknowledgments

I would like to thank my supervisor, Prof. Manfred Strecker for his continuous support, and encouragement, providing valuable corrections to my work, I would like to say thank you for his inspiring lessons of neotectonics in the field and in the classroom, and for give me the opportunity to develop this thesis at the University of Potsdam. I would like acknowledging my mentor and friend Daniel Melnick for attending my questions, and for those fruitful discussions, and also for his personal support in all fields. I would like to thank my mother and my family in Chile and Germany for their tolerance, and love during the ups and downs of my research.

I would like to thank Prof. Helmut Echtler, Prof. Kevin Pedoja, Prof. Andres Tassara, Prof. Rolando Armijo, Prof. Sven Nielsen, Prof. Cengiz Yildirim, Prof. Dietrich Lange, Patricio Zambrano, Paula Marques Figueiredo, Anne Bernhardt, Marco Meschis, and Isabel Urrutia for the fruitful and inspiring discussions and insights about tectonics, stratigraphy, geomorphology, earthquake geology, and marine terraces and many other things. I would like to thank my student colleagues Gino De Gelder, Yacine Benjelloun, Christian Hilleman, and Saptarshi Dey for their interest and valuable feedback about morphometry, marine terraces, Matlab®, and the performance of modular software developed during this thesis.

I want to give special thanks to Kenneth Fisk, for his essential supports during the two-field campaigns, of 45-days each one, developed between 2012 and 2013 in Central Chile. I would like to thank Fanor Velazco for providing the climbing gear and keeping us safe on the cliffs, Juan Carlos Basualto, Hugo Muñoz, Don Doroteo Henríquez, Don Toti, and Alejandro Araneda, for their field assistance in the field. Also deserve thanks the crew of the Bismark, the boat used to explore the Arauco Bay, and the two brave tactical divers that performed sampling at ~40 m depth.

I must express my gratitude to University of Concepcion (Chile), Prof. Veronica Pineda, Prof. Abraham Gonzalez, and Prof. Andres Tassara, for facilitating the laboratories of the Geology Department, Pedro Bravo, and Iván Orellana for their help in the laboratory. I thank Servicio Hidrográfico y Oceanográfico de la Armada de Chile (SHOA) and Boris Argandoña, Gobierno de Chile and Dirección de Obras Municipales, Markus Rombach and Digimapas Chile that facilitate high-resolution topography and bathymetry from coastal areas. I thank the GFZ Potsdam in particular to Hella Wittmann for her teachings in the laboratory.

Finally I would like to thank the University of Potsdam, and all the members of the staff, and especially to Tanja Klaka-Tauscher, I am in indebted for her help. This study was developed within the framework of the project MARISCOS (MAule eaRthquake: Integration of Seismic Cycle Observations and Structural investigations) supported by the German Science Foundation (DFG).

Contents

Allgemeine Zusammenfassung	IX
Abstract	XI
Zusammenfassung	XIII
Resumen	XV
Acknowledgments	XVII
Contents	XIX
List of figures	XXIII
List of tables	XXV
1 Introduction	1
1.1 The tectonic signal	1
1.2 The climatic signal	2
1.3 Geomorphic markers: marine terraces	2
1.4 The Maule earthquake rupture zone	3
1.4.1 Tectonic and geomorphic framework	3
1.4.2 The 2010 Maule earthquake.....	4
1.5 Thesis organization	5
2 Unraveling sea-level variations and tectonic uplift in wave-built marine terraces, Santa María Island, Chile	7
2.1 Introduction	9
2.2 Geologic setting of Santa Maria Island	10
2.3 Stratigraphy and chronology of the Santa Maria Formation	11
2.4 Setting of wave-built terraces	12
2.5 Methods	12
2.5.1 Stratigraphic sections of the Santa María Formation.....	12
2.5.2 Granulometric analysis	12
2.5.3 Sample collection for radiocarbon dating.....	13
2.5.4 Construction of relative sea-level curves	13
2.6 Results	14
2.6.1 Sedimentary facies.....	14
2.6.2 Radiocarbon ages	18
2.6.3 Erosional and depositional surfaces within the SMI	19
2.6.4 Granulometric Model and stratigraphic architecture	20
2.7 Discussion	23
2.7.1 Influence of tectonic uplift and sea-level oscillations on the SMF stratigraphy.....	23
2.7.2 Depositional history of SMF.....	26
2.7.3 Reoccupation thresholds in MIS 3 marine terraces	27
2.7.4 Correlating wave-cut and wave-built terraces.....	28
2.8 Conclusions	29
3 TerraceM: a MATLAB® tool to analyze marine and lacustrine terraces using high-resolution topography	31

3.1	Introduction	33
3.2	Background and motivation	35
3.3	TerraceM: specifications and calibration site	38
3.3.1	GUI Interface	38
3.3.2	Workspace and Workflow	39
3.3.3	TerraceM Calibration Site: Santa Cruz Marine Terraces	40
3.4	Analytical tools	41
3.4.1	Staircase Marine Terraces	41
3.4.2	Sea Stacks at Rough Coasts	43
3.4.3	Scarp Diffusion	44
3.4.4	Cliff Free-Face	45
3.5	Postprocessing tools	46
3.6	Precision and accuracy of measurements	47
3.7	Repeatability of measurements	49
3.8	Summary	51
4	Segmentation of the 2010 Maule Chile earthquake rupture from a joint analysis of uplifted marine terraces and seismic-cycle deformation patterns	53
4.1	Introduction	55
4.2	Tectonic and geomorphic framework	56
4.2.1	Regional tectonic and geologic setting	56
4.2.2	Quaternary crustal faults and previous estimates of coastal uplift rates	57
4.2.3	Historical earthquakes in south-central Chile	58
4.2.4	The 2010 Maule earthquake	58
4.3	Background and methods	60
4.3.1	Marine terraces as geomorphic markers of permanent deformation	60
4.3.2	Mapping marine terraces	61
4.3.3	Estimating shoreline angle elevations	62
4.3.4	Stratigraphy and luminescence dating of marine terrace deposits	64
4.3.5	Estimating uplift rates from shoreline angle elevations and luminescence ages	68
4.4	Results	69
4.4.1	Geomorphology, stratigraphy and luminescence ages of marine terraces	69
4.4.1.1	Sector 1: Arauco Peninsula - Coronel	69
4.4.1.2	Sector 2: Coronel - Penco	71
4.4.1.3	Sector 3: Penco - Curanipe	71
4.4.1.4	Sector 4: Curanipe - Pelluhue	71
4.4.1.5	Sector 5: Pelluhue - Constitucion	74
4.4.1.6	Sector 6: Constitucion - Pichilemu	75
4.4.1.7	Sector 7: Pichilemu - Navidad	78
4.4.2	Distribution of Quaternary faults and uplift rates along the Maule rupture	79
4.5	Discussion	80
4.5.1	Uplift mechanisms responsible for emerged marine terraces	80
4.5.2	Relationships between earthquake barriers and permanent deformation patterns	82
4.5.3	Comparison of seismic cycle and permanent deformation patterns	85
4.6	Conclusions	85
5	Quantifying offshore forearc deformation and splay-fault slip using Pleistocene drowned shorelines, Arauco Bay, Chile	87

5.1	Introduction	89
5.2	Seismotectonic and geomorphic setting	91
5.2.1	The 2010 Maule earthquake.....	91
5.2.2	Structures in the Arauco Bay area.....	92
5.2.3	Activity of the Santa María Fault System during the seismic cycle.....	93
5.2.4	Marine terraces in the Arauco Bay area.....	93
5.2.5	Modern depositional environments in the Arauco Bay.....	95
5.3	Background and Methods	95
5.3.1	Drowned sea-level markers.....	95
5.3.2	Mapping drowned shorelines using high-resolution bathymetry.....	97
5.3.3	Morphometric analysis.....	97
5.3.4	Submarine imaging and sampling.....	99
5.3.5	Estimating uplift rates using a Landscape Evolution Model.....	99
5.4	Results	102
5.4.1	Submarine geomorphology of the Arauco Bay.....	102
5.4.2	In-situ observations at drowned shorelines.....	106
5.4.3	Distribution of uplift rates inferred from drowned shorelines.....	110
5.4.4	Active structures in the Arauco Bay area mapped from multibeam bathymetry.....	112
5.5	Estimating fault-slip rates using dislocation models	114
5.5.1	Structural model setups.....	114
5.5.1.1	Structural setup 1: Deep reverse faults and shallow normal faults.....	115
5.5.1.2	Structural setup 2: normal faults.....	115
5.5.2	Model results.....	116
5.6	Discussion	118
5.6.1	Age and preservation of drowned shorelines in the Arauco Bay area.....	118
5.6.2	Millennial-scale kinematics and slip rate of the SMFS.....	119
5.6.3	Splay-fault slip during the megathrust seismic cycle.....	120
5.7	Conclusions	122
6	Summary and discussion	125
7	References	128
Appendix A: Sedimentology and dating of the Santa Maria Formation		152
A.1	Mineralogy of the Santa María Formation (SMF) and sediment source.....	152
A.2	Modern and Holocene depositional environments.....	153
A.3	Grain size distributions.....	153
A.4	Granulometric model of depositional environments.....	154
A.4.1	Factor analysis.....	154
A.4.2	Discriminant analysis.....	157
A.5	Radiocarbon samples.....	159
A.6	References of appendix A.....	164
Appendix B: TerraceM, detailed description and operation		165
B.1	TerraceM functions.....	165
B.2	TerraceM workspace.....	166
B.3	TerraceM workflow.....	166
B.3.1	Inputs interface.....	167
B.3.2	Profile extraction interface.....	168
B.3.3	Display Interface.....	169

B.3.4 Swath profile preview.....	169
B.3.5 Analytical functions	170
B.3.6 Analysis parameters	173
B.3.7 Outputs.....	173
B.3.8 Table viewer interface	174
B.3.9 Shoreline projection interface.....	175
B.3.10 Shoreline filtering interface	176
B.3.11 Export functions	177
B.3.12 Debugging	177
B.4 Known issues	177
B.5 TerraceM fits at Santa Cruz	179
B.6 References of appendix B.....	190
Appendix C: Topography, IRSL dating, and geological maps along the 2010 Maule earthquake rupture.	191
C.1 Topographic datasets	191
C.2 Luminescence dating	192
C.2.1 Sample preparation	192
C.2.2 Experiments: OSL measurements on quartz.....	193
C.2.3 IRSL equivalent dose	195
C.3 Geology and stratigraphy of marine terraces	197
C.4 Estimates of shoreline angle elevations.....	205
C.5 Geometric parameters of the Margin	206
C.6 References of appendix C.....	206
Appendix D: Quantifying offshore deformation using Pleistocene drowned shorelines, Arauco Bay, Chile.	209
D.1 Comparison of surface texture of drowned and active wave-cut platforms	209
D.2 Testing the Landscape Evolution model with other sea-level proxies.....	210
D.3 Cliff erosion rates.....	211
Appendix E: Online Material	213

List of figures

Figure 1.1: Schematic representation of a marine terrace.....	3
Figure 1.2: Strain accumulation and release along the Maule earthquake rupture zone.	4
Figure 2.1: Regional setting and geology of Santa María Island.	10
Figure 2.2: Field views of facies in the SFM.....	15
Figure 2.3: Box-and-whisker plots of granulometric parameters for each facies.	16
Figure 2.4: Radiocarbon ages of the SMF.	19
Figure 2.5: Depositional surfaces within the SMF.	20
Figure 2.6: Detailed stratigraphic sections of the SMF.	22
Figure 2.7: Composite profile illustrating the stacking pattern of the SMF.....	23
Figure 2.8: A: Stratigraphic sections, radiocarbon ages and patterns of relative sea-level	24
Figure 2.9: Correlation between relative sea level and stratigraphic units.....	25
Figure 2.10: Schematic representation of the chronology and stratigraphy of the SMF.....	26
Figure 2.11: Distribution of MIS 3 shorelines in the cirum-Pacific region.....	27
Figure 2.12: Schema of spatial relationships between different types of marine terraces.	29
Figure 3.1: Oblique aerial view of uplifted marine terraces.....	32
Figure 3.2: Processes associated with the generation of shoreline angles.	34
Figure 3.3: Examples of processes responsible for the modification of marine terraces	37
Figure 3.4: TerraceM interface and structure of directories.....	38
Figure 3.5: Mapping interface and workspace.....	40
Figure 3.6: Calibration site.	41
Figure 3.7: Example of shoreline angles obtained using the Staircase Analysis function....	42
Figure 3.8: Stack Analysis function for rough coasts.....	43
Figure 3.9: Examples of the Diffusion Analysis function.	44
Figure 3.10: Example of the Free-Face Analysis function.	45
Figure 3.11: Comparison of shoreline-angle elevations from different types of surveys...	48
Figure 3.12: Results of the repeatability experiment.....	51
Figure 4.1: Deformation patterns, historical earthquakes and regional geology.....	57
Figure 4.2: Shaded-relief map showing sampling locations for age dating.	60
Figure 4.3: Example of mapping and analysis of marine terraces at Pelluhue.....	63
Figure 4.4: Example illustrating the methodology used at rough coasts.....	64
Figure 4.5: Luminescence dating results.....	67
Figure 4.6: Marine terraces and geology of the Arauco Peninsula.	70
Figure 4.7: Field views showing the geomorphic expression of MIS 5 terraces.	72
Figure 4.8: Wave-built marine terrace at Curanipe.	73
Figure 4.9: Marine terraces and geology at Carranza.	75
Figure 4.10: Geology and stratigraphy south of Constitución, at the locality of El Yolki.....	76
Figure 4.11: Geology and stratigraphy at Putu.	77
Figure 4.12: Marine terraces and geology between Pichilemu and Topocalma.	78
Figure 4.13: Permanent deformation patterns along the Maule rupture.	79
Figure 4.14: Comparison between permanent uplift rates coseismic and interseismic	82
Figure 4.15: Permanent and seismic-cycle deformation patterns.....	83
Figure 5.1: Regional tectonic setting.....	91
Figure 5.2: Shallow active structures in the Arauco Bay Area.....	94
Figure 5.3: Sea-level variations since MIS 5e and constraints of the LEM.	96
Figure 5.4: Extent of 2-m resolution multibeam bathymetry.....	98
Figure 5.5: Morphology and structures along the Eastern Domain.	102

Figure 5.6: Examples of geomorphic features along the Eastern Domain.	103
Figure 5.7: Morphology and structures along the Western Domain.	104
Figure 5.8: Examples of geomorphic features along the Western Domain.	105
Figure 5.9: Morphology of the Santa Maria scarp.	106
Figure 5.10: In-situ observations of a drowned shoreline	107
Figure 5.11: Sedimentological and morphoscopic analysis of submarine samples.....	108
Figure 5.12: Landscape Evolution Model.....	110
Figure 5.13: Examples of forward model results.	112
Figure 5.14: Active structures inferred from multibeam bathymetry.....	113
Figure 5.15: Uplift rates predicted by elastic dislocation modes.....	117
Figure 5.16: Stacked swath profiles of uplift rates from elastic dislocation models	120
Figure 5.17: Plots of slip rate against surface uplift and recurrence.....	121

List of tables

Table 2.1: Radiocarbon ages of SMF.....	18
Table 3.1: Open source functions used in TerraceM.....	39
Table 3.2: Spatial information of datasets used for comparisons of TerraceM results.....	47
Table 4.1: IRSL ages.....	65
Table 4.2: IRSL and CRN age calibrations with geomorphic and stratigraphic markers and their corresponding higstand.....	66
Table 5.1: Parameters of elastic models.	116
Table 5.2: Distribution of residual values of each elastic model.....	119

1 Introduction

Coastal realms in active subduction zones are one of the most dynamic environments on earth, shaped by the overprinted signals of sea-level variations and vertical tectonic displacement through several mega earthquakes. These two combined signals are usually depicted in the morphology as extensive surfaces generated by waves and defined as marine terraces (Lyell, 1832; Chappell, 1974; Bloom and Yonekura, 1985). These geomorphic markers represent past sea-level positions, but also long baseline geodetic tracers of permanent deformation accumulated through several cycles of mega-earthquakes at millennial time-scales (Anderson and Menking, 1994; Melnick et al., 2006; Burbank and Anderson, 2011). Along the chapters of this thesis I focus on deconvolving the tectonic from sea-level signals using the landscape, determining patterns of permanent deformation. I developed new quantitative methods to achieve this objective based in sedimentology and morphometry. I used these methods to assess deformation rates at millennial time-scales and different spatial-scales to discuss several aspects of the earthquake cycle along the M8.8 Maule earthquake (2010) rupture zone in central Chile.

1.1 The tectonic signal

Tectonically active coastal regions in subduction zones are recurrently affected by mega-earthquakes within a cycle of accumulation and release of elastic strain (Savage, 1983; Thatcher, 1984), these phases have been documented by GPS velocities during and before the (2010) Maule earthquake (Kendrick et al., 2001; Klotz et al., 2001; Brooks et al., 2003; Khazaradze and Klotz, 2003; Wang, 2007; Moreno et al., 2008; Ruegg et al., 2009; Vigny et al., 2009; Moreno et al., 2010) (Fig. 1.2). In a simplistic manner the earthquake cycle comprises: A) An interseismic phase of strain accumulation, characterized by locking of the plate interface and surface displacements inlands (Fig. 1.2C). B) Coseismic rupture and strain release, characterized by slip at the plate interface and trenchward displacements at the upper plate (Fig. 1.2 D). Eventually, a third phase or post-seismic may follow the coseismic phase, characterized by transient complex processes in the years to decades following the earthquake (Wang, 2007). Theoretically, after several earthquake cycles the deficit of elastic deformation may be stored as permanently in the crust and producing active uplift and mountain building at thousand to million years time-scales (Darwin, 1851).

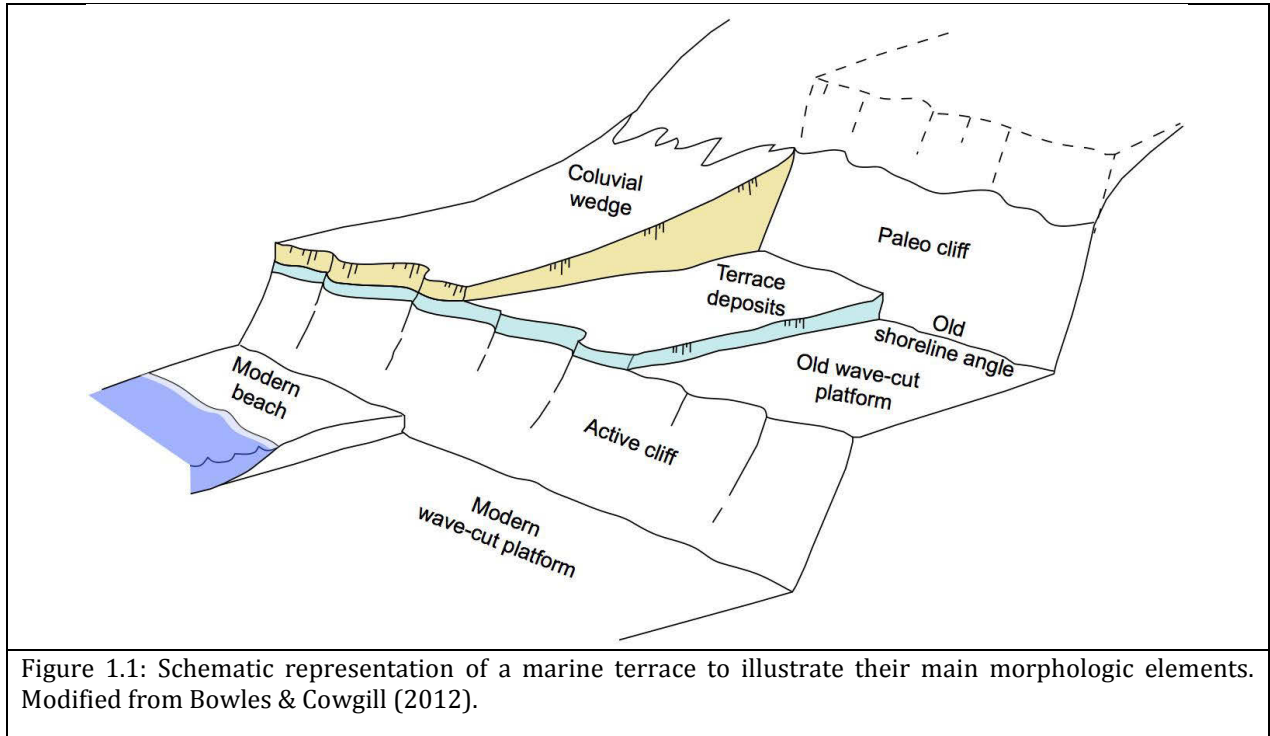
Forearcs regions in subduction zones are usually segmented into semi-independent seismotectonic blocks, geomorphic entities that may retain their style and rate of deformation over long timescales (Taylor et al., 1987; Melnick et al., 2009). Similarly, the slip distribution of great to giant (Mw 8 to 9) megathrust earthquakes exhibits a clear segmentation, as during the 2004 Sumatra (Chlieh et al., 2007), 1960 Chile (Moreno et al., 2009), and 2010 Maule events (Moreno et al., 2010); nevertheless, the correlation between coseismic slip and the sustained long-term segmentation of forearcs, particularly in Chile, remains poorly understood, likewise, is not known how much permanent deformation is being accrued along these segments in the course of several earthquake cycles; in addition, it is not known why forearcs may rupture recurrently along parts or the full length of such seismotectonic segments or why do some earthquakes rupture across such boundaries (Taylor et al., 2008; Udías et al., 2012). Along **Chapters 4** and **5** I attempt to answer these questions, which are primer research topics in the field of earthquake geology and crucial for the understanding of the spatiotemporal characteristics of seismic hazards along coastal areas in the (2010) Maule earthquake region.

1.2 The climatic signal

The register of paleo-temperatures during the Quaternary has been determined from measurements of oxygen isotopes in ocean sediment cores (Shackleton et al., 1983; Kukla et al., 2002; Shackleton et al., 2003) showing a pattern of oscillations defined as glacial and interglacial periods. The recurrence of these periods has been associated to “Milankovitch” cycles causing orbital insolation forcing of the ice ages due variability in the orbital eccentricity, axial tilt, and procession (Imbrie et al., 1992). The record of oxygen isotopes represents the temperature of the sea and has been described as the ratio between ^{18}O and ^{16}O . Variations of this ratio are produced by distillation, also known as fractionation, of water between the atmosphere and ocean; precipitations in the ocean remove ^{16}O that increases progressively in the atmosphere, in colder regions ^{16}O is concentrated in ice crystals depleted of ^{18}O . At millennial time-scales, major peaks, and in the record of oxygen isotopes were assigned a numbered MIS, with odd numbers for interglacial and even numbers for glacial cycles (Siddall et al., 2008). The temperature is converted to sea-level variations by accounting for the volume of water accumulated by ice sheets, during the Late Pleistocene the amplitude of sea-level oscillation reached ~ 120 meters (Siddall et al., 2003; Bintanja et al., 2005; Arz et al., 2007; Rohling et al., 2009) comprising several sea-level low stands and high stands that have been correlated with emerged and submerged geomorphic features like drowned shorelines, rasas, uplifted sequences of strand lines, and marine terraces worldwide (Pedoja et al., 2011; Pedoja et al., 2014).

1.3 Geomorphic markers: marine terraces

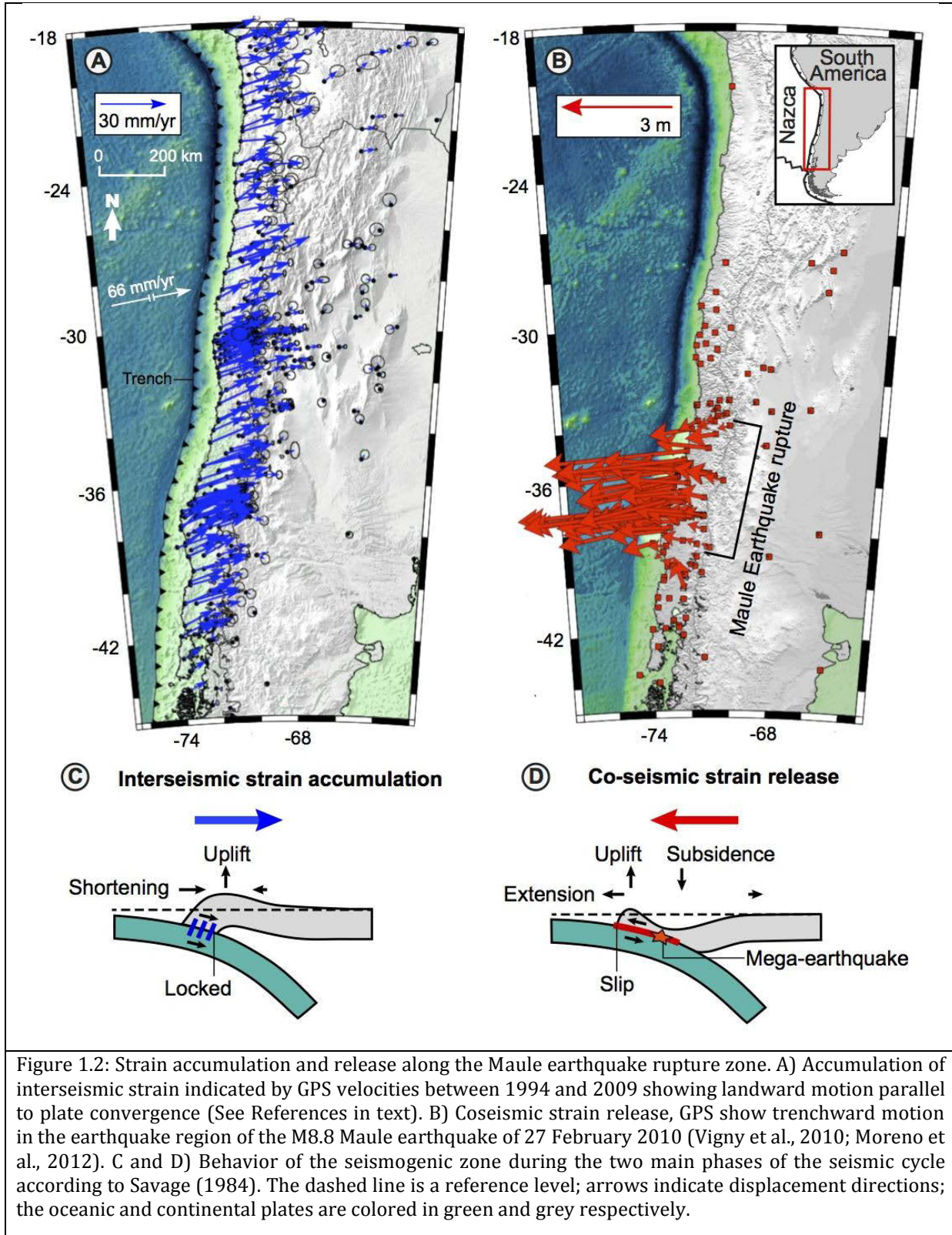
The tectonic and eustatic signals can be decoded from the landscape by using geomorphic markers, ephemeral features generated by the interaction of sea-level variations, erosion, accumulation, and tectonic displacements. Geomorphic markers can be used as a datum or piercing points to estimate the amount of vertical or lateral displacements, producing a reference frame against which to gauge differential or permanent deformation, then this data can be used to reconstruct vertical or lateral displacements (e.g. Anderson and Menking, 1994; Zielke et al., 2010; Burbank and Anderson, 2011). The geometry of a pristine geomorphic feature is a crucial attribute to select an adequate geomorphic marker, because the deformation of the surface of such feature records the tectonic signal (Burbank and Anderson, 2011). Marine terraces have been one of the most used geomorphic markers due its sharp morphology (Fig. 1.1), their extended geographic expression, the potential for successfully dating their surfaces, and the possibility to isolate tectonic from climatic signals using paleo sea-level proxies. However, due the interaction of accumulation and erosion processes the pristine morphology of marine terraces may be obliterated increasing the uncertainty of deformation rate estimates; in the other hand, the methods used to assess vertical displacements from marine terraces are diverse, but predominantly based on non-repeatable and qualitative approaches, this situation contrast with the increasing resolution of digital elevation models, such as Light detection and Ranging (LiDAR), which allows producing a vegetation-free surface digital terrain models, opening new possibilities for quantitatively study marine terraces in detail. Along this thesis I developed two methodologies described in **Chapters 2, 3** to assess permanent deformation rates and associated errors from wave built and wave-cut marine terraces. These methods were tested on exceptional exposures of marine terraces at several sites along the 500 ~km-long (2010) Maule earthquake rupture zone in Central Chile.



1.4 The Maule earthquake rupture zone

1.4.1 Tectonic and geomorphic framework

The M8.8 (2010) Maule earthquake occurred along a 500-km-long rupture in central Chile (34° - 38° S) an integral part of the tectonically active forearc of South America, where the oceanic Nazca plate is subducted beneath the South American continent at a convergence rate of 66 mm/yr (Angermann et al., 1999). This area poses a Mediterranean climate, with a wet season between April and August, with 600 to 1000 mm of accumulated annual precipitations. These climatic setting is controlled by the presence of a ~400 m height coastal range that extends N-S separating the central valley from the coastal area and controlling the drainage pattern at regional-scale (Rehak et al., 2008). The core of the Coastal Range is formed by a high-pressure Paleozoic accretionary complex intruded by a granitic batholith (Kato, 1985), overlaid at some localities by Mesozoic and Cenozoic sedimentary sequences (Gonzalez, 1990; Le Roux and Elgueta, 2000; Encinas et al., 2006b; Finger et al., 2007). The coastal range is traversed by the Bio-Bio river at the southern part of the rupture, by the Itata, Maule, and Mataquito rivers at the central part, and by the Rapel river at the northern part of the rupture; all of them actively transporting sediments from the central depression and volcanic arc, controlling the sedimentation patterns in coastal areas, and eroding the shelf and continental slope, as depicted by submarine canyons formed at their outlets (Thornburg and Kulm, 1987b, a; Völker et al., 2014). These geomorphic, geologic, and climatic conditions have been favorable for the preservation of marine terraces along the western slope of the coastal range for several glacial cycles (Kaizuka et al., 1973; Melnick et al., 2009).



1.4.2 The 2010 Maule earthquake

The 2010 Maule earthquake of February 27 was nucleated in the central part of its rupture reaching a moment magnitude of 8.9 and producing a catastrophic tsunami that devastated several populated coastal cities producing hundreds of casualties and enormous economic lost. This event

corresponds to the sixth largest instrumentally recorded earthquake and the third largest in the era of space geodesy (Vigny et al., 2011) reaching ~16m of slip at the plate interface (Moreno et al., 2010) and 3 m of coastal uplift (Farias et al., 2010b). Before 2010, this region had been long recognized as a mature seismic gap (Barrientos, 1987; Campos et al., 2002; Melnick et al., 2012c), its predecessor, the 1835 M~8.2 Concepcion earthquake had similar magnitude and extent as the 2010 Maule earthquake, producing a catastrophic tsunami and coastal uplift documented by Darwin and Fitz Roy during the voyage of the Beagle (FitzRoy et al., 1839; Darwin, 1851).

The Maule earthquake has been one of the better-studied mega-earthquakes with a register of geodetic GPS velocities since one decade before the event (Kendrick et al., 2001; Klotz et al., 2001; Brooks et al., 2003; Khazaradze and Klotz, 2003; Wang, 2007; Moreno et al., 2008; Ruegg et al., 2009; Moreno et al., 2010; Yue et al., 2014), allowing observing the pattern of surface displacements during two phases of the seismic cycle (Fig 1.2 A and B). In addition, the recent study of Wesson et al. (Wesson et al., 2015) has documented the pattern of vertical deformation through a complete seismic cycle between the 1835 Concepcion and the 2010 Maule earthquakes using historic nautical charts, presenting for first time empirical evidence to sustain the slip-predictable recurrence of subduction mega-earthquakes.

1.5 Thesis organization

This cumulative thesis is constituted by four main chapters. Chapters 2, 3, and 4 of this thesis have been already published in first-tier scientific journals during 2015, including: Quaternary Research, GSA Geosphere, and Quaternary Science Reviews respectively; Chapter 5 has been submitted to AGU Journal of Geophysical Research and is currently under review.

Chapter 2 describes the stratigraphic architecture of an archetypical example of wave-built terrace in Santa Maria Island. Excellent exposures along the cliff that surround the island displays continuous sequences of Pleistocene deposits overlying a tertiary bedrock. A novel method is used to estimate uplift rates based on statistical analysis of grain-size distributions coupled with facies descriptions and radiocarbon dating. I detected depositional cycles that I used to correlate with relative sea-level curves to obtain uplift rates. This study demonstrates that wave-built marine terrace deposits along clastic shorelines in temperate regions are useful to distinguish between tectonic uplift and climate-induced sea-level changes and can be used as reliable markers to obtain permanent vertical deformation rates.

The precise assessment of marine terrace elevations is crucial to obtain consistent uplift rates estimates. Along **Chapter 3** I address this topic developing TerraceM(*), a MATLAB® Graphic User Interface to assess and map wave-cut marine terraces using high-resolution topography. This study centers on detecting the shoreline angle, a geomorphic marker used as a proxy for estimating vertical deformation rates. Two test sites to study the morphology of wave-cut marine terraces were selected, at Santa Cruz California, and along the Maule earthquake rupture. Both areas are characterized by similar climatic conditions and located in tectonically active coastal realms. TerraceM allows extracting and processing bulk of profiles using quantitative and repeatable methods.

(*) See www.terracem.com

Chapter 4 Is a regional-scale study of marine terraces along the (2010) Maule earthquake rupture zone. Wave-cut and wave-built marine terraces distributed along 500 km of coastal realms were

analyzed using the methodologies developed in **Chapter 2** and **3**. Geomorphic observations were coupled with 12 IRSL ages to obtain an almost continuous register of permanent deformation rates along the rupture. Patterns and magnitudes of permanent deformation rates from marine terraces were compared with interseismic locking and coseismic slip during the 2010 Maule earthquake, as well as historic mega-earthquake ruptures in this area to discuss the nature of earthquake barriers and the processes governing earthquake segmentation over hundreds of thousands of years time-scales.

Chapter 5 is a local-scale study of drowned shorelines distributed offshore at the Arauco Bay at the southern boundary of the 2010 Maule earthquake rupture. This area comprises an active splay fault, defined as Santa Maria Fault System, which breached from plate interface during the (2010) Maule earthquake producing surface rupture and ~2 m of coseismic uplift at Santa Maria Island. The kinematic of this structure, has been recently debated due its importance for the mechanisms of upper plate deformation during mega earthquakes. I recognized and mapped drowned shorelines using a multi-disciplinary approach including submersible observations using a Remote Operated Vehicle, sedimentology, 3D morphoscopy of samples, paleontology, and the morphometric methods for mapping marine terraces developed in **Chapter 3** but oriented to submarine realms. Permanent deformation rates were obtained using a landscape evolution model that simulates the formation of drowned shorelines. Uplift rates from onshore marine terraces surveyed in **Chapter 4** were included, obtaining an extended pattern of permanent deformation. An elastic deformation model was used to estimate the slip rate and kinematics of the Santa Maria Fault System. Scaling laws and different recurrence rates are applied to estimate the magnitude of an earthquake produced by the reactivation of this splay fault. This study highlights a previously unrecognized tsunamigenic source in the Arauco Bay area.

2 Unraveling sea-level variations and tectonic uplift in wave-built marine terraces, Santa María Island, Chile.

The architecture of coastal sequences in tectonically active regions results mostly from a combination of sea and land-level changes. Along this chapter I develop a method to unravel these signals by combining sequence stratigraphy and sedimentology of near-shore sedimentary sequences in wave-built terraces. I focus on Santa María Island at the southern part of the 2010 Maule earthquake rupture, which hosts excellent exposures of coastal sediments from Marine Isotope Stage 3. A novel method based on statistical analysis of grain-size distributions coupled with facies descriptions provided a detailed account of transgressive–regressive cycles. Radiocarbon ages from paleosols constrain the chronology between ~ 53 and ~ 31 cal ka BP. Because the influence of glaciations can be neglected, we calculated relative sea-level curves by tying the onset of deposition on a bedrock abrasion platform to a global sea-level curve. The observed depositional cycles match those predicted for uplift rates between 1.2 and 1.8 m/ka. The studied sedimentary units represent depositional cycles that resulted in reoccupation events of an existing marine terrace. Our study demonstrates that wave-built marine terrace deposits along clastic shorelines in temperate regions can be used to distinguish between tectonic uplift and climate-induced sea-level changes.

2.1 Introduction

Coastal geomorphic features such as modern sandy beaches, rocky shores and wave-cut platforms are largely generated by waves action and sediment availability, resulting in constructive (moving sediment shoreward) or destructive (causing erosion) end members (Bird and Bird, 2000). Marine terraces are the fossil counterparts of such modern coastal features, expressed as low-relief surfaces resulting from the combined effects of tectonic uplift and eustatic sea-level fluctuations (e.g. Bloom and Yonekura, 1985; Lajoie, 1986; Kelsey and Bockheim, 1994; Anderson et al., 1999).

Marine terraces in temperate regions fall into two broad categories according to their genesis: wave-cut terraces and wave-built terraces. The former are gently sloping surfaces produced by wave erosion and cliff retreat (Anderson et al., 1999), with either a thin sedimentary cover or no cover at all. In turn, wave-built terraces, also referred to as constructional terraces, are gently sloping coastal features at the sea-ward edge of a wave-cut bedrock platform formed of sediment accumulations carried by rivers and drifted either along the coastline or across the wave-cut platform (e.g. Gilbert, 1890; Bird and Bird, 2000; Jackson et al., 2005). At the end of an interglacial period, wave-cut platforms will be left subaerially exposed by falling sea-levels. Depending on the local uplift rate, these platforms may be abandoned and new platforms formed at lower elevations during subsequent highstands generating the classic staircase morphology of marine terrace sequences (e.g. Bloom et al., 1974; Anderson et al., 1999). Under low uplift rates, terrace reoccupation episodes resulting from superimposed highstands may generate characteristic wide treads or rasas through cliff retreat (Kelsey and Bockheim, 1994; Pedoja et al., 2014). If there is adequate sediment input, reoccupation events may also contribute to generate thick sedimentary packages, resulting in composite depositional surfaces that record the combined effects of sea-level variations and/or tectonic uplift (e.g. Cantalamessa and Di Celma, 2004).

The relative role of sea-level variations and tectonic uplift in the development of wave-built terraces and their significance as markers of tectonic deformation, have not yet been in the context of marine terrace formation processes. Furthermore, from a global compilation of 935 sites with coastal sequences including the Marine Isotope Stage (MIS) 5 benchmark, wave-built terraces have been described at only 13 locations (Pedoja et al., 2011). No clear distinctions have yet been made in terms of definition between thick coastal deposits overlying a fossil rocky shore platform (i.e., thick marine terrace or thick raised beach) and a wave-built terrace. Consequently, many of the preserved coastal Quaternary sequences may be classified as wave-built terraces. Considering these elements, the improvement in the knowledge of wave-built terraces might help to expand the records of global sea-level variations and to improve regional-scale correlations.

The objective of this study is to unravel tectonic uplift from sea-level variations in wave-built terraces, and to assess their use as deformation markers. To achieve the objective we implemented a new method to distinguish sea-level variations from tectonic uplift using the stratigraphic patterns of depositional environments and a sea-level curve. This study focuses on Santa María Island (SMI), located in the temperate south-central Chile convergent margin (Fig. 2.1A). We analyze an up to 60-m-thick sequence of coastal sediments deposited during MIS 3 on a Tertiary bedrock platform, exceptionally well exposed in coastal cliffs. We further compare our

results with independent estimates of uplift rate obtained previously at SMI and with the timing of wave-cut terrace formation in the Pacific region.

2.2 Geologic setting of Santa María Island

SMI is located immediately north of the Arauco Peninsula, on an uplifted part of the Chilean continental shelf, where the Nazca oceanic plate is subducted below South America (Fig. 2.1A). During the 2010 Maule earthquake (Mw 8.8) SMI was uplifted between 1.6 and 2.2 m associated with motion of a crustal fault (Melnick et al., 2012a; Melnick et al., 2012d).

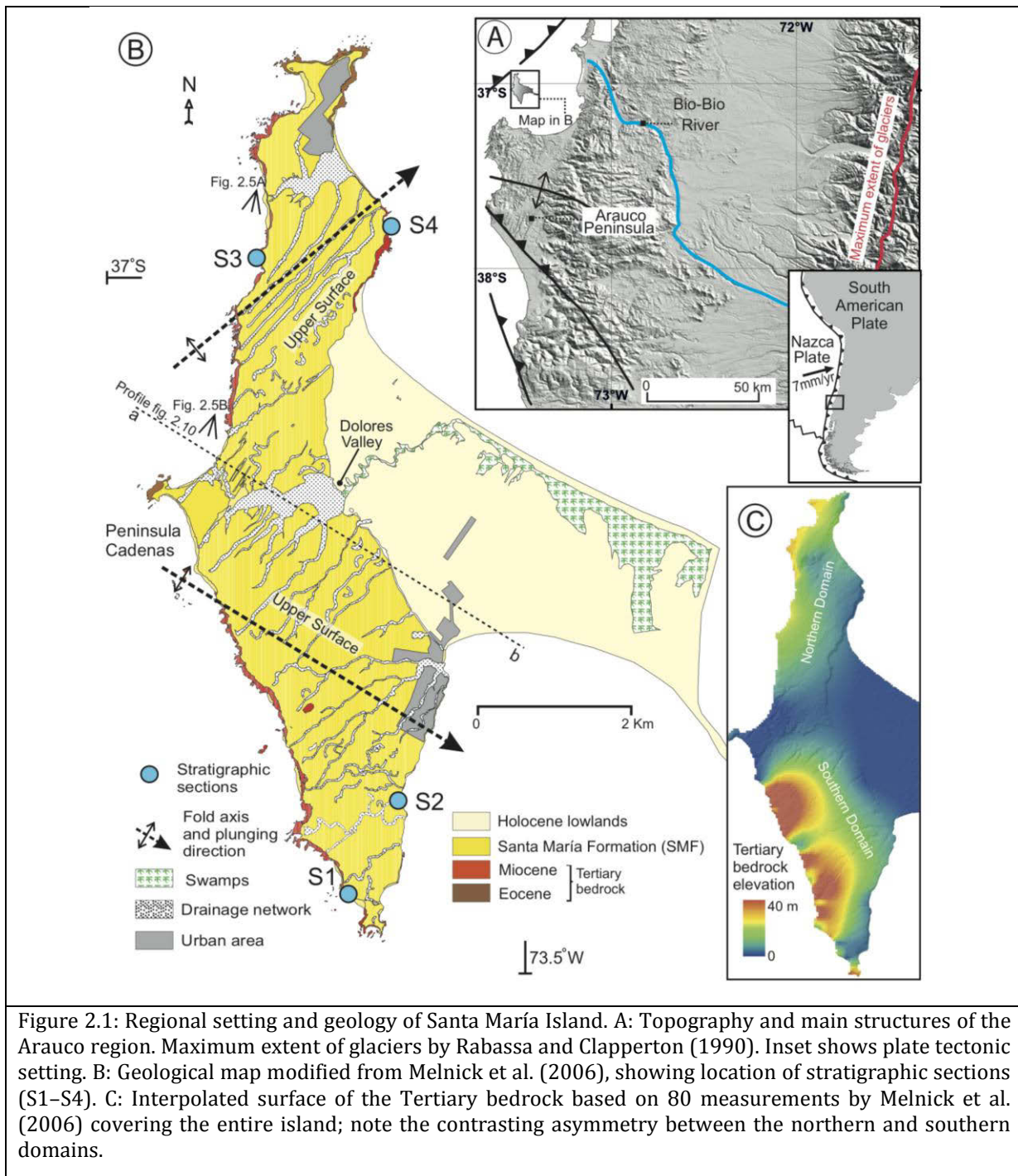


Figure 2.1: Regional setting and geology of Santa María Island. A: Topography and main structures of the Arauco region. Maximum extent of glaciers by Rabassa and Clapperton (1990). Inset shows plate tectonic setting. B: Geological map modified from Melnick et al. (2006), showing location of stratigraphic sections (S1–S4). C: Interpolated surface of the Tertiary bedrock based on 80 measurements by Melnick et al. (2006) covering the entire island; note the contrasting asymmetry between the northern and southern domains.

The surface morphology of SMI comprises two main units (Fig. 2.1B): the upper surface and the Holocene lowlands (Melnick et al., 2006). The upper surface consists of a 40- to 80-m-high planar surface that slopes gently ($\sim 2^\circ$) eastward and is bounded by steep, actively eroding cliffs. This surface is divided into northern and southern domains by a valley at the center of the island. The Holocene lowlands lie to the east of the upper surface at elevations below ~ 10 m (Fig. 2.1B) comprising active dunes, shore deposits, and a sequence of raised beach ridges (Bookhagen et al., 2006).

The geology of SMI includes three lithological units (Fig. 2.1B): an Eocene to Miocene sedimentary bedrock overlaid by clastic Pleistocene deposits of the Santa María Formation (SMF), and Holocene deposits. The elevation pattern of the Tertiary–Pleistocene unconformity was derived by interpolating 80 measurements collected by Melnick et al. (2006) from the island's cliffs (Fig. 2.1C). This unconformity surface exhibits a north–south asymmetry; it reaches 60 m elevation in the south and is characterized by an irregular paleo-relief, while to the north it forms a smooth surface with elevations of between 10 and 20 m (Fig. 2.1C). The unconformity surface dips towards the east in both the northern and southern domains, mimicking the surface topography, interpreted as a result of the progressive tilting of the island (see Melnick et al. (2006) for details on the structural setting).

Two previous studies estimated uplift rates at SMI based on different techniques obtaining similar results. Bookhagen et al. (2006) estimated a mean uplift rate of 2.3 ± 0.2 m/ka over approximately the last ~ 4 ka, using luminescence ages from raised beach berms in the Holocene lowlands. In turn, Melnick et al. (2006) determined an uplift rate based on the assumption that the paleosols from the SMF were formed close to sea level under similar conditions to the present-day depositional environments observed in the back swamps of the Holocene lowlands (see Section 2.3), obtaining a mean uplift rate of 1.8 ± 0.4 m/ka over the past ~ 50 ka. Because the exact paleo-position of the dated samples with respect to the sea level at that time is difficult to ascertain, these authors emphasized that these uplift rate estimates should be considered as maximum.

2.3 Stratigraphy and chronology of the Santa Maria Formation

This sedimentary sequence was first defined by Melnick et al. (2006) and consists of black volcanic sands from coastal depositional environments deposited above Tertiary bedrock. Two distinct units have been differentiated within the SMF: a lower unit (U1) and an upper unit (U2), separated by a conformable transitional contact. The lower unit consists of poorly consolidated, stratified, medium- to coarse-grained sandstone with cross-bedding, wavy flaser bedding, and occasional vertical bioturbation; the thickness of this unit increases eastwards. The upper unit comprises very well sorted, semi-consolidated, gray to brownish medium to fine sandstone, forming a characteristic rhythmic succession of homogeneous beds with alternating sets of horizontal and inclined laminations. These units were interpreted as deposited in shallow marine and eolian environments, respectively.

Fourteen radiocarbon ages obtained by Melnick et al. (2006) suggest that these sediments belong to MIS 3. Minimum ages obtained from the base of the SMF indicate that the onset of SMF deposition occurred before ~ 53 ka. The onset of eolian deposition in the SMF was constrained at

31.5 cal ka BP, on the basis of a sample obtained from the base of U2. The authors inferred that eolian deposition lasted between 31.5 and ~ 27 ka, based on the relatively stable sea level over this time interval (Siddall et al., 2003b) and the observation that present-day dunes in this area are active only below 20 m.

2.4 Setting of wave-built terraces

Coastal currents, accumulation processes, and tectonic uplift along coastal areas are all known to play important roles in the development of wave-cut platforms and beach bar systems (e.g. Anderson et al., 1999; Trenhaile, 2002a; Trenhaile, 2002b; Storms and Swift, 2003). Exposure of present-day headlands to wave erosion favors the development of wave-cut platforms sculpted into the bedrock, while wave refraction in bays favors the accumulation of sediment bodies (e.g. Trenhaile, 2002a). Wave-built terraces have for many years been considered to be composed of shallow marine or lacustrine sequences (e.g. Gilbert, 1890; Dietz, 1963) deposited during sea-level highstands and dominated by the architecture of regressive sedimentary cycles (e.g. Naish and Kamp, 1997; Storms and Swift, 2003; Cornée et al., 2006; Reuter et al., 2009). Furthermore, recent studies have shown that wave-built terraces may also be formed during sea-level lowstands (Fracaccasia et al., 2013) providing extended records of paleo-sea level in contrast to wave-cut terraces, which usually are formed during high stands.

Stratigraphic studies on coral-reef terraces have revealed that the sedimentary architecture and thickness of the sequences are controlled by the shape and amplitude of the relative sea-level variations (Zecchin et al., 2009). If the sea-level variations are of low amplitude the tectonic uplift will have a major influence on the characteristics of the resulting transgressive–regressive events, which will therefore be reflected in the terrace shape and the stratigraphic architecture (e.g. Strecker et al., 1986; Zecchin et al., 2009).

2.5 Methods

2.5.1 Stratigraphic sections of the Santa María Formation

Four stratigraphic sections were analyzed along complete exposures of the SMF on fresh sea-cliffs, extending from the Tertiary unconformity to the depositional top of the SMF. Sediment samples were obtained to analyze their grain-size distribution. Considering that the SMF consists of meter-thick strata with sharp boundaries, samples were collected at a ~ 2-m vertical interval along each section. The stratigraphic sections were described by facies including, color, grain size, mineralogy and sedimentary structures, and sampled continuously using rappel techniques (details in Appendix A).

2.5.2 Granulometric analysis

Along the stratigraphic sections of the SMF, 77 samples were collected and a further 28 from modern depositional environments (including the swash zone, shore face, berms, and active dunes; details in Appendix A.2). The samples consisted of unconsolidated to partially consolidated sands and sandy clays; the sand fraction was separated and analyzed using the sieving methodologies proposed by Folk (1980). The granulometric distribution of the 105 samples was examined using the GRADISTAT software (Blott and Pye, 2001) obtaining the grain-

size population parameters (mean, sorting, skewness, and kurtosis) using the moment measure method (Krumbein and Pettijohn, 1938; Boggs, 1987) (details in Appendix A.3). The results were grouped into two matrixes with dimensions of 77×4 for the SMF and 28×4 for the modern depositional environments. The statistical parameters of the grain-size populations were studied through multivariate statistical analysis (Figure A3 and Table A1 in Appendix A), in order to complement the environmental interpretations deduced from the facies. We used the granulometric signature of modern depositional environments on SMI as representative equivalents of the SMF depositional environments (details in Appendix A.4).

2.5.3 Sample collection for radiocarbon dating

The new ages obtained in this study complement those of Melnick et al. (2006), which were collected mostly from the lower parts of the SMF. The 2010 earthquake triggered many landslides and occasionally the total collapse of the sea cliffs surrounding the island, allowing better accessibility to the SMF. We took advantage of this opportunity and collected six new samples for radiocarbon dating analyzed at the Poznan Laboratory accelerator mass spectrometer (AMS) facility in Poland.

The dated material consists mostly of charcoal and a wood fragment collected from paleosol horizons. The fragments were picked in the laboratory and studied with Energy Dispersive spectrometry (SEM) imaging, in order to analyze the micromorphology and composition (further details in Appendix A.5). All the ages used in this study have been converted to calendric ages using the OxCal 4.2 software (Ramsey, 1994) and the SHCal13 calibration curve (Hogg et al., 2013).

2.5.4 Construction of relative sea-level curves

To unravel the relative influence of sea-level variations and tectonic uplift on the architecture of the SMF, we compared two independent sea-level records. The first based on the stratigraphic and sedimentological analysis of the SMF, and the second on relative sea-level curves derived for SMI under the assumptions described below.

Relative sea level at a defined location is controlled mostly by the local tectonic uplift rate and variations in eustatic sea level, but other regional to sub-regional factors may also exert and influence such as flexural rebound associated with loading and unloading of ice sheets, the syphoning of water into subsiding ocean basins, and the lateral gravitational attraction of ice sheets, among others (e.g. Berryman, 1993; Mitrovica and Davis, 1995; Stewart et al., 2000; Ota and Yamaguchi, 2004; Shepherd and Wingham, 2007). From the latter three processes, only flexural rebound may have possibly affected SMI.

The Earth's crust behaves as a stiff, elastic solid when subjected to changes in surface loads, and the areal extent of flexural rebound associated with loading and unloading of ice sheets will mostly depend on the flexural rigidity of the lithosphere (e.g. Turcotte and Schubert, 1982). At the latitude of SMI (37°S), Pleistocene glaciers were restricted to elevations above ~ 2000 m in the Main Cordillera (Fig. 2.1A; Rabassa and Clapperton, (1990), ~ 180 km inland. Flexural rebound at $45\text{--}52^{\circ}\text{S}$ affects a ~ 120 -km-wide region surrounding the Patagonian Ice fields (Dietrich et al., 2010), and this wavelength should be similar at the latitude of SMI as the flexural rigidity remains

relatively constant (e.g. Pérez-Gussinyé et al., 2008). Therefore it is unlikely that significant amounts of flexural rebound associated with ice sheets affected relative sea level at SMI.

Furthermore, the largest changes in ice sheet loading and unloading occurred during the last glacial maximum (LGM) at ~ 20 ka, after deposition of the SMF. Because our analysis is not based on the elevation of the stratigraphic units but on their depositional patterns, the results are independent of any post-depositional flexural rebound during and after the LGM. Therefore, the effect of LGM glaciation will not affect relative sea-level estimates at SMI during the MIS 3.

The relative sea-level curves were constructed by calculating the difference between a constant uplift rate and an absolute sea-level curve. We use a range of uplift rates between 1.0 and 2.6 m/ka (the range of previously published estimates, see Section 2.1) and the absolute sea-level curve of Arz et al. (2007), which is the most detailed record during MIS 3. Finally, we narrowed down the range of uplift rates by finding the submerged periods predicted by the relative sea-level curves that best fit the observed stratigraphy. A relative sea-level curve estimates the duration of sea-level change episodes at a given site, and will be independent of the uncertainties in absolute sea level. Thickness, sedimentation rate and post-depositional sediment compaction do not influence the uplift rate estimates, which are only based on the correlation between variations in relative sea-level and the stratigraphy.

2.6 Results

2.6.1 Sedimentary facies

The SMF is formed of multiple backshore–shore successions that can be recognized by their depositional facies. Six depositional facies were distinguished on the basis of color, texture, and sedimentary structures (Figs. 2.2 and 2.3), as detailed below.

a) The Sm facies (Massive sandstones) consists of massive, brown to gray, medium-grained sandstones (Figs. 2.2A and 2.3A) with partially preserved in-situ trace fossils exposed on the uppermost surfaces of individual beds and occasional lenticular paleosols, 0.5 to 2 m thick. The trace fossils consist of 15-cm-long horizontal cylindrical cavities that curve upwards into 3-cm-long vertical sections. These features can be classified as insect burrows belonging to the family of tiger beetles (*Cicindelidae* sp.), which are restricted to dry sandy environments (Pearson, 1988). The facies is commonly observed in the upper portions of the sequence, with thicknesses ranging between 1.5 and 2.5 m. The mud content varies between 3% and 20%, depending of the degree of pedogenesis and the presence or absence of paleosol horizons (Fig. 2.3E). The presence of lenticular brown mud lenses and *Cicindelidae* sp. suggests that the Sm facies was probably formed in the transition to the backshore, such as on the berm, with the lenticular paleosol (Ps facies) representing back swamp conditions.

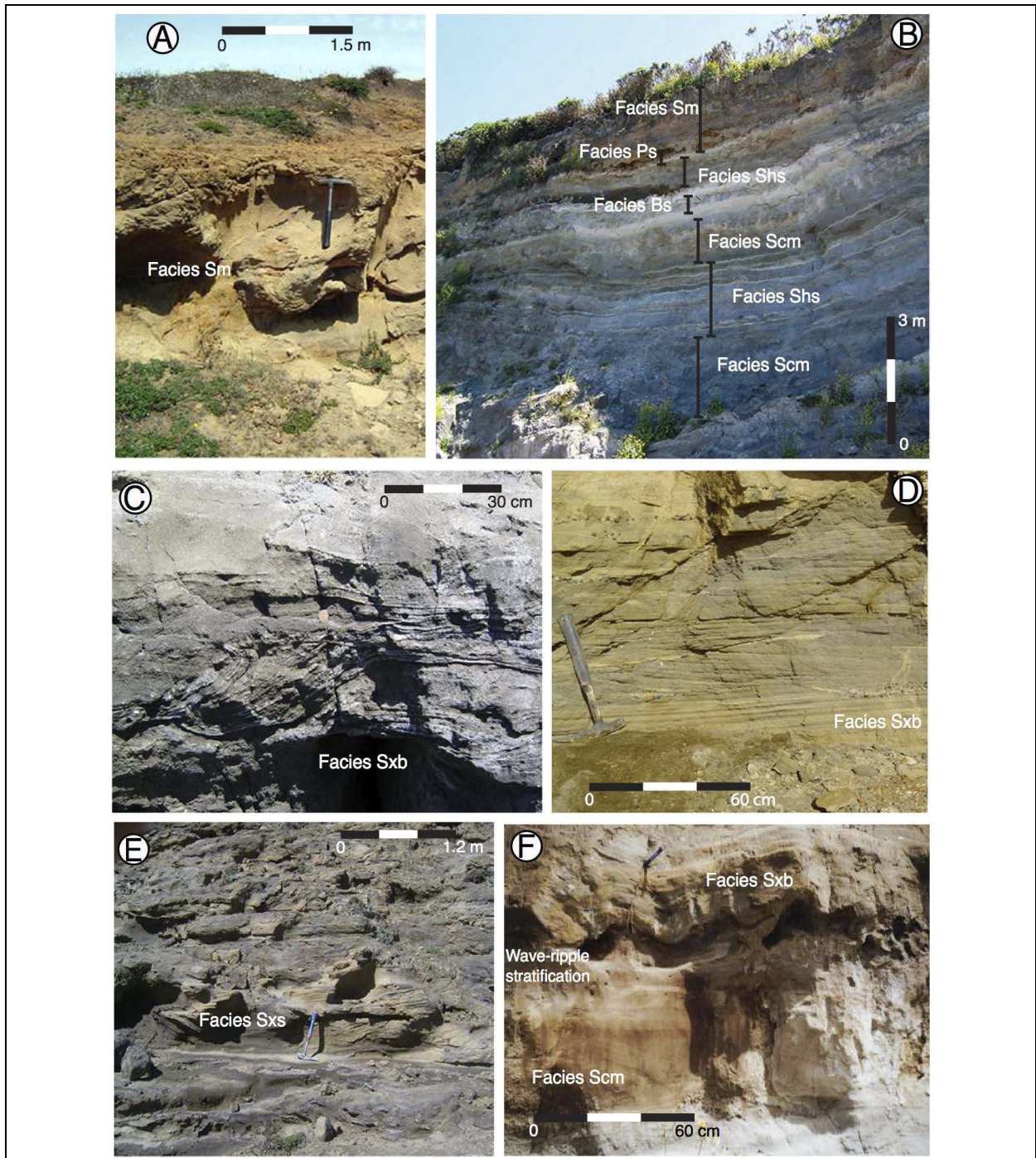
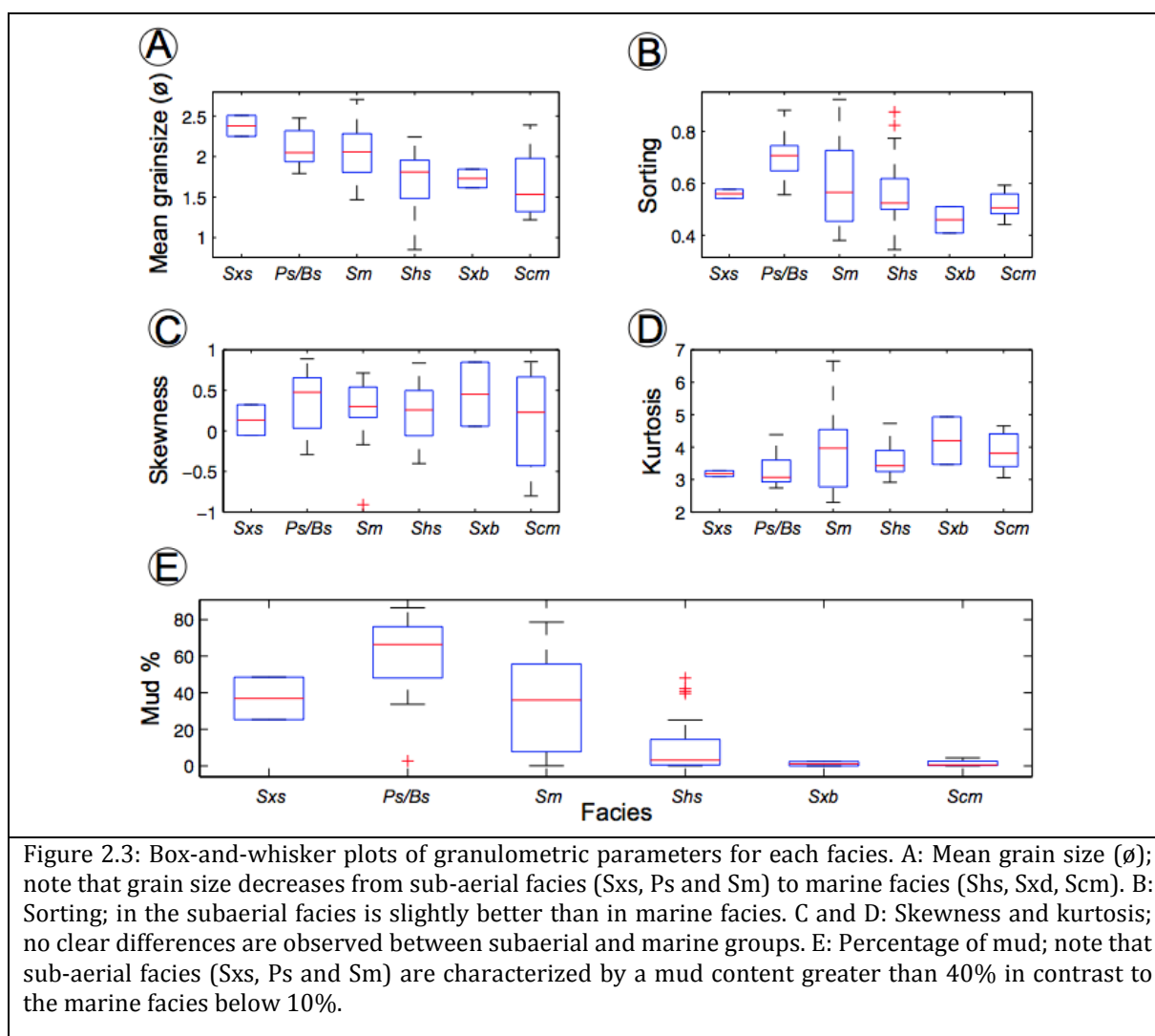


Figure 2.2: Field views of facies in the SFM. A: Typical massive aspect of the Sm facies, with the characteristic brownish color. B: Example of the transition between marine facies (Shs and Scm) and sub-aerial facies (Sm and Ps). C: Example of irregular cross-bedding in the Sxd facies. D: Hummocky stratification in the Sxd facies. E: Inclined stratification of the Sxs facies in the upper parts of the sequence. F: Example of wave-ripple stratification developed between Sxb and Scm facies at the lower parts of the sequence.

b) The Ps facies (Paleosol) is composed of light reddish brown (5YR 6/3) to strong brown (7.5YR 4/6) silty clay with remnants of charcoal fragments and iron oxide precipitates. The mud content is greater than 50% (Fig. 2.3E) and their thickness ranges between 0.5 and 1 m (Fig. 2.2B). Texturally, it shows normal grading to medium sands; the upper contact of this facies is generally

sharp and irregular often characterized by the presence of colloidal iron precipitates. This facies occurs mainly in the upper parts of the SMF as lenticular irregular bodies within the Sm facies, Sxs facies and occasionally associated with Shs facies. Because of its high mud content, color, the normal grading, and the occurrence of erosional upper boundaries, this facies is interpreted to represent a loam-type soil developed in situ under oxidizing conditions, where iron precipitates are associated to leaching.



c) The Bs facies (Back-swamp) consists of gray (5YR 6/1) to greenish gray clays with 2% of distinct, dark greenish gray mottles, 2 to 5 mm diameter of organic matter content; this facies is often overlaid by a light gray clay layer that likely represent an E horizon. It ranges in thickness between 0.5 and 1.5 m and is characterized by the presence of roots and large carbonized branches up to 30 cm long, which we used for dating (See Appendix A.4). This facies occurs normally in the lower and central parts of the sequence, the upper contact is sharp and irregular associated with Shs, Sxd and Scm facies. Considering the texture and color we classified this facies as a gley-type soil horizon, developed in a humid and anoxic environment. The latter is corroborated by the presence of charcoal and well preserved partly carbonified wood fragments. A present day analog to such an environment may be represented by wetlands observed within

the Dolores valley and in the Holocene lowlands, which are developed at elevations below 5 m above msl.

d) The Sxs facies (Cross-stratified sandstone) consists of fine-to medium-grained (Fig. 2.3A), partially consolidated brown sands with centimeter to meter scale inclined-stratification and small relicts of *Cicinellidae* sp. tubes (Fig. 2.2E). This facies is also present in the upper part of the sequence and has been observed only in the S1 section. It is characterized by a 25% to 40% mud content (Fig. 2.3E) observed as partially oxidized and argillized sand fragments attributed to the effects of leaching processes. Because of the presence of *Cicinellidae* sp., the inclined stratification, the medium to fine grain size, the narrow range in sorting and positive skewness (Figs. 2.3B and C), this facies is thought to represent dunes formed in the backshore area, away from the influence of tides and waves.

e) The Shs facies (Horizontally stratified sandstone) is characterized by medium to coarse moderately sorted sand (Figs. 2.3A and B) over a thickness of 10 to 70 cm and sub-horizontal or gently seaward dipping stratification (Fig. 2.2B). The fine fraction content varies from 0.5% to 10% (Fig. 2.3E), mainly associated with interbedded silt layers about 5 cm thick that exhibit small-scale normal gradation to coarse sand. The only fossils found within this facies were small bioclastic fragments of unidentified *Mollusca* sp. shells in some of the coarser grained layers. The thickness of the Shs facies varies between 1 and 8 m; it was probably formed in an upper shore face to foreshore environment, as indicated by the presence sub-horizontal stratification.

f) The Sxb (Cross-bedded sandstone) facies has been identified in the lower parts of the sequences. It is composed of poorly sorted consolidated medium-grained sands (Figs. 2.3A and B) with cm- to m-scale trough cross-bedding (Figs. 2.2C, D and F) and occasional hummocky stratification in which the tops of the foreset beds have usually been eroded. Centimeter-scale wave ripple cross-stratifications have also been observed in this facies (Fig. 2.2F). The mud fraction composes up to 10% of the total (Fig. 2.3E) and this facies is devoid of fossils. Trough cross-bedding and wave ripple cross-stratification are indicative of shallow-water conditions, and the truncated foresets are indicative of wave reworking or diffusive processes. The Sxd facies is therefore thought to have formed in a wave-influenced environment such as the upper and central parts of the shore face.

g) The Scm facies (massive coarse sandstone) is characterized by medium-grained homogeneous sands, with occasional thin coarse-grained layers. The fine fraction comprises between 0.5% and 5% (Fig. 2.3E), commonly increasing with depth. The facies thickness ranges between 1 and 6 m (Figs. 2.2B and F) and it is confined to the base of the sequence. Small shell fragments of unidentified *Mollusca* sp. were found at a few locations. This facies can be differentiated from the Sm facies on the basis of its lower fine sediment content, its medium to coarse granulometry, and the absence of oxidized and argillic clasts related to sub-aerial pedogenic processes. In view of the absence of indicative sedimentary structures and the occasional presence of bioclastic fragments, a marine depositional environment beyond the influence of waves is interpreted for the Scm facies; the sporadic occurrence of coarse-grained layers is attributed to storm wave base transport effects. This facies is therefore thought to have formed at a depth only occasionally affected by turbulent flows, such as is found in the lower and central parts of the shore face.

2.6.2 Radiocarbon ages

The ages obtained in this study range between 32 and 49.5 cal ka BP (Table 2.1). The material was typically embedded as isolated fragments inside a clayey matrix (Figures A5 to A7 in Appendix A). Charcoal fragments were preserved in Ps and Bs facies and had variable sizes ranging from 0.5 to 5 cm with elongated and angular shapes, evincing no transport and suggesting in-situ formation. We dated four concretions formed by charcoal coated by iron colloidal oxides, manganese and pyrite in loamy soils (Table 2.1). The bulk sediment of one paleosol layer lacking of charcoal or wood fragments yielded an age of 32.8 ± 0.5 cal ka BP. Further information and detailed descriptions of both outcrop setting and microtextures of the dated material from electron microscope imagery can be found in the Appendix A.5.

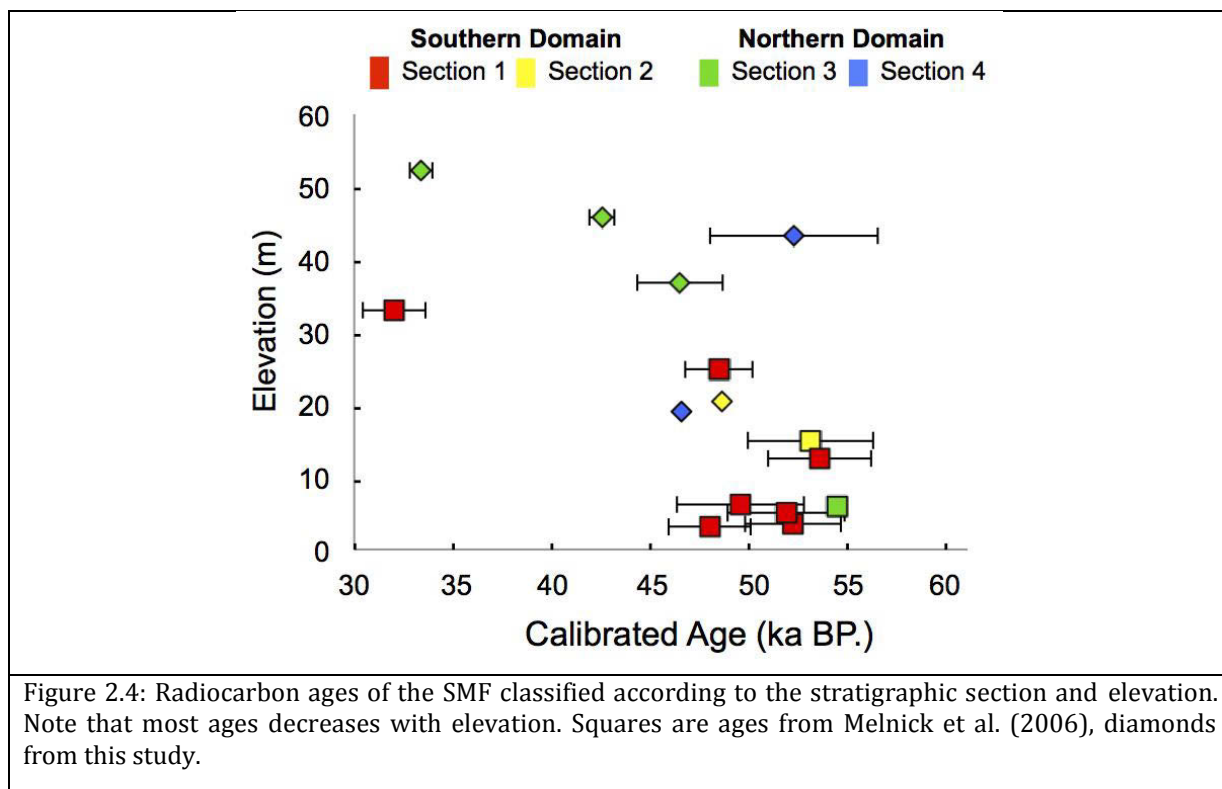
The dated material was considered unlikely to be contaminated because of: (1) stratigraphic concordance — ages obtained from lower stratigraphic levels were consistently older than those from higher levels (Fig. 2.4); (2) the thickness of the sedimentary sequence — the samples were collected from fresh sea-cliff exposures without roots or modern contamination, more than 6 m below the top of the sequence; and (3) the type of material used — dating was performed on centimeter-sized charcoal fragments and a large piece of well-preserved carbonized wood. Contamination from Eocene coal seams can be discarded, as their outcrops are restricted to a single location near the northern point of the island (Fig. 2.1B), and coal chunks were not observed, neither in palosol horizons nor in any layers of the SMF.

Table 2.1: Radiocarbon ages of SMF

Lab code	Material	Stratigraphic		Age (yr B.P.)	error (yr)	Calibrated	1 σ error (yr)	Elevation (m)
		section	position			Age# (yr B.P.)		
Poz-55108	wood	S4	C2a-C2b	47000	3000	49572	4620	43.2
Poz-55122	charcoal	S3	C1a-C1b	42000	2000	46028	1770	36.8
Poz-55123	charcoal	S4	C1a-C1b	46000*		49514		19
Poz-55159	charcoal	S2	C1-C2	48000*				20.4
Poz-55109	charcoal	S3	C2a-C2b	37400	900	41810	738	45.8
Poz-55619	Bulk	S3	C2b-C3	28820	450	32838	575	52.2
KIA24186	paleosol	S1	C2b-C3	27380	1750	32186	2151	33
KIA24181	paleosol	S1	Base	52750	2530	54419	3521	12.5
KIA24182	peat	S3	Base	53600*				6
KIA25773	clay	S1	C2a-C2b	44480	725	47865	840	24.8
KIA24187	paleosol	S2	C1a-C1b	48080	1900	48902	2293	15

The upper age limit for radiocarbon dating has been commonly assumed to be ~ 40 ka (e.g. Bowman, 1990), and thus many of our ages are beyond the limit of this method (Table 2.1). However, recent advances in AMS dating have allowed obtaining ages as old as 50.4 ka validated by varve counting and used in a recent calibration study (Ramsey et al., 2012). For example, ages of 45, 47 and 40 ka have been obtained from paired samples using radiocarbon, Uranium-series

and luminescence, respectively, in marine terrace sediments of MIS 3 (Gurrola et al., 2014). These dates, which were obtained from sediments very similar to those of the SMF, emphasize the occasional validity of old radiocarbon ages. Although our ages might be interpreted as minimum estimates, the arguments mentioned above, in addition to their stratigraphic concordance, suggest they are reliable chronologic benchmarks for the SMF.

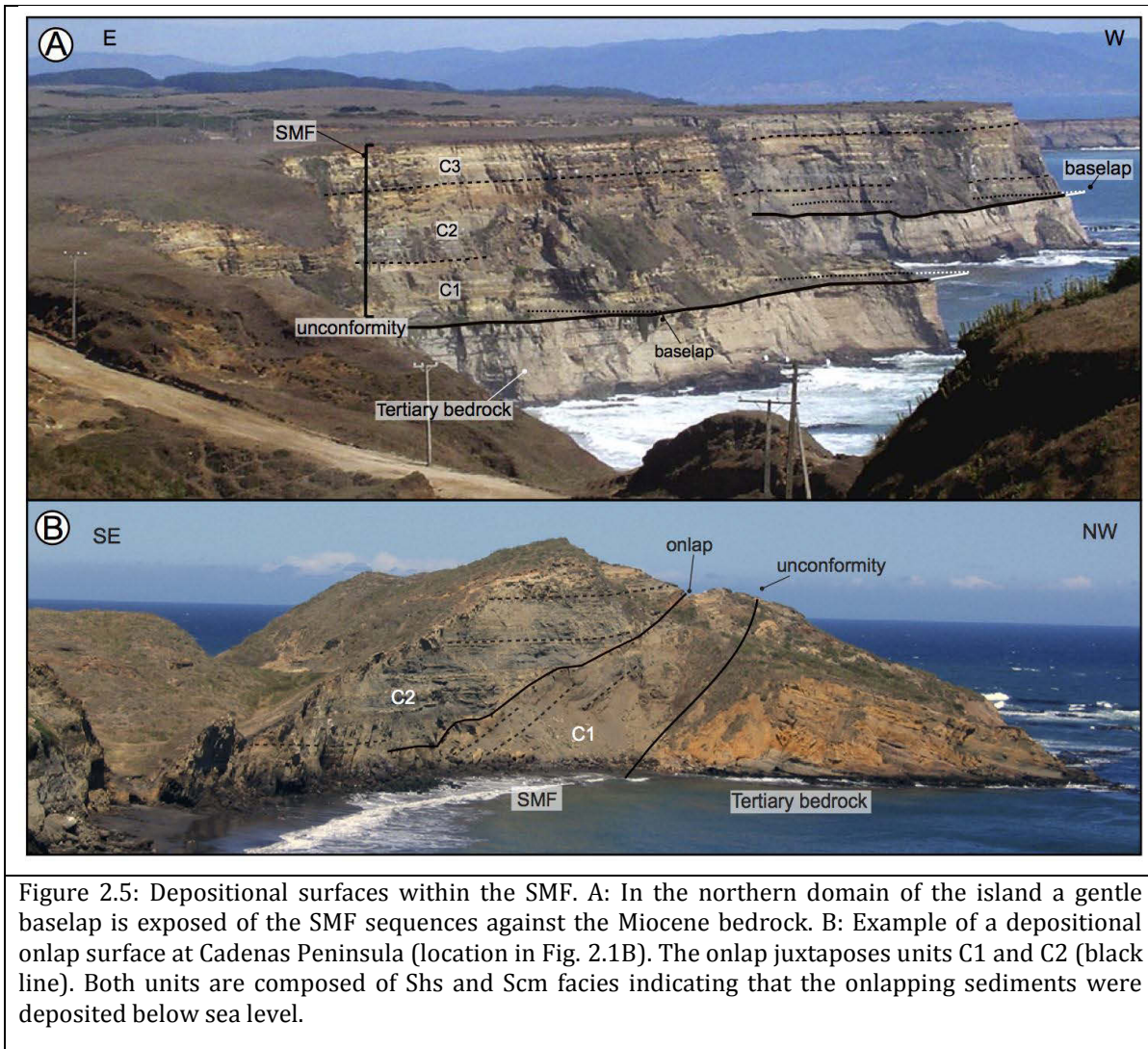


2.6.3 Erosional and depositional surfaces within the SMI

A flooding surface is a sharp discontinuity that may be erosional and marks an abrupt change in the depositional environment and/or facies in response to a transgressive event (Arnott, 1995). Five flooding surfaces have been identified within the SMF and used to trace the depositional history of the sequence. The most relevant flooding surface is represented by the unconformity between the Tertiary bedrock and the SMF. This basal flooding surface is associated with a 30- to 100-cm-thick zone of breccia within the bedrock, overlain by a 40- to 80-cm-thick Bs horizon, which yielded a minimum radiocarbon age of 53 ka (See Appendix A.5). The presence of this paleosol indicates that the abrasion platform must have been above sea level and subaerially exposed long enough to support soil formation. The SMF rests directly on the paleosol with a baselap relationship, as can be observed in the northwestern cliffs of the island; here the strata approach asymptotically towards the flat and slightly inclined unconformity (Fig. 2.5A) suggesting lateral progradation of the shore system.

Offlap structures have been recognized in the southwestern cliffs, comprising Shs facies truncated upwards, overlain by sub-aerial Sm and Ps facies. Onlap structures occur against the basal unconformity only in the western cliffs of the island as well as within the SMF. Onlaps onto the

bedrock are well developed in the southern domain of the island, where the SMF deposits have accumulated in pockets filling the paleo-topography of the Tertiary bedrock. The Cadenas Peninsula hosts an onlap structure developed within the SMF, formed by an irregular surface inclined between 35° and 45° juxtaposing two marine units (Fig. 2.5B) indicating that the surface was formed below sea level.



2.6.4 Granulometric Model and stratigraphic architecture

The classification obtained by analyzing the granulometric distributions of sediment samples using discriminant analysis depicts the sequence of depositional environments in the SMF. This environmental classification, referred to as the Granulometric Model (See tables A2 and A3 in Appendix A), is complementary with the analysis of facies and discriminates two types of environments: dune (d) for foreshore deposits, and beach (b) for onshore deposits (details in Appendix A.4).

The results from the Granulometric Model are largely consistent with those from the facies analysis (Fig. 2.3), with only seven misfits corresponding to 10% of the population (Fig. 2.6). The misfits observed in the S1, S3, and S4 sections, for example, are associated with the Sm facies, characterized by massive medium sands with no distinctive sedimentary structures. Most of the misfits also occur in the upper parts of the sequence, which tend to be affected by pedogenesis and by the precipitation of oxides and secondary minerals, making facies recognition difficult in the field.

Despite the aforementioned misfits, the integration of both classification methods enabled the generation of a high-resolution vertical sequence of depositional environments documenting a number of sedimentary cycles. Fig. 2.6 illustrates the stratigraphy, sedimentology, and facies distribution for each stratigraphic section. The thickness of the sequence generally increases eastward and the facies distributions within the sections indicate that the lower part of the SMF is made up mainly of marine deposits, with minor intercalations of sub-aerial sediments. The thickness of the sub-aerial deposits increases up the sequence and is mirrored by a reduction in grain size (Fig. 2.6) indicating a general upward shoaling trend. This suggests a seaward displacement of the shoreline during deposition of the SMF.

The Granulometric Model and facies analysis revealed a higher degree of complexity within the sedimentary sequence, allowing the identification of three stratigraphic units (C1, C2 and C3) bounded by flooding surfaces. Unit C1 overlies the basal flooding surface sculpted into the Tertiary bedrock and covered by a paleosol. Four minor paleosol horizons occur within the C1 and C2 units, likely reflecting small transgressive–regressive cycles. Minor transgressive episodes divide C1 and C2 in two small-scale asymmetric cycles each, defined as C1a, C1b, C2a and C2b (Fig. 2.6). These can be clearly followed in most of the sections, but for the sake of simplicity and to facilitate lateral correlation, we grouped the units into C1 and C2. No characteristic coarse-grained transgressive deposits have been observed above the flooding surfaces that delimit units C1 and C2. These flooding surfaces are irregular and sharply defined, suggesting a certain amount of sub-aerial exposure and possibly a small amount of erosion.

Unit C3 is located in the upper part of the SMF and only exposed in the west-facing cliffs of the island. Sm and Ps facies dominate the stratigraphy of C3, suggesting a backshore environment. The unit is bounded below by a well-defined and regular flooding surface, overlain by a thin marine horizon (Shs facies). The available ages indicate that the flooding event occurred between ~ 42 and ~ 30 ka; it represents a smaller transgressive episode than those associated with the two underlying units. Unit C3 suggests a pronounced regression of the shoreline, favoring the development of lowlands and eolian deposits similar to those that can be observed at present in the Holocene lowlands. In view of the baselap and offlap structures, and the generally regressive trend of the SMF, the internal arrangement of the sequences is likely to result from progradation following the classic stacking pattern of shallow marine sequences (Fig. 2.7).

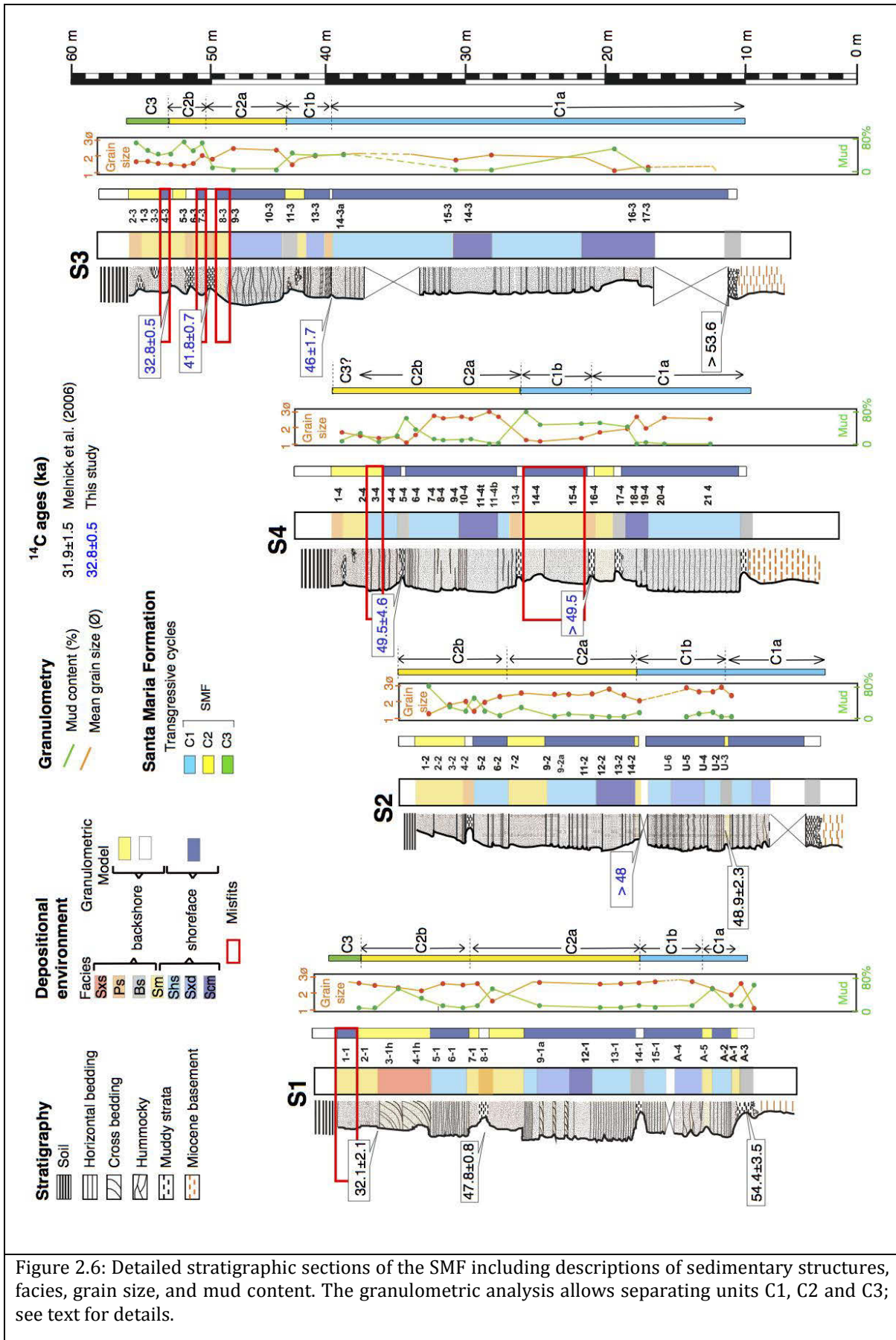
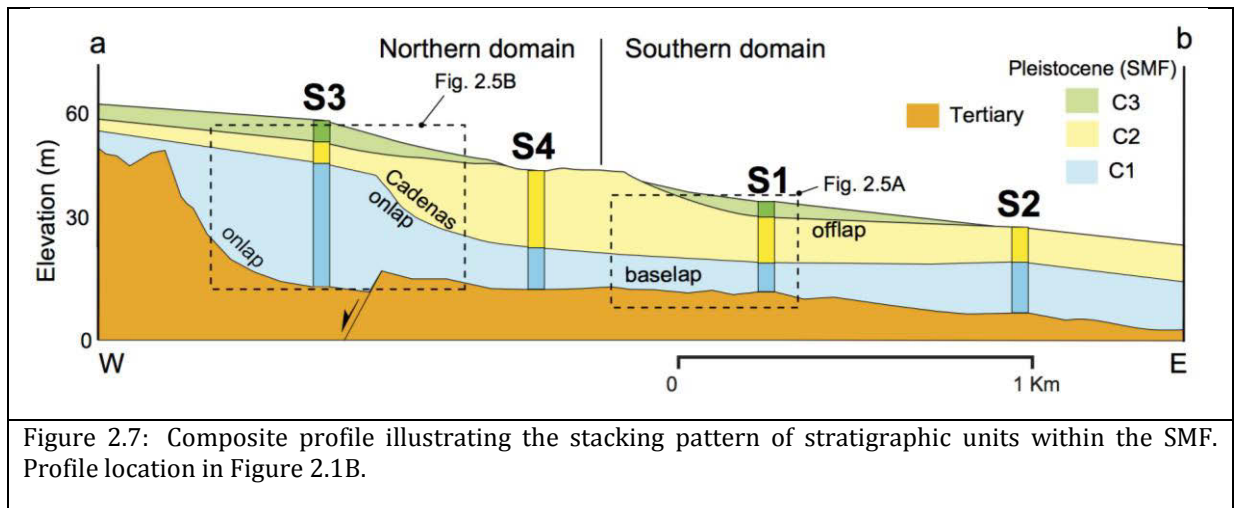


Figure 2.6: Detailed stratigraphic sections of the SMF including descriptions of sedimentary structures, facies, grain size, and mud content. The granulometric analysis allows separating units C1, C2 and C3; see text for details.

The record of flooding surfaces, together with the sequence of depositional environments, can therefore be used to trace relative sea-level curves for the SMF under the assumptions discussed in the Construction of relative sea-level curves section. From the relative depth of each facies succession we generated a relative sea-level curve for each stratigraphic section and calculated the polarity of its gradients (RSL change in Fig. 2.8). We also used the flooding surfaces to define the highstand positions, using the same nomenclature as for the identified sedimentary units.



2.7 Discussion

2.7.1 Influence of tectonic uplift and sea-level oscillations on the SMF stratigraphy

We interpret the SMF as the sedimentary fill of a wave-built marine terrace above a wave-cut platform, in which the identified flooding surfaces mark reoccupation episodes resulting from oscillations in relative sea level. Changes in the depositional environments of the SMF as revealed by our combined analysis of grain-size distributions and facies can be used to infer changes in relative sea level. These changes can be further used to estimate the uplift rate, when eustatic sea-level variations are incorporated under the assumptions discussed in the Construction of relative sea-level curves section (Fig. 2.8).

In order to obtain relative sea-level curves for a range of uplift rates, we first fixed a tie point at 53 ka when the island was at or very closely to sea level (Fig. 2.9A). This was based on 5 radiocarbon ages from the paleosol level at the base of the SMF (Fig. 2.4), directly above the Tertiary bedrock, which are approximately coincident with a low stand in the absolute sea-level curve. Fig. 2.9 shows the temporal evolution of depositional depths predicted by our analysis for a range of uplift rates, highlighting those episodes that appeared to correlate with the transgressive events observed in the SMF.

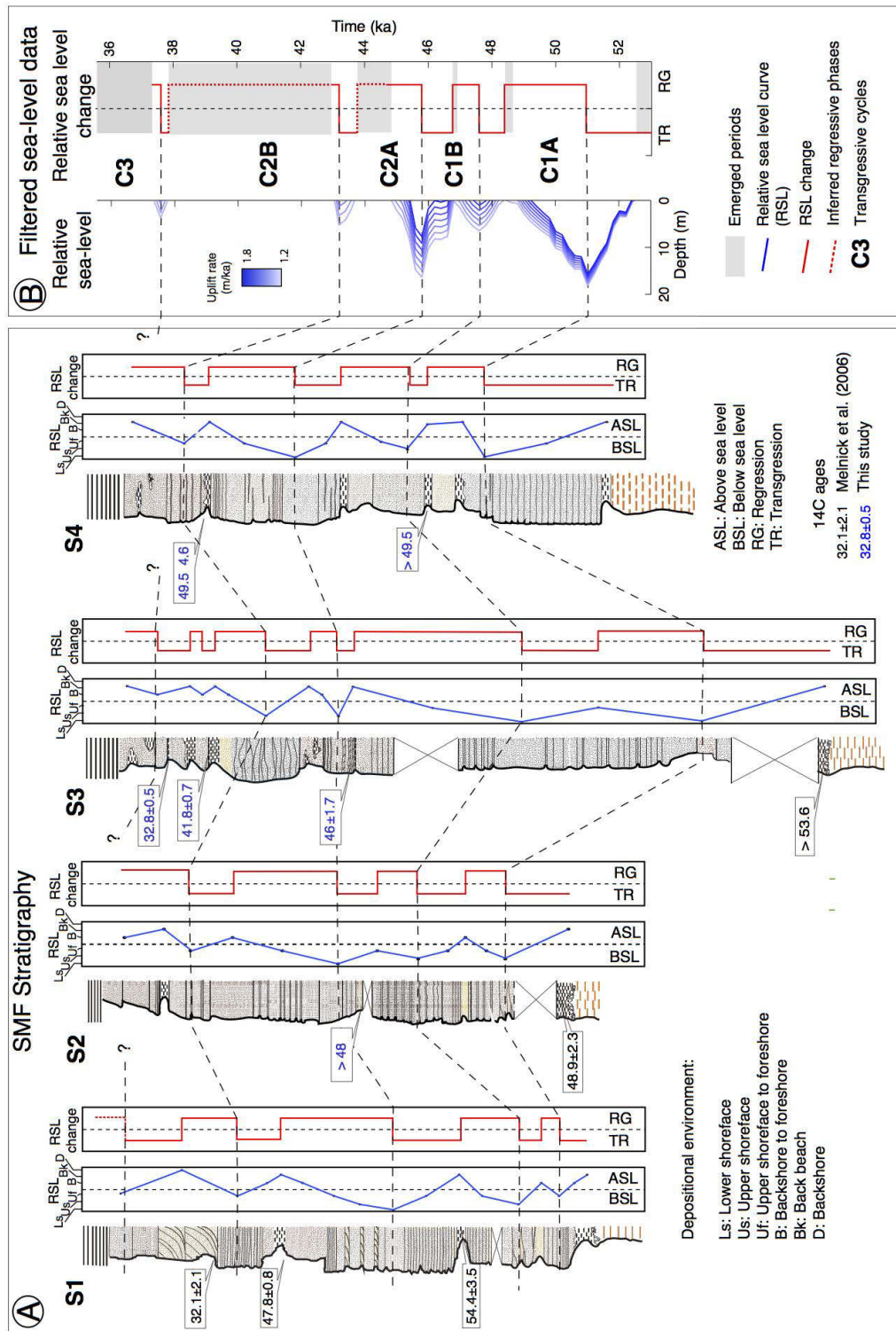
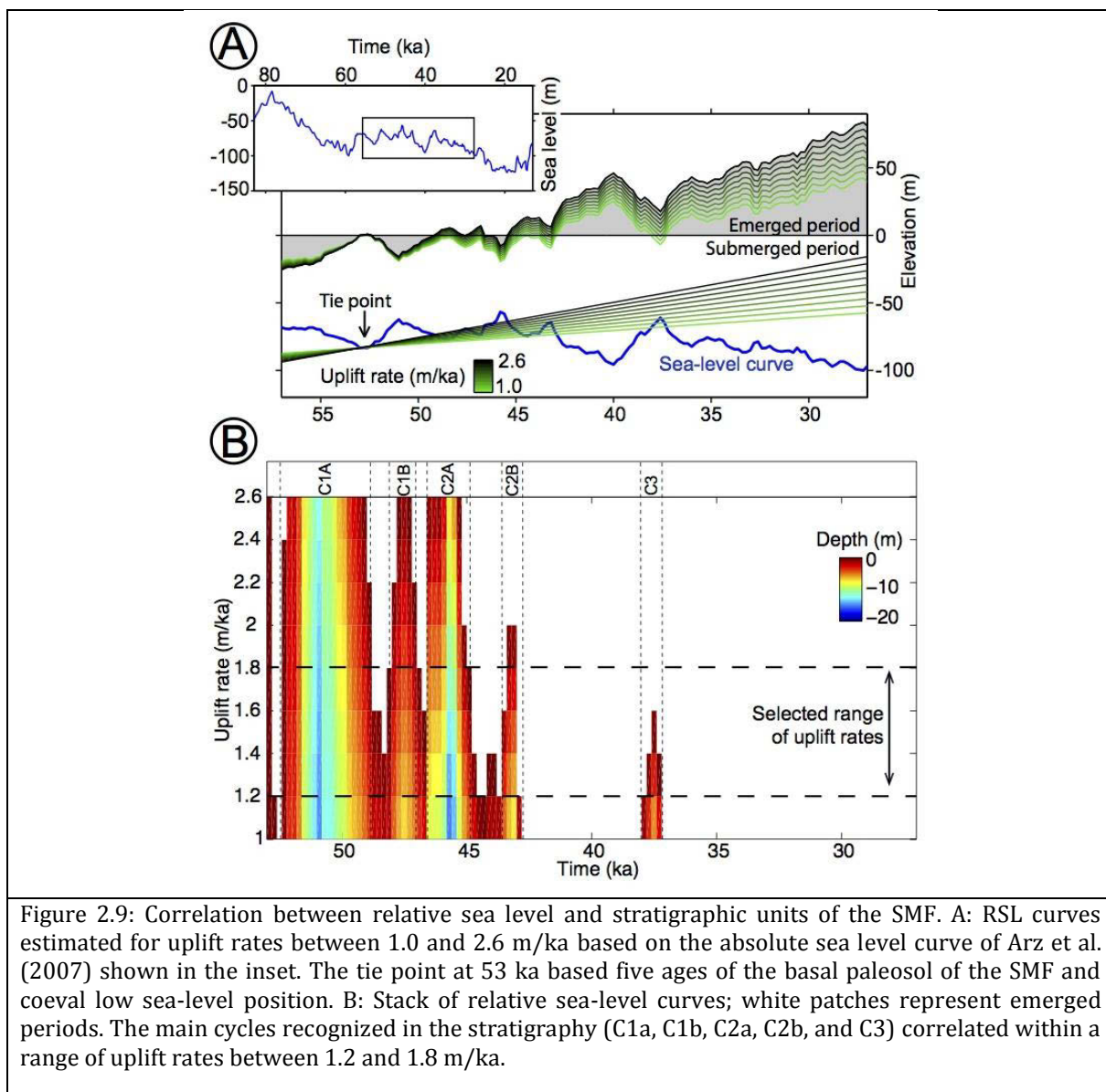


Figure 2.8: A: Stratigraphic sections, radiocarbon ages and inferred patterns of relative sea-level change. Relative sea level (RSL) estimated from the gradient in depositional depth of each facies (blue lines) and its polarity (red lines). B: RSL curve obtained using the eustatic curve of Arz et al. (2007) and uplift rates ranging between 1.2 and 1.8 m/ka (see text for details). The red line shows the polarity of the RSL change and correlation with transgressive and regressive cycles deduced from the stratigraphic sections. Black dashed lines highlight the correlation.

As might be expected, the pattern and amplitude of submerged periods are shown to be a function of the uplift rate. Relative sea-level curves obtained for uplift rates between 1.2 and 1.8 m/ka predict five submerged periods that are contemporaneous with the distinct transgressive episodes observed in the SMF (Fig. 2.9B). Uplift rates greater than 1.8 m/ka do not correlate with the observed pattern of marine sediment intercalations, resulting in longer emerged periods between C1 and C2, and no transgressive C3 cycle between 31 and 42 ka. In contrast, uplift rates lower than 1.2 m/ka produce only a protracted submerged period and no clear distinction between C1 and C2 (Fig. 2.9B).



There is a qualitative correlation between the predicted submerged periods and the sedimentary cycles in the SMF, and in particular between the transgressive surfaces in the SMF and the pattern of submerged periods. The best fits between the relative sea-level curves and the sedimentary cycles of the SMF occur at uplift rates of between 1.2 and 1.8 m/ka (Fig. 2.9B). The transgressive periods within each stratigraphic section agree with the modeled relative sea level for uplift rates

between 1.2 and 1.8 m/ka (Fig. 2.8). Thus, we can constrain the mean uplift rate to 1.5 ± 0.3 m/ka, which is slightly lower than the 1.8 ± 0.4 m/ka obtained as a maximum value by Melnick et al. (2006), based on the assumption that the paleosol horizons were formed at sea level.

2.7.2 Depositional history of SMF

On the basis of our combined analysis of depositional environments and relative sea levels, we propose the following depositional history of the SMF (Fig. 2.10):

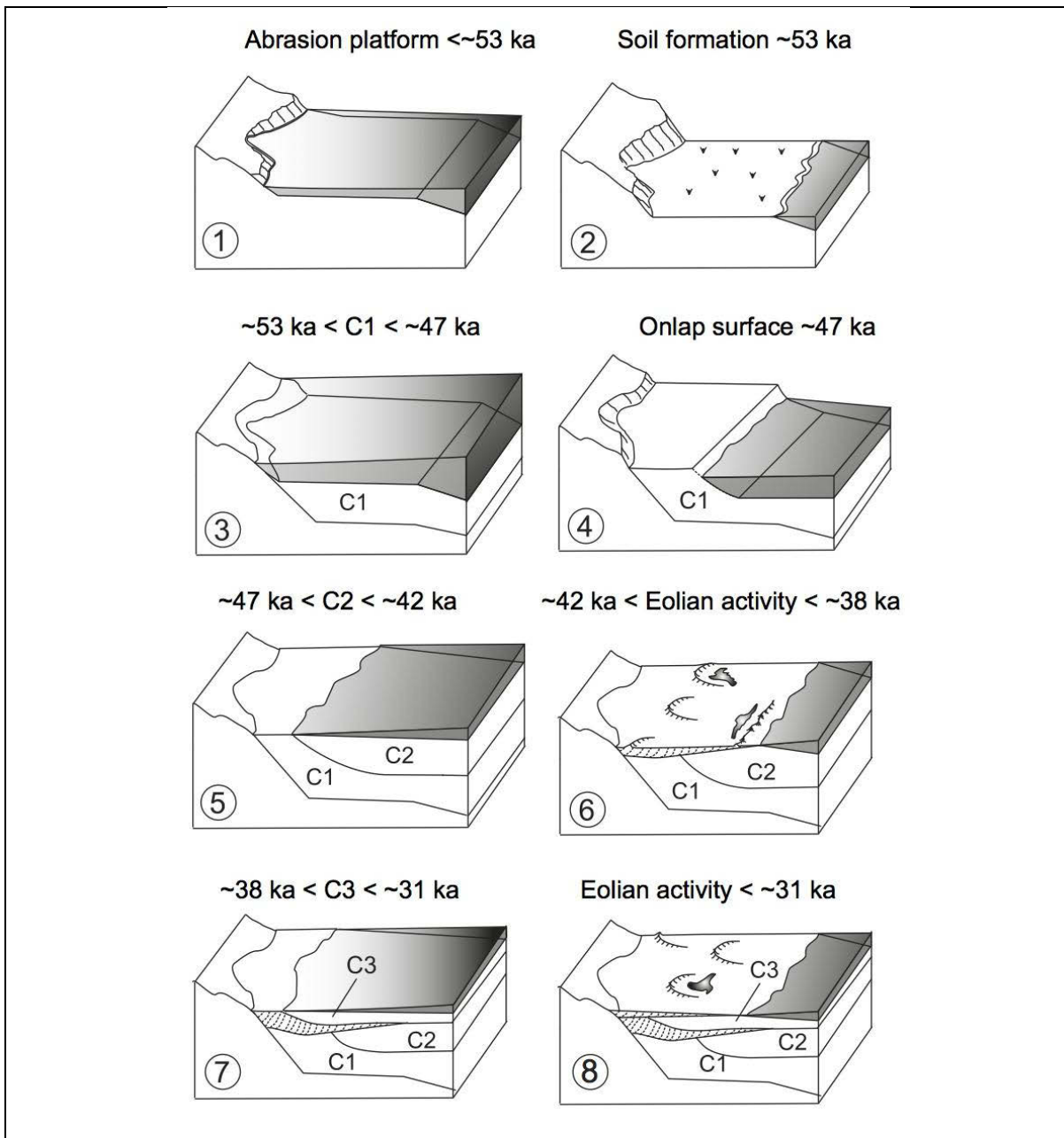
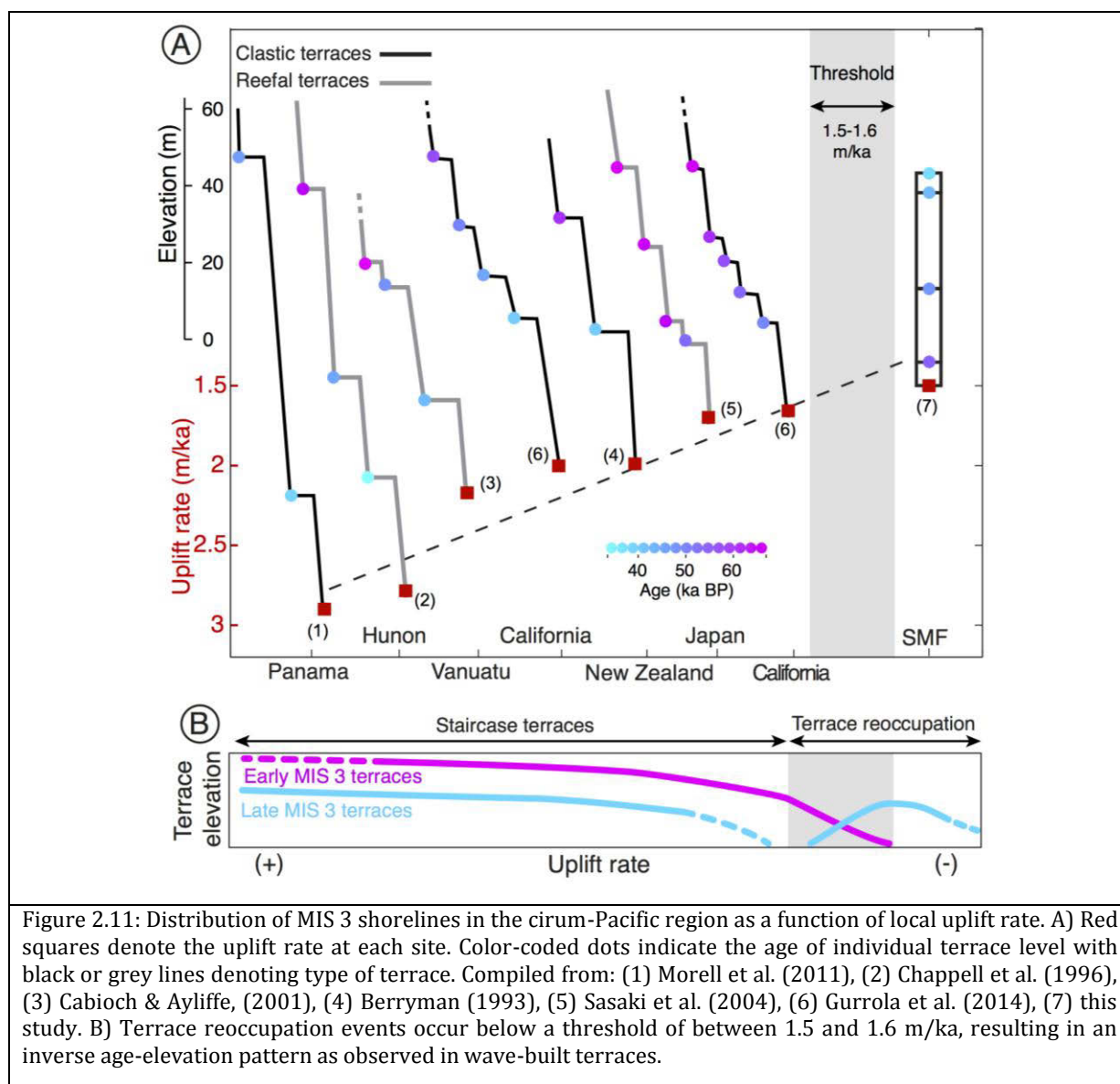


Figure 2.10: Schematic representation of the chronology and stratigraphy of the SMF. The proposed depositional history of the SMF follows a stepwise development of multiple transgressive and regressive episodes. The depositional history of each stratigraphic unit (C1, C2 and C3) is represented under conditions of oscillating sea level and constant uplift at rates between 1.2 and 1.8 m/ka (see the Depositional history of the SMF section for further information).

(1) Before a minimum age of ~ 53 ka, a sub-horizontal wave-cut platform was formed in the Tertiary bedrock; (2) sub-aerial exposure led to weathering of the bedrock and development of a paleosol horizon; (3) between ~ 53 and ~ 47 ka, a period of rising sea-levels resulted in partial reoccupation of the abrasion platform and deposition of unit C1; (4) after ~ 47 ka, a slight fall in sea level resulted in partial erosion of the shore profile removing a portion of the C1 deposits and sculpting the Cadenas onlap surface; (5) between ~ 47 and ~ 42 ka, a new terrace reoccupation episode started with deposition of unit C2 as an onlapping sequence; (6) between ~ 42 and ~ 38 ka, a more pronounced fall in sea level led to the onset of eolian activity, resulting in deposition of berms, dunes and wetlands; (7) at ~ 38 ka, the last terrace reoccupation episode resulted in deposition of unit C3 consisting of a thin, shallow transgressive sequence; and (8) a broad fall in sea level was likely associated with the accumulation of the eolian deposits in the upper part of the SMF after ~ 32 ka. Eolian deposition probably ceased at ~ 27 ka when the sea level fell dramatically at the end of MIS 3, resulting in the complete emergence of the island.

2.7.3 Reoccupation thresholds in MIS 3 marine terraces



A common feature of MIS 3 shoreline records is their rapid uplift rates, usually greater than ~ 2 m/ka, which led to rapid emergence and prevented deposits and geomorphic features from being eroded during the post-LGM transgression (e.g. Bloom et al., 1974; Chappell, 1974; Berryman, 1993; Chappell et al., 1996; Cabioch and Ayliffe, 2001; Sasaki et al., 2004; Morell et al., 2011; Gurrola et al., 2014) (Fig. 2.11A). Terrace reoccupation episodes produced by superimposed sea-level positions are often associated with low rates of uplift or high-frequency sea-level oscillations and may be expressed as rasas or wave-built terraces (e.g. Kelsey and Bockheim, 1994; Yildirim et al., 2013; Pedoja et al., 2014).

Considering that the uplift rate of SMI is the lowest documented so far for a MIS 3 site in the circum-Pacific region, we tentatively locate the reoccupation threshold for MIS 3 at an uplift rate of between 1.5 and 1.6 m/ka. This means that at uplift rates above this threshold MIS 3 staircase terrace morphologies are likely to be preserved in the landscape, while at uplift rates near or below this threshold MIS 3 records could be preserved below sea level, eroded during the post-LGM transgression, or may have formed a wave-built terrace as at SMI (Fig. 2.11B).

2.7.4 Correlating wave-cut and wave-built terraces

The stratigraphic architecture of the SMF correlates in part with terrace ages from the circum-Pacific region. For instance, terrace levels dated between ~ 42 and ~ 47 ka in Vanuatu (Cabioch and Ayliffe, 2001), California (Gurrola et al., 2014) and on the Hunon Peninsula (Chappell et al., 1996) may be correlated with units C1 and C2 of the SMF, and the lower terrace level dated at ~ 38 ka in Panama (Morell et al., 2011), New Zealand (Berryman, 1993) and California (Gurrola et al., 2014) with unit C3. This correspondence suggests that reoccupation events in wave-built terraces may be tentatively correlated with terrace levels in wave-cut terraces. The stratigraphic analysis of the SMF shows that reoccupation events in wave-built terraces appear to coincide in time with interstadial highstands; for this reason flooding surfaces, within wave-built terraces, can be considered to be chronological benchmarks of past sea-level positions.

To date, most marine terrace studies are based on their surface geomorphic expression, commonly used to perform correlations based on distinct geomorphic markers such as the shoreline-angle or the inner edge. In contrast, wave-built terraces are characterized by a smooth geomorphic expression, where the paleo-cliff is in most cases partly or totally obscured by the deposits. The use of stratigraphic benchmarks together with geomorphic markers can significantly improve the resolution of regional-scale marine terrace correlations (see Chapter 3).

So far, no clear distinction between the sedimentary cover of a wave-cut terrace and the sedimentary sequence of a wave-built terrace has been formally made. The thin veneer of sediments that covers wave-cut terraces, commonly used to obtain absolute ages, is usually deposited during the regressive phase that immediately follows the sea-level highstand during which the abrasion platform and sea cliff were carved (e.g. Bradley, 1957; Dupré, 1984; Lajoie, 1986; Anderson et al., 1999). In contrast, we propose that sedimentary packages such as the SMF that includes depositional cycles with transgressive and regressive phases associated with a distinct bedrock abrasion platform are characteristic and may be used as distinct criteria to define wave-built terraces. This implies that reoccupation events evident in the sedimentary

sequence may be distinctive to wave-built terraces. In turn, reoccupation events evident in the surface morphology are rather characteristic of wave-cut terraces. Both end-member scenarios and their main features are schematically represented in Figure 2.12.

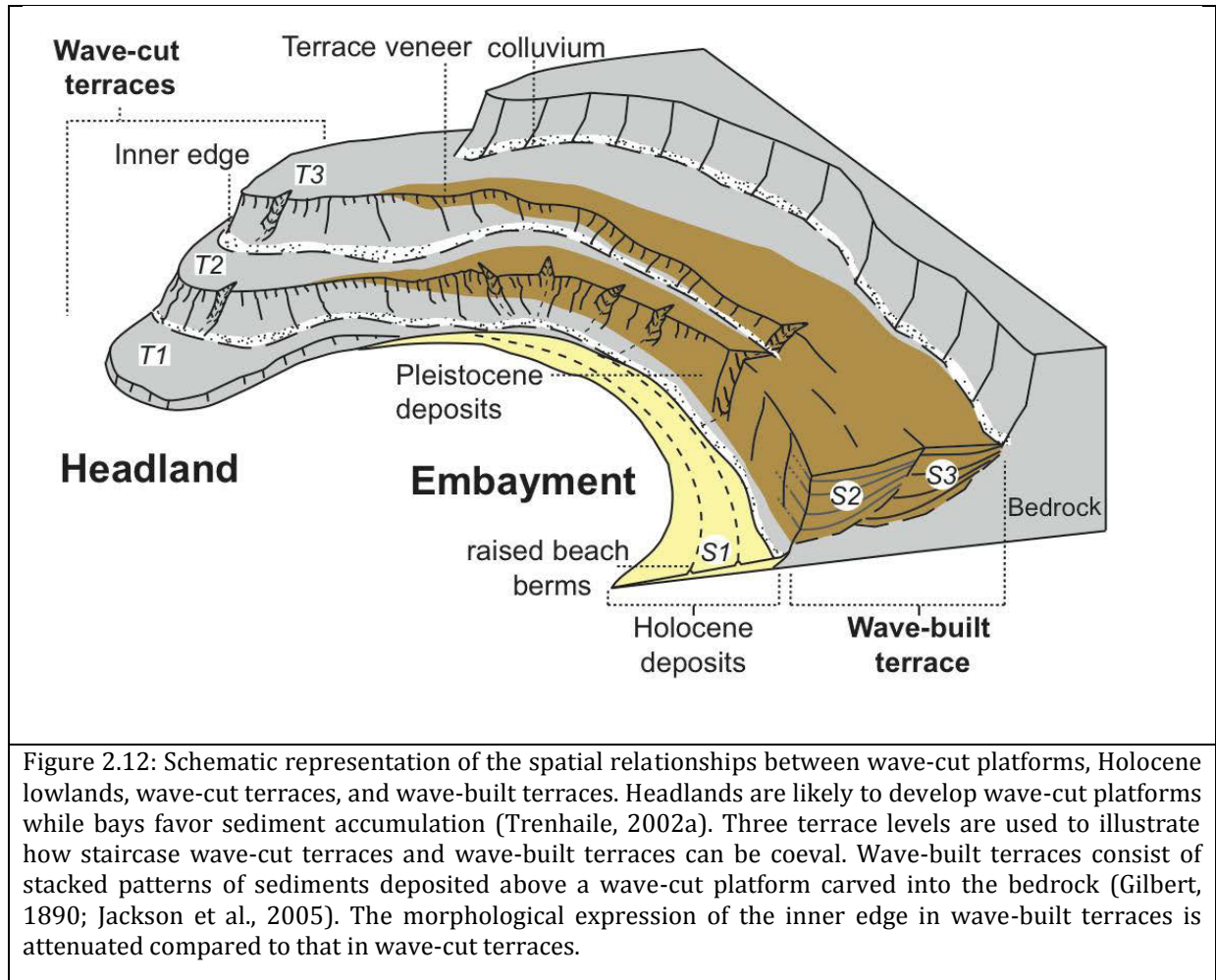


Figure 2.12: Schematic representation of the spatial relationships between wave-cut platforms, Holocene lowlands, wave-cut terraces, and wave-built terraces. Headlands are likely to develop wave-cut platforms while bays favor sediment accumulation (Trenhaile, 2002a). Three terrace levels are used to illustrate how staircase wave-cut terraces and wave-built terraces can be coeval. Wave-built terraces consist of stacked patterns of sediments deposited above a wave-cut platform carved into the bedrock (Gilbert, 1890; Jackson et al., 2005). The morphological expression of the inner edge in wave-built terraces is attenuated compared to that in wave-cut terraces.

2.8 Conclusions

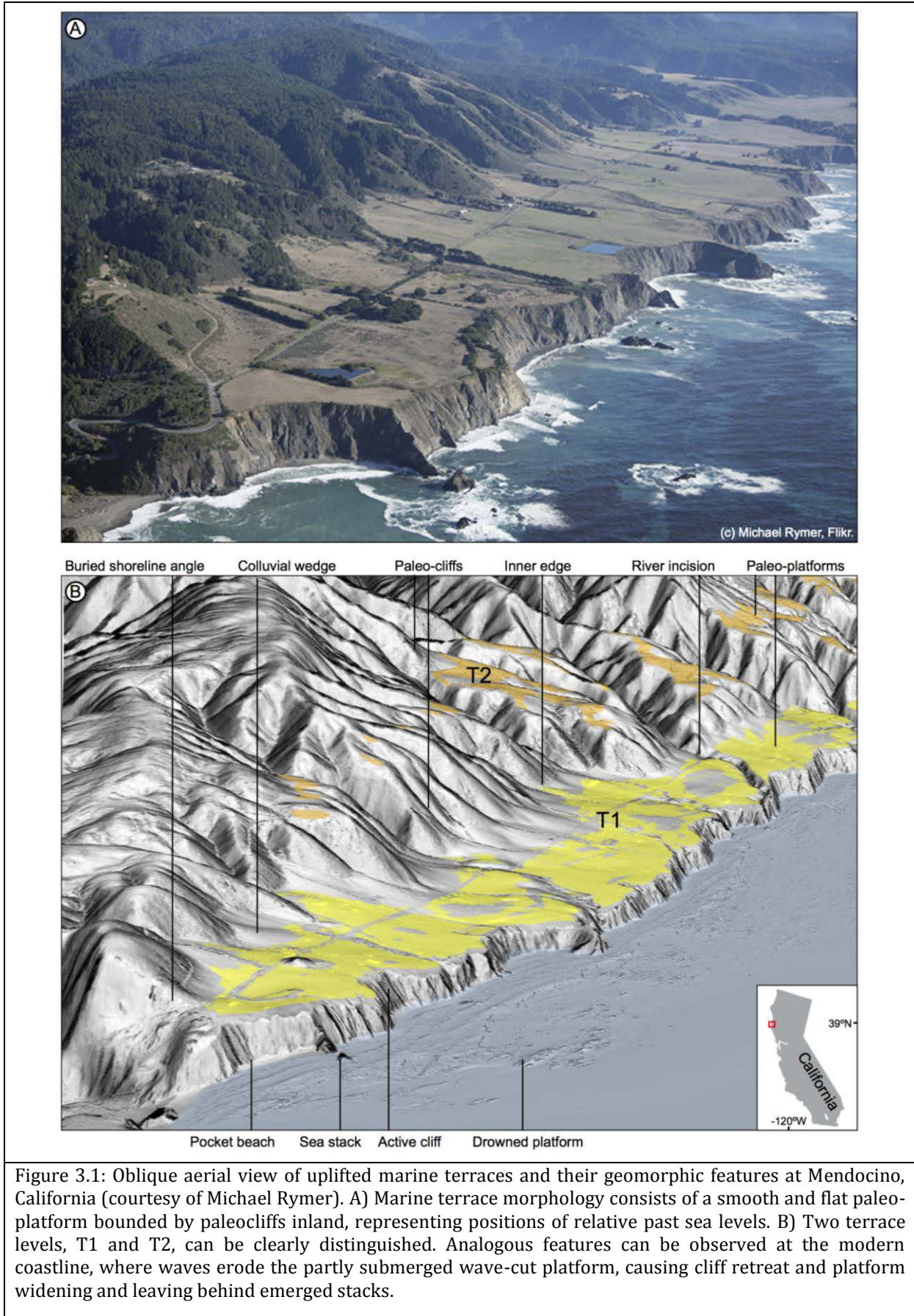
We have used a novel method that combines classic stratigraphic descriptions with statistical analyses of grain-size distributions to unravel the influence that sea-level variations and tectonic uplift have on the architecture of a coastal sedimentary sequence. We associate the relation between transgressive–regressive cycles deduced from the sedimentary sequence and the underlying bedrock abrasion platform as distinct to wave-built marine terraces.

Both the stratigraphy and sedimentology of the SMF suggest it may be divided into three units, each associated with a discrete transgressive period. We interpret these cycles to represent terrace reoccupation episodes during distinct phases of elevated sea-level positions. In order to isolate the tectonic signal from the eustatic signal we compared relative sea-level curves (derived from the sedimentary sequences and constructed from the absolute sea-level curve) for a range of uplift rates. The preferred uplift rate of 1.5 ± 0.3 mm/yr is slightly lower than a previous estimate at the same ~ 50 ka time scale of 1.8 ± 0.4 mm/yr.

By comparing the pattern of wave-built terrace reoccupation and the record of MIS 3 around the circum-Pacific region, we propose that flooding surfaces in wave-built terraces may be considered to be analogous to wave-cut terrace surfaces, both formed during distinct sea-level positions. We propose that the transgressive–regressive cycles found in sedimentary packages overlying a bedrock abrasion platform, which imply reoccupation events may be a distinctive characteristic and primary criteria to define wave-built terraces. These criteria might be used to distinguish among wave-built and wave-cut terraces, which are end-member scenarios of marine terraces.

3 TerraceM: a MATLAB® tool to analyze marine and lacustrine terraces using high-resolution topography

High-resolution topographic data greatly facilitate the remote identification of geomorphic features, furnishing valuable information concerning surface processes and characterization of reference markers for quantifying tectonic deformation. Marine terraces have been used as long baseline geodetic markers of relative past sea-level positions, reflecting the interplay between vertical crustal movements and sea-level oscillations. Uplift rates may be determined from the terrace age and the elevation of its shoreline angle, a geomorphic feature that can be correlated with past sea-levels positions. A precise definition of the shoreline angle in time and space is essential to obtain reliable uplift rates with coherent spatial correlation. To improve our ability to rapidly assess and map shoreline angles at regional and local scales, we have developed TerraceM, a MATLAB® graphical user interface that allows the shoreline angle and its associated error to be estimated using high-resolution topography. TerraceM uses topographic swath profiles oriented orthogonally to the terrace riser. Four functions are included to analyze the swath profiles and extract the shoreline angle, from both staircase sequences of multiple terraces and rough coasts characterized by eroded remnants of emerged terrace surfaces. The former are measured by outlining the paleocliffs and paleo-platforms and finding their intersection by extrapolating linear regressions, whereas the latter are assessed by automatically detecting peaks of sea-stack tops and back-projecting them to the modern sea cliff. In the absence of rigorous absolute age determinations of marine terraces, their geomorphic age may be estimated using previously published diffusion models. Postprocessing functions are included to obtain first-order statistics of shoreline-angle elevations and their spatial distribution. TerraceM has the ability to process series of profiles from several sites in an efficient and structured workflow. Results may be exported in Google Earth and ESRI shapefile formats. The precision and accuracy of the method have been estimated from a case study at Santa Cruz, California, by comparing TerraceM results with published field measurements. The repeatability was evaluated using multiple measurements made by inexperienced users. TerraceM will improve the efficiency and precision of estimating shoreline-angle elevations in wave-cut terraces in both marine and lacustrine environments.



3.1 Introduction

Recent increases in the availability of high-resolution topographic data have greatly helped the accuracy of quantitative analyses of landforms and the processes generating them, particularly by furnishing valuable information on geomorphic markers that may help to constrain the spatiotemporal characteristics of tectonic deformation processes. Marine terraces along tectonically active coasts, either related to constructional or erosional processes, are commonly used as long baseline geodetic markers of relative past sea-level positions, reflecting the interplay between vertical tectonism and superposed sea-level oscillations. By studying terrace elevation and dating their exposed surfaces or associated sediments, geologists have discovered an extensive archive of information about past sea-level variations and temperatures, as well as paleogeographic and paleoenvironmental change (e.g. Bloom et al., 1974; Chappell et al., 1996; Cabioch and Ayliffe, 2001; Sasaki et al., 2004; Cornée et al., 2006; Zecchin et al., 2009). Marine terraces have been also used as reference horizons to track tectonic deformation and associated fault-slip rates along tectonically active coasts. In numerous studies on marine terraces, detailed topographic information has provided the necessary data to infer earthquake recurrence at millennial time scales (e.g. Fairbanks and Matthews, 1978; Matsuda et al., 1978; Plafker and Rubin, 1978; Bloom and Yonekura, 1985; Strecker et al., 1986; Ota et al., 1991; Valensise and Pantosti, 1992; Armijo et al., 1996; Gesch et al., 2002; Melnick et al., 2009; Athanassas and Fountoulis, 2013; Yildirim et al., 2013; Shikakura, 2014). Furthermore, the staircase morphologies of differentially uplifted marine terraces have also helped to identify coastal seismo-tectonic segments that sustain their geomorphic characteristics over much longer time scales (e.g. Taylor et al., 1987; Gesch et al., 2002; Chen et al., 2011; Victor et al., 2011). Similarly, lacustrine terraces have provided detailed records of lake-level variations associated with the local effects of climate change (e.g. Garcin et al., 2012; Kliem et al., 2013). As in the marine environment, if lacustrine shorelines can be dated, they potentially constitute geomorphic marker horizons that can be used to infer rates of tectonic deformation and tectonic segmentation (e.g. Melnick et al., 2012b). In this study, we focus on morphometric analyses of marine terraces, but the broad spectrum of methods presented here may be equally applied to analyze their lacustrine counterparts.

The linked effects of tectonic uplift, sea-level variations, and erosional and depositional processes are responsible for shaping coastal landscapes. Marine terraces are ephemeral coastal landforms characterized by flat and generally smooth surfaces or paleoplatforms that dip gently seaward. The terrace surfaces are bounded by scarps or paleocliffs inland that delimitate each terrace level (Figs. 3.1A and 1B) formed during protracted sea-level highstands (Lajoie, 1986; Anderson et al., 1999). Such coastal geomorphic sequences include wave-cut or wave-built terraces, *rasas*, strandflats, and compound paleocoasts (e.g. Guilcher et al., 1986; Regard et al., 2010; Keskin et al., 2011; Pedoja et al., 2014; Jara-Muñoz and Melnick, 2015). Active wave-cut platforms and sea cliffs are generated by the effects of wave erosion, which in stable sea-level conditions may be intensified depending on the morphology of the shore profile, such as slope, concavity, and external climatic factors (e.g. Komar and Allan, 2008; Kline et al., 2014). During episodes of sea-level rise or stable sea levels, wave-erosion processes along rocky coasts are more pronounced, resulting in the carving of wave-cut platforms above bedrock associated with rapid cliff retreat (Challinor, 1949; Sunamura, 1983; Anderson et al., 1999; Trenhaile, 2000) (Fig. 3.2A). Conversely, during sea-level lowstands, previously cut terraces may be obliterated by river incision, slope diffusion, and eolian deposition

(Figs. 3.2B, 2C, and 3.3A). The shoreline angle is located at the intersection between the wave-cut platform and the adjacent landward cliff. According to Lajoie (1986), the shoreline angle defines the elevation of sea level at the time of terrace formation, and as such, this is an important datum for any kind of morphologic or tectonic reconstruction along the coast. After several millennia, surface uplift may preserve these snapshots of past sea-level positions and subsequent processes impacting the terraces, creating a staircase morphology, such as that observed along the California coast (e.g. Bradley and Griggs, 1976; Merritts and Bull, 1989; Anderson and Menking, 1994; Rosenbloom and Anderson, 1994; Gurrola et al., 2014; Muhs et al., 2014) and other areas along the Pacific Rim (e.g. Bloom et al., 1974; Ota et al., 1991; Hsu, 1992).

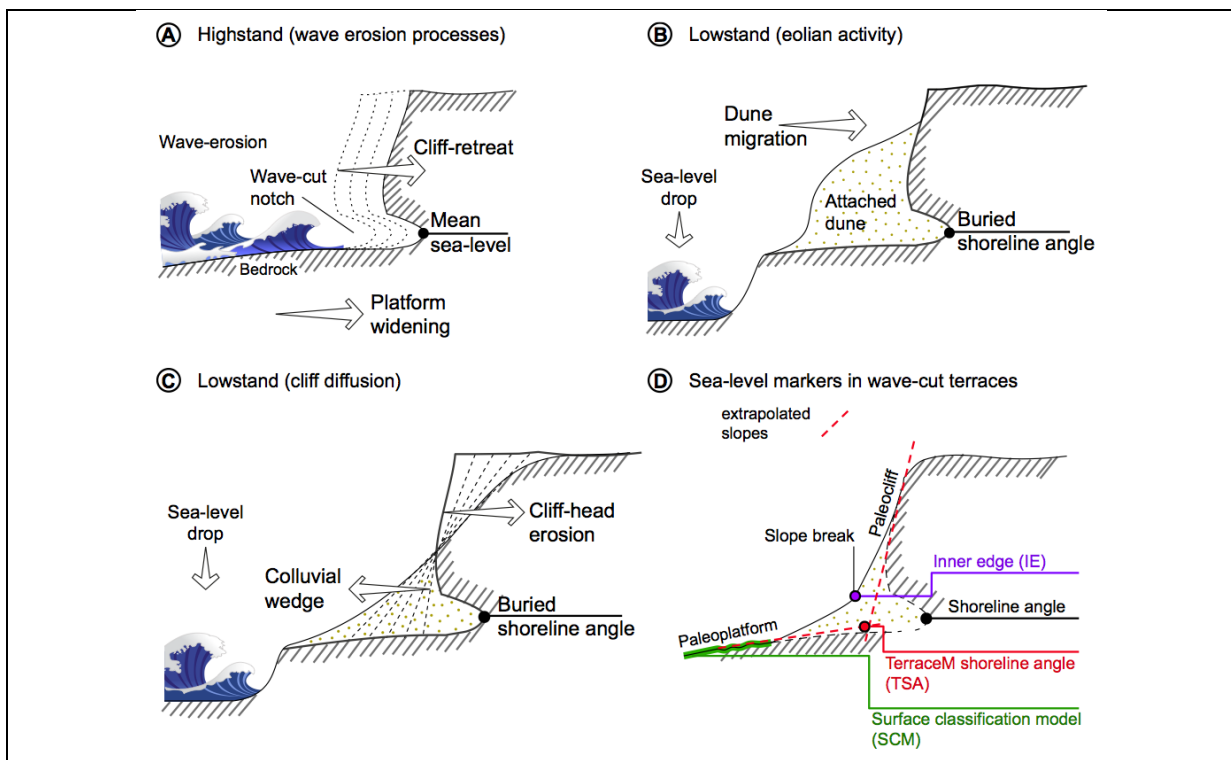


Figure 3.2: Processes associated with the generation of shoreline angles and their preservation. (A) Wave-cut platforms result from the effects of wave erosion leading to cliff retreat during sea-level highstands. Wave erosion may generate a wave-cut tidal notch that marks the position of mean sea level. (B) During sea-level low-stands, the shoreline angle may be covered by sediments transported along the beach, such as during the formation of dunes. (C) Shoreline angles may be covered by colluvium, or they may be eroded by the effects of fluvial incision (see text for further details). (D) Different geomorphic markers commonly used to estimate marine terrace elevation using high-resolution topography, and location of shoreline angles estimated by TerraceM (for references see “Background and Motivation” section).

Neotectonic research has benefited enormously from the recent advances in high-resolution topography led by light detection and ranging (LiDAR) (Meigs, 2013). LiDAR technology uses a pulsed laser to measure distance to the surface of Earth. The return time of these pulses combined with global positioning system (GPS) and an inertial navigation system allows three-dimensional point clouds of Earth’s surface to be generated. One of the main advantages of LiDAR is the possibility of generating “bare-earth” digital terrain models (DTM) using only the last returns of the laser survey. This method allows vegetation to be filtered out, imaging the terrain morphology in great detail (e.g., Fig. 3.1B). LiDAR DTMs have enabled remote identification of geomorphic

features at submeter scale, providing valuable information for earthquake geology and tectonic geomorphology (e.g. Cunningham et al., 2006; Kondo et al., 2008; Fritz et al., 2012; Zielke and Arrowsmith, 2012; Zielke et al., 2015).

Here, we present a new tool for the analysis of wave-cut terraces using high-resolution topography. By combining the concepts of marine terrace analysis, statistical methods, and high-resolution topography, we have developed TerraceM (Fig. 3.4), a MATLAB® graphical user interface (GUI) that can be used to analyze wave-cut terraces with efficiency, precision, and accuracy over large regions. This GUI can produce repeatable measurements by analyzing bulk topographic swath profiles in sequence. Swath profiles are studied using descriptive geometry and statistics to obtain the location of the shoreline angle (see next section).

We describe the different functions of TerraceM in the context of a case study based on the marine terraces at Santa Cruz, California, where climatic conditions relative to deformation rates have been favorable for creating and preserving flights of emerged marine terraces uplifted during repeated earthquakes along the San Andreas fault system (Anderson and Menking, 1994). We further compare the results of TerraceM with terrace elevations measured in the field compiled by Anderson and Menking (1994). We also include examples of rough coasts and staircase terrace morphologies along the coast of central Chile. Furthermore, we discuss the accuracy and precision of TerraceM measurements by comparing our results using digital elevation models (DEMs) with different resolution, and we assess the repeatability of measurements with an experiment carried out by 10 inexperienced users.

3.2 Background and motivation

The elevation of a marine terrace is usually estimated from its surface morphology, and it is used as a proxy for estimating the amount of relative sea-level change, or tectonic uplift since the terrace was formed. There are several extended methods and markers that have been used to estimate terrace elevations (Fig. 3.2D), for instance, by manually picking slope changes along topographic profiles that include the foot of a sea cliff, commonly referred to as the terrace inner edge (e.g. Armijo et al., 1996; Saillard et al., 2009; Regard et al., 2010; Roberts et al., 2013), or with more sophisticated methods, such as isolating terrace-platform surfaces from a combined analysis of slope and roughness of the terrain from high-resolution DTMs (Palamara et al., 2007; Bowles and Cowgill, 2012). However, terrace elevations estimated from different markers may result in disparate estimates and large ranges in the derived uplift rates. In actively forming wave-cut platforms the shoreline angle is located at the base of the cliff, and in emerged wave-cut terraces, it should coincide with the intersection between paleocliff and paleoplatform (Fig. 3.2D). The uplift rate (Ur) may be estimated from (Lajoie, 1986):

$$Ur = (Te - Sl)/t, \quad (1)$$

or (Pedoja et al., 2008)

$$Ur = Te/t, \quad (2)$$

where Te is the present-day terrace elevation, and Sl is the sea-level position at the time of formation, t . If we assume $Sl = 0$, following Pedroja et al. (2008), we can discard errors attributed to past eustatic sea-level positions, obtaining a relative uplift rate with respect to present-day sea level (Eq. 2); however, this approach may introduce a substantial bias in areas of slow tectonic uplift. Clearly, from both equations, uplift rates estimated for younger marine terraces will strongly depend on the precision of the terrace elevation measurements (Te).

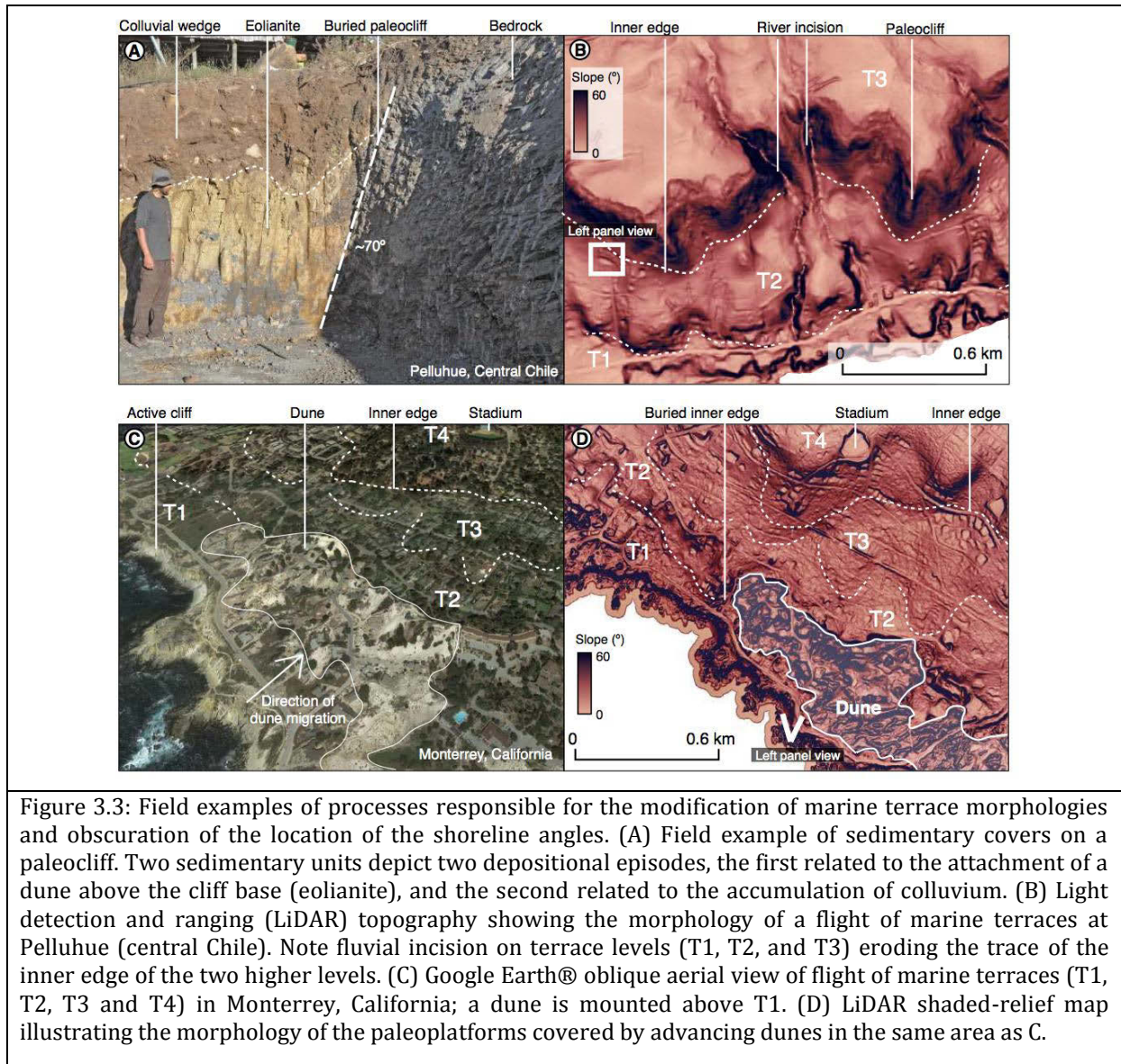
The difficulty of estimating uplift rates from marine terraces lies in the correlation of the deformation markers in time and space. For instance, the inner edge calculated from slope maps (Palamara et al., 2007) often represents the contact between a colluvial wedge and the paleoclipf, which is systematically located at a higher elevation than the shoreline angle (Fig. 3.2D) (Matsu'ura et al., 2014). Along these lines, supervised surface classification models (SCM) (e.g. Bowles and Cowgill, 2012), which have been used to map the elevation of terrace paleoplatforms, will tend to underestimate uplift rates because these markers usually form below mean sea level and prior to the highstand period when the cliff actively retreats (Fig. 3.2D). Thus, inappropriate assessment of geomorphic markers may lead to disparate uplift rates with underestimated uncertainties. Therefore, and following the definition of Lajoie (1986), we consider the shoreline angle as the most adequate marker to use for estimating uplift rates from terrace-elevation data, as it can be compared directly with past sea-level positions.

The shoreline angle of emerged older marine terraces is commonly concealed when the paleocliffs and/or paleoplatforms are affected by (1) scarp diffusion, (2) river incision, or (3) eolian depositional processes, or a combination thereof (Figs. 3.2B, 3.2C, and 3.3A–3D). Next, we assess these different effects on terrace morphology:

(1) Scarp diffusion is one of the processes that transfers material from the upper parts of the cliff to the foot and ultimately covers the shoreline angle. Scarp diffusion processes were modeled by Hanks et al. (1984) using Equation 3 and applied to marine terraces based on the assumption that mass transport resulting from erosional processes occurs exclusively in the downhill direction at a rate (M), which is proportional to the local gradient of topography ($\delta u/\delta x$). The conservation of mass holds at a local scale and is defined by the constant of proportionality (K), which depends on the diffusivity (k) and the density of the bedrock (ρ) (see Eq. 4). The material removed from the top of the scarp and accumulating at the base is thus adjusted symmetrically along the profile over time, implying that the shoreline angle might be covered by an increasing amount of colluvium as the slope of the cliff progressively decreases (Figs. 3.2C and 3.3A).

$$\text{Mass transport equation (Hanks et al., 1984): } M = -K(\delta u/\delta x). \quad (3)$$

$$\text{Proportionality constant (Hanks et al., 1984): } K = k/\rho. \quad (4)$$



(2) River incision of terrace surfaces is a response to changes in base level, which in these settings is determined by oscillations in sea level (Bishop et al., 2005). Thus, most of the river incision observed on marine terrace surfaces occurs during sea-level lowstands, when stream power is greater (Talling, 1998). Consequently, oscillating sea levels will force different fluvial adjustments to new base levels and may be expressed by retreating fluvial knick-points in the river long profiles (Crosby and Whipple, 2006; Loget and Van Den Driessche, 2009). As the channel network evolves, incision into the landscape increases, progressively reducing the spacing between the main tributaries and obliterating the terrace morphology (Anderson et al., 1999). Along uplifting coasts, incision generally increases with terrace age and height, progressively degrading the morphology of both paleoplatforms and paleocliffs (Figs. 3.1B and 3.3A).

(3) Erosion and sediment transport along coasts either result in the formation of rocky platforms or sandy beaches, respectively, depending on the shore morphology, the amount of sediments transported, tidal range, and wave exposure (e.g. Trenhaile, 2001; Ruz and Meur-Ferec, 2004; Twidale et al., 2005). Eolian transport usually increases during sea-level lowstands due the

seaward retreat of the shoreline (e.g. Bradley and Addicott, 1968; Cantalamessa and Di Celma, 2004; Masselink et al., 2014). Remobilization of fluvial and marine sediments is determined by local winds and sediment availability, leading to coastal dune systems that usually migrate inland (Bailey and Bristow, 2004; Carr et al., 2006). Similar to the other processes, dunes may cover the terrace platforms and even the paleoclimbs, burying the shoreline angle (Figs. 3.2B and 3.3B).

The aforementioned features of marine terraces have been compared worldwide in order to understand their origin and the genesis of uplifted paleo-coasts in the context of the history of sea-level changes (e.g. Pedoja et al., 2014). However, the influences of surface processes affecting the morphology of marine terraces, and consequently the errors concerning uplift rates, have not yet been fully addressed quantitatively. To quantify these processes in light of the increased availability of high-resolution topographic data, we have developed TerraceM. This new approach allows us to: (1) explore different methodologies to quantify and isolate erosive and depositional processes that usually mask the exact position of the shoreline angle; (2) extract shoreline angles continuously along terrace exposures using a large number of profiles; and (3) visualize and export the results.

3.3 TerraceM: specifications and calibration site

3.3.1 GUI Interface

TerraceM is designed to run on standard desktop computers with MATLAB® 2011b or higher; the Mapping Toolbox is required for exporting results in ESRI® shapefile and Google Earth® formats and to display the DEM; online Google-Maps® terrain and satellite images can also be displayed in the main interface (Fig. 3.4).

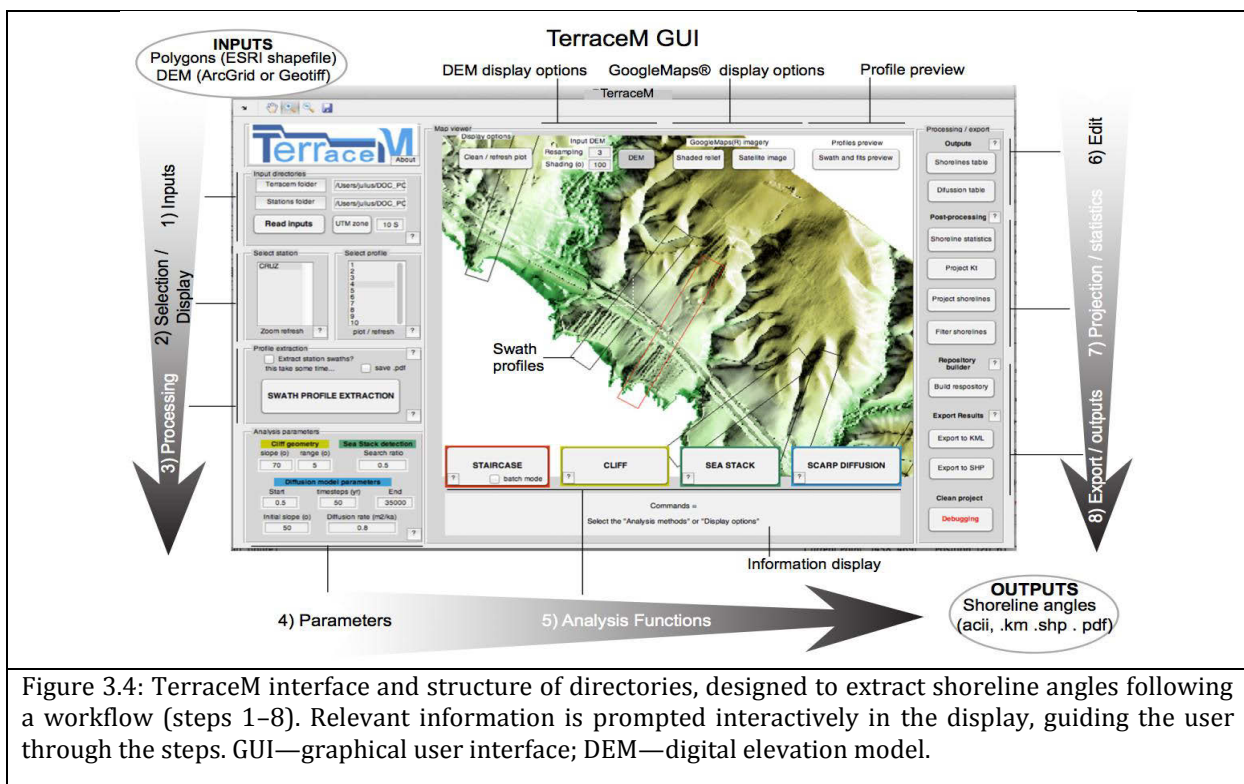


Figure 3.4: TerraceM interface and structure of directories, designed to extract shoreline angles following a workflow (steps 1–8). Relevant information is prompted interactively in the display, guiding the user through the steps. GUI—graphical user interface; DEM—digital elevation model.

TerraceM includes open-source functions for coordinate transformations, exporting options, and DEM visualization (Table 3.1). Shoreline angle processing, analysis, and postprocessing functions are designed interactively in a workflow (Fig. 3.4). The user is guided through the workflow by a console-style interface that prompts interactive information to follow each step. TerraceM inputs are ESRI® shapefiles containing rectangular polygons and a floating-point DEM in either Ascigrd or Geotiff formats (Fig. 3.5B), in Universal Transversal Mercator (UTM) projection; these files can be created in any geographic information system (GIS) platform. TerraceM extracts swath topographic profiles that allow distinctive elements of the landscape to be isolated. By analyzing the ranges of topography, the fluvial incision may be isolated from the pre-incision relief, which is usually marked by the maximum distribution.

Table 3.1: *Open source functions used in TerraceM.*

Function	Author	Release	Version	Copyright
LatLon.m	Rafael Palacios	2006	1	Free
vline.m	Brandon Kuczenski	2001	1	Free
plot_google_map.m	Zohar Bar-Yehuda	2013	1.3	Free
acii2xyz.m	Andrew Stevens	2008	1	Free
d1mcell.m	Roland Pfister	2010	1	(c) Roland Pfister
errorbar_tick.m	Arnaud Laurent	2009	R2007a	Free
peakdet.m	Eli Billauer	2005	1	Free
dem.m	François Beauducel	2014	10	(c) François Beauducel

Swath profiles should be oriented orthogonal to the trace of the paleoclipf or the terrace inner edge, encompassing the paleoplatform and extending beyond the paleoclipf (Fig. 3.6B). One profile may include as many terrace levels as needed. The width of the rectangular profiles must be set according to the raster resolution and the terrace morphology. At the calibration site (see “TerraceM Calibration Site: The Santa Cruz Marine Terraces” section), for instance, we used 100-m-wide rectangular profiles with variable length (Fig. 3.6B). The obtained swath profiles can be visualized using the “swath profile viewer,” which also allows the data to be exported.

3.3.2 Workspace and Workflow

TerraceM is designed to process and analyze many profiles in a systematic manner, organized in a tree structure of subfolders (Fig. 3.5B). Stations (or sites) are arranged in independent folders that contain the inputs and outputs of TerraceM. We recommend defining a four-letter station code for each site (e.g., CRUZ), which will also be the name of the station folder. Each input file is named according to the corresponding station; for instance, the DEM for station CRUZ would be named CRUZ_dem.tif, and the associated shapefile with polygons for swath profiles would be named CRUZ_clip.shp (Fig. 3.5B). This shapefile should include all desired polygons and should be in the standard two-dimensional format (See Appendix B.2 for further details).

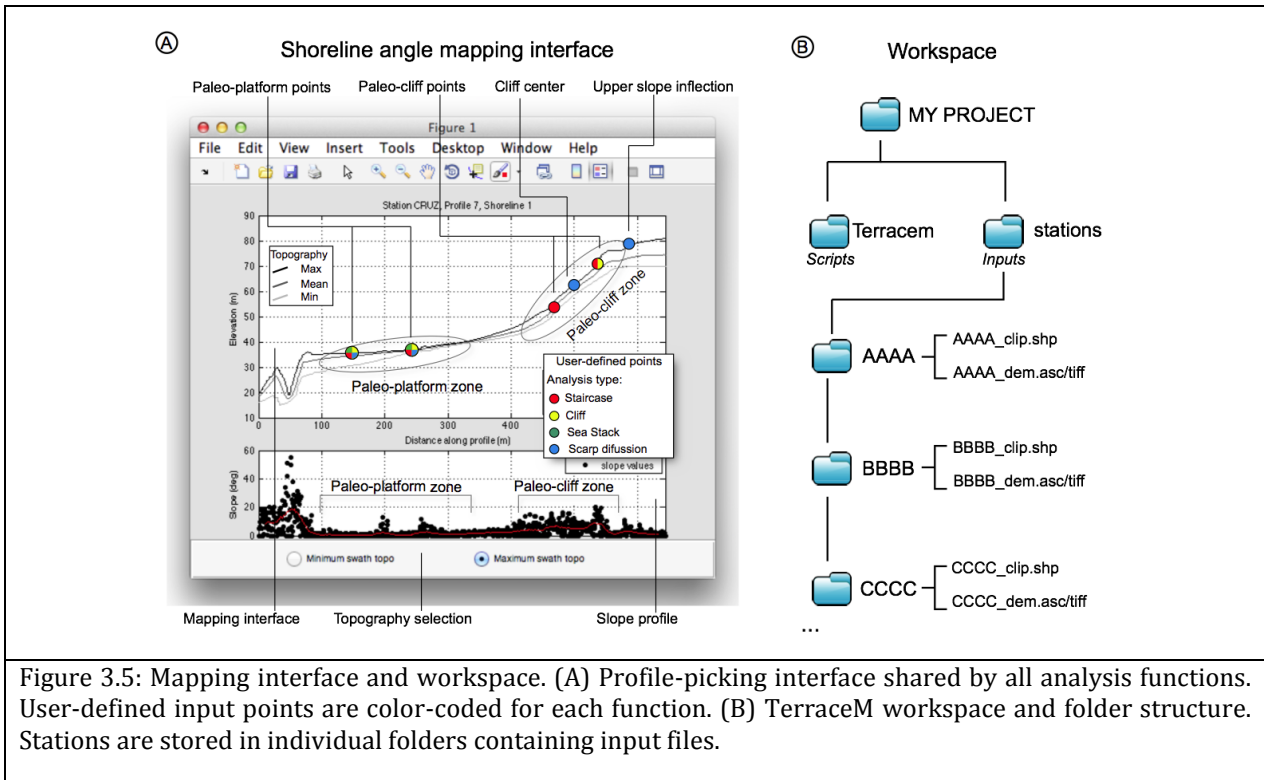


Figure 3.5: Mapping interface and workspace. (A) Profile-picking interface shared by all analysis functions. User-defined input points are color-coded for each function. (B) TerraceM workspace and folder structure. Stations are stored in individual folders containing input files.

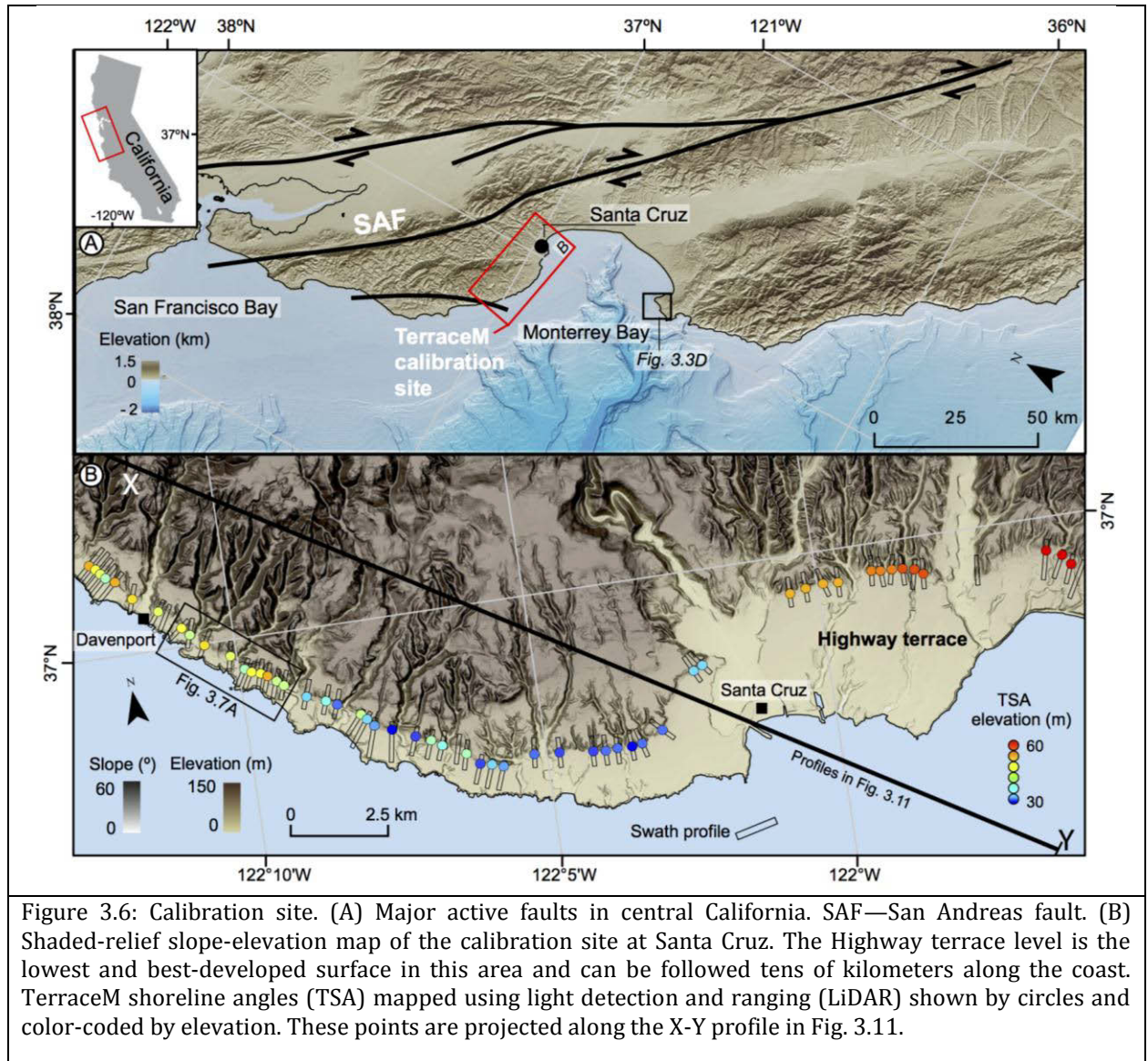
The TerraceM workflow consists of eight steps that should be executed sequentially to analyze the set of profiles (Fig. 3.4). Steps 1–5 (Input, Display, Processing, and Analysis tools) allow raw shoreline angles to be obtained, which can be filtered, exported, and projected along profiles in the following steps 6–8 (Editing, Projecting, and Export). While TerraceM is running, information messages are prompted inside the command bar, guiding users through the different steps to calculate shoreline angles (Fig. 3.4A) (See Appendix B.3 for further details)

3.3.3 TerraceM Calibration Site: Santa Cruz Marine Terraces

We compared shoreline angles estimated with TerraceM with field measurements made along the coast of Santa Cruz, California (Figs. 3.6A and 3.6B), in an area characterized by excellent and continuous exposures of several levels of marine terraces. In addition, this area is well suited as a test site, because LiDAR data are available from the OpenTopography portal (www.opentopography.org) and National Oceanic and Atmospheric Administration (NOAA; www.noaa.gov).

Marine terrace studies in the Santa Cruz area started with the pioneering work of Alexander (1953) and Bradley and Griggs (1976), who first described and mapped several flights of marine terraces. Subsequently, Anderson and Menking (1994) integrated both surveys, estimating uplift rates and earthquake recurrence of the adjacent San Andreas Fault (Fig. 3.6A). The Highway terrace level is the lowest in the area with an estimated marine isotope stage (MIS) 5e age (ca. 125 ka) (Anderson and Menking, 1994), and it is characterized by well-developed paleoclimbs that can be followed over distances of hundreds of kilometers along the coast (Figs. 3.1A and 3.6B). The elevation pattern of the Highway terrace increases southward from ~30 to ~70 m (see “Precision and Accuracy of Measurements” section). According to Anderson and Menking (1994), errors of shoreline estimations arise from: (1) low precision of shoreline-elevation measurements; (2)

measurement errors of the initial investigators (for example, Bradley and Griggs (1976) reported 1–2 m error, whereas Alexander (1953) reported 5 m error); and (3) the error in reading the data from the plots provided in these publications.



3.4 Analytical tools

TerraceM includes four functions that use different methods to determine the shoreline angle in different geomorphic scenarios. These functions are included in step 5 of the workflow (Fig. 3.4) and described in detail in Appendix B.1.

3.4.1 Staircase Marine Terraces

Multiple marine terraces across a vertical transect are analyzed using the Staircase function, which is based on the concept of shoreline angle defined by Lajoie (1986) (see “Background and

Motivation” section). This is particularly useful when working with well-preserved paleoplatform and paleoclip morphologies (e.g., Figs. 3.5A and 3.7A).

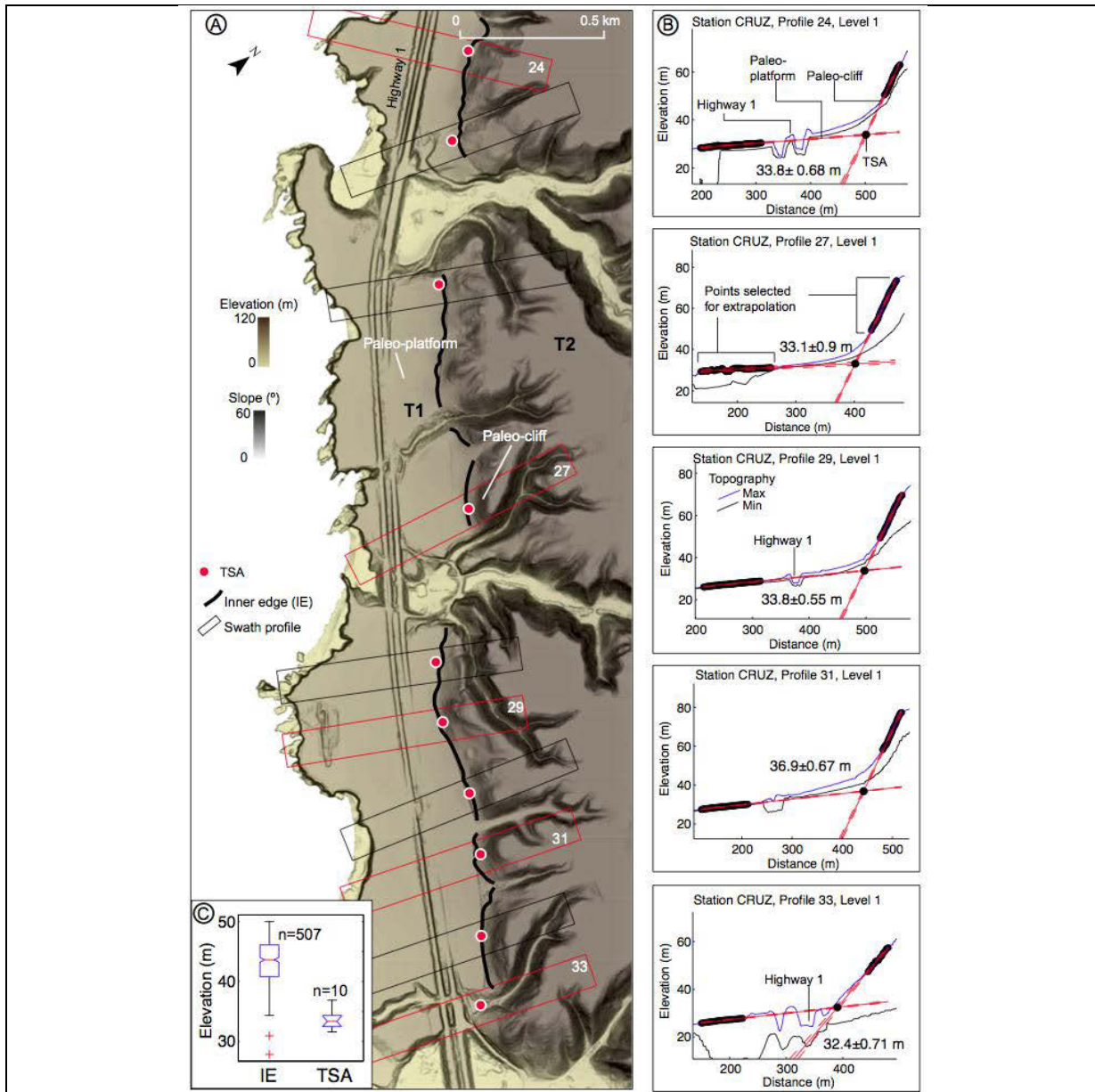


Figure 3.7: Example of shoreline angles obtained using the Staircase Analysis function. (A) Light detection and ranging (LiDAR) shaded-relief map showing two marine terraces (T1 and T2) and the location of swath profiles oriented perpendicular to the T1 inner edge (IE, thick black line). (B) Swath profiles with Staircase Analysis function, extrapolation lines and position of obtained TerraceM shoreline angle (TSA) by linearly extrapolating sections of the paleoplatform and paleoclip slope between points defined by user. (C) Box-and-whisker plots of IE and TSA distributions. Note that the IE elevations are higher than the TSA due to systematic overestimations associated with the presence of a colluvial wedge.

The determination of the shoreline angle can be accomplished using the maximum or minimum topographic distribution obtained from topographic swath profiles. The maximum distribution of elevation in topographic swath profiles allows the pre-incision topography to be deciphered; however, the maximum topography may be biased locally by climbing dunes. In this particular

case, the minimum elevations can be used to isolate the base of the dune field that should represent a maximum estimate of the original paleoplatform surface (see “Background and Motivation” section). Examples of the analysis of terraces with staircase morphologies and covered by dunes can be found at the Chile convergent margin, as described by Jara-Muñoz et al. (2015a).

The Staircase function is designed to analyze swath profiles interactively, calculating the shoreline angle by clicking directly above the topographic swath profiles (Fig. 3.5A). Two user-defined points along the steepest part of the profile define the paleocliff, and two additional points delineate the extent of the paleoplatform (Fig. 3.7B). Linear regressions are then calculated upon the enclosed segments on the profile and extrapolated to find the intersection that marks the position of the shoreline angle. Vertical errors of shoreline angles are based on the extrapolation of the 2σ ranges in the linear regressions (Fig. 3.7B).

3.4.2 Sea Stacks at Rough Coasts

The Sea-Stack Analysis function allows shoreline-angle elevations along rough, rocky coasts to be analyzed. Sea stacks and stumps form where portions of a retreating coast become isolated through erosion and dissection of the cliff base (Trenhaile et al., 1998; Bird and Bird, 2000); these features are detached from the cliff, forming isolated promontories (Figs. 3.8A and 3.8B), columns, stack-arcs, and caves, which represent fragments of partly eroded terrace levels (e.g. Bishop, 1985; Saillard et al., 2011; Jara-Muñoz et al., 2015a).

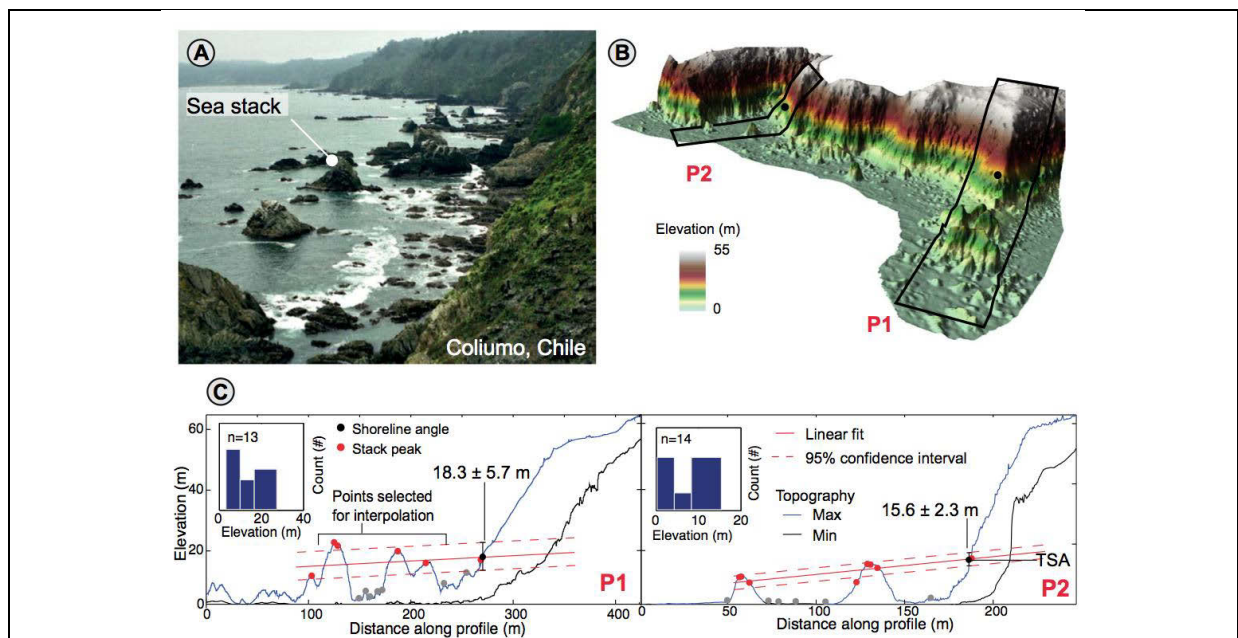


Figure 3.8: Stack Analysis function for rough coasts. (A) Field view of a rough coast characterized by sea stacks, stumps, and cliffs that represent eroded remnants of a marine isotope stage (MIS) 5e paleoplatform in central Chile (Jara-Muñoz et al., 2015). (B) Three-dimensional oblique view of 0.5 m light detection and ranging (LiDAR) digital terrain model, showing location of swath profiles (P1 and P2). Stacks used for the analysis can be clearly seen. (C) Swath profiles analyzed using the Stack function. Red lines indicate linear fits used to reconstruct the paleoplatform morphology. Points are automatically extracted using a peak-detection algorithm. The TerraceM shoreline angle (TSA) is located at the intersection of the reconstructed surface with the cliff. Histograms in insets show distribution of peak elevations used for interpolation; gray peaks associated with a lower level were not considered.

The maximum elevation of the swath profiles highlights stack morphology and the location of peaks, which delineate the degraded terrace platform (Fig. 3.8A). By using a peak-detection algorithm (Billauer, 2008), individual stack positions and their maximum elevations are extracted along the profile (Fig. 3.8C). Peaks are grouped in classes and linearly interpolated to reconstruct the paleotopography of the platform. The user defines the roof or upper limit of each range interactively, and then the linear regression of peaks is extrapolated backward toward the cliff to find the elevation of the shoreline angle and the associated 2σ error (Fig. 3.8C). Spatially consistent distributions of shoreline angles have been estimated using this method for a partly degraded MIS 5e terrace in central Chile (Fig. 3.8A) (Jara-Muñoz et al., 2015a).

3.4.3 Scarp Diffusion

The geomorphic age of a paleoclip abutting a terrace (Kt) may be estimated from the linear diffusion equation (Hanks et al., 1984) (Eq. 3 herein; see “Background and Motivation” section). The first step of the Scarp Diffusion function is to define the temporal resolution of the model by specifying the range of iterations and the geometry of the profile, which is defined by the upper-slope break, the extent of the paleoplatform, and the profile center (Fig. 3.9). Finally, the cliff height ($2a$), and the far-field slope (f_s) are calculated from the parameters; the best-fitting model is selected by minimizing the root mean square error, obtaining the geomorphic age of the cliff (Fig. 3.9).

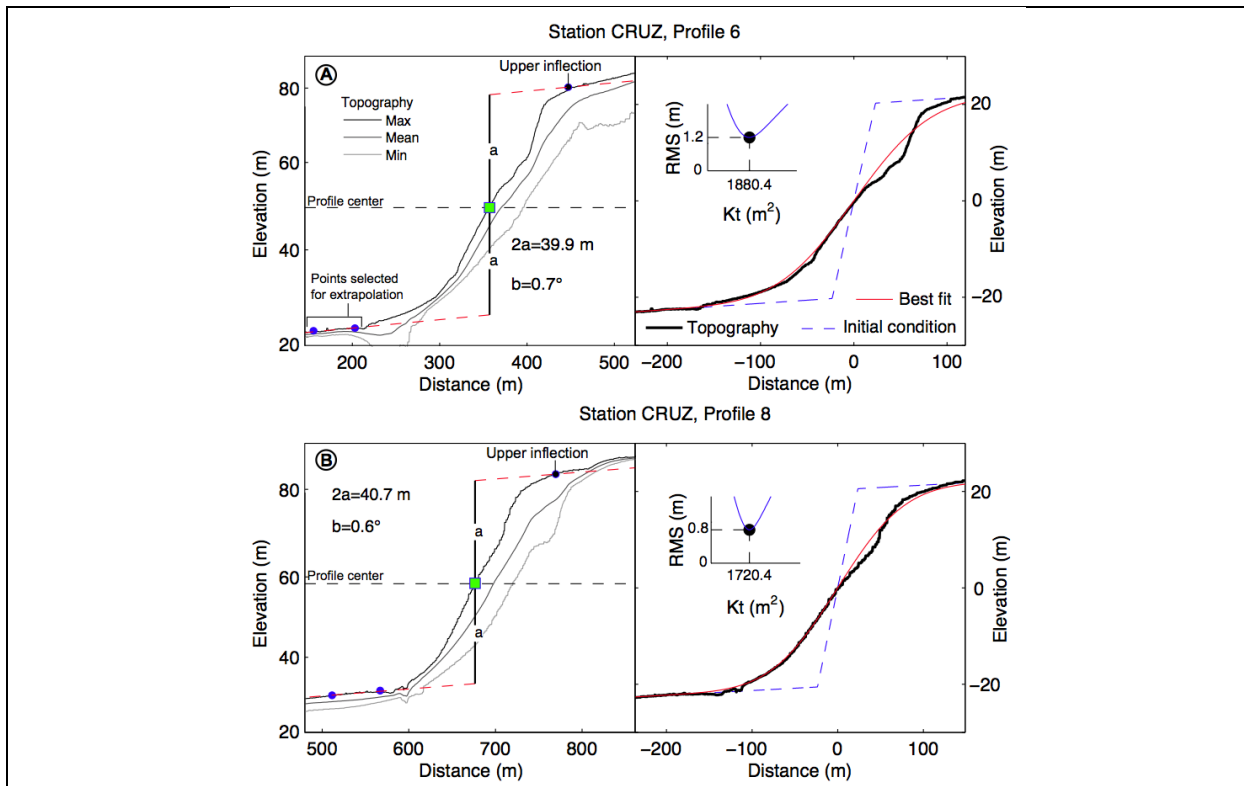


Figure 3.9: Examples of the Diffusion Analysis function based on Hanks et al. (1984). (A–B) Two different swath profiles of the calibration site at Santa Cruz, California. The left panels show the profile geometry and user-defined upper inflection of paleoclip and paleoplatform (blue points), and center of the profile (green square) used to calculate cliff height ($2a$) and the far field slope (b). Right panels show best fit of diffusion models and resulting geomorphic age (Kt). The user defines the number of iterations used to minimize the root mean square error (RMS, inset), allowing the best fit for Kt to be determined.

3.4.4 Cliff Free-Face

The Cliff Free-Face function allows the shoreline angle to be located by using the slope distribution of modern cliffs as input angle to extrapolate the slope of a paleoclipf below the colluvial wedge to find the shoreline angle (Fig. 3.10).

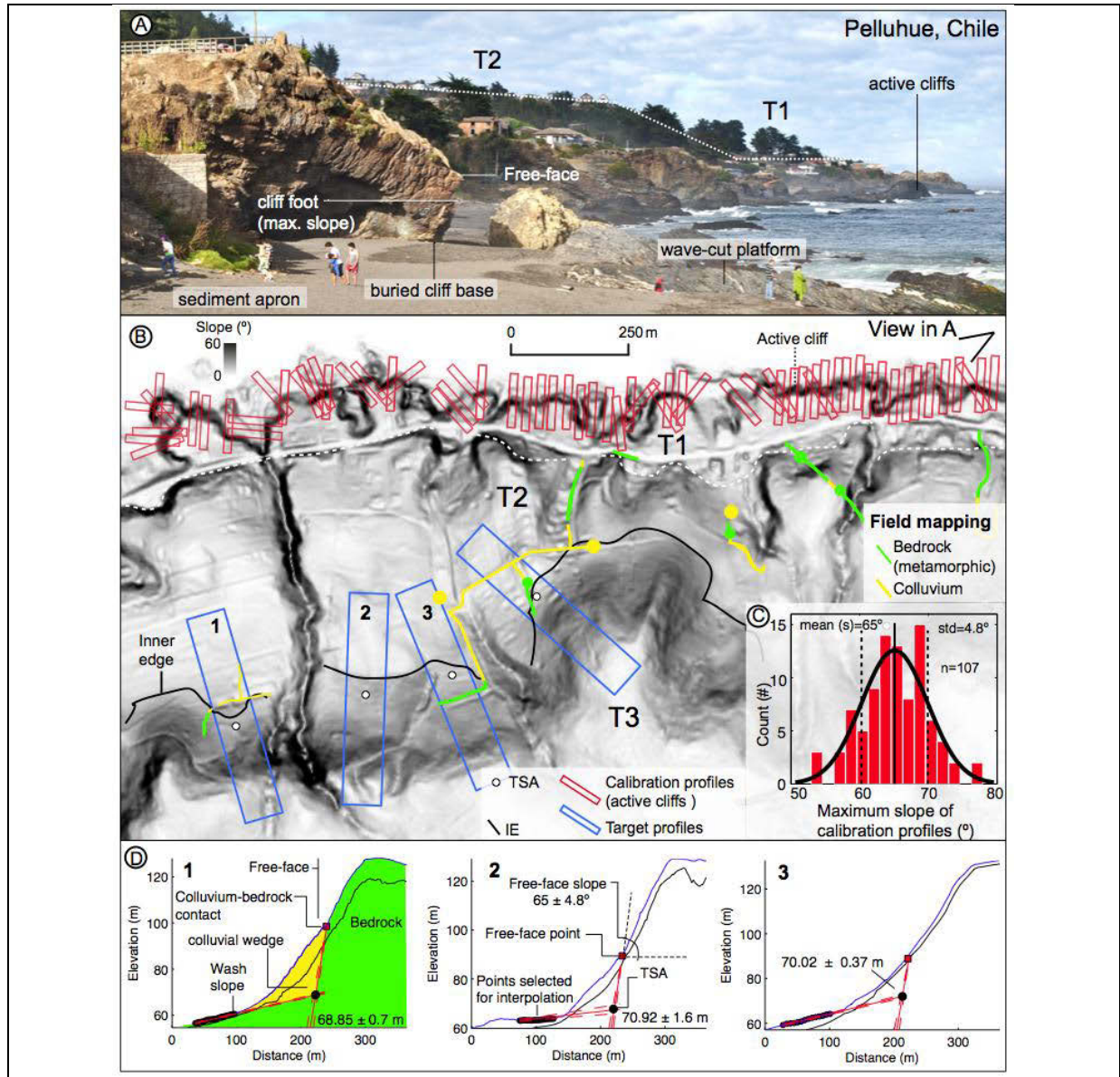


Figure 3.10: Example of the Free-Face Analysis function. (A) Field view of a Holocene cliff used to estimate the free-face slope; the maximum slope is typically located near the base of the cliff. (B) Light detection and ranging (LiDAR) slope map displaying three terrace levels (T1, T2, and T3), swath profiles, and field mapping at Pelluhue, Chile. We used 107 calibration profiles on Holocene cliffs (red boxes) determining the maximum slope of metamorphic bedrock, which was subsequently used for the analysis of the T2 using swath profiles (blue boxes). IE—inner edge, TSA—TerraceM shoreline angle. (C) Histogram of maximum slope angles of the Holocene cliff, where the standard deviation and mean were used as inputs for the free-face slope in D. Black line shows a theoretical Gaussian distribution. (D) Example of swath profiles analyzed with the Free-Face function. The shoreline angle is located at the intersection between the linear interpolation of the paleoplatform and a point defining the free-face base. The free-face slope intersects the paleoplatform to locate the shoreline angle.

The concept of free-face refers to the exposed part of fault scarps above colluvium (e.g. McCalpin, 2009), which we extend to a wave-cut scarp features in this study. This analysis is recommended for terraces with well-defined colluvial wedges below exposed cliffs with restricted heights, but sculpted into resistant bedrock, or for smoothed paleocliffs with marked transitions at the top of colluvium. This method is furthermore recommended for terraces covered by calcrete or beach rock, where low diffusion rates are favorable to preserving the free-face morphology over longer periods of time.

The Cliff Free-Face function is analogous to the Staircase function. However, in this case, the slope of the cliff is not estimated by linear regression, but is defined by the user and incorporated by graphically selecting a single point on the paleocliff. This point should be defined at the lower limit of the free face or at the contact between colluvium and exposed bedrock (Fig. 3.10D). Two additional points enclosing the paleoplatform are defined beyond the wash slope to find the shoreline angle and its associated 2σ error.

We present an example of this method at Pelluhue in south-central Chile with the analysis of modern cliffs and emerged terraces, where we estimated the slope of 107 Holocene cliffs and used the mean value and standard deviation as input to obtain the elevation of buried shoreline angles of emerged terraces levels (Fig. 3.10). At Pelluhue, the bedrock consists of homogeneously distributed schist; however, in case of variable bedrock lithologies, we recommend estimating cliff-slope distributions for each lithologic unit.

3.5 Postprocessing tools

TerraceM involves straightforward procedures for rapid visualization of shoreline-angle distributions and the filtering of outliers. A projection routine is included to display shoreline angles along a user-defined line, and an additional filtering routine has been included to remove outliers and improve the interpolation results for multiple shoreline angles and terrace levels. Errors in measurements may increase due to incorrect profile orientation, due to presence of sedimentary bodies near the base of the cliff, or due to incorporation of artificial structures (see “Repeatability of Measurements” section). Filtering is based on a nearest-neighbor interpolation with a user-defined bin size and exclusion range. The exclusion range is usually the standard deviation of the shoreline distribution and can be adjusted to improve the smoothness of the profile; we usually adjust this value by removing less than 10% of the shoreline-angle population. Along the terrace flights in Santa Cruz, we obtained shoreline angles for 90 profiles, excluding five of them (6% of the population) after filtering.

Visualization of shoreline-angle distributions is useful when comparing spatially disparate locations. The statistics routine calculates a histogram for each station, depicting the distribution of the elevation of shoreline angles or Kt values, including mean and standard deviation. Topographic profiles with shoreline angles determined from the analysis functions can be formatted inside 8×2 subplots and presented as a ready-to-print data repository in Adobe® pdf format. (Shoreline angle data used for plots of the Santa Cruz case study are included in Appendix B.5).

3.6 Precision and accuracy of measurements

We compared the results of shoreline-angle morphometry from the Santa Cruz Highway terrace using TerraceM, and different DEM resolutions, with actual field measurements (Anderson and Menking, 1994). This comparison allowed us to evaluate the errors and determine the precision and accuracy of TerraceM.

Accuracy and precision are defined in terms of systematic and random errors, respectively. Field measurements of shoreline angles were first compared with the results of TerraceM using a 2.5-m-resolution LiDAR DTM by linearly interpolating the shoreline angles using a 2 km bin size (Fig. 3.11A). Residuals calculated from the difference between the linear interpolations were not significantly different from a Gaussian distribution with a mean of 0.16 m and a standard deviation of 2.5 m. The obtained mean value is very low and smaller than the vertical error reported in the field measurements; the standard deviation is equal to the horizontal resolution of the DTM. Consequently, we assume the 0.16 m mean value to represent the accuracy and the 2.5 m standard deviation to represent the precision of TerraceM measurements for this case study.

Table 3.2: *Spatial information of datasets used for comparisons of TerraceM results.*

Types of dataset	LiDAR	NED	ASTER	Field survey
Horizontal Datum	NAD83	NAD83	NAD83	Unknown
Vertical Datum	NAVD88	NAVD88	NAVD88	Altimeter
Resolution (px/m)	2	10	30	-
Vertical accuracy (m)	0.3	2.55	20	5
Reference	Open Topography	Gesch et al., 2002	Aster, 2011	Alexander, 1953 / Bradley and Griggs, 1976

Unfortunately, LiDAR topography is not yet available along all coastlines of the world, and thus we tested the dependence of TerraceM results obtained using different resolutions from the 10 m National Elevation Data set (NED, U.S. Geological Survey) and 30 m Advanced Spaceborne Thermal Emission and Reflection Radiometer (ASTER) Global Digital Elevation Model (GDEM, J-spacesystems) topographic data sets (Gesch et al., 2002; Maune, 2007; Aster, 2011) (see details in Table 3.2). The comparisons between DEMs were performed using the same datum (North American Vertical Datum 1983 [NAD83]/NAVD88). We used the LiDAR-derived shoreline angles as base values to compare the deviations of the other data sets, and we calculated the residuals using linear interpolation (Fig. 3.11B). The distribution of errors was used to estimate the precision and accuracy of each topographic data set. As expected, precision and accuracy were inversely related to DEM resolution (Fig. 3.11D). During the analysis, we noticed that shoreline angles estimated using the ASTER DEM might result in erroneous interpolations of paleocliffs for short profiles, and consequently we recommend increasing swath sizes for low-resolution DEMs.

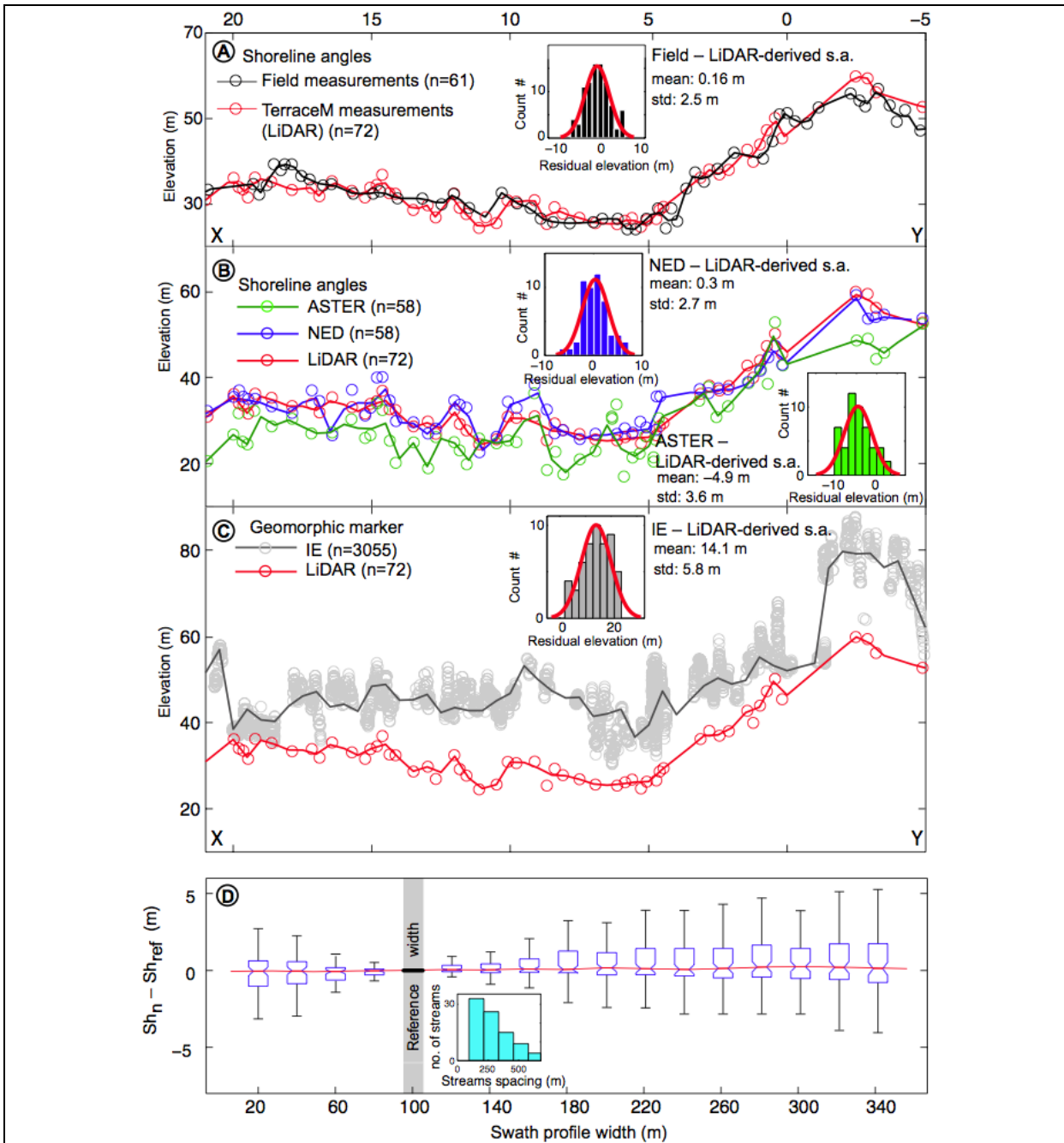


Figure 3.11: Comparison of shoreline-angle elevations obtained from different types of surveys, digital elevation model (DEM) resolutions, and geomorphic markers. (A) Coast-parallel profile (indicated in Fig. 3.6) with shoreline-angle elevations for different surveys. Field survey is from Alexander (1953) and Bradley and Griggs (1976) compiled by Anderson and Menking (1994). Shoreline angles were derived from 2.5-m-resolution light detection and ranging (LiDAR) topography. Inset shows the distribution of residuals. (B) Profile of shoreline-angle elevations estimated from LiDAR, National Elevation Data set (NED), and Advanced Spaceborne Thermal Emission and Reflection Radiometer (ASTER) topographic data sets. The insets show distribution of residuals to LiDAR-derived shoreline angles. (C) Profile of inner-edge (IE) elevations and LiDAR-derived shoreline angle. Note IE values are always higher than the shoreline angles. Inset shows distribution of residuals to LiDAR-derived shoreline angles. (D) Relation between swath width and shoreline-angle elevations. Box-and-whisker plots show shoreline-angle elevation difference from a reference swath width of 100 m (Sh_{ref}) for the 90 measured profiles. In total, 1530 profiles were analyzed. Note consistency of the mean and increase in skewness toward positive values with higher swath width and toward negative values with lower widths; see text for discussion. Inset shows the distribution of channel spacing along the inner edge of the Highway terrace, for channels that cut the riser.

To quantitatively assess the differences between shoreline angle and inner-edge measurements (described in “Background and Motivation” section), we compared both geomorphic markers by means of their residuals (Fig. 3.11C). We started mapping the inner edge on LiDAR-derived slope maps using two slope ranges between 0° to 30° and 30° to 90°, following the method proposed by Palamara et al. (2007). We first extracted the elevation of the inner edge (e.g., Fig. 3.7A) and calculated the differences from the LiDAR-derived shoreline angles (Fig. 3.11C) by comparing linear interpolations. The obtained residuals had a mean of 14.1 m and a standard deviation of 5.8 m. These values suggest that the inner-edge measurements overestimate terrace elevation, and they are characterized by a relatively low precision and low accuracy with respect to the shoreline angles.

Another factor that may influence the precision and accuracy of TerraceM shoreline angle-elevations is the width of the swath profile. Channel incision will tend to reduce the maximum elevation of swath profiles, with the amount of reduction depending on the position of the swath with respect to the channels and on its width. We tested the influence of swath width by incrementally increasing the width of profiles along the Santa Cruz Highway terrace (Fig. 3.11D). First, we calculated the spacing of channels that cut the terrace riser, finding a minimum spacing close to 100 m (inset in Fig. 3.11D) and used this value to estimate reference shoreline-angle elevations. Then, we calculated shoreline angles by incrementally increasing the swath width from 20 to 340 m and compared them with the reference estimates.

This experiment shows that the range of shoreline-angle elevations is dependent on the swath width, although changes in median elevation change are rather limited (<1 m). As could be expected, the amplitude of the elevation change increases with swath width; the general tendency shows that narrower swaths result in predominantly lower elevations, and wider swaths result in higher values (Fig. 3.11D). Larger widths could be biased by irregularities along the strike of the terrace riser, causing an apparent seaward position of the cliff and thus lowering the shoreline angle; in turn, the higher probability to have greater elevations in the platform would cause the opposite effect, resulting in higher shoreline elevations. This could explain the increase in the dispersion of the shoreline elevations observed for larger widths. For narrower widths, lower elevations will arise in areas where both the platform and cliff have been dismantled by channel incision, whereas the higher probability to include drainages in the swath would result in an apparent increase of the platform slope, resulting in higher shoreline elevations. Based on these results, we suggest using a value close to the minimum drainage spacing for the width of swath profiles in TerraceM.

3.7 Repeatability of measurements

To evaluate the repeatability of shoreline-angle measurements, we performed an experiment with a group of 10 inexperienced users following the six conditions proposed by Bland and Altman (Bland and Altman, 1986) to evaluate uncertainty: (1) the same experimental tool (TerraceM); (2) the same observer (we carried out the experiment and processed the data); (3) the same measuring instrument under the same conditions (the users carried out this experiment simultaneously using TerraceM); (4) the same location (the experiment was performed in a computer pool at the University of Potsdam); (5) repetition over a short period of time (the

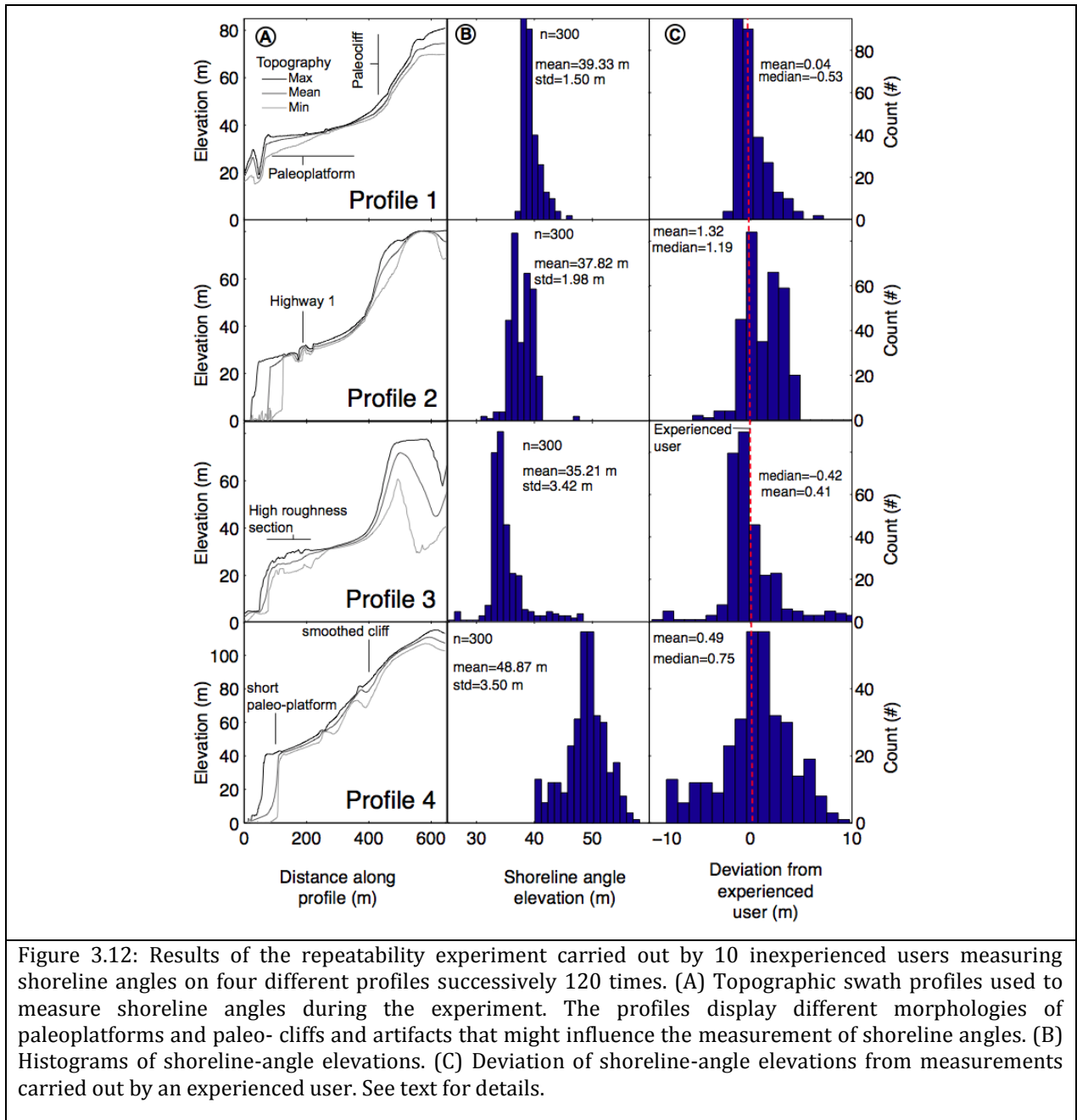
experiment consisted of repeating a series of four profiles continuously for 120 times; and (6) the same objective (map the shoreline angles in all profiles).

The profiles selected for the experiment exhibit small differences in topography that we used to evaluate possible sources for error in the measurements (Fig. 3.12A). For instance, profiles 1 and 2 are characterized by sharp subvertical paleoclimbs with small artifacts along the paleoplatform due the intersection with Highway 1; profile 3 is characterized by high-roughness sections at the outer edge of the paleoplatform; and profile 4 has a relatively narrow paleo-platform and smoothed paleoclimb, probably associated with eolian and/or colluvium accumulation.

The results of the experiment show narrow distributions of shoreline-angle elevations for all profiles (Fig. 3.12B), but χ^2 tests indicate that these distributions are not Gaussian, suggesting the data are theoretically invalid for a repeatability analysis. Nevertheless, we used a heuristic approach to study the distribution and sources of errors using the standard deviation, the mean, and the median of each profile. Geomorphic differences between profiles appear to be expressed in the standard deviation of shoreline-angle distributions (Fig 3.12B). For instance, profile 1, which has a sharp paleoclimb and paleoplatform, yielded the lowest standard deviation (1.5 m). Instead, profile 4 has the highest standard deviation of 3.4 m, possibly associated with the ambiguity in interpreting smoothed paleoclimbs, hence resulting in a more scattered distribution of shoreline angles. Artificial structures, such as the Highway 1 crossing the terraces along the paleoplatform in profiles 2 and 3 (Fig. 3.12A), are associated with a positive bias in shoreline angles. Profile 2 displays a bimodal distribution, and profile 3 displays a positive tail. We conclude that the incorporation of Highway 1 into the area used to interpolate the paleoplatform may bias shoreline-angle elevations toward higher values; these different criteria of shoreline angle mapping may be associated with inexperienced users.

To estimate the precision of measurements carried out by first-time users, we subtracted the shoreline-angle elevation from terrace measurements carried out by an experienced user (Fig. 3.12C). The mean and median of the centered distributions were used to estimate the precision of the measurements. Profiles 1, 3, and 4 are characterized by low mean and median values (mean: 0.04–0.5 m, median: 0.4–0.75 m), indicating higher accuracy when compared with profile 2, which yielded the highest mean and median values of 1.32 m and 1.19 m, respectively; the lower accuracy of this profile is associated with the bimodal distribution of elevations.

The distributions of shoreline angles for the different profiles are non-Gaussian and probably contain both systematic and random errors in an unknown proportion. However, through the comparison of morphologic elements of marine terraces with the statistics of shoreline-angle distributions in a heuristic manner, we detected possible sources for systematic errors. To minimize these errors, we suggest the following: (1) select the smoothest and most representative segment of the paleoplatform for fitting, avoiding the influence of artifacts; (2) for smoothed paleoclimbs, try other mapping methods, such as the Cliff Free-Face function; and (3) maximize user experience, which is important to increase the accuracy of the measurements, by training first-time users with TerraceM in batch mode and with different case studies.



3.8 Summary

Wave-cut terraces formed in marine as well as lacustrine environments are important geomorphic marker horizons that help researchers assess the impact of tectonic and climatic processes on landscape evolution. TerraceM is a Matlab GUI designed to study terraces in the marine and lacustrine realms quantitatively by incorporating several methods developed and tested using high-resolution LiDAR topography in different coastal settings. The interface and structure of TerraceM are designed to manage large amounts of profiles grouped in separated stations simultaneously. By comparing TerraceM measurements using LiDAR topography with a field survey of shoreline angles in the region of the Highway marine terrace in Santa Cruz, California, we estimated 0.16 m accuracy and 2.5 m precision. By taking advantage of high-resolution

topography, TerraceM will help to expand and facilitate regional studies of marine terraces. For further information visit www.terracem.com (See Appendix B.4 for version details).

4 Segmentation of the 2010 Maule Chile earthquake rupture from a joint analysis of uplifted marine terraces and seismic-cycle deformation patterns

Along this chapter I combined the methodologies developed in Chapters 2 and 3 to study marine terraces and estimate permanent vertical deformation rates, which were compared with seismic cycle deformation patterns along the 2010 Maule earthquake rupture zone.

The segmentation of major fault systems in subduction zones controls earthquake magnitude and location, but the causes for the existence of segment boundaries and the relationships between permanent deformation and the extent of earthquake rupture, are poorly understood. We compare permanent and seismic-cycle deformation patterns along the rupture zone of the 2010 Maule earthquake (M8.8), which ruptured 500 km of the Chile subduction margin. We analyzed the morphology of MIS-5 marine terraces using LiDAR topography and TerraceM, establishing their chronology and coeval origin with twelve luminescence ages, stratigraphy and geomorphic correlation, obtaining a virtually continuous distribution of uplift rates along the entire rupture zone. The mean uplift rate for these terraces is 0.5 m/ka. This value is exceeded in three areas, which have experienced rapid emergence of up to 1.6 m/ka; these sectors correlate with boundaries of eight great earthquakes dating back to 1730. The Topocalma and Arauco sectors, located at the boundaries of the 2010 rupture, consist of broad zones of crustal warping with wavelengths of 60 and 90 km, respectively. These two regions coincide with the axes of oroclinal bending of the entire Andean margin and correlate with changes in curvature of the plate interface. Rapid uplift at Carranza, in turn, is of shorter wavelength and associated with footwall flexure of three crustal-scale normal faults. The uplift rate at Carranza is inversely correlated with plate coupling as well as with coseismic slip, suggesting permanent deformation may accumulate interseismically. We propose that the zones of upwarping at Arauco and Topocalma reflect changes in frictional properties of the megathrust resulting in barriers to the propagation of great earthquakes. Slip during the 1960 (M9.5) and 2010 events overlapped with the ~90-km-long zone of rapid uplift at Arauco; similarly, slip in 2010 and 1906 extended across the ~60-km-long section of the megathrust at Topocalma, but this area was completely breached by the 1730 (M~9) event, which propagated southward until Carranza. Both Arauco and Topocalma show evidence of sustained rapid uplift since at least the middle Pleistocene. These two sectors might thus constitute discrete seismo-tectonic boundaries restraining most, but not all great earthquake ruptures. Based on our observations, such barriers might be breached during multi-segment super-cycle events.

4.1 Introduction

The seismic cycle of great subduction earthquakes has been described as a repetitive sequence of crustal deformation phenomena constituting three main steps: strain accumulation during the interseismic period, release of strain by an earthquake during the coseismic stage, and the post-seismic period, characterized by complex transient processes in the years to decades following the earthquake (e.g. Wang, 2007). The cumulative, permanent deformation, which is expressed in mountain building and the formation of sedimentary basins, integrates this cycle over long timescales. The pioneering observations of coseismic uplift during the 1835 Chile earthquake by Darwin and Fitz-Roy are considered to be the first empirical confirmation of the relationship between earthquakes and mountain building (Darwin, 1851; Kölbl-Ebert, 1999). However, neither the spatial nor the temporal relationships between both processes or the different steps of the seismic cycle and mountain building are fully understood.

It has been proposed that forearc regions are divided into semi-independent seismotectonic segments. Such segments may reflect the long-term structural and topographic expression of numerous earthquake cycles, thus forming geomorphic entities that sustain their style and rate of deformation over long timescales (e.g. Ando, 1975; Taylor et al., 1987; Chen et al., 2011; Victor et al., 2011). This notion is partly based on the observation that the slip distribution of some great to giant ($M \geq 9$) megathrust earthquakes exhibits a clear segmentation into distinct sectors. Examples include the 1964 Alaska (Suito and Freymueller, 2009), 2004 Sumatra (Chlieh et al., 2007), and the 1960 and 2010 Chile (Moreno et al., 2009; Moreno et al., 2012) earthquakes. In contrast to these observations, slip during the 2011 Tohoku ($M9.1$) event in Japan was rather localized in a single region (Ozawa et al., 2011).

Slip distributions of the 1960 Chile ($M9.5$) and the 2011 Tohoku ($M9.1$) earthquakes exhibit a certain degree of coherence with the pattern of pre-seismic locking determined from modeling of geodetic data (Moreno et al., 2010; Loveless and Meade, 2011; Moreno et al., 2012). Despite these recent advances in assessing the mechanics of slip distribution and how deformation is accrued in repeated large earthquakes, the correlations between coseismic slip and the sustained long-term segmentation of forearcs, particularly in Chile, remain poorly understood. In addition, it is not known why forearcs may rupture repeatedly along the full length of segments (e.g. Shennan et al., 2009) or why ruptures propagate across segment boundaries under certain circumstances (e.g. Nanayama et al., 2003; Taylor et al., 2008). Gaining insight into the mechanical causes for segmentation, rupture propagation, and the characteristics of seismic-cycle vs. permanent deformation patterns of forearcs may help define the stable or transient nature of forearc-segment boundaries and furnish information vital to seismic hazard assessments.

In an attempt to contribute to this important topic we studied marine terrace systems, which occur at different elevations along the Chile margin. Multiple flights of marine terrace systems are ideal geomorphic strain markers that allow for an analysis of surface-uplift rates, spatiotemporal variation in deformation and uplift patterns, and the characteristics of potential forearc segmentation (e.g. Lajoie, 1986; Pedoja et al., 2011). In this study we use detailed geologic mapping, morphometric analysis, and age determinations of interglacial marine terraces to assess

long-term seismotectonic segmentation in light of the ~500-km-long rupture zone of the 2010 Maule (M8.8) earthquake along the south-central part of the Chile convergent margin.

Over the last decade earthquake research has benefited from the availability of LiDAR (light detection and ranging) topographic data, which allows producing a vegetation-free surface digital terrain models. Here we use such bare-earth models to analyze terrace sequences along the entire Maule rupture. Based on age determinations as well as stratigraphic and morphologic criteria, we correlate marine terraces along the rupture zone to obtain virtually continuous uplift rate estimates spanning the past ~105 years. Furthermore, we compare the pattern of uplift rates and their gradients with the extent of historical megathrust earthquakes and coseismic slip distribution during the Maule earthquake and interseismic coupling in the decade before the event. Based on these correlations, we infer the relation between the position and nature of earthquake barriers, proposing a seismotectonic segmentation comprising persistent and transient boundaries in the realm of the Maule earthquake in south-central Chile.

4.2 Tectonic and geomorphic framework

4.2.1 Regional tectonic and geologic setting

Coastal south-central Chile is an integral part of the tectonically active forearc, where the oceanic Nazca plate is subducted beneath the South American continent at a convergence rate of 66 mm/yr (Angermann et al., 1999). The age of the Nazca plate along the Maule rupture increases continuously northward, from ~25 to 32 My (Tebbens and Cande, 1997). This segment of the margin has been in an accretionary tectonic mode since the Pliocene (Bangs and Cande, 1997), with a frontal accretionary wedge extending ~60 km inland from the trench along the continental slope and limited by a system of landward-dipping splay faults (Geersen et al., 2011) (Fig. 4.1B). The continental platform includes several up to ~3-km-deep Cenozoic forearc basins, which taper toward the slope and coast (e.g. (Mordojovich, 1981). Onshore, the main morphotectonic province is the Coastal Range. Its core includes a high-pressure Paleozoic accretionary complex intruded by a granitic batholith (Fig. 4.1B) (Kato, 1985). Limited exposures of forearc basins at the western flank of the Coastal Range consist of Cretaceous to Quaternary marine and continental sedimentary sequences in three main depocenters bounded by basement highs: the Arauco, Carranza, and Topocalma-Navidad basins (Cecioni, 1983; Gonzalez, 1990; Encinas et al., 2006b). Offshore seismic profiles and focal mechanisms suggest that the forearc has been under compression during the Quaternary (Bohm et al., 2002; Geersen et al., 2011). The contractional inversion of normal faults in forearc basins along the south-central Andes has been associated with a shift from erosive to accretionary conditions during the Pliocene (Melnick and Echtler, 2006). Rocky coasts and Holocene lowlands characterize the coastal geomorphology of the Maule rupture zone. The former are associated with resistant crystalline bedrock and are subjected to intense wave attack, whereas the latter occur mainly at the mouths of major rivers that carry predominantly volcanic detritus derived from the Andean volcanic arc (e.g. Mardones and Jaque, 1991). Northward-directed longshore drift further transports these sediments along the coast.

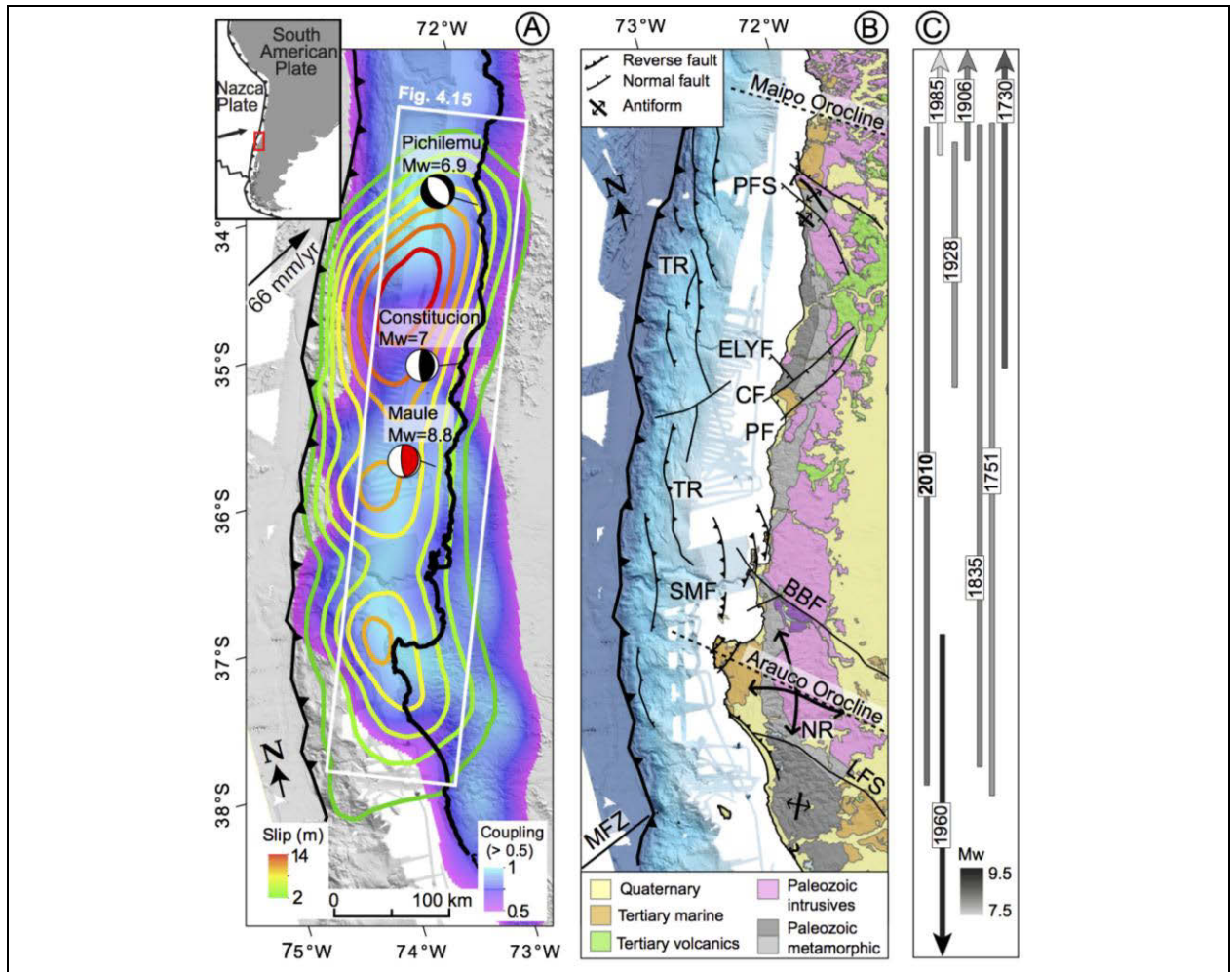


Figure 4.1: Deformation patterns, historical earthquakes and regional geology along the 2010 Maule earthquake rupture. (A) Coseismic slip during the Maule earthquake (Moreno et al., 2012) and interseismic coupling before the event (Moreno et al., 2010). Slip contours every 2 m, red star represents the location of the epicenter (Vigny et al., 2011). The white rectangle indicates area of swath profiles in Fig. 4.14. Focal mechanism based on Fariás et al. (2008), Vigny et al. (2011), Ruiz et al., 2013. (B) Geology and Quaternary structures. Black lines denote major upper plate faults. TR-thrust ridge, PFS-Pichilemu Fault System, SMF-Santa Maria Fault System, NR-Nahuelbuta Range, LFS-Lanahue fault System, MFZ-Mocha Fracture Zone, BBF-Bio-Bio Fault, ELYF-El Yolki Fault, PF-Pelluhue Fault, CF-Carranza Fault. The black dashed lines indicate the symmetry axis of oroclines after Fariás et al. (2008) and Melnick et al. (2009), (C) Rupture zone of historical earthquakes color-coded by estimated magnitude, see text for sources.

4.2.2 Quaternary crustal faults and previous estimates of coastal uplift rates

Quaternary faults have been described exclusively at the southern and northernmost sectors of the Maule rupture, namely the Lanahue, Santa Maria and Pichilemu faults (Fig. 4.1B). The Lanahue fault zone reactivates a Permian shear zone (Glodny et al., 2008) and bounds the southern Arauco Peninsula and Nahuelbuta Range, which form a major, ~100-km-wide, dome-like structure (Fig. 4.1B) (Rehak et al., 2008). Deformation patterns and the evolution of fluvial networks suggest domal uplift has been ongoing since the Late Pliocene and has been associated with the collision of a forearc sliver that extends to the south for ~1000 km (Melnick et al., 2009). The Santa Maria Fault system consists of a series of back-thrusts rooted in the interplate zone (Melnick et al., 2006), which generated surface ruptures during the Maule earthquake (Melnick et al., 2012d). The main

Quaternary structures in the northern part of the Maule rupture zone are two NW-SE trending antiforms with associated normal faults at Pichilemu and Topocalma (Farías et al., 2011) (Fig. 4.1B). The Pichilemu normal fault generated two crustal M6.7 and M6.9 earthquakes 11 days after the Maule mainshock (Fig. 4.1A) and a cluster of aftershocks extending from the plate interface to almost the surface (Lange et al., 2012; Ryder et al., 2012).

Quaternary uplift rates along the coast have been obtained at only a few sites within the Maule rupture zone. Melnick et al. (2009b) calculated a maximum uplift rate of 1.8 ± 0.2 m/ka using the ~ 125 -ka-old marine terrace level at the Arauco Peninsula. North of Arauco Peninsula, at Santa Maria island, uplift rates between 1.8 ± 0.4 m/ka for the past ~ 50 ka (Melnick et al., 2006) and 2.1 ± 0.3 m/ka during the past ~ 4 ka (Bookhagen et al., 2006) were estimated. Farther south at Lanalhue Lake, Stefer et al. (2010) obtained a mean Holocene uplift rate of 0.42 ± 0.71 m/ka. Southwest of Arauco, at Mocha Island, Nelson and Manley (1992) determined uplift rates between 2 and 10 m/ka during the Holocene. At Algarrobo, Encinas et al. (2006a) calculated a Holocene uplift rate of 0.4 m/ka. These disparate estimates suggest large spatial variability in uplift rates along the Maule region.

4.2.3 Historical earthquakes in south-central Chile

Until 2010 the Maule area was considered to be a mature seismic gap in Chile (Barrientos, 1987; Campos et al., 2002; Ruegg et al., 2009). The historical earthquakes in the Maule segment include at least four well-documented megathrust events in 1730, 1751, 1835 and 1928 (Darwin, 1851; Campos et al., 2002; Lomnitz, 2004; Udías et al., 2012) (Fig. 4.1C) and the deeper intra-slab Chillan event of 1939 (Beck et al., 1998). The giant 1730 ($M \sim 9$) event caused damage for a length of ~ 800 km along the coast with destructive tsunamis in Concepcion and Valparaiso (Udías et al., 2012; Cisternas et al., 2014). Both the 1751 and 1835 events were great earthquakes very similar to the 2010 event and had estimated magnitudes of 8.5-8.8 (Udías et al., 2012). During the 20th century two further subduction events affected this region: the 1906 ($M \sim 8.6$) earthquake, which overlapped about 200 km of the northern Maule rupture (Okal, 2005) and the 1928 ($M \sim 8.4$) event that began near Constitucion and ruptured to the north within the Maule segment (Lomnitz, 2004). The giant 1960 Valdivia ($M 9.5$) earthquake, the largest recorded by modern seismology (Plafker and Savage, 1970; Cifuentes, 1989; Moreno et al., 2009), overlapped with the southern ~ 90 km of the Maule rupture across the Arauco Peninsula. The 1985 ($M 8.0$) Valparaiso earthquake (Barrientos, 1988) partly overlapped with the northern Maule rupture (Fig. 4.1C).

4.2.4 The 2010 Maule earthquake

The Maule earthquake of February 27 nucleated in the central part of its 500-km-long rupture zone and reached a moment magnitude of 8.8. This event corresponds to the sixth largest instrumentally recorded earthquake and the third largest in the era of space geodesy. Slip distributions for the Maule earthquake have been obtained by at least 12 studies using various methods and approaches (Delouis et al., 2010; Farias et al., 2010b; Shao et al., 2010; Tong et al., 2010; Lorito et al., 2011; Pollitz et al., 2011; Pulido et al., 2011; Vigny et al., 2011; Moreno et al., 2012; Bedford et al., 2013; Lin et al., 2013; Yue et al., 2014). In spite of the differences among these model results, all the slip distributions derived from near-field geodetic data show a similar pattern formed by two main areas of high slip separated by a sector of reduced slip near the epicenter (e.g. Moreno et al., 2012; Lin et al., 2013) (Fig. 4.1A). The largest slip of more than 16 m

occurred north of the epicenter in one major patch located mostly offshore (Moreno et al., 2012; Bedford et al., 2013; Lin et al., 2013). The southern part of the rupture involved a secondary slip patch located mostly below the coastline with maximum slip of ~12 m. The down-dip termination of the rupture reached ~50 km depth (Tong et al., 2010; Moreno et al., 2012) coinciding at the surface with the trace of the coastline, except at the Arauco Peninsula where slip propagated farther inland. Kiser and Ishii (2011) suggested that slip in the northern part of the rupture dynamically triggered slip along the southern patch, both separated by a gap in rupture propagation, probably related to a mechanically weak zone.

Zones of coeval surface uplift and subsidence were recorded during the Maule earthquake, registered by GPS and field measurements using intertidal fauna (Farias et al., 2010b; Vargas et al., 2011; Vigny et al., 2011; Jaramillo et al., 2012; Melnick et al., 2012a; Moreno et al., 2012). Slip in the northern offshore patch caused subsidence along the adjacent coastline while in the southern patch slip concentrated below the coastline resulting in coastal uplift. The maximum coseismic uplift, estimated from measurements of intertidal fauna, was 2.5 m at Lebu and 2.4 m at Morguilla, both sites are located in the southwestern part of the Arauco Peninsula (Melnick et al., 2012a). Coseismic coastal subsidence reached a maximum estimate of 0.5 m at Bucalemu, in the northern part of the rupture (Vargas et al., 2011). The hinge line between coseismic uplift and subsidence was located at ~115 km from the trench (Fig. 4.2).

During the decade that preceded the Maule earthquake several studies attempted to quantify interseismic coupling along the Chile margin based on surface velocities estimated from GPS data (Klotz et al., 2001; Brooks et al., 2003; Khazaradze and Klotz, 2003; Moreno et al., 2008; Ruegg et al., 2009; Vigny et al., 2009). These studies suggested that interseismic coupling is characterized by lateral variations at scales of tens to hundreds of kilometers. Newer high-resolution and better-constrained models have revealed a heterogeneous distribution of interseismic coupling preceding the Maule earthquake (e.g. Moreno et al., 2010; Metois et al., 2012). The model of Moreno et al. (2010), which uses a detailed geometry of the megathrust based on Tassara et al. (2006), shows two highly coupled patches (>90%) separated by a region of reduced coupling (50-70%) at the center of the rupture (Fig. 4.1A). According to Moreno et al. (2012) these coupled patches are roughly coincident, but not blueprint copies of the coseismic slip distribution during the Maule earthquake (Fig. 4.1A). In this study we use the inter- and coseismic models of Moreno et al. (2010) and (2012), respectively, because these authors adopted the same modeling strategy as well as detailed geometries of the plate interface and lithosphere constraints by geophysical data, the largest number of GPS stations as well as InSAR and coastal land-level change data.

In an attempt to characterize the mechanism of segmentation of the Maule earthquake rupture different approaches have been used. For instance, Aron et al. (Aron et al., 2013) suggested that faults with suitable orientation with respect to the coseismic slip are likely to be active during the coseismic phase segmenting the rupture zone. At the southern boundary of the rupture, Lin et al. (2013) inferred that a velocity-weakening patch just below the Arauco Peninsula might facilitate the propagation of dynamic ruptures into the area but not through it, probably due to its large size (~100 km). At the northern part of the rupture, Farias et al. (2011) suggested that lithological heterogeneities locally increase the normal stresses on the mega-thrust causing a permanent barrier that has stopped earthquake propagation throughout the Quaternary. In the search for a tectonic control of earthquake segmentation, Moreno et al. (2012) noticed that the pattern of

coseismic slip correlates with inflections in the curvature of the slab, which may produce variations in shear stresses on the megathrust, also affecting the dynamic propagation of the rupture. The proposed correlation between long-term tectonic features and patterns of coseismic deformation implies that the Maule segment has probably been sustained over longer timescales, although, the northern limit of the Maule rupture was certainly breached by the 1730 earthquake (Fig. 4.1C), (Udías et al., 2012).

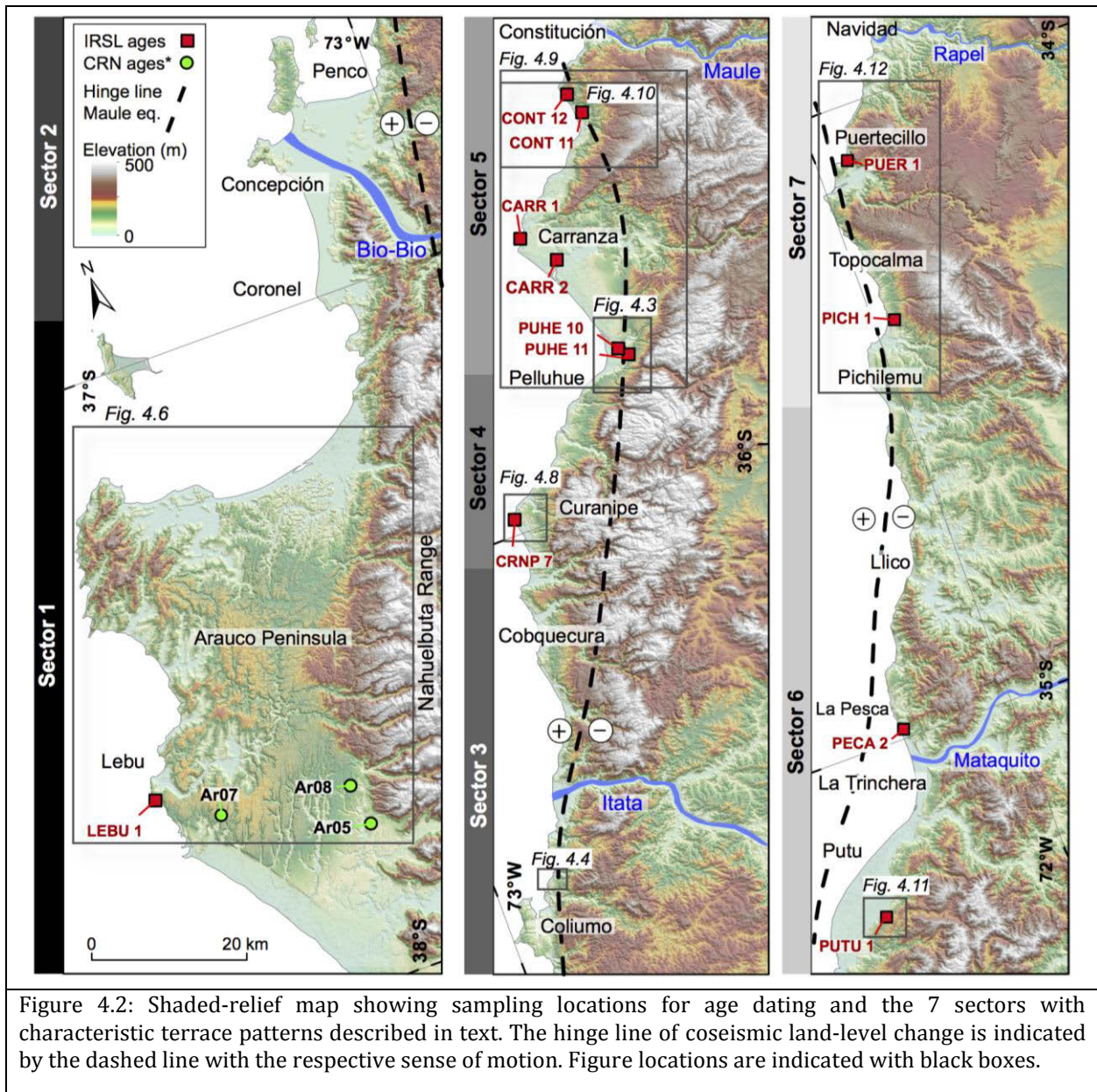


Figure 4.2: Shaded-relief map showing sampling locations for age dating and the 7 sectors with characteristic terrace patterns described in text. The hinge line of coseismic land-level change is indicated by the dashed line with the respective sense of motion. Figure locations are indicated with black boxes.

4.3 Background and methods

4.3.1 Marine terraces as geomorphic markers of permanent deformation

Marine terraces are geomorphic markers that may provide relevant information about coastal paleo-dynamics and vertical tectonic movements (e.g. Dupré, 1984; Trenhaile, 2002a; Marquardt

et al., 2004; Saillard et al., 2009; Limber and Murray, 2011). Marine terraces are formed by the interaction between eustatic sea-level fluctuations and tectonic uplift (Bradley, 1957; Lajoie, 1986; Muhs et al., 1990; Anderson et al., 1999); during episodes of sea-level rise and during highstand periods a wave-cut platform is carved into the landscape whenever wave erosion forces cliff retreat (Anderson et al., 1999). The wave-cut platform may be abandoned during the next lowstand period, leaving behind a terrace deposit or veneer of marine and continental sediments (Bradley, 1957). If the uplift rate is fast enough the platform can be preserved during the next highstand period at higher elevations and remain unaffected by rising sea level. An emerged marine terrace is thus pre-served, while a new platform will be sculpted at lower elevation (e.g. Rosenbloom and Anderson, 1994). Considering that presently sea-level is at the highest position since the Marine Isotope Stage (MIS) 5e (Shackleton et al., 2003; Hearty et al., 2007), marine terraces formed during or after the MIS 5 that are still recognizable in the landscape are generally preserved as a result of rapid tectonic uplift (Lajoie, 1986; Pedoja et al., 2011).

Wave-cut marine terraces consist of smooth planar surfaces with slope angles between 1 and 15° that may be covered by a thin veneer of sediments (Merritts et al., 1991; Anderson et al., 1999; Bowles and Cowgill, 2012). Geomorphic features such as sea-stacks, landslides and gullies can locally increase the roughness of marine terraces (Scott and Pinter, 2003). Some authors have used the terrace tread directly as a proxy for terrace elevation (e.g. Scott and Pinter, 2003; Bowles and Cowgill, 2012) although uplift rates estimated from such markers will be systematically underestimated. The terrace tread is usually bounded inland by a paleo-cliff and characterized by the shoreline angle located where the paleo-cliff intersects the tread. The shoreline angle has been considered as the best horizontal datum of past sea-level positions (e.g. Bradley and Griggs, 1976; Lajoie, 1986; Ashby et al., 1987; Scott and Pinter, 2003). The elevation of the shoreline angle has been directly correlated with sea-level highstands (Eq. (1)) providing a measure to estimate the net vertical displacement and associated uplift rate of a particular terrace level (e.g. Berryman et al., 1989; Weber, 1990). Nevertheless, uplift rates that include a correction for eustatic sea level might be biased by the uncertainties in the chosen sea-level curve (e.g. Pedoja et al., 2011; Yildirim et al., 2013). In contrast to wave-cut terraces, constructional or wave-built terraces are gently sloping landforms formed by thick piles of sediments transported either along the coastline or across the wave-cut platform (Gilbert, 1890; Jackson et al., 2005). The sedimentary cover of wave-built terraces records transgressive-regressive cycles associated with repeated terrace reoccupation episodes, commonly resulting in a flat composite surface devoid of clear geomorphic indicators of past sea-level positions. We therefore used the stratigraphic information to infer past sea-level positions as described in Chapter 2 (Jara-Muñoz and Melnick, 2015).

Marine terraces are ephemeral landforms, which start to be degraded by fluvial and hillslope processes immediately after their abandonment (Anderson et al., 1999). For instance, terrace treads and cliffs tend to be dismantled by river incision, while the shoreline angle is often obscured by eolian and colluvial deposits. In order to unmask the original terrace morphology, we developed a new method based on the analysis of the maximum elevation extracted from swath profiles.

4.3.2 Mapping marine terraces

Geologic field mapping focused on identifying the type of terrace surface, location of paleo-cliffs, bedrock lithology, and the stratigraphy and thickness of associated sedimentary deposits. This

information was used to help correlating isolated terrace levels. To increase the precision of our analysis we used bare-earth digital elevation models derived from LiDAR point clouds filtered and interpolated at 0.5 and 2.5 m grid size for selected sites (Fig. 4.3A and Fig. C1 in Appendix C). Additional sites were analyzed using contour maps at 2 and 5 m spacing from Chilean governmental sources (further details in Appendix C.1). Contours were interpolated using the Topo-to-Raster tool in ArcGis® to create hydrologically-corrected digital elevation models (DEMs).

To identify and map terrace surfaces we used the surface classification model (SCM) (Fig. 4.3A) of Bowles and Cowgill (2012). The SCM linearly combines the terrain roughness and slope, highlighting the extent of low-relief and smooth surfaces. SCM maps facilitate the identification of different terrace levels, their extent and distribution of elevations (Fig. 4.3B). However, SCM maps by themselves cannot be used directly to determine the shoreline angle elevation, which requires a profile-based analysis.

4.3.3 Estimating shoreline angle elevations

The accurate assessment of terrace elevation is essential to obtain reliable uplift rates. One of the major problems when estimating the elevation of the shoreline angle of Pleistocene marine terraces is the presence of colluvial wedges obscuring the original cliff morphology (Hanks et al., 1984). Direct measurements of terrace elevations using the foot of the paleo-cliff (or terrace inner edge) commonly result in an overestimation of the uplift rate; this bias will be greater in regions of low uplift rate.

To precisely measure the elevation of shoreline angles in wave-cut terraces we developed TerraceM, a graphical user interface in MATLAB® and described in Chapter 3. (Jara-Muñoz et al., 2015b). This algorithm uses the maximum elevation extracted from swath profiles (Figs. 4.3C and 4.4), in order to avoid the effects of fluvial overprints. Points representing the undisturbed abrasion platform and paleo-cliff are picked and fitted by linear regression. Both linear fits are extrapolated and intersected to determine the elevation of the buried shoreline angle. The associated error is based on the linear regressions of both the abrasion platform and the paleo-cliff at the 95% confidence interval (2s) (Fig. 4.3C).

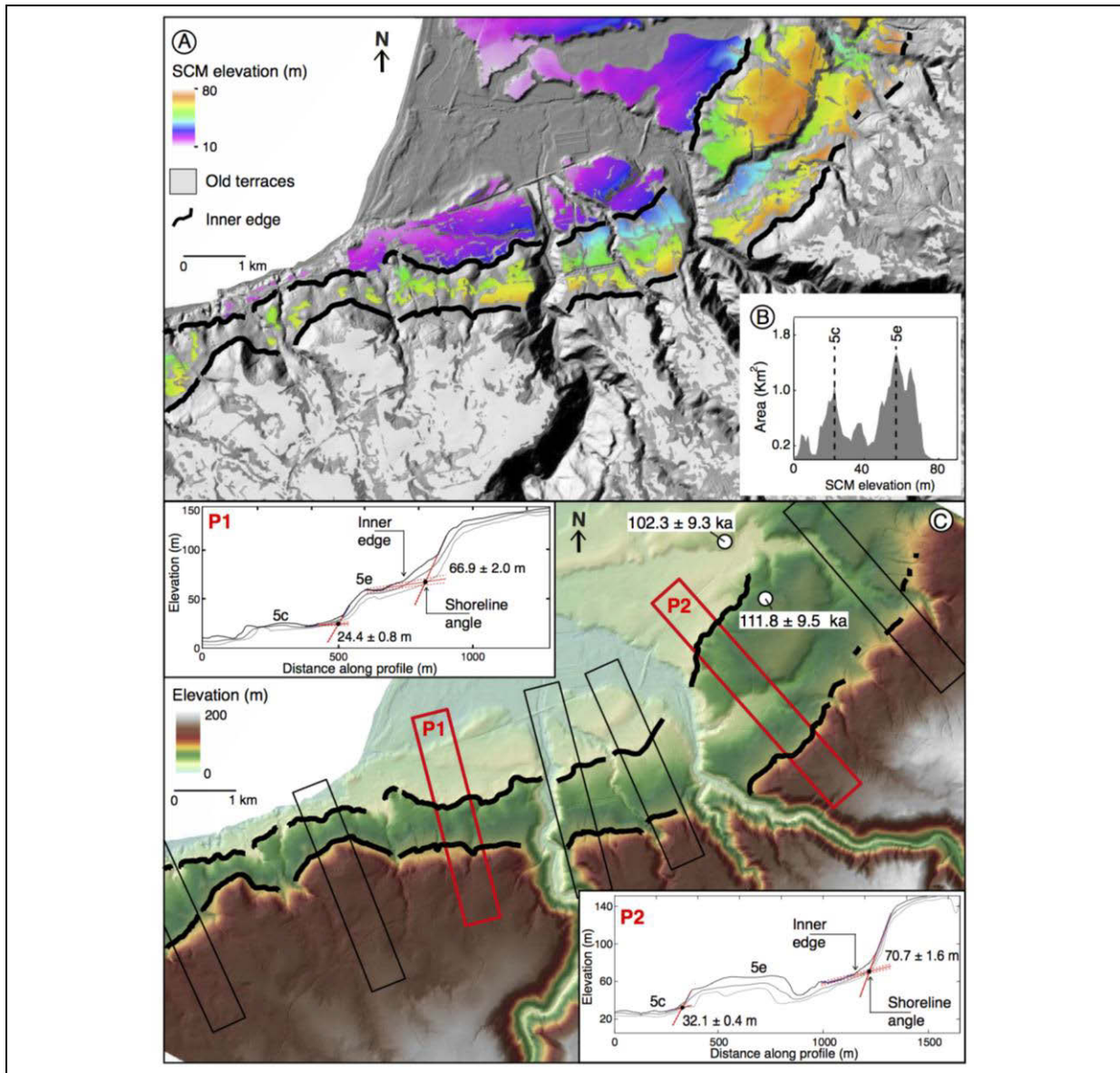
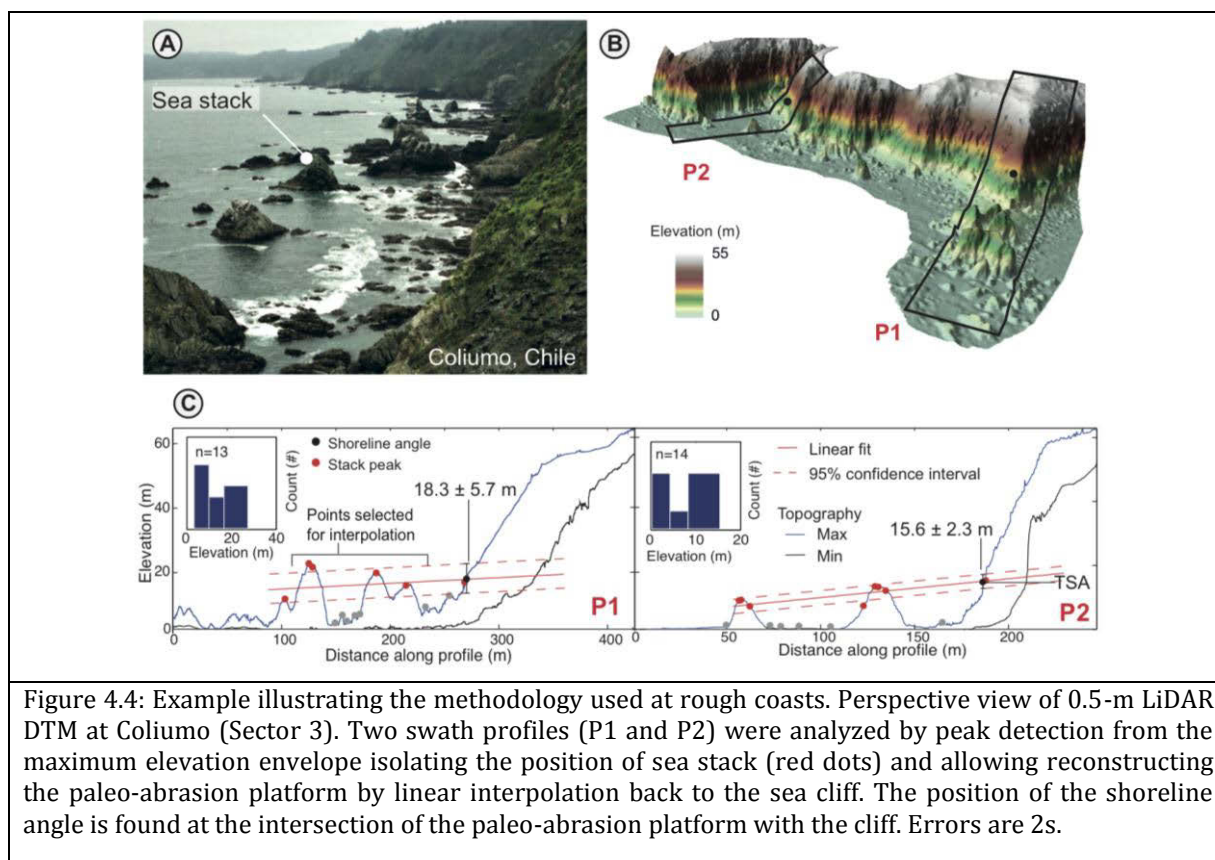


Figure 4.3: Example of mapping and analysis of marine terraces at Pelluhue (Sector 4). (A) Shaded LiDAR relief with color-coded elevation of the surface classification model used for automated mapping of terrace levels, after Bowles and Cowgill (2012). (B) Histogram of elevations obtained from classified areas. Note peaks at the two distinct terrace levels. (C) 2.5-m LiDAR DTM with inner edges of MIS 5c and 5e terrace levels denoted by thick black lines. Rectangles indicate location of swath profiles analyzed using TerraceM (see text for details). Insets show two examples of the analysis (P1 and P2) highlighting the position of shoreline angles and inner edge.

Rough coasts are analyzed by extrapolating the top of sea stacks to the cliff locating the shoreline angle (Fig. 4.4). We detected peaks from the maximum elevation of swath profiles using an automated algorithm based on spectral analysis and feature recognition. Peaks were separated according to elevation classes and linearly interpolated to reconstruct the paleo-topography of the eroded platform, and the elevation of the shoreline angle was estimated from the intersection of the extrapolated linear fit and the cliff. The error estimates of the shoreline angle elevation are based on the extrapolation of linear regressions of peak populations at a 95% confidence interval (2s) (Fig. 4.4).



4.3.4 Stratigraphy and luminescence dating of marine terrace deposits

Sediments covering marine terraces can be used to approximate their minimum age (e.g. Muhs, 2002; Zazo et al., 2003; Zecchin et al., 2009; Bianca et al., 2011; Gurrola et al., 2014). Terrace deposits commonly consist of regressive sequences deposited in high-energy nearshore environments immediately after a sea-level highstand; their stratigraphy is controlled by the local relative sea level and coastal dynamics (e.g. Bradley, 1957; Dupré, 1984). Depending on the supply of sediments and the number of involved sedimentary cycles, these deposits can generate wave-built terraces. In this study, we analyze the stratigraphy of MIS 5 terraces to assist in spatial correlations among disparate sites. We infer the depositional environment and determine the number of sedimentary cycles. The stratigraphic sections were described according to different facies including sedimentary structures, mineralogy, and grain-size distribution, with particular emphasis on characterizing flooding surfaces.

Table 4.1: IRSL ages.

Sample code	Long	Lat	Elevation (m)	Sample depth (m)	Palaeodose (Gy)	Aliquot size (mm)	Number of aliquots	RSD (%)	OD (%)	U (ppm)	Th (ppm)	K %	Water content (%)	Age (ka)
PUTU1	72.25	35.16	79	2.4	123.3±8.2	8	13	17	15.4	0.8±0.04	2.69±0.1	0.39±0.0	13	84.7 ± 7.6
PUHE11	72.54	-35.8	45	3.6	212.4±12.2	8	12	11.2	8.98	1.05±0.0	4.24±0.2	0.78±0.0	16	111.8 ± 9.5
PUHE10	72.55	-35.8	35	1.8	194.0±12.9	8	12	16.02	14.8	1.12±0.0	4.72±0.2	0.68±0.0	16	102.3 ± 9.3
CONT11	72.47	35.44	72	4.5	229.5±14.2	8	11	13.4	11.7	0.86±0.0	3.5±0.20	0.81±0.0	15	124.1 ±
PICH1	71.97	34.38	51	2.8	242.1±13.5	8	5	7.16	1.98	1.44±0.0	4.94±0.2	0.86±0.0	5	106.1 ± 9.3
CONT12	72.49	35.4	21	4.3	220.1±14.1	8	18	18.4	16.4	1.30±0.0	5.05±0.2	1.07±0.0	17.8	99.1 ± 8.4
PUER1	71.94	34.09	50	1.7	231.8±13.44	8	17	11.7	11.3	1.18±0.0	3.94±0.2	1.40±0.0	4.6	87.3 ± 6.9
PECA2	72.18	34.98	20	4.2	572.6±53.5	8	17	35.07	31.8	1.48±0.0	7.37±0.4	1.57±0.0	9.5	192.9 ±
CARR1	72.61	35.58	30	3.8	157.6±11.7	8	19	26.1	23.4	1.32±0.0	5.02±0.2	1.30±0.0	7.7	67 ± 5.7
LEBU1	73.67	37.62	100	1.4	157.7±13.9	8	18	31.1	29.9	1.01±0.0	3.96±0.2	0.53±0.0	20.1	89.2 ± 9.4
CARR2	72.54	35.64	33	2.8	240.6±16.2	8	19	20.8	19.5	1.32±0.0	4.84±0.2	1.15±0.0	14.7	103.5 ± 9
CRNP7	72.78	35.97	17	1.8	485.9±41.6	8	19	30.06	29.8	0.68±0.0	4.24±0.3	0.74±0.0	16.6	265 ± 28.5
SM mb*	73.51	37.04	2	0.5	3.4±0.1	8	15	9.7	8.5	-	-	-	3.6	1.5 ± 0.09

RSD = relative standard deviation, OD = overdispersion, U = uranium, Th = thorium, K = potassium. * modern beach berm sample
(Long and Lat) are southern hemisphere. SA = shoreline angle, BU = bedrock unconformity. *

Sample code	Sector	Sample elevation (m)	Age (ka)	MIS	Sea-level** (m)	Apparent			Assigned age# (ka)	Assigned MIS	Sea-level (m)##	Corrected Uplift rate (m/ka)
						Uplift rate*** (m/ka)	Marker elevation (m)	Type of marker				
PICH 1	7	51	106.1 ± 9.3	5c	-23.4	0.70	60 ± 0.4	SA	106 ± 5	5c	-20	0.75 ± 0.06
PUER 1	7	50	87.3 ± 6.9	5b	-66.24	1.33	75.91 ± 4.6	SA	106 ± 5	5c	-20	0.90 ± 0.08
PUTU 1	6	79	84.7 ± 7.6	5a	-20	1.16	32.7 ± 3	BU	106 ± 5	5c	-20	0.50 ± 0.06
PECA 2	6	20	192.9 ± 20.1	7	-62.19	0.43	15 ± 1.0	BU	200 ± 5	7	-5	0.10 ± 0.03
CONT 11	5	72	124.1 ± 10.8	5e	0.21	0.58	72 ± 1.0	SA	125 ± 5	5e	5	0.54 ± 0.05
CONT 12	5	21	99.1 ± 8.4	5c	-28.3	0.50	38.9 ± 0.2	SA	106 ± 5	5c	-20	0.56 ± 0.05
CARR 1	5	30	67 ± 5.7	4	-89.03	1.78	44 ± 5.0	SA	84 ± 5	5a	-20	0.76 ± 0.1
CARR 2	5	33	103.5 ± 9	5d	-30.9	0.62	53 ± 5.0	SA	125 ± 5	5e	5	0.38 ± 0.06
PUHE 11	4	45	111.8 ± 9.5	5d	-38.7	0.75	71.3 ± 1.8	SA	125 ± 5	5e	5	0.53 ± 0.05
PUHE 10	4	35	102.3 ± 9.3	5c	-28.3	0.62	33 ± 0.5.0	SA	106 ± 5	5c	-20	0.50 ± 0.05
CRNP 7	3	17	265 ± 28.5	7	-80	0.37	17 ± 1.0	BU	125 ± 5	5e	5	0.10 ± 0.04
LEBU 1	1	100	89.2 ± 9.4	5b	-56.3	1.75	120.72 ± 5.6	SA	106 ± 5	5c	-20	1.33 ± 0.09
Ar08 *	1	50	130 ± 14	5e	-1	0.39	142.69 ± 6.1	SA	125 ± 5	5e	5	1.10 ± 0.08
Ar08 *	1	50	133 ± 14	5e	-28	0.59	142.69 ± 6.1	SA	125 ± 5	5e	5	1.10 ± 0.08
Ar05 *	1	61	130 ± 13	5e	-1	0.48	107.55 ± 5.7	SA	125 ± 5	5e	5	0.82 ± 0.07
Ar07 *	1	150	127 ± 13	5e	4	1.15	142.69 ± 6.1	SA	125 ± 5	5e	5	1.10 ± 0.08

CRN samples from Melnick et al. (2009). ** sea-level references in text *** Apparent uplift obtained directly from sample age and elevation, #assigned nearest last highstand age. ## Sea-level at assigned highstand.

Table 4.2: IRSL and CRN age calibrations with geomorphic and stratigraphic markers and their corresponding highstand.

Twelve sediment samples from terrace deposits were dated using the post-IR Infrared stimulated luminescence (IRSL) signal of K-feldspar. Samples consisted of sandy sediments, either of eolian or beach berm depositional environments, and were collected at depths between 1.8 and 4.5 m below the surface (Table 4.1; Fig. C3 in Appendix C). Given that quartz is known to generate unstable luminescence signals for some Andean sediments (e.g. Steffen et al., 2009), we used exclusively coarse grains of K-Feldspar (100e250 mm) measured according to the pIRIR290 SAR protocol (See Appendix C.2 for more details). The suitability of the terrace samples for luminescence dating was indicated by high feldspar signals with adequate reproducibility; dose recovery tests after signal resetting in a solar simulator for 12 h resulted in acceptable ratios between measured and laboratory dose (0.9-1.1) for all samples. Burial doses were calculated on the basis of 14-19 accepted aliquots, with a diameter of 8 mm, using the central age model (CAM) of Galbraith et al. (1999), and corrected for residual doses afterwards (Fig. 4.5B and C). In addition, the completeness of signal resetting (bleaching) was evaluated on the basis of a present-day sample from a beach berm (sample SM mb, Table 4.1).

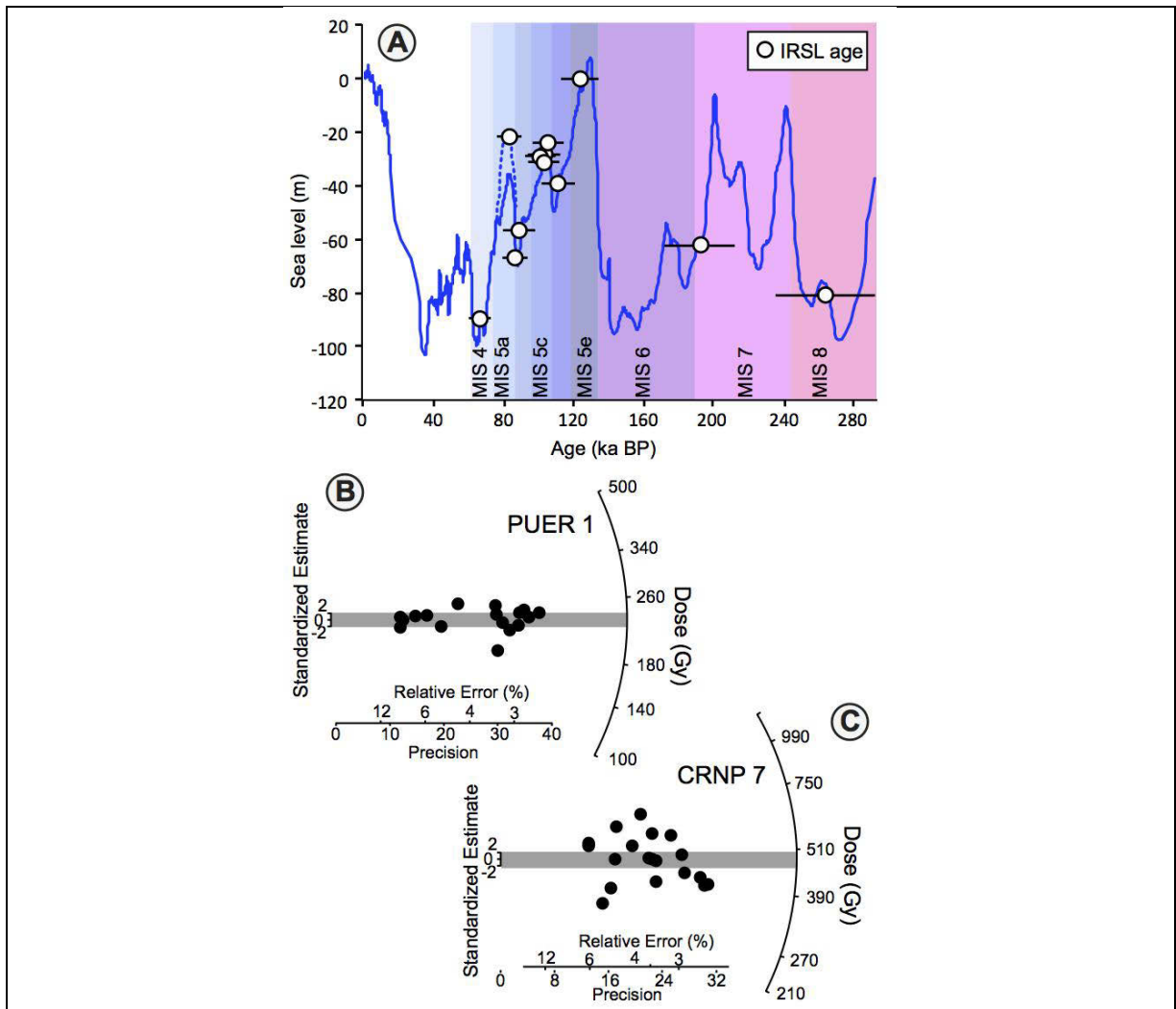


Figure 4.5: Luminescence dating results. (A) Global sea-level curve of Rohling et al. (2009) with IRSL ages (2s errors) plotted at their corresponding paleo sea-level position, the sea-level during MIS 5a is based on (Potter et al., 2004) and indicated by dashed lines. (B and C) Radial plots of equivalent dose data of samples PUER 1 and CRNP 7. Note scattering in dose distribution for sample CRNP 7. (See section 4.1.4).

Radionuclide analysis (uranium, thorium and potassium) for dose-rate estimation was carried out using high-resolution gamma-spectrometry to estimate the dose rate. Attenuation of radiation by pore water was considered by using measured water contents between 5 ± 5 and 16 ± 5 weight-%. Sampling depth, geographical position and altitude above sea level were used to calculate the contribution of cosmic radiation (Prescott and Hutton, 1994). For estimation of internal dose rates, a potassium content of $12.5 \pm 0.5\%$ was adopted (Huntley and Baril, 1997).

4.3.5 Estimating uplift rates from shoreline angle elevations and luminescence ages

Eustatic sea-level variations during MIS 5 have been well documented worldwide (e.g. Kukla et al., 2002; Muhs, 2002; Shackleton et al., 2003; Hearty et al., 2007). MIS 5 is divided into three highstand periods between 80 and 135 ka (Shackleton et al., 2003; Dumas et al., 2006). Most studies have concluded that sea-level was approximately 5 m above its present-day elevation during MIS 5e (Hearty et al., 2007; Pedroja et al., 2011; Pedroja et al., 2014), and 20 m below during both MIS 5a and 5c (e.g. Potter and Lambeck, 2004; Rohling et al., 2009). In order to correlate our IRSL ages with their corresponding MIS stage we used the sea-level curve of Rohling et al. (2009) (Fig. 4.5A), which is the most recent high-resolution sea-level curve for the southern hemisphere, spanning the last 550 ka. Uplift rates have been estimated using the relation: (Lajoie, 1986)

$$u = (E - e)/T$$

We first calculate the relative sea-level position (H) based on the difference between the terrace elevation (E) and sea-level position at the time of terrace formation (e). By dividing the relative sea-level by the age of the terrace level (T) we obtained the uplift rate (u). The standard error (Se(u)) is calculated using the following relation: (Gallen et al., 2014)

$$Se(u)^2 = u^2 \left(\left(\sigma^2 H / H^2 \right) + \left(\sigma^2 T / T^2 \right) \right)$$

Where σH is the error in relative sea-level:

$$\sigma H = \text{sqrt}(\sigma E^2 + \sigma e^2)$$

Standard error estimates include the 5-m uncertainty in absolute sea level (σe) (Rohling et al., 2009), error estimates of the shoreline angle elevations (σE), and an arbitrary range of 5 ka for the duration of the highstands (σT). The highstand duration has been inferred from the mean ranges of MIS 5e lasting from 130 to 119 ka Hearty et al. (2007) and MIS 5c from 107 to 98 ka (Potter and Lambeck, 2004; Rohling et al., 2009). Before applying Eq. (1), we first corrected the ages and elevation of terrace surfaces depending on their type (Table 4.2). For instance, for wave-cut terraces or for terraces covered by a thin sedimentary veneer, we correlate the terrace age with the nearest older sea-level highstand; finally, to calculate the uplift rate we use both, the shoreline angle elevation and the corrected age of the terrace. For wave-built terraces, based on the ages obtained within the sedimentary sequence we follow the method developed in Chapter 2 (Jaramuñoz and Melnick, 2015) approximating the age of the bedrock unconformity with the preceding highstand. Then, we use the bedrock elevation and its corrected age to calculate the vertical displacement rate. This is based on the following assumptions: a) terrace veneer formation starts immediately after the highstand (Dupré, 1984); b) the age of the bedrock discontinuity is coeval with the onset of deposition; and c) The cumulative wave energy necessary to carve the bedrock abrasion platform can only occur during a protracted period of time, mostly during highstands (Anderson et al., 1999).

4.4 Results

4.4.1 Geomorphology, stratigraphy and luminescence ages of marine terraces

Marine terraces are broadly distributed along the Maule coast. Based on the distribution of their geomorphic characteristics, ages, geology, and elevation patterns, we subdivided the 2010 rupture zone into seven sectors described below from south to north as labeled in Fig. 4.2. The sedimentary sequences associated with marine terraces along the Maule rupture have been used to correlate the age of the terrace surfaces. These sequences have a clear mineralogical signature depending on their age. The nature of sedimentary sequences, their geomorphic setting, their ages, and correlations with highstands are described below and are illustrated in Figs. 4.6 -4.12 (further details in Appendix C.3).

4.4.1.1 Sector 1: Arauco Peninsula - Coronel

The Arauco Peninsula is located in front of the Nahuelbuta Range, the highest region of the Coastal Range within the Maule rupture with maximum elevations reaching 1500 m (Fig. 4.2). Marine terraces assigned to MIS 5e in this area were collectively named the Cañete surface by Kaizuka et al. (1973) and dated to between 127 and 133 ka (MIS 5e) by Melnick et al. (2009b) with cosmogenic nuclide exposure dating using ^{10}Be and ^{26}Al . The terrace morphology consists of a wide eastward tilted erosion surface (Fig. 4.6A) covered by near-shore deposits that increase in thickness towards the north and south (Fig. 4.6C and D). The shoreline angles are located at a maximum distance of ~ 30 km inland from the present-day coastline. The terraces are warped along a northwest-southeast-oriented uplift axis reaching a maximum elevation of 200 m at the central part of the peninsula (Fig. 4.6B).

Sequences of coastal sediments defined as the Cañete Formation (MIS 5e) are associated with the Cañete surface along the Arauco Peninsula (Fig. 4.6C). The thickness of these deposits increases from a minimum of 20 m at the central part of the peninsula to 50 m in the northern part (Fig. 4.6D). At its base the Cañete Formation comprises horizontally and cross-stratified black volcanic sandstone overlain by massive medium sandstone with insect burrows, fine lamination and paleosols.

At Lebu, in the southwestern edge of the Arauco Peninsula, a lower terrace level with a shoreline angle elevation at 122 ± 1 m is located 1.4 km inland from the coastline (Fig. 4.6A). This terrace is sculpted into Tertiary sedimentary bedrock and covered by nearshore marine and eolian deposits (Fig. C7 in Appendix C). This up to 8-m-thick sequence consists of black volcanic sandstone and conglomerate, and can be divided into two units, each representing a distinct sedimentary cycle separated by a 40-cm-thick paleosol horizon. The lower level is formed by a matrix-supported polymictic and well-rounded conglomerate that grades upward into medium sandstone. The upper unit consists of massive and horizontally stratified coarse to medium black volcanic sandstone. An IRSL age obtained from the eolian unit yielded 89.2 ± 9.4 ka suggesting this terrace level was formed during MIS 5c. Thus, the first unit was likely associated with transgressive deposition synchronous with a sea-level rise episode during MIS 5c, whereas the second unit appears to have been associated with a sea-level fall followed by eolian deposition during MIS 5b.

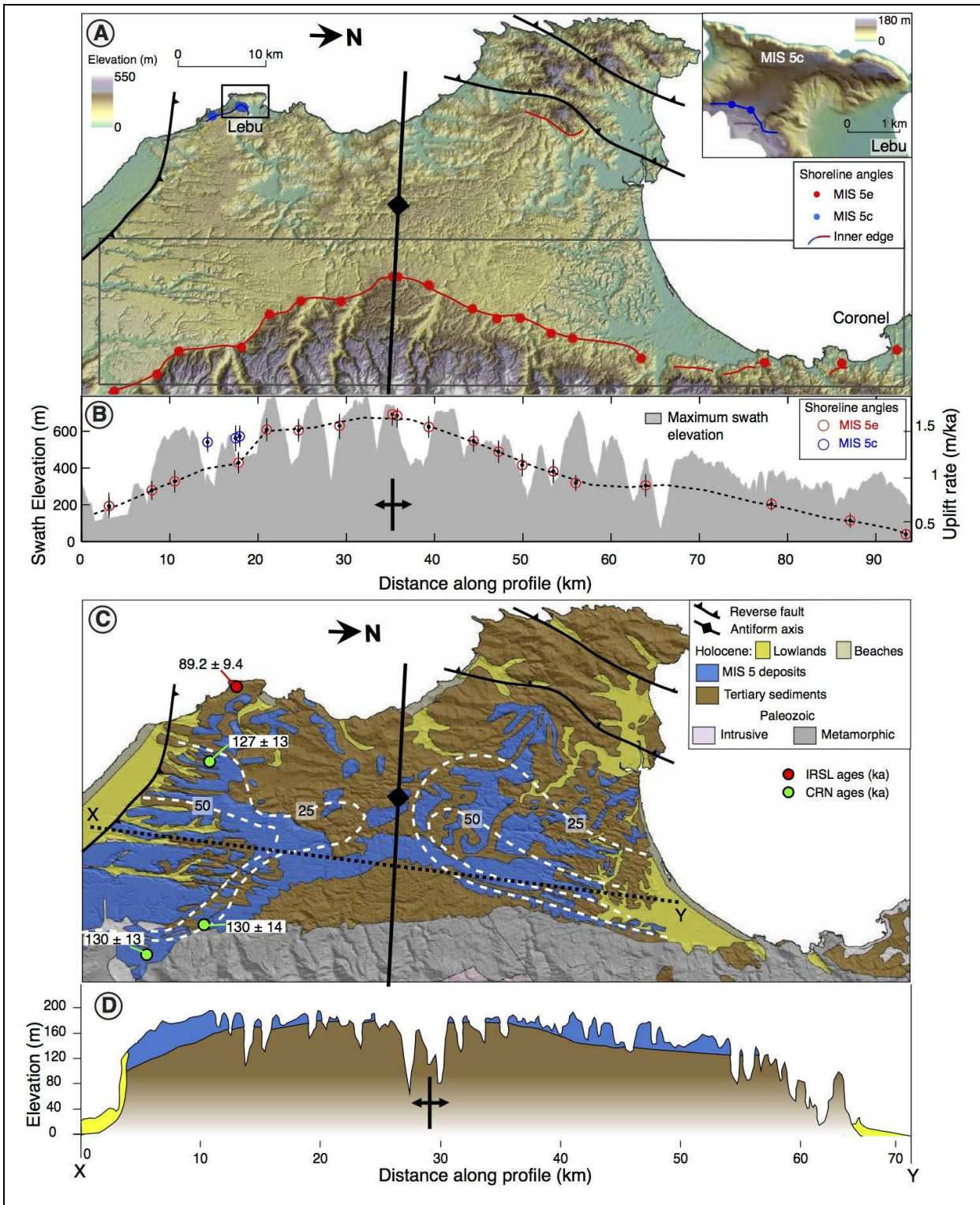


Figure 4.6: Marine terraces and geology of the Arauco Peninsula. (A) Distribution of MIS 5 shorelines and main Quaternary structures in the Arauco Peninsula. Inset shows distribution of MIS 5c terraces at Lebu on a 2-m DEM, black rectangle indicates location of swath profile in B. (B) Profile showing uplift rates for MIS 5e and MIS 5c terraces above topographic swath profile. (C) Simplified geologic map. White dashed line indicates isopach contours of MIS 5e deposits from Melnick et al. (2009). (D) Geologic profile highlighting the axis of the Arauco anticline and increase in sediment thickness of MIS 5e sequences suggesting syntectonic deposition. The axis coincides with the maximum elevation of MIS 5e shorelines.

4.4.1.2 Sector 2: Coronel - Penco

MIS 5e terraces are well preserved and decrease in elevation northward (Fig. 4.13A, Fig. C8 in Appendix C). The terraces are sculpted into metamorphic rocks and are covered by a ~10-m-thick veneer of eolian and shallow marine siliceous sandstone in the southern part of this sector. No ages could be obtained from siliceous sediments due to the absence of feldspars; however, terrace surfaces in this area are virtually continuous toward the south with those of Sector 1 across the Arauco Peninsula. A ~15-km-wide zone of upwarping identified at Coronel is likely associated with local faulting (Fig. 4.13B). Shoreline angle elevations of the MIS 5e level increase northward from 51 to 83 m immediately south of the Bio-Bio River. MIS 5e terrace elevations decrease abruptly across the Bio-Bio down to 6.3 ± 0.6 m at Penco, the lowest elevation along the Maule rupture. This abrupt change in terrace elevation is also likely associated with the local influence of the Bio-Bio Fault (Fig. 4.13B).

4.4.1.3 Sector 3: Penco - Curanipe

In the southern part of this sector the coastline is rough, rocky and narrow, enclosed by 30- to 70-m-high sea cliffs with only small pocket beaches. Marine terraces from MIS 5e in this sector are narrow and discontinuous, sculpted into intrusive and metamorphic rocks, and located adjacent to the present-day rocky coastline. The MIS 5e level is partially destroyed by ongoing wave erosion forming sea stacks and stumps (Fig. 4.7C) as well as isolated narrow wave-cut terraces. Stacks form where portions of a retreating coast become isolated through erosion and dissection of the cliff base (e.g. Trenhaile et al., 1998); these features are detached from the cliff forming columns, stack-arcs and caves (Fig. 4.7B). The base of these features is usually submerged whereas the tops are distributed at similar elevations thus suggesting they represent fragments of an eroded terrace level. We analyzed the elevation of these terrace remnants using the peak detection method (Fig. 4.4) obtaining shoreline angle elevations that increase northward from 9 to 48 m (Fig. 4.13A).

At Cobquecura, we identified an older well-defined terrace level located ~1 km inland from the coastline and at ~80 m elevation covered by a veneer of layered arkose (Fig. C9 in Appendix C). This terrace level is older than MIS 5 and was not considered in the morphometric analysis, but the distinct stratigraphic and the mineralogic signature of the arkosic deposits could be found at several locations and thus helped to infer the position of pre-MIS 5 levels (Fig. C10 in Appendix C).

4.4.1.4 Sector 4: Curanipe - Pelluhue

Two distinct terrace levels with continuous geomorphic expression could be clearly differentiated in this area and correlated along the coast for more than 30 km. Wave-cut terraces are exposed with narrow treads north of Curanipe changing to staircase morphology at Pelluhue. Based on two IRSL ages obtained at Pelluhue of 111.8 ± 9.5 and 102.3 ± 9.3 ka, we correlated these levels with MIS 5e and MIS 5c, respectively (Figs. 4.3A and 4.7F). At Pelluhue the MIS 5 paleo-coast follows the shape of the bay forming a well-exposed flight of marine terraces. Terraces are partly covered by elongated littoral bars that progressively widen northwards obscuring the paleo-cliff morphologies (Figs. 4.3A and 4.9A). Terrace elevations in this area increase locally northward defining a small-scale flexure where the MIS 5e level reaches a maximum elevation of 75 m (Fig. 4.13A).

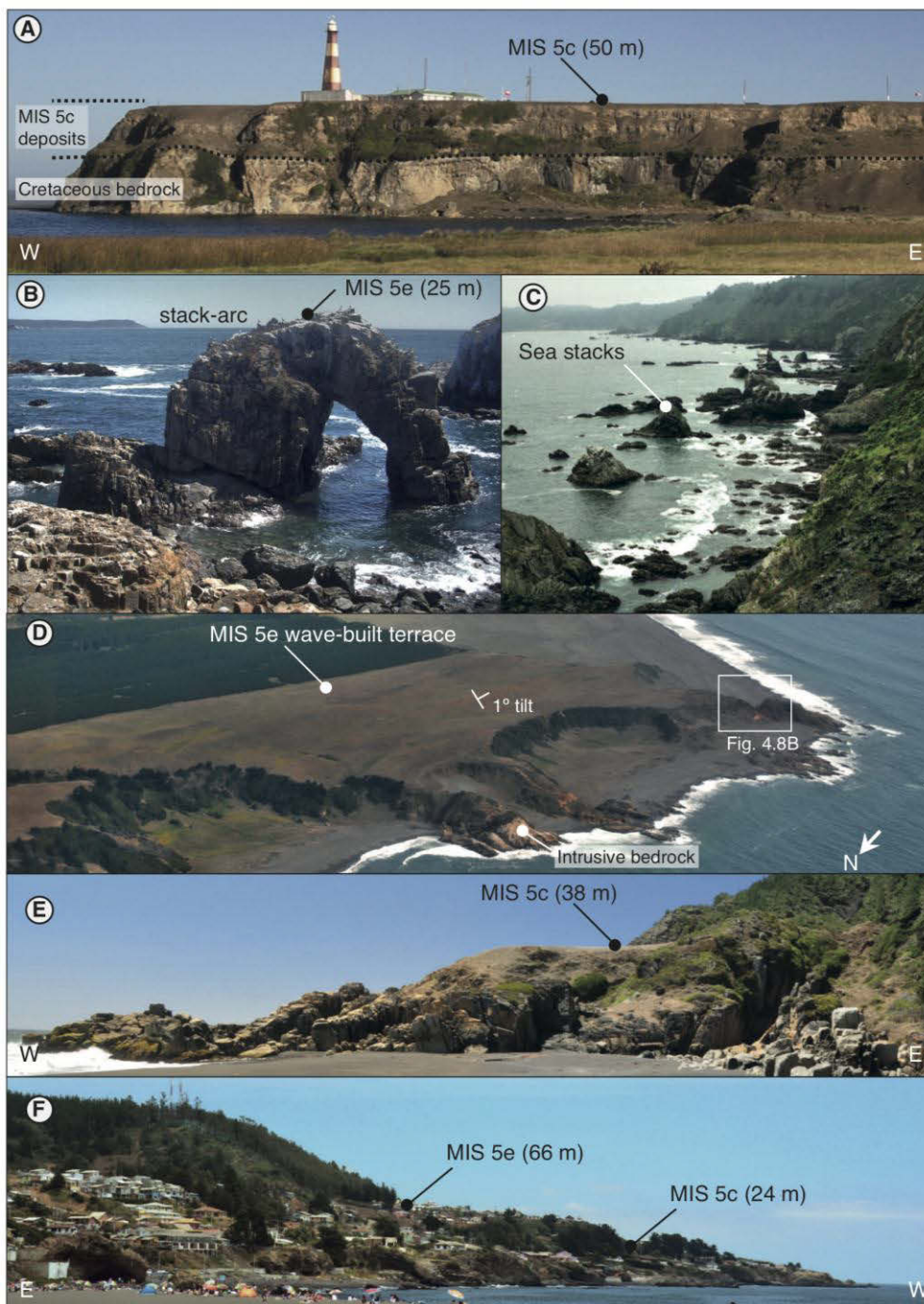


Figure 4.7: Field views showing the geomorphic expression of MIS 5 terraces. (A) Prominent terrace level at Carranza (Sector 5). Deposits consist of eolian sandstones deposited above Cretaceous bedrock. (B, C) Geomorphic features of rough coasts including stack-arcs and clustered sea stacks at Coliumo (Sector 3). (D) Oblique aerial view of a wave-built terrace at Curanipe. Terrace surface is tilted 1° southward, see detailed map and LiDAR DTM in Fig. C7 in Appendix C. (E) Example of a sharp wave-cut terrace north of El Yolki (Sector 5) correlated with MIS 5c. (F) Example of a staircase terrace sequence at Pelluhue (Sector 4).

A wave-built terrace with a wedge-like geometry is exposed at Curanipe and overlies the intrusive bedrock (Fig. 4.8D and 4.8E). The absence of clear paleo-cliff morphologies prevented the estimation of a shoreline angle. Nevertheless, we could measure a $\sim 1^\circ$ southward tilt of the terrace surface, which follows the elevation change of the MIS 5 terrace levels (Fig. 4.7D).

The Curanipe sedimentary sequence is divided into a lower unit predominantly formed by arkose with fine layers of magnetic minerals (Fig. 4.8C) and an upper unit consisting of black stratified volcanic sandstone, separated by a ~2-m-thick paleosol (Fig. 4.8A). The upper unit consists of massive and cross-stratified eolian sandstone with lenticular paleosol intercalations and horizontally bedded volcanic sandstone. The upper unit is pervasively affected by post-depositional precipitation of iron oxide in convolute crusts as well as disseminated in the matrix.

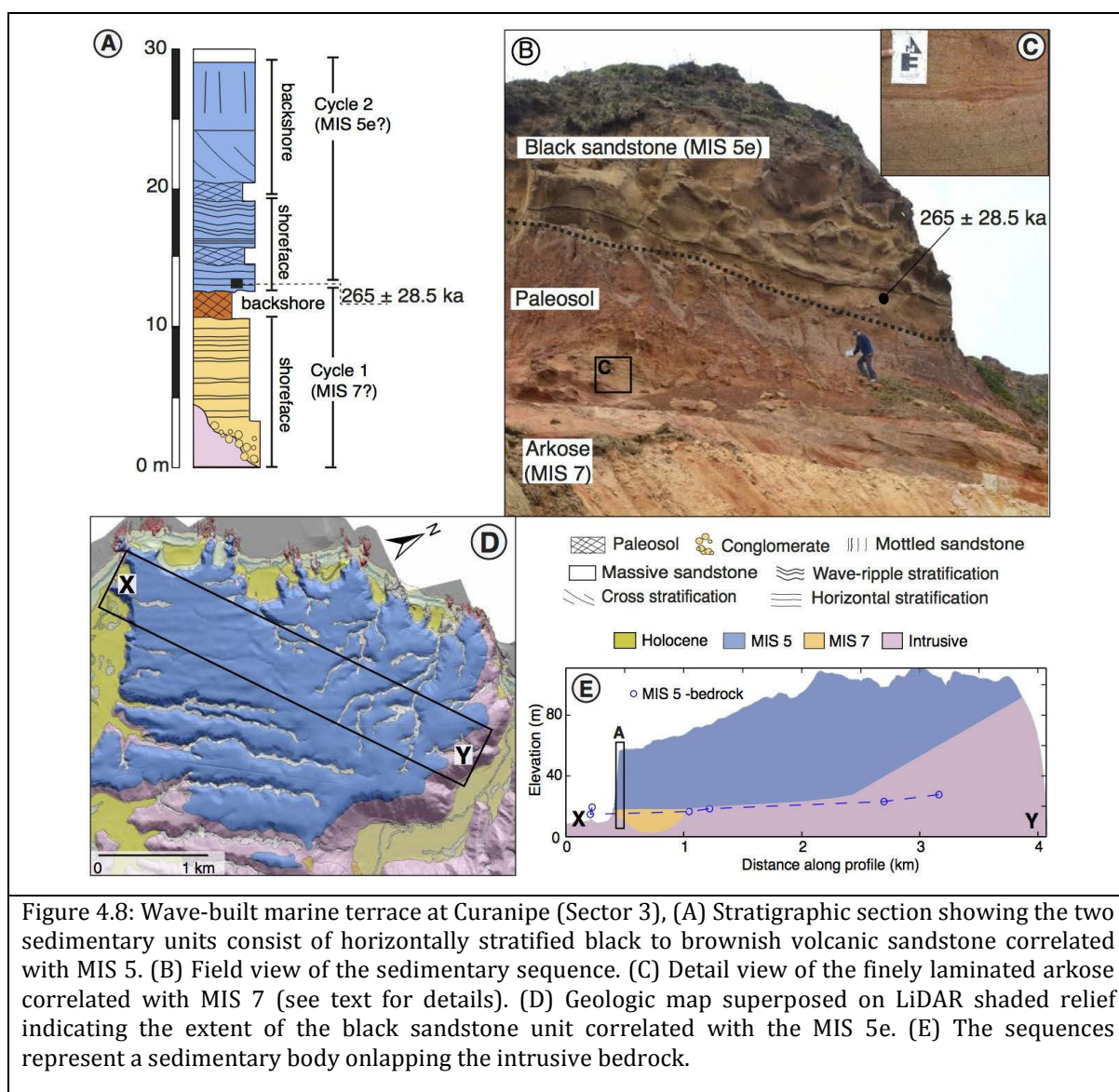


Figure 4.8: Wave-built marine terrace at Curanipe (Sector 3), (A) Stratigraphic section showing the two sedimentary units consist of horizontally stratified black to brownish volcanic sandstone correlated with MIS 5. (B) Field view of the sedimentary sequence. (C) Detail view of the finely laminated arkose correlated with MIS 7 (see text for details). (D) Geologic map superposed on LiDAR shaded relief indicating the extent of the black sandstone unit correlated with the MIS 5e. (E) The sequences represent a sedimentary body onlapping the intrusive bedrock.

An IRSL age of 265 ± 28.5 ka was obtained from black sandstone at the base of the upper unit (Fig. 4.8B). Black volcanic sandstone is almost exclusively found in the MIS 5 deposits, which in turn are devoid of arkosic lithologies. Arkosic sediments characterize MIS 7 and possibly older deposits found in Sectors 3, 4 and 6. Therefore the apparent MIS 7 age obtained from black sandstone of the upper unit at Curanipe (Fig. 4.8A) is inconsistent with the characteristic regional mineralogical signatures. No direct connection exists between the Main Cordillera and this sector of the coast that could have locally transported volcanic material during MIS 7.

Alternatively, we infer that pervasive post-depositional precipitation of iron at this site might have affected the luminescence age. Potential effects of mineral precipitation on luminescence dating have been inferred to dilute radioelements (U, Th) and thus lower the dose rate (e.g. Mauz, 1999). Such effects would have an effect on dosimetry, changes in porosity and thus water contents as well as radiogenic element concentrations. Although effects on dose rates (in form of temporal variations) are hard to detect, comparably high values of dose scatter can be observed in the dated sample at Curanipe (CRNP 7) (34% over dispersion compared to ~20% in most other samples; Fig. 4.5B and 4.5C). These high values could result from spatially inhomogeneous dosimetry due to radiation hotspots at iron concentrations affecting the final age results as well. Considering the potential inaccurate age estimate of this sample and based on the mineralogical signature, we tentatively correlate the upper unit at Curanipe with the MIS 5e level.

4.4.1.5 Sector 5: Pelluhue - Constitucion

In the southern part of this sector (between Pelluhue and Carranza) the terraces are partly covered by Pleistocene sediments and active dunes, making the measurement of shoreline angles difficult (Fig. 4.9C).

The morphology is characterized by a ~5-km-wide smooth surface that increases in elevation progressively towards the southeast. At Pelluhue MIS 5 sediments form two stacked sequences comprising massive black volcanic sandstone with horizontal and cross stratification dated as 102.3 ± 9.3 ka and 111.8 ± 9.5 ka, respectively. Given that each sequence represents a distinct sedimentary cycle and the obtained ages are coincident with distinct sea-level highstands, we correlate the two terraces surfaces with MIS 5c and 5e. At Carranza terrace levels consist of a wave-cut platform sculpted into Cretaceous sediments forming a broad surface covered by Pleistocene deposits (Fig. 4.9A). These strata consist of a sequence of almost exclusively massive black volcanic sandstone deposited in an eolian environment and of fluvial deposits found on relict fluvial terraces along the main drainages. An age of 67 ± 5.7 ka was obtained from eolian deposits, suggesting deposition during the MIS 4. We infer that these eolian deposits cover a poorly preserved terrace inner edge south of Carranza that probably was formed during MIS 5c. This is supported by the presence of dated MIS 5c marine sediments at the southern and northern parts of this sector. Fluvial deposits yielded an age of 103.5 ± 9 ka (MIS 5d), suggesting relict terraces formed during MIS 5e.

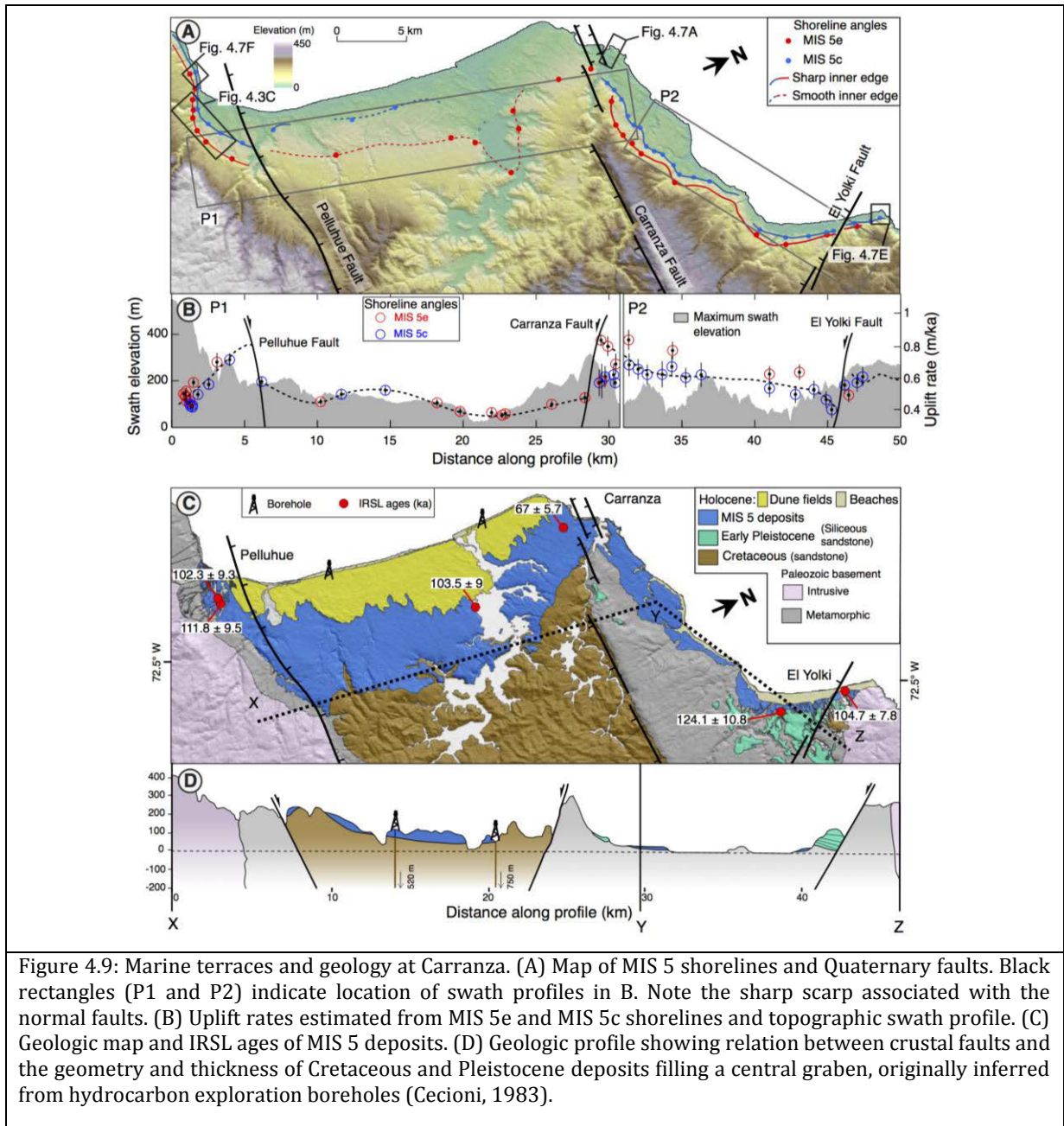


Figure 4.9: Marine terraces and geology at Carranza. (A) Map of MIS 5 shorelines and Quaternary faults. Black rectangles (P1 and P2) indicate location of swath profiles in B. Note the sharp scarp associated with the normal faults. (B) Uplift rates estimated from MIS 5e and MIS 5c shorelines and topographic swath profile. (C) Geologic map and IRSL ages of MIS 5 deposits. (D) Geologic profile showing relation between crustal faults and the geometry and thickness of Cretaceous and Pleistocene deposits filling a central graben, originally inferred from hydrocarbon exploration boreholes (Cecioni, 1983).

4.4.1.6 Sector 6: Constitucion - Pichilemu

Between Sector 5 and 6, at El Yolki, two distinct terrace levels could be identified at ~40 and ~80 m. Sediments associated with these levels consist of black marine and eolian sandstone that can be divided in two stacked sequences deposited on the metamorphic basement and above an older unit of white siliceous sandstone (Fig. 4.9C and 4.10A). Both sequences are formed by a transition from shoreface to backshore deposits, each representing a distinct sedimentary cycle. Based on IRSL ages of 124.1 ± 10.8 and 104.75 ± 7.8 ka obtained for each sequence, we correlate them with MIS 5e and 5c stages, respectively (Fig. 4.10C). North of this area, an up to ~7-km-wide Holocene coastal plain with a field of active dunes extending for ~40 km from Putu to La Trinchera characterizes this sector (Fig. 4.2). These lowlands are bounded by a ~60-m-high steep paleo-cliff limiting the MIS 5 terraces at Putu. In this sector the elevation of MIS 5 terraces decreases northward and their surface expression becomes discontinuous.

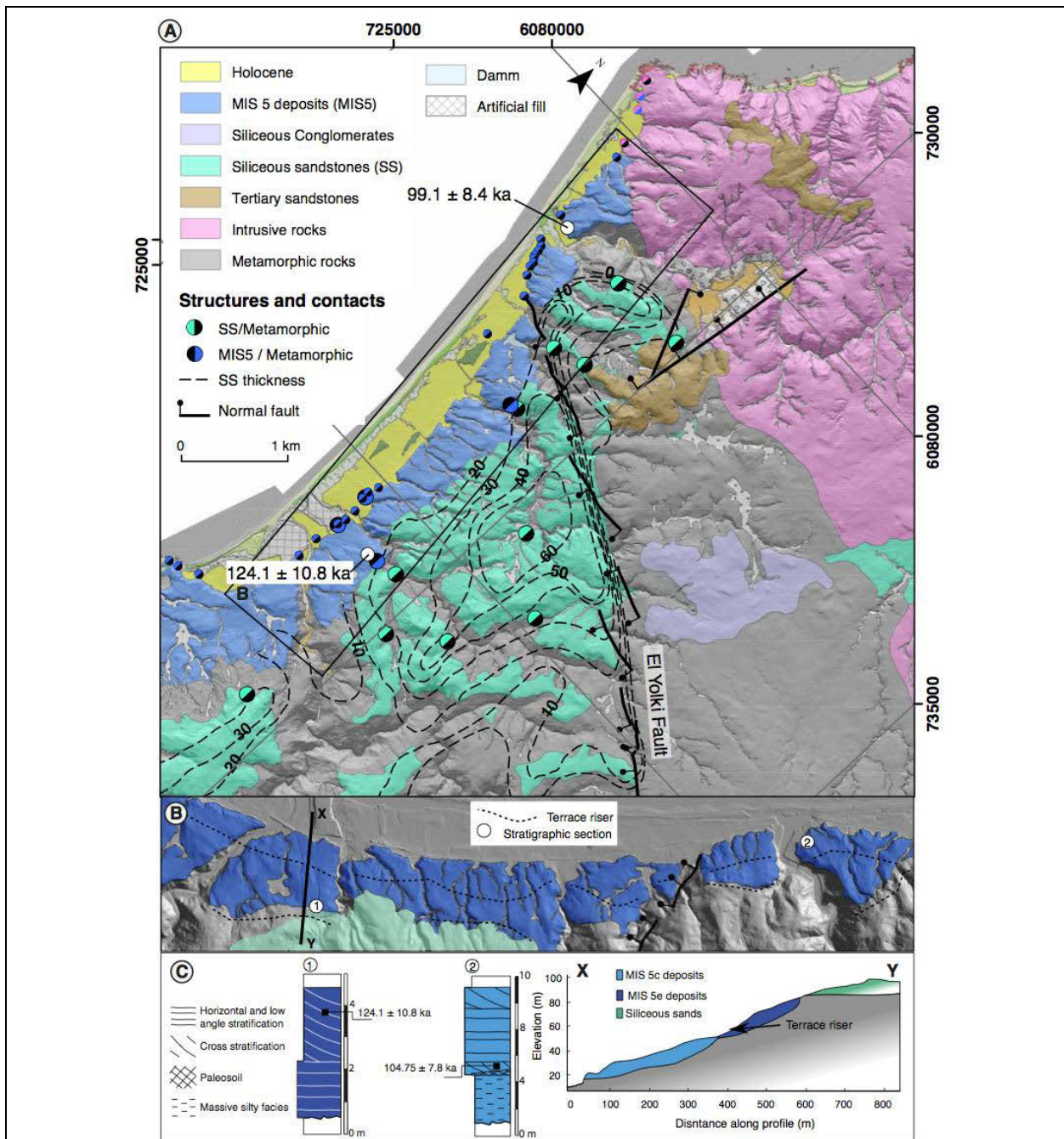


Figure 4.10: Geology and stratigraphy south of Constitución, at the locality of El Yolki. (A) Geologic map above LiDAR shaded-relief, highlighting sites of contact measurements. (B) Detailed map of the MIS 5 sequences indicating position of smooth terrace riser coincident with a basement high as is observed in C. (C) Stratigraphic sections of MIS 5 deposits. These can be divided in two stacked sequences formed at the upper part by cross stratified volcanic sandstones that represents back shore deposits, and fine sandstones at the lower part of the sequences representing estuarine deposits.

A wave-built terrace crops out at Putu (Fig. 4.11A and 4.11C). The sequence consists of stratified black volcanic sandstone divided in three units that represent two sedimentary cycles (Fig. 4.10B). The lower unit consists of horizontally laminated sandstone with magnetic minerals, representing upper shoreface sedimentation above a wave-cut platform (Fig. 4.11D). This unit is overlain by cross-stratified massive sandstone interbedded with clay lenses that represent backshore deposits.

The upper unit is formed by horizontally stratified coarse to medium sandstone deposited in an upper shoreface environment overlain by massive and cross stratified sandstone deposited in a backshore environment (Fig. 4.11B). The upper unit is correlated with MIS 5a based on an age of 84.7 ± 7.6 ka. We correlated the two lower units with a regressive episode during MIS 5b immediately after formation of the wave-cut platform during MIS 5c.

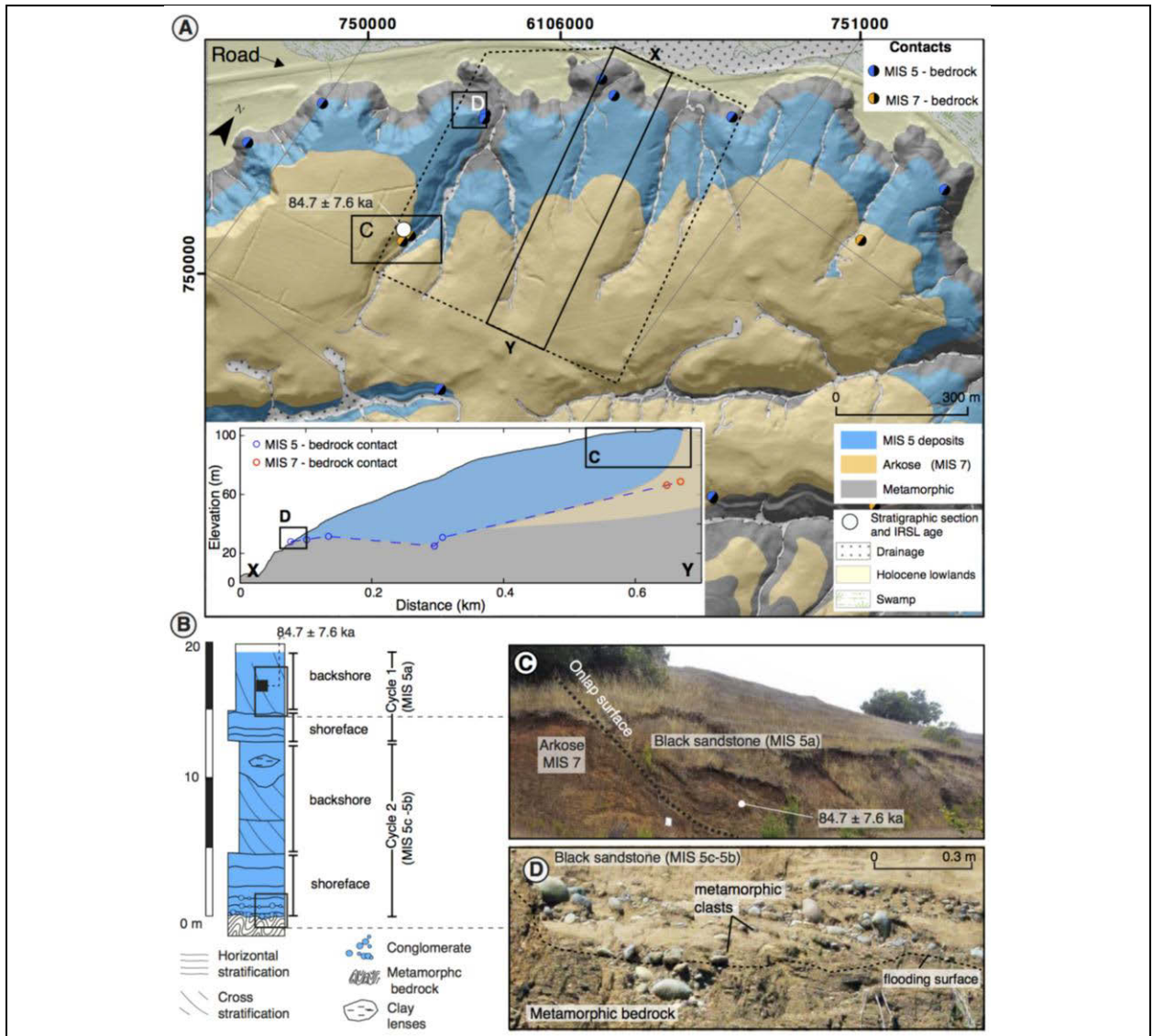


Figure 4.11: Geology and stratigraphy at Putu. (A) Geology superposed on LiDAR shaded relief map. The site consists of black volcanic sandstone deposited above the metamorphic bedrock and arkosic sequences. Inset shows a geologic profile highlighting the wedge-shaped geometry of the wave-built terrace and measurement points. (B) Stratigraphic section showing the two sedimentary cycles. (C) Field view showing the onlap between the MIS 5c back sandstone and the MIS 7 arkosic unit. (D) View of the basal conglomerate that characterize the flooding surface.

A pronounced terrace level defined as La Trinchera by Araya-Vergara (1976) occurs at ~ 200 m elevation in the central part of Sector 6 and extends northwards (Fig. 4.2 and C13 in Appendix C). This wave-built terrace consists of a ~ 70 -m-thick sequence of arkose and sandstone with lithic fragments, and at least four distinct interbedded paleosol horizons. We obtained an age of 205.6 ± 22.3 ka near the base of the sequence confirming that the arkosic sediments are older than MIS 5

(Fig. C13 in Appendix C). The geomorphic markers of this terrace were not considered in our analysis, which was restricted to MIS 5 levels. A preserved terrace remnant was identified in the northern part of Sector 6 at the outlet of the Llico River, where it forms a fluvio-marine terrace partly covered by active dunes (Fig. C12 in Appendix C). We tentatively correlate this level with MIS 5e based on its position below an older level formed by arkosic sediments. The tentative MIS 5e shoreline angle is at an elevation of ~15 m.

4.4.1.7 Sector 7: Pichilemu - Navidad

Terraces in this sector were sculpted into the metamorphic basement and Tertiary marine deposits of the Navidad Formation (Encinas et al., 2006b), and are covered by black marine and eolian sandstones, which decrease in thickness northward (Fig. 4.12C). Marine terraces are offset across the Pichilemu Fault and at Topocalma these surfaces display a broad warping pattern with elevations increasing from 40 to 180 m (Fig. 4.12B). At Puertecillo, a normal fault deforms the sedimentary sequences and offsets the MIS 5e level from ~180 to ~150 m; the fault-line scarp of another N-S-striking normal fault has been reoccupied by the MIS 5c and 5e sea-cliffs (Fig. C15 in Appendix C).

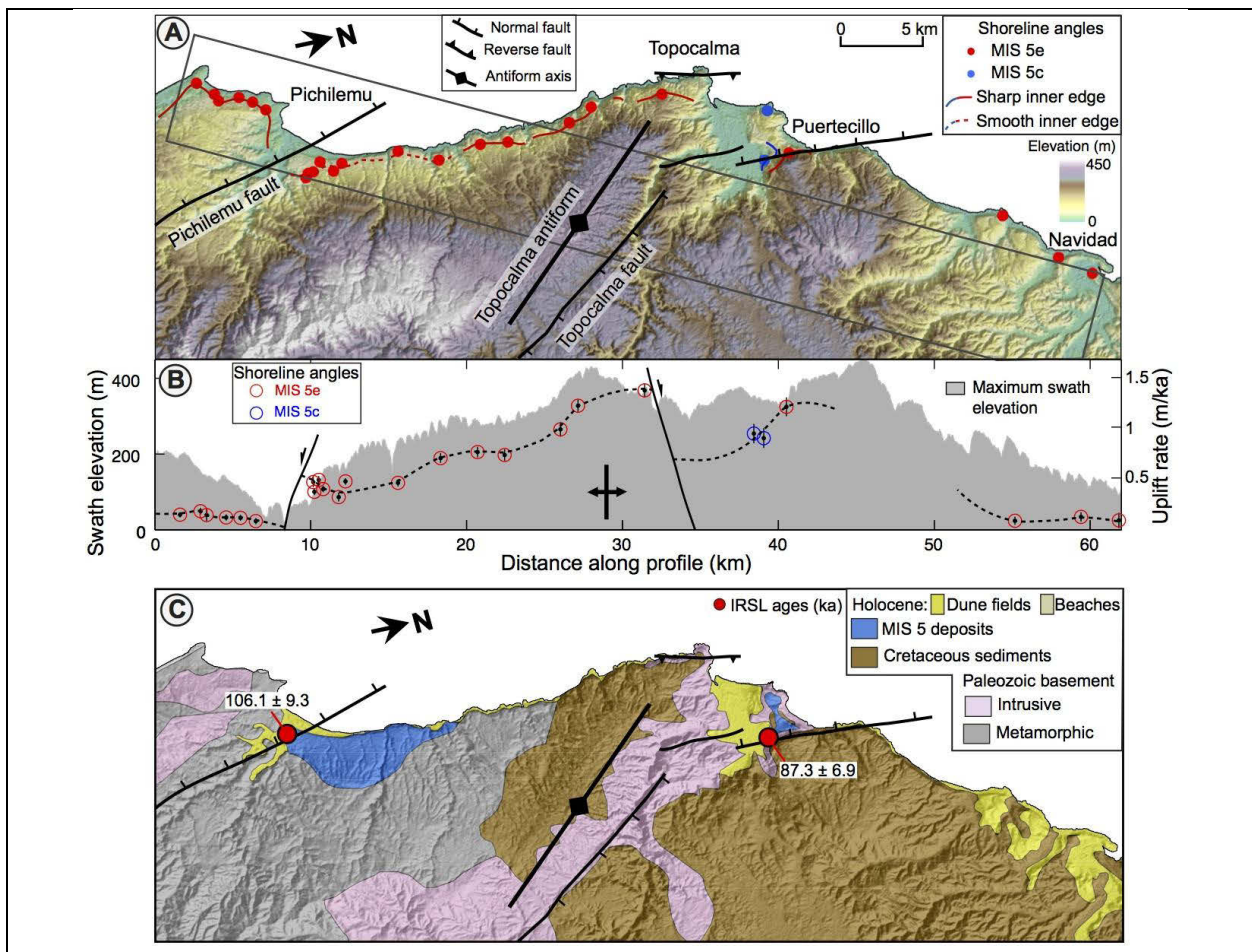


Figure 4.12: Marine terraces and geology between Pichilemu and Topocalma. (A) Map showing the distribution of MIS 5 inner edges and Quaternary structures, the black rectangle indicates location of swath profile in B. (B) Profile showing uplift rates estimated from MIS 5e and MIS 5c shoreline angles and topographic swath profile. Note offsets associated with the Topocalma and Pichilemu faults. (C) Simplified geologic map modified from Farías et al. (2011) and references therein, notice IRSL ages from MIS 5 levels.

MIS 5c deposits at Pichilemu comprise mostly stratified black volcanic sandstone (Fig. C14 in Appendix C). The terrace deposits consist of two units that represent a sedimentary cycle deposited above a wave-cut platform sculpted into metamorphic rocks. The lower unit consists of horizontally stratified sandstone, representing upper-shoreface deposits, and the upper unit constitutes cross-stratified and massive sandstone, deposited in eolian environment. An age of 106.1 ± 9.3 ka obtained from the lower unit suggests deposition during MIS 5c. The northernmost outcrops of MIS 5 deposits occur at Puertecillo (Fig. C15 in Appendix C), where they form a sedimentary body laterally attached to the bedrock. The sequence was dated at 88.2 ± 6.9 ka (MIS 5b) and consists of massive and cross-stratified black volcanic sandstones deposited in an eolian environment. Considering that eolian deposits represent the ultimate phase of sedimentation, immediately after a sea-level fall episode, we correlate the age of this terrace surface with MIS 5c. In the northern part of Sector 7 terrace elevations become progressively lower and discontinuous. At Navidad we correlated terrace remnants at an elevation of 17 m with MIS 5e. This level is absent farther north where the coast is characterized by plunging cliffs sculpted into Tertiary rocks suggesting rather stable tectonic conditions.

4.4.2 Distribution of Quaternary faults and uplift rates along the Maule rupture

We were able to estimate uplift rates for 170 elevation measurements of shoreline angles from MIS 5c and 5e terrace levels (Fig. 4.13, details in Appendix C.4). Uplift rates of marine terraces along the Maule rupture have a mean of 0.5 m/ka (estimated from a 5-km linear interpolation to avoid spatial bias). Importantly, this mean rate is exceeded at Arauco, Carranza and Topocalma, where uplift rates reach maximum values of 1.59, 0.85, and 1.35 m/ka, respectively. In turn, the areas between these three sectors are characterized by relatively low uplift rates between 0.1 and 0.2 m/ka (Fig. 4.13B).

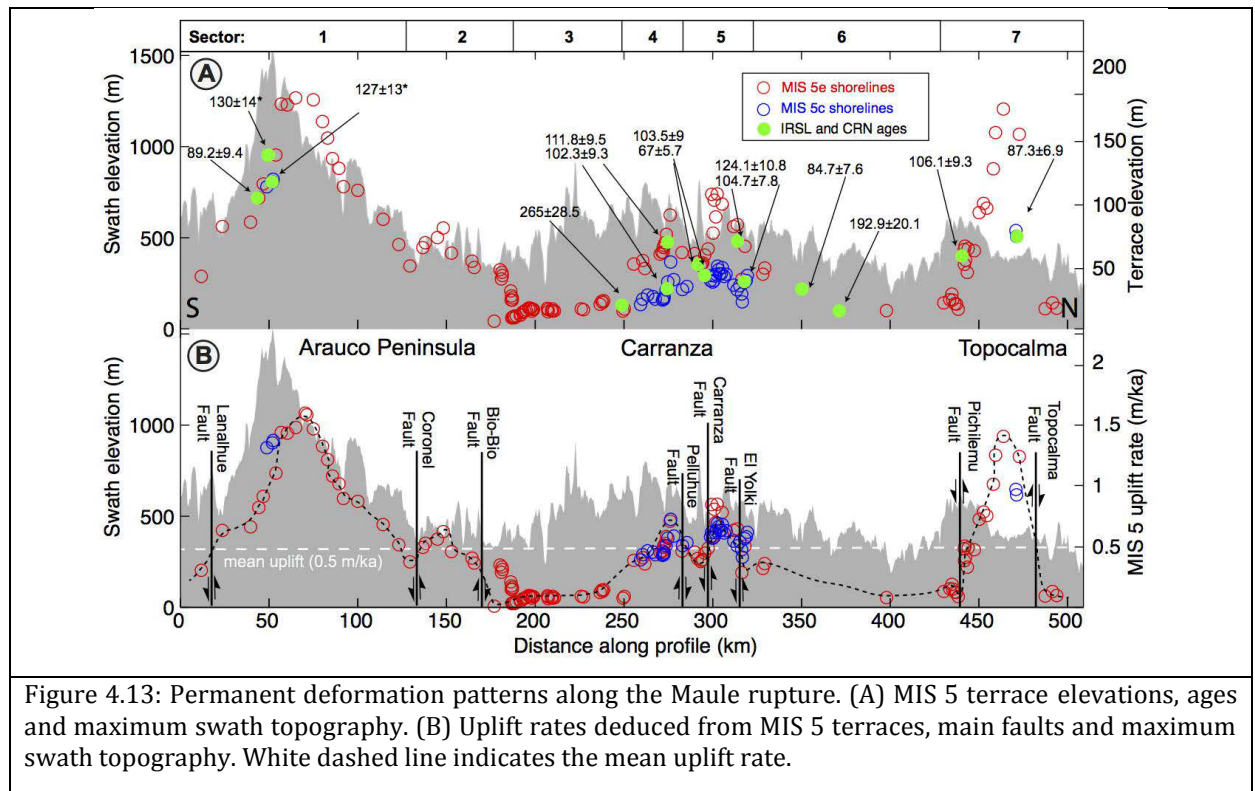


Figure 4.13: Permanent deformation patterns along the Maule rupture. (A) MIS 5 terrace elevations, ages and maximum swath topography. (B) Uplift rates deduced from MIS 5 terraces, main faults and maximum swath topography. White dashed line indicates the mean uplift rate.

Interestingly, the fastest uplifting regions, Arauco and Topocalma, are both located at the boundaries of the Maule rupture and are characterized by wide antiformal structures with wavelengths of 90 and 60 km, respectively. The Arauco antiform is delineated by an increase in elevations of MIS 5e shoreline angles, the maximum elevation of the topography, and a decrease in thickness of MIS 5e deposits toward the center of the peninsula (Fig. 4.6). These opposite variations in thickness and shoreline elevation are consistent with coeval growth of the antiform (Melnick et al., 2009). The Topocalma antiform is delineated by an increase in elevation of both MIS 5c and 5e terraces and in maximum topography (Fig. 4.12). The Topocalma antiform is bounded by two NW-SE-striking normal faults at Pichilemu and Puertecillo, which offset the terraces by ~ 30 m with an associated minimum vertical displacement rate of ~ 0.5 m/ka (Fig. 4.13B and Fig. C15 in Appendix C). The distribution of shoreline angle elevations, mimicking the topographic expression of the Topocalma antiform, is consistent with an NW-SE oriented uplift axis (Fig. 4.12A). This structure apparently extends across the entire Coastal Range (Farias et al., 2010a).

The region of moderately fast uplift (0.85 m/ka) at Carranza is located in the central part of the Maule rupture and disrupted by the Pelluhue, Carranza, and El Yolki faults (Fig. 4.9B and D). These extensional structures locally offset and fold the MIS 5 terraces along a 45-km-long stretch of coast. The Carranza Fault is associated with an NE-striking and SE-facing steep topographic break and together with the Pelluhue Fault juxtaposes Cretaceous sedimentary rocks with the metamorphic basement forming a symmetric graben (Fig. 4.9D). Both structures control the local drainage pattern formed by a drowned valley in the central part of the graben and perched paleo-surfaces in the uplifted footwall block of the Carranza Fault (Fig. 4.9A).

Immediately north of Carranza the MIS 5c terrace is well exposed forming a ~ 2 -km-wide platform at elevations that rise from ~ 40 to ~ 100 m and then decrease gently northward back to ~ 40 m at the hanging wall of the El Yolki Fault, another hitherto unrecognized Quaternary structure (Fig. 4.10). This scissor-type normal fault dips to the southwest and progressively increases in throw towards the northwest, forming a small half-graben filled with Pleistocene siliceous sandstone (Fig. 4.10). The fault consists of several segments arranged in a left-stepping en echelon geometry suggesting a minor left-lateral horizontal component. The MIS 5e level is offset by ~ 25 m and the MIS 5c level by ~ 10 m across the El Yolki Fault. The MIS 5e terrace level is displaced vertically ~ 23 and ~ 50 m across the Pelluhue and Carranza faults, respectively. Based on these offsets we estimated minimum vertical displacement rates of ~ 0.2 m/ka for the Pelluhue and El Yolki faults, and ~ 0.4 m/ka for the Carranza Fault.

4.5 Discussion

4.5.1 Uplift mechanisms responsible for emerged marine terraces

Our detailed assessment of variable uplift rates estimated from marine terraces along the Maule earthquake rupture reveals that permanent deformation is distributed heterogeneously along strike, probably reflecting the segmentation of the forearc into discrete blocks. The central part of the rupture zone at Carranza is characterized by moderate uplift rates, sharp fault offsets, and short-wavelength flexures related to footwall back-tilting and rollover monoclinical folding. In turn, the boundaries of the Maule rupture are characterized by broad zones of crustal upwarping

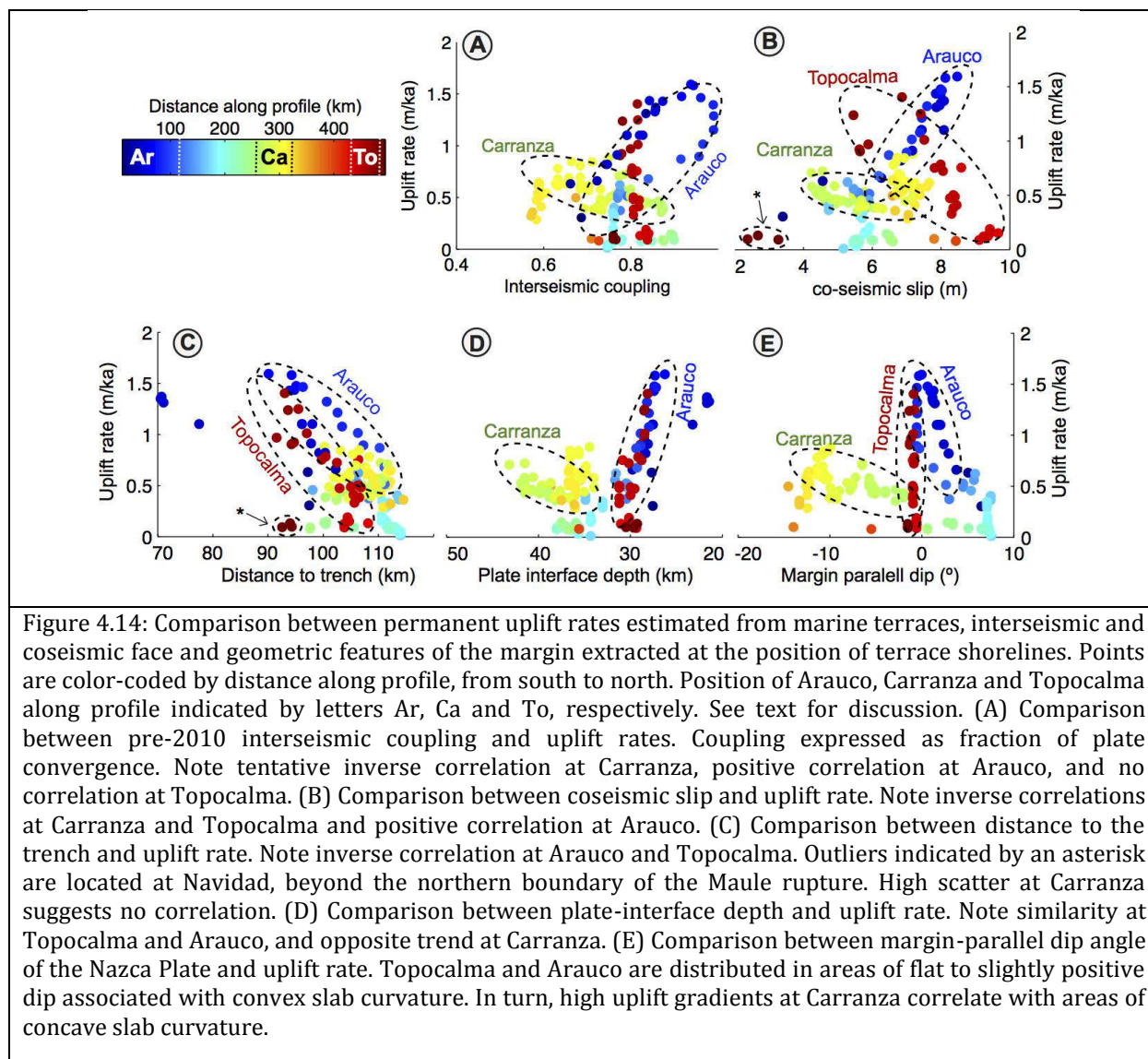
associated with the highest uplift rates. The origin of long-wavelength structures has been related with deep-seated sources (e.g. Melosh and Raefsky, 1980; Watts and Daly, 1981), which along the Maule segment are possibly related to changes in the mechanical behavior of the megathrust and/or the entire crust.

Interestingly, Arauco and Topocalma are both located at the shortest distances from the trench of 75 and 90 km, respectively, and both spatially correlate with well-known morphotectonic features of the entire Andean orogen. For instance, Topocalma is located immediately south of the Maipo Orocline (Farías et al., 2008; Farias et al., 2010a), interpreted to result from the collision of the Juan Fernandez Ridge with the continental margin since ~10 Ma. Analogously, the Arauco Peninsula is located at the symmetry axis of the Arauco Orocline (Fig. 4.1B), associated with the northward motion of a forearc sliver that extends for 1000 km southward resulting in margin-parallel shortening (Melnick et al., 2009). Along-strike changes in the margin-parallel dip (curvature) of the plate interface also occur at the position of these oroclines (Fig. C16 in Appendix C), emphasizing the profound changes in the geometry of the entire margin across these two zones.

Hypothetically, the geometry of the plate interface could control the pattern of long-term permanent deformation, generating long-wavelength structures above curved segments (e.g. Bonnardot et al., 2008). To test this hypothesis we compared uplift rates with distance to the trench, slab depth, and the margin-parallel component of slab dip (Fig. 4.14C-E and Fig. C16 in Appendix C). Arauco and Topocalma show an inverse relationship between distance-to-trench and uplift rate (Fig. 4.14A), suggesting areas closer to the trench rise faster. Conversely, these parameters are not correlated at Carranza. Topocalma and Arauco also show a wide range of uplift rates at shallower plate interface depths with respect to Carranza (Fig. 4.14D), suggesting areas where the slab is shallower may uplift faster. An interesting relationship emerges when the margin-parallel slab dip is compared with the uplift rate. Carranza is correlated with a concave-upward portion of the plate interface whereas Arauco and Topocalma are associated with convex to planar sectors (Fig. 4.14E). We infer that the curvature and depth of the plate interface may control the distribution of uplift rates and extent of long-wavelength structures that are ultimately associated with boundaries of subduction-zone earthquakes. Changes in slab curvature may facilitate local underplating and basal accretion of subducting trench sediments forming duplex structures that could account for the generation of the long-wavelength zones of upwarping (Glodny et al., 2005). However, to date no direct evidence of basal accretion has been documented by geophysical studies along the Chile margin. Alternatively, these long-wavelength structures may be related to oblique plate convergence and margin-parallel motion of forearc slivers in the upper plate as inferred at Arauco (Melnick et al., 2009) and also at the latitude of the Maipo orocline in the Main Cordillera (Lavenue and Cembrano, 1999).

Zones of rapid coastal uplift inferred from marine terraces have been commonly associated with subducted bathymetric features such as ridges, fracture zones and seamounts (e.g. Taylor et al., 1987; Macharé and Ortlieb, 1992). However, besides the subducted Mocha Fracture Zone no major oceanic features enter the subduction zone in the Maule segment (Fig. 4.1B). The Mocha Fracture is very narrow and has only ~200 m of associated relief, and it is thus considered unlikely to have an influence on the broad patterns of coastal uplift at Arauco (also see discussion in Melnick et al. (2009b)). The epicenter of the Maule earthquake was located immediately south of Carranza (Fig. 4.1A), above a zone of high seismic velocity in the upper plate correlated with a positive gravity

anomaly, interpreted to be associated with a subducted seamount with several kilometers of relief; this seamount is thought to have facilitated initiation of the rupture sequence (Hicks et al., 2012). However, we found low uplift rates (0.1e0.3 m/ka) along ~30 km of coast above the high-velocity region, suggesting that if a seamount had been subducted at this location, it must have detached from the lower plate more than ~125 ka ago.



4.5.2 Relationships between earthquake barriers and permanent deformation patterns

The three areas of rapid uplift along the Maule rupture approximately coincide with the boundaries of at least 8 historic earthquakes, despite uncertainties in their rupture zone terminations (Fig. 4.15A). For instance, Topocalma at the northern boundary of the 2010 Maule earthquake was also the limit of the 1751 (M~8.8), 1835 (M~8.5), 1906 (M8.6), 1985 (M8.0), and probably the 1928 (M~8) earthquakes. Similarly, Arauco is at the northern boundary of the giant 1960 (M9.5) and at the southern limit of the 1751,1835 and 2010 events, although with substantial

overlap. The area of Carranza was the boundary for the 1928 and giant 1730 ($M \sim 9$) earthquakes. However, there are certainly differences in the along-strike distance over which slip during these earthquakes overlapped that may hint to variations in mechanical properties. The best-documented and largest zone of rupture overlap is at Arauco where slip during the 1960 and 2010 events occurred over a ~ 90 -km-long zone. At Topocalma the overlap between historic earthquakes reached ~ 60 km (Fig. 4.15A). In turn, Carranza apparently has so far acted as a barrier only for ruptures that propagated from the north such as the 1730 event. Interestingly, the width of the zones of overlap is similar to the wavelength of the region of crustal upwarping and fast uplift rate, suggesting they are related to similar processes.

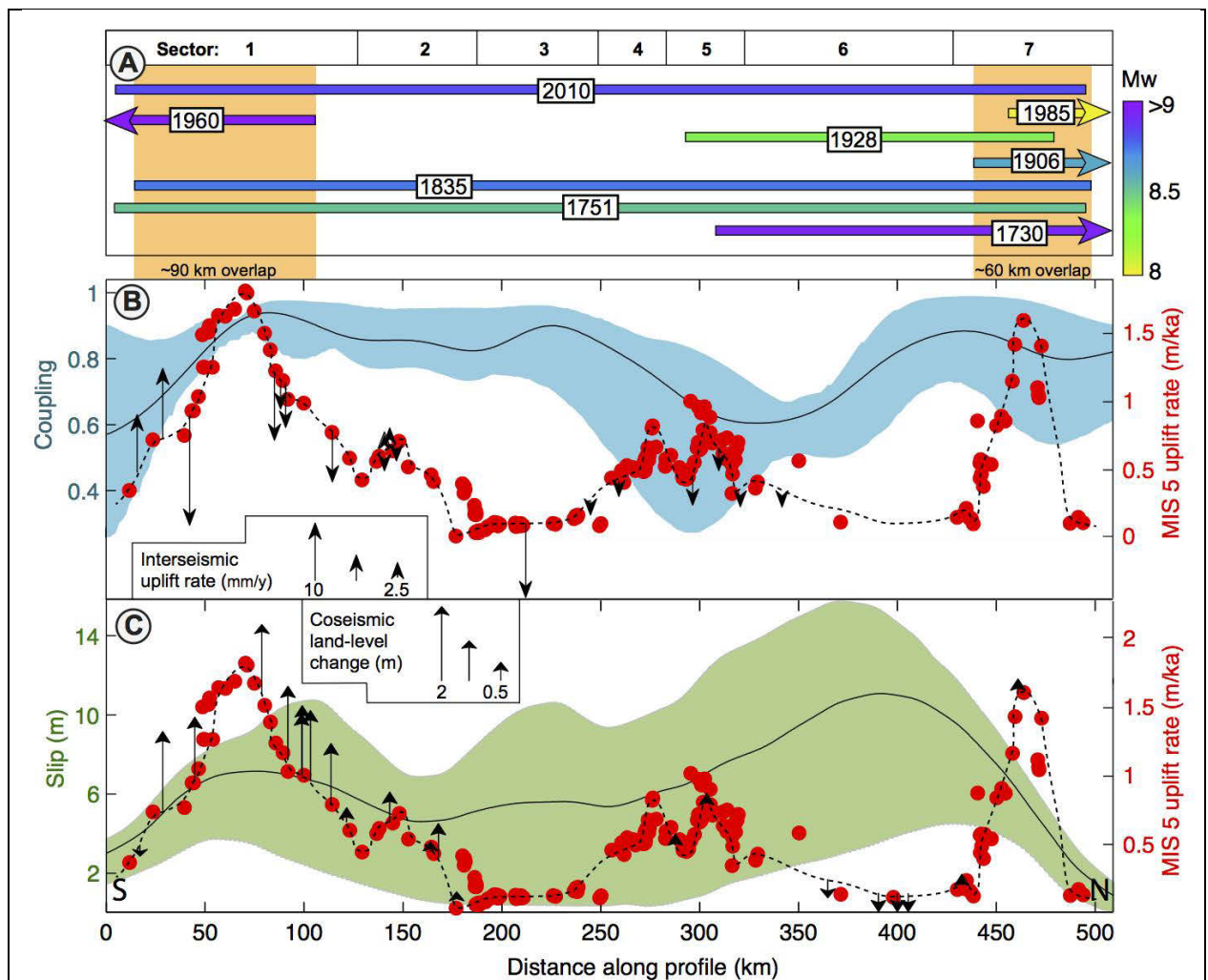


Figure 4.15: Permanent and seismic-cycle deformation patterns along the Maule rupture. The area used for topography, coupling and slip swaths is indicated in Fig. 1A. (A) Rupture length of historical earthquakes color-coded by magnitude (from sources in the text), overlapping areas at Arauco and Topocalma discussed in the text highlighted by orange rectangles. (B) Swath profile of pre-2010 earthquake interseismic coupling (Moreno et al., 2010) and MIS-5 uplift rates. Arrows indicates the GPS velocity measured between 2004 and 2008 (Moreno et al., 2010; Metois et al., 2012). (C) Swath profile of Maule earthquake coseismic slip (Moreno et al., 2012) with MIS-5 uplift rates, the arrows indicates co-seismic land-level changes (Farias et al., 2010; Melnick et al., 2012a).

The nature of these earthquake boundaries is not yet understood. Melnick et al. (2009b) proposed that a sharp gradient in petrophysical properties of the upper plate across the Lanalhue Fault, which juxtaposes different rock units, might be responsible for causing an inhomogeneous earthquake barrier at Arauco. However, Haberland et al. (2009) found no major changes in seismic velocities and v_p/v_s ratios across this fault, suggesting that petrophysical conditions do not vary significantly. Thus, other crustal-scale processes probably associated with the rather broad patterns of crustal upwarping at Arauco and Topocalma should be responsible for arresting the propagation of mega-thrust ruptures across these regions. The changes in the curvature of the megathrust might act as geometric or inhomogeneous barriers that arrest propagation of megathrust ruptures. In addition, underplating of trench sediments at curved sectors of the plate interface could induce local changes in the frictional behavior of the megathrust accounting for the segmentation of earthquake ruptures.

The longer wavelength of the bending zone affecting the megathrust and crust at Arauco with respect to Topocalma might explain the higher efficiency to restrain earthquake ruptures of the former, as suggested by historical records. Along these lines, only rupture propagation associated with two historical earthquakes terminated at Carranza (Fig. 4.15A), where the zone of high uplift is of even shorter wavelength and rather associated with discrete crustal faults. Areas of low or reduced coupling have been associated with intersegment regions that separate areas dominated by velocity-weakening frictional behavior at the interplate (Hetland and Simons, 2010). Carranza might be such a velocity-weakening dominated region whose capability of restraining rupture propagation will depend on the degree of interseismic coupling (e.g. Kaneko et al., 2010). Thus, lower interseismic coupling at Carranza with respect to the pre-2010 rate might have led to arrest rupture propagation of the 1730 event.

The existence of discrete seismotectonic blocks and barriers to rupture propagation along the south-central Chile margin is similar to observations from other subduction zones. Earthquake barriers have been commonly associated with lower or upper-plate anomalies. For example, Shennan et al. (2009), Audin et al. (2008), and Collot et al. (2004) related earthquake-rupture segmentation to upper-plate structures in Alaska, southern Peru, and Ecuador-Colombia, respectively. Along the same lines, Perfettini et al. (2010), Subarya et al. (2006) and Bilek et al. (2003) related bathy-metric anomalies to sustained earthquake-rupture barriers in central Peru, Sumatra and Costa Rica, respectively. However, segmentation patterns in subduction zones do not seem to follow a unique pattern, because in some cases earthquakes are not constrained by structural features and rupture across segment boundaries. This has been observed in the Solomon Islands (Taylor et al., 2008), Japan (Nanayama et al., 2003), and in Chile during the 1730 ($M \sim 9$) earthquake (Udías et al., 2012). The latter ruptured across the area where the Juan Fernandez Ridge intersects the continental margin, illustrating the ambiguous role of inferred lower-plate earthquake barriers. Segmentation of historical ruptures along the Maule region coincides with patterns of permanent deformation and the overall geometric characteristics of the fore-arc, which are ultimately reflected in the upper plate.

Normal faults in forearc regions have been commonly related to megathrust ruptures (e.g. Loveless et al., 2010; Sherrod and Gomberg, 2014). Farías et al. (2011) and Ryder et al. (2012) proposed that faults between Pichilemu and Topocalma accommodate interseismic shortening by reverse motion and associated zones of wide folding. In their interpretation these structures are re-

activated as normal faults by stress transferred from great earthquakes, as postulated for the region along the Pichilemu fault after the Maule earthquake. However, the 60-km width of the anticline at Topocalma is difficult to account for by reverse or normal faulting, and should rather result from deeper-seated processes such as margin-parallel shortening or underplating of subducted sediments. The Pelluhue and Carranza faults are also favorably oriented to slip as a result of stress transfer during slip in the northern patch of the Maule rupture. Thus, the arc-shaped pattern formed by the Pelluhue and Carranza faults in the south and the Pichilemu Fault in the north (Fig. 4.1B) could indicate that the high-slip northern patch of the Maule earthquake is a persistent feature characteristic of many earthquake cycles.

4.5.3 Comparison of seismic cycle and permanent deformation patterns

We tested whether deformation patterns at the time scale of the seismic cycle are correlated with the distribution of permanent deformation along the Maule rupture by directly comparing interseismic coupling measured in the decade before the earthquake with deformation during the earthquake and our estimates from MIS 5 marine terraces. Both coseismic slip and interseismic coupling are distributed in two patches with different degrees of correlations with uplift rates deduced from marine terraces (Figs. 1A, 14B and C).

The comparison of coseismic vertical displacements, based on intertidal fauna (Farias et al., 2010b; Melnick et al., 2012a), with permanent uplift rates shows that these parameters are correlated mostly at Arauco and partly also at Topocalma (Fig. 4.15C). In the central part of the rupture, coastal subsidence occurred in an area of low uplift rates (Sector 6 and 7). Interseismic vertical velocities based on GPS measurements between 2004 and 2008 (Metois et al., 2012; Moreno et al., 2012) show subsidence at sites close to the trench along the Arauco Peninsula where the highest magnitudes of coseismic emergence were registered. The remaining sectors of the Maule coast appear to have been located near the coseismic hinge line.

A direct comparison of coseismic slip and interseismic coupling with permanent uplift rates at the location of the shoreline angles shows different relationships along the rupture zone (Fig. 4.14A and 4.14B). At Arauco slip and coupling exhibit a certain degree of correlation with uplift rate, suggesting permanent deformation may accumulate during great earthquakes. Arauco was uplifted during both the 1960 (M9.5) and 2010 Maule earthquakes (Plafker and Savage, 1970; Melnick et al., 2012a), and thus the high permanent uplift rates might result from cumulative effect of ruptures from these two neighboring segments. Uplift rate and coupling are inversely correlated at Carranza but not correlated at Topocalma (Fig. 4.14A). Similarly, no clear correlation can be inferred between uplift rate and slip at these two sites (Fig. 4.14B). At Carranza an alternative source of permanent uplift might be deduced from the 2012 Constitucion (M7.0) earthquake that caused slip along deeper portions of the plate boundary (39 km) resulting in ~15 cm of uplift (Ruiz et al., 2013) in an area that subsided ~5 cm during the Maule earthquake. This suggests that a portion of the permanent uplift might be accumulated by such deep events that occur during the post- and interseismic phases.

4.6 Conclusions

We deciphered and compared the pattern of permanent coastal deformation estimated from emerged marine terraces and seismic-cycle deformation along the 2010 Maule earthquake rupture zone of south-central Chile. We estimated uplift rates from 170 measurements of shoreline angles

interpreted from high-resolution topographic data, tying the marine terrace chronology by means of 12 IRSL ages, stratigraphy and geomorphic mapping, and correlating them with different levels of the Marine Isotope Stages (MIS) 5e and 5c to obtain a long-term temporal and spatial signal of forearc deformation.

The mean terrace uplift rate along the entire Maule rupture of 0.50 m/ka is exceeded at Arauco (1.59 m/ka), Carranza (0.85 m/ka) and Topocalma (1.35 m/ka), located at the southern, central, and northern sectors of the 2010 rupture. These three rapidly uplifting sectors are characterized by different structural settings. The Arauco and Topocalma peninsulas are both located at the boundaries of the rupture and are characterized by broad antiformal structures with wavelengths of ~ 90 and ~ 60 km, respectively.

Instead, Carranza is located at the center of the rupture zone and characterized by moderate uplift rates, sharp offsets across normal faults and short-wavelength flexures related to the elastic response of crustal faulting. These three areas coincide with the spatial limit of at least 8 historical megathrust ruptures (M8-9.5). We argue that these three areas can be understood as earthquake barriers, where overall deformation patterns, both at seismic-cycle and longer timescales, are controlled by the morphotectonic and geometric characteristics of the margin. These conclusions are based on the following arguments:

1. The boundaries of the Maule rupture spatially coincide with the symmetry axis of the Maipo and Arauco oroclines. These two features can be traced across the entire Andean margin, from fore-to back-arc, and have been active over the past few million years.
2. The long-wavelength zones of upwarping at Arauco and Topocalma are likely associated with deep-seated sources probably along the plate interface and/or the entire crust. We suggest that these zones might be associated with basal accretion of sub-ducted trench sediments or with margin-parallel shortening resulting from oroclinal bending and motion of forearc slivers driven by oblique plate convergence.
3. The zones of rapid uplift and broad upwarping at Arauco and Topocalma coincide with the boundaries of historic earthquake ruptures. We infer that deformation of the upper plate might have played a role in the propagation of megathrust earthquakes in both regions. Instead, Carranza seems to arrest certain types of ruptures, possibly as a result of reduced interseismic coupling.
4. Fast coastal uplift at Topocalma and Arauco occurs in regions where the plate interface is shallower than elsewhere along the Maule rupture, and where coseismic slip is to a certain degree correlated with long-term uplift rates. This suggests that permanent deformation in these regions is accumulated during great earthquakes. In turn, in regions where the subducting slab is deeper, i.e. areas that are located farther inland from the trench, such as Carranza, show inverse relationships between long-term uplift rate and interseismic coupling, suggesting they might rise permanently during the interseismic period.

5 Quantifying offshore forearc deformation and splay-fault slip using Pleistocene drowned shorelines, Arauco Bay, Chile

Along this chapter I developed a detailed study of drowned sea-level markers at the southern part of the (2010) Maule earthquake rupture. To measure these markers, a variation of the methodologies developed in Chapter 3 was used, but oriented to study drowned sea-level markers. Likewise, onshore uplift rates, surveyed in Chapter 4, were combined with uplift rates from Santa Maria Island estimated in Chapter 2 and our measurements in offshore areas, obtaining an extended pattern of permanent deformation.

Most of the deformation associated with the seismic cycle in subduction zones occurs offshore, and has been therefore difficult to quantify with direct observations at millennial time scale. Here we study the pattern of permanent deformation associated with a splay fault system in the Arauco Bay Area off south-central Chile, which slipped during the 2010 Maule megathrust earthquake (M8.8). We first characterize hitherto-unrecognized drowned shorelines using high-resolution multibeam bathymetry, geomorphic, sedimentologic and paleontologic observations, and quantify uplift rates using a landscape evolution model. Along a margin-normal profile, uplift rates are 1.3 m/ka near the edge of the continental shelf, 1.5 m/ka at the emerged Santa Maria Island, -0.1 m/ka at the center of the Bay, and 0.3 m/ka along the mainland coast. The multibeam bathymetry images a complex pattern of kilometer-scale anticlines and small normal faults, which we interpret as the surface expression of the Santa Maria crustal-scale splay fault system, and a broad syncline at the center of the Arauco Bay. We modeled the surface deformation produced by these structures with two different scenarios including deep-reaching normal faults and deep-reaching reverse faults with shallow extensional structures. Our preferred model comprises a blind reverse fault extending from 3 km depth down to the plate interface at 16 km that slips at a rate between 3.0 and 3.7 m/ka, with shallow normal faults along crests of anticlines. If all the motion on the crustal-scale splay fault occurs during every great megathrust earthquake, which have a recurrence interval of ~150-200 years, the fault would slip ~0.5 m per event, releasing the moment equivalent to a magnitude ~4 earthquake. However, if the splay fault slips only together with a megathrust earthquake every ~1000 years, then a slip of ~3.5 m per event would account for the long-term rate, equivalent to a magnitude ~6.7 earthquake. Such an event could trigger a high-amplitude local tsunami. Our study highlights the application of quantitative geomorphology with high-resolution bathymetry to estimate deformation rates in submarine forearcs.

5.1 Introduction

In subduction zones, most of the deformation associated with the plate-boundary megathrust both over short- and long-term timescales occurs predominantly in the offshore forearc (e.g. Moore, 1979; Savage, 1983; Hyndman and Wang, 1995; Wells et al., 2003). Shortening and extension may alternate in the accretionary wedge and in areas that overlie the locked portion of the megathrust (e.g. Wang and Hu, 2006), where secondary structures in the upper plate, such as splay-fault systems, play a pivotal role in shaping the architecture of subduction zones (e.g. Barnes et al., 2002; Park et al., 2002; Mukoyoshi et al., 2006; Moore et al., 2007; Collot et al., 2008; Singh et al., 2011; Melnick et al., 2012d; Waldhauser et al., 2012; Chapman et al., 2014).

However, linking the predominantly elastic deformation associated with the plate-boundary seismic cycle to the deformation recorded in the geology and geomorphology of the upper plate is not straightforward as it requires offshore observations at centennial to millennial timescales. Fortuitously, islands and peninsulas in the continental shelf areas may furnish valuable data to evaluate vertical land-level changes at various temporal scales (e.g. Berryman, 1993; Briggs et al., 2008; Victor et al., 2011; Lin et al., 2013; Briggs et al., 2014; Kitamura et al., 2014; Wesson et al., 2015); however, islands are not very common along most subduction margins, and thus offshore observations are required to quantify deformation rates and to link the kinematics of upper-plate faults to the stick-slip cycle of the plate-boundary megathrust. Drowned shorelines, geomorphic markers that have been revealed by high-resolution multibeam bathymetric surveys (Chaytor et al., 2008; Johnson et al., 2014; Leclerc et al., 2015), may provide key information on deformation rates in offshore realms if their relationship with climatically controlled past sea-level positions and age are properly assessed. We adopt a multidisciplinary approach to provide a quantitative assessment of drowned shorelines in a forearc setting affected by great megathrust earthquakes and characterized by complex offshore upper-plate structures.

Recent megathrust earthquakes such as the M9.1 Sumatra (2004), M8.8 Maule (2010), M9.2 Tohoku (2011), and M8.1 Pisagua (2014) events revealed that most of the plate-boundary slip occurred below the offshore forearc (e.g., Chlieh et al., 2007; Moreno et al., 2010; Moreno et al., 2012; Satake et al., 2013; Schurr et al., 2014). Most of these earthquakes were associated with the reactivation of splay faults in the upper plate, both in offshore and onshore areas (e.g. Kodaira et al., 2012; Melnick et al., 2012d; Waldhauser et al., 2012; Lieser et al., 2014; González et al., 2015). For example, the 2010 Maule earthquake was followed by motion along the Santa Maria and Pichilemu faults (Farías et al., 2011; Melnick et al., 2012d; Ryder et al., 2012). Both structures are trenchward dipping faults, but of apparently different kinematics during instantaneous coseismic reactivation and integrated over millennial timescales (e.g. Farías et al., 2011; Lange et al., 2012; Melnick et al., 2012d; Allmendinger et al., 2013; Aron et al., 2013; Melnick et al., 2013). Understanding the relation between the motion of such structures during great megathrust earthquakes and their role in controlling the long-term evolution of the forearc, including build-up of topography and basin development, may contribute to our understanding of seismotectonic segmentation processes in subduction zones.

The reactivation of splay faults in forearc settings has been discussed in the context of Coulomb wedge theory (e.g. Dahlen et al., 1984; Wang and Hu, 2006), suggesting that faults with suitable

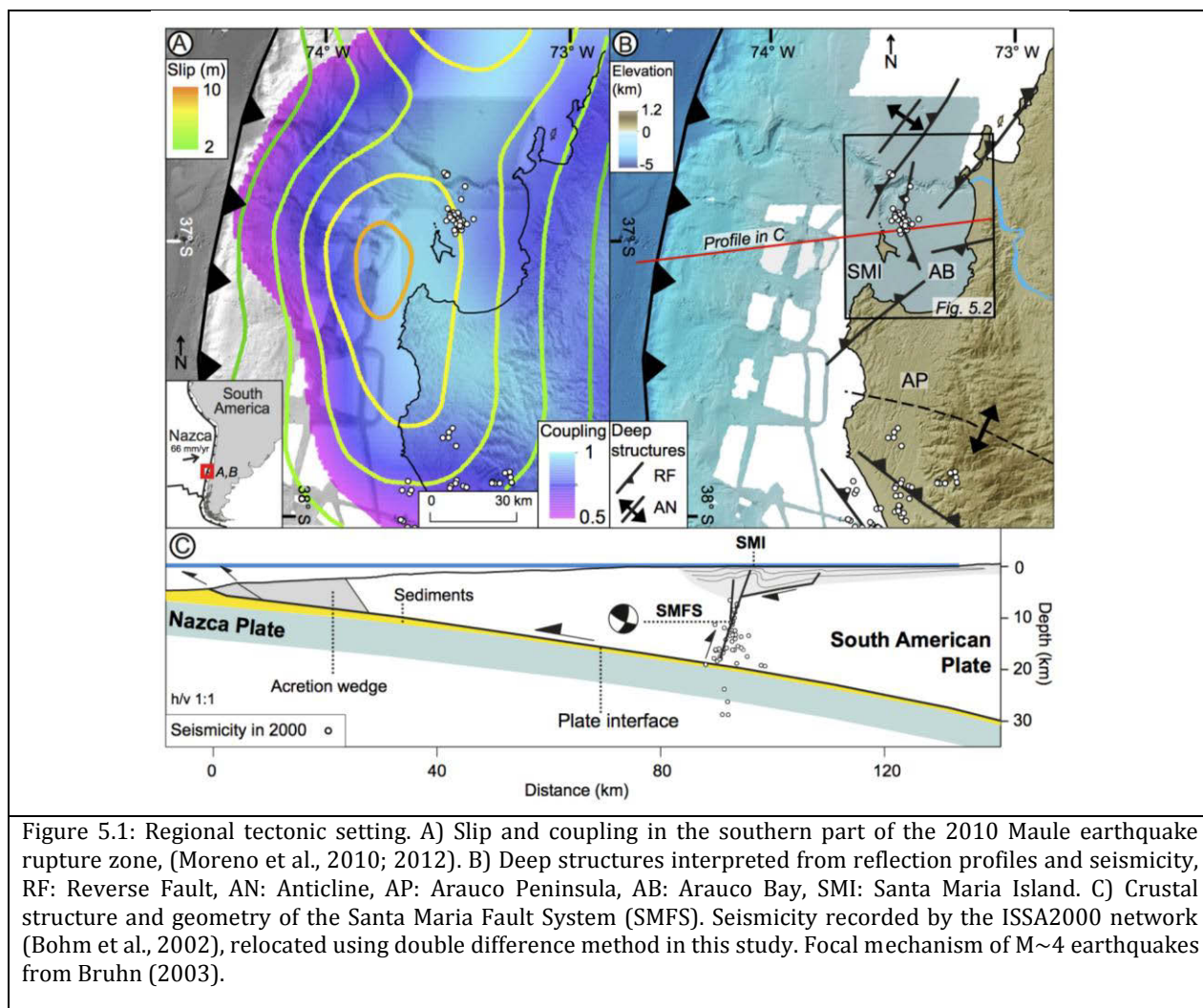
orientation with respect to the local stress field are likely to be reactivated during megathrust earthquakes (e.g. Sibson, 1985; Morris et al., 1996; Loveless et al., 2010; Aron et al., 2013). In addition, modeling experiments have shown that the kinematics of reactivated splay faults will depend on their position with respect to the locus of coseismic slip along the plate interface, favoring normal or reverse reactivation, if most of the slip is located trench- or landward from the branching point, respectively (Li et al., 2014). Because splay faults usually reach the seafloor at a steeper angle than the megathrust at the plate interface, their reactivation may enhance deformation locally (e.g. Waldhauser et al., 2012; Chapman et al., 2014) and influence the temporal evolution of tsunami waveforms (Fukao, 1979; Wendt et al., 2009). Thus, inversions of plate-interface slip that consider tsunami data may be strongly biased if splay faults are not considered; however, including such structures in tsunami-hazard models requires a detailed understanding of their geometry and kinematics.

Emerged marine terraces and deformed shorelines have been long used as geomorphic markers for estimating surface permanent deformation and inferring the kinematics and slip rate of local faults and folds (e.g. Bloom et al., 1974; Lajoie, 1986; Anderson and Menking, 1994; Dickinson, 2013). These markers have been formed by the combined effects of tectonic uplift, wave-erosion and cliff retreat during past sea-level highstands. Tectonic uplift is responsible for preserving the emerged terrace remnants forming staircase sequences if the uplift rate is higher than 0.2 mm/yr (Pedoja et al., 2014). At lower rates, marine terraces may be polygenetic and record recurrent reoccupation during successive sea-level highstands resulting in the development of a *rasa*, a wide coastal plain bounded by a steep cliff (Paskoff, 1977; Regard et al., 2010; Pedoja et al., 2014; Melnick, 2016). Under favorable conditions shorelines can also be preserved below modern sea-level in areas of moderate uplift rate (e.g. Emery, 1958; Sherman et al., 1999); the detection and quantitative assessment of such drowned features opens new opportunities for the quantification of deformation rates in the offshore forearcs of subduction margins.

To bridge observations of splay-fault deformation on different timescales, and to estimate the amount of permanent deformation accrued by such structures in a forearc setting, we analyze drowned shorelines of the Arauco Bay Area of south-central Chile, a region affected by recurrent megathrust earthquakes and documented splay faulting (Moreno et al., 2008; Melnick et al., 2012d; Moreno et al., 2012; Wesson et al., 2015). We evaluate hitherto unrecognized drowned shorelines using high-resolution bathymetry and direct field observations using a Remotely Operated Vehicle and sampling of datable terrace material by professional divers. We further combine our offshore assessment of deformation rates with previous estimates inferred from the deformation of onshore geomorphic markers. Our objectives are threefold: (1) identify and map active structures and drowned former sea-level markers; (2) present a new method to estimate uplift rates from drowned geomorphic markers using a landscape-evolution model; and (3) assess the kinematics and associated deformation rates of an offshore splay-fault system. Our study reveals the offshore pattern of permanent deformation derived from drowned shorelines, suggesting slip along a trenchward-dipping reverse fault rooted at the plate interface.

5.2 Seismotectonic and geomorphic setting

The Arauco Bay Area is located on the continental shelf between 70 and 110 km east of the Chile trench (Fig. 5.1A), where the ~32-m.y.-old Nazca Plate is subducted beneath the South American Plate at ~66 mm/yr (Angermann et al., 1999). The area is bounded to the south by the Arauco Peninsula, by the Santa Maria Island (SMI) to the west, and by the Bio-Bio Canyon and the Hualpén-Tumbes peninsulas to the north (Fig. 5.2). The Arauco Peninsula and the adjacent Nahuelbuta ranges (Fig. 5.1B) are rapidly uplifting areas (>1 mm/yr) associated with the growth of a large-scale antiform bounded by crustal reverse faults (Fig. 5.1B) (Kaizuka et al., 1973; Melnick et al., 2006; Melnick et al., 2009; Jara-Muñoz et al., 2015a).



5.2.1 The 2010 Maule earthquake

The Arauco Bay area is located in the southern part of the 2010 Maule earthquake rupture that affected ~500 km of the south-central Chile margin (Fig 1A). This event had a moment magnitude of 8.8 and was characterized by a complex slip distribution with two main patches with peak slip of ~17 m and ~12 m at the northern and southern sectors of the rupture, respectively (Tong et al., 2010; Moreno et al., 2012; Lin et al., 2013). Based on GPS velocities from the decade prior to the

Maule earthquake, kinematic models have revealed a heterogeneous distribution of interseismic coupling that resembles the main pattern of coseismic slip distribution during the earthquake (Moreno et al., 2010).

The Maule earthquake was preceded by the 1835 Concepción event ($M > 8.5$) documented by FitzRoy and Darwin (FitzRoy et al., 1839; Darwin, 1851). Inundation by tsunamis and coastal uplift during the 2010 and 1835 earthquakes suggest that both events were very similar (Cisternas et al., 2010; Moreno et al., 2010; Melnick et al., 2012c). Wesson et al. (2015) combined decadal and centennial-scale observations of relative sea-level changes at SMI, including both the 1835 and 2010 earthquakes, to estimate land-level changes through the entire earthquake cycle, concluding that 0.15-0.3 m of coseismic uplift in 1835 may have been stored as net permanent deformation in the crust. This is equivalent to 10-20% of net uplift at SMI, and would be equivalent to a mean uplift rate of ~ 1.5 mm/yr estimated over the past ~ 50 ka (Jara-Muñoz and Melnick, 2015).

5.2.2 Structures in the Arauco Bay area

The scale of structural observations made in the Arauco Bay Area can be divided into three groups based on their resolution and depth range: a) crustal-scale seismicity observations reveal an aligned cluster of microseismicity between 5 and 20 km depth (Bohm et al., 2002), interpreted to reflect activity along the Santa Maria splay-fault system (SMFS; Fig. 5.1B) (Melnick et al., 2006); b) mesoscale structural observations from industry seismic reflection profiles provide images of faults and syntectonic units from the upper crust between 0.5 and 2 km, but lacking resolution at very shallow levels (Melnick et al., 2006; Melnick et al., 2012d); c) local observations include uplift rates estimated from marine terraces onshore, structures mapped in coal mines on the eastern part of the Arauco Bay at depths of up to ~ 1000 m, faults inferred from multibeam bathymetry along the flanks of the Bio-Bio Canyon, and from outcrops at SMI (Melnick et al., 2006; Bernhardt et al., 2015; Jara-Muñoz and Melnick, 2015; Jara-Muñoz et al., 2015a).

Faults identified using seismic reflection profiles comprise high-angle normal faults and reverse fault-cored anticlines affecting Cretaceous to Quaternary units (Melnick et al., 2006; Melnick and Echtler, 2006). The reverse faults were interpreted to result from the compressional inversion of normal faults (Melnick and Echtler, 2006). Near the surface the SMFS comprises multiple strands over an area of ~ 30 km² that ultimately merge into a single master fault at greater depths as suggested by the aligned seismicity (Fig. 5.1B and 5.2). North of SMI and across the Bio-Bio Canyon a series of NNE-SSW oriented fractures, faults, and folded sedimentary rocks have been recognized using high-resolution (5-m) multibeam bathymetry (Bernhardt et al., 2015). These features delineate the hinge of a ~ 13 -km-wide anticline associated with a ~ 150 -m-high knickzone of the canyon thalweg. In the eastern part of the bay off Coronel, WSW-ENE and NW-SE striking normal faults have been mapped in coal mines (Wenzel et al., 1975) offsetting Tertiary rocks. In the adjacent onshore area, shoreline angles of the emerged MIS-5e marine terrace record a ~ 10 -km-broad warping pattern and discrete offsets associated with a local fault of unknown kinematics (Jara-Muñoz et al., 2015a). Normal faulting affecting Plio-Quaternary units at shallow levels have been associated either with a persistent crustal tensional stress regime (Lavenu and Cembrano, 1999) or with shallow, bending-moment extension localized in the hinge of the fault-cored anticlines (Melnick et al., 2006). At SMI several grabens and halfgrabens have been documented to be associated with NE-SW and NW-SE oriented anticlines deforming late Pleistocene sediments.

5.2.3 Activity of the Santa María Fault System during the seismic cycle

The deformation rates of the SMFS have not yet been assessed, mostly due to its predominantly offshore location. At SMI, in the uplifted hanging-wall block, land-level changes and uplift rates have been estimated over decadal to millennial timescales (e.g. Bookhagen et al., 2006; Melnick et al., 2012d; Wesson et al., 2015). Using resurveyed nautical charts Wesson et al. (2015) estimated that between the 1835 and 2010 earthquakes SMI subsided about 1.6 m at a rate of 11.3 ± 4 mm/yr, which is similar to the 10.2 ± 3.4 mm/yr subsidence rate determined from campaign GPS measurements between 2004 and 2010. Subsidence has been inferred to result from interseismic plate locking. Moreno et al. (2008) used campaign GPS velocities to estimate the slip rate of the SFMS assuming homogeneous interseismic plate coupling at full plate-convergence rate, obtaining a vertical slip rate of 2.8 mm/yr and dextral slip of 6.9 mm/yr. However, these estimates are strongly dependent on the assumption of complete plate coupling, and have to be considered with caution.

In the year 2000 a temporary local network was deployed as part of the Integrated Seismological experiment in the Southern Andes (ISSA) with a duration of 3 months (Bohm et al., 2002). A cluster of 74 events localized in a ~ 90 km² area located 7 km northeast of SMI was recorded; the events form a NNE-SSW oriented and W-dipping alignment between 0.6 km depth and the plate interface at ~ 15 km (Figs. 5.1 and 5.2). Focal-mechanism solutions for two $M > 4$ events are compatible with reverse kinematics along a steeply dipping NNE-striking fault with a minor dextral strike-slip component (Bruhn, 2003; Melnick et al., 2006). These seismological observations have been interpreted to reflect transient interseismic contraction along the SMFS (Melnick et al., 2006). The pulse of seismicity was apparently a transient phenomena as no events were subsequently recorded by the TIPTEQ seismic network that had been installed in this region for the duration of one year in 2004-2005 (Haberland et al., 2005).

The coseismic reactivation of the SMFS was inferred during the 2010 earthquake based on field observations at SMI. Uplift estimated from displaced sessile intertidal biota, campaign GPS measurements, and synthetic aperture radar interferometry show that during the event the SMI was uplifted between 1.6-2.2 m with a northward tilt (Melnick et al., 2012d). In addition, surface ruptures were observed along a normal fault at the northern part of the island and offshore in side-scan sonar images. Together with the overall tilt of the island these structures were interpreted to result from growth of a reverse-fault cored anticline (Melnick et al., 2012d).

5.2.4 Marine terraces in the Arauco Bay area

Emerged shorelines follow the physiography of the Arauco Bay area. The younger shorelines comprise sequences of raised Holocene beach ridges reaching elevations of 8 m at SMI. The older shorelines correspond to a staircase sequence of higher marine terraces correlated with Marine Isotope stage (MIS) 3, 5, 7, and 9 (Kaizuka et al., 1973; Melnick et al., 2009; Jara-Muñoz et al., 2015a) (Fig. 5.2). MIS 5 terraces have been dated using IRSL and cosmogenic radionuclides with ages defining substages 5a and 5e (Melnick et al., 2009; Jara-Muñoz et al., 2015a). The MIS 5e terrace level reaches ~ 200 m at the center of the Arauco Peninsula, implying an uplift rate of 1.6 m/ka, and progressively decreasing in elevation northwards to between 55 and 75 m at Coronel; here, uplift rates vary between 0.4 and 0.6 m/ka (Jara-Muñoz et al., 2015a).

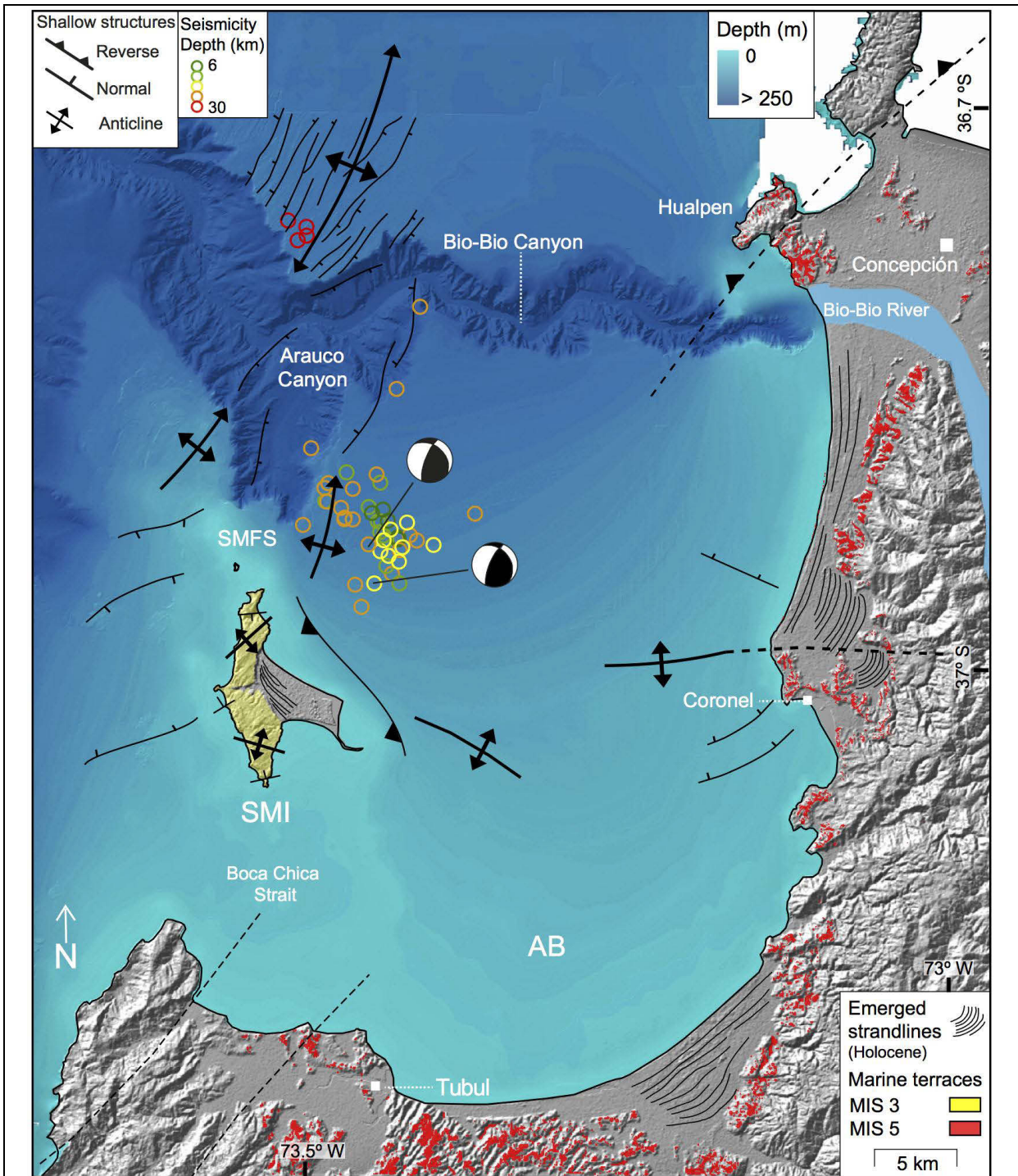


Figure 5.2: Shallow active structures in the Arauco Bay Area interpreted from multibeam bathymetry in this study and previous studies, see text for details. Patterns of uplifted Holocene strandlines and marine terraces based on (Jara-Muñoz & Melnick, 2015; Jara-Muñoz et al., 2015; Kaizuka, et al., 1973; Melnick et al., 2009, Bookhagen et al., 2006; Isla et al., 2012). Relocated microseismicity from the ISSA2000 experiment and processed in this study, color-coded by depth. SMFS: Santa Maria Fault System; SMI: Santa Maria Island.

SMI is capped by the Santa Maria Formation, which consists of several sequences of beach deposits and paleosol horizons deposited during MIS 3 (Melnick et al., 2006; Jara-Muñoz and Melnick, 2015). MIS 3 was a period of low-amplitude climatic variability between 60 and 25 ka (Fig. 5.3A)

(Imbrie et al., 1984; Shackleton, 2000; Swann et al., 2005), characterized by a relatively stable sea level at 65 to 75 mbsl that lasted for ~ 9 ka (Fig. 5.3B). This period comprises two episodes of subordinate sea-level fluctuations associated with Dansgaard-Oeschger warming events (DO-events) at -60 and 90 mbsl (Bloom et al., 1974; Chappell, 1974; Cabioch and Ayliffe, 2001; Arz et al., 2007; Siddall et al., 2008) (Fig. 5.3A). By correlating these DO-events with the sequence of shore environments identified in the Santa Maria Formation, Jara-Muñoz and Melnick (2015) estimated and uplift rate of 1.5 ± 0.3 m/ka at SMI.

The MIS 1 is represented by sequences of parallel Holocene strandlines surrounding the Arauco Bay (Fig. 5.2). Some of these strandlines were dated at SMI and Arauco using Optically Stimulated Luminescence (OSL) and radiocarbon dating, respectively, to between 1.8 and 4.3 ka (Bookhagen et al., 2006; Isla et al., 2012). Bookhagen et al. (2006) proposed that strandlines at SMI have emerged as a result of recurrent coseismic uplift during megathrust earthquakes at a mean uplift rate of 2.3 ± 0.2 m/ka, which is slightly higher than the 1.5 ± 0.3 m/ka uplift rate estimated from MIS 3 deposits (e.g. Jara-Muñoz and Melnick, 2015). Furthermore, the mean recurrence of strandline-forming events of ~ 180 years obtained by Bookhagen et al. (2006) is very similar to 175 years that separated the 1835 and 2010 earthquakes, supporting coseismic uplift as viable mechanism to explain long-term land-level changes and emergence of the island.

5.2.5 Modern depositional environments in the Arauco Bay

The patterns of modern sedimentation in the Arauco Bay are controlled by combined hydrodynamic and morphologic elements that lead to a low residence time of sediments on the shelf (Völker et al., 2014; Bernhardt et al., 2015). The Arauco Bay is a north-facing embayment strongly affected by local seasonal upwelling causing near-surface divergence and bottom flow about a pair of counter-rotating gyres (e.g. Valle-Levinson et al., 2003). West of the bay and south of SMI marine currents are disrupted across the shallow Boca Chica straight (depths < 20 m) (Fig. 5.2). An analysis of multibeam bathymetry suggests these currents cause only very minor erosion of sea floor in the Arauco Bay (Bernhardt et al., 2015). During the Holocene sedimentation in the Arauco Bay has mostly consisted of terrestrial fluvial input of sand transported by the Bio-Bio river from volcanic sources in the high Andes, and dispersed along the bay by littoral drift (Mardones and Jaque, 1991; Muñoz et al., 2004; Raitzsch et al., 2007). The bottom of the bay comprises patches of volcanic sand and pelagic mud shaping the smooth and gentle ($\sim 0.5^\circ$) slope of the Arauco Bay (Vargas, 2005). High-resolution bathymetry and back-scatter echosound profiles have shown that the sea-floor north of SMI contains several rocky patches at ~ 140 m depth, indicating no recent sedimentation, and probably associated with past sea-level positions and localized active deformation (Melnick et al., 2003; Bernhardt et al., 2015).

5.3 Background and Methods

5.3.1 Drowned sea-level markers

Abrupt climate change and rapid sea-level rise have produced catastrophic flooding events in coastal areas during the switch between glacial and interglacial periods (Hanebuth et al., 2000). During MIS 2 the sea-level fell to 120 mbsl at ~ 20 ka (Fig. 5.3A), and was followed by a rapid sea-level rise at rates of 25 m/ka starting at ~ 17 ka, flooding shallow continental shelves around the

world (e.g. Fairbanks, 1989; Bard et al., 1996; Hanebuth et al., 2000; Lambeck et al., 2002; e.g. Munhoven, 2002; Sommerfield and Lee, 2004; Stanford et al., 2011). Such dramatic flooding events may erode the earlier coastal landscape, but depending on the local slope the resulting wave erosion along the shore profile might be reduced allowing for the preservation of drowned snapshots of past sea-level positions below the wave base (Bradley, 1958). Drowned coastal geomorphic features have been recognized along littoral realms in tectonically uplifting, subsiding, and/or glacially influenced regions, documenting a diversity of landforms (e.g. Webster et al., 2004; Van Andel and Perissoratis, 2006; Brooke et al., 2014; Cawthra et al., 2014). However, the use of drowned sea-level markers for the assessment of tectonic deformation is challenging due to difficulties in collecting material for isotopic dating and performing direct on-site observations.

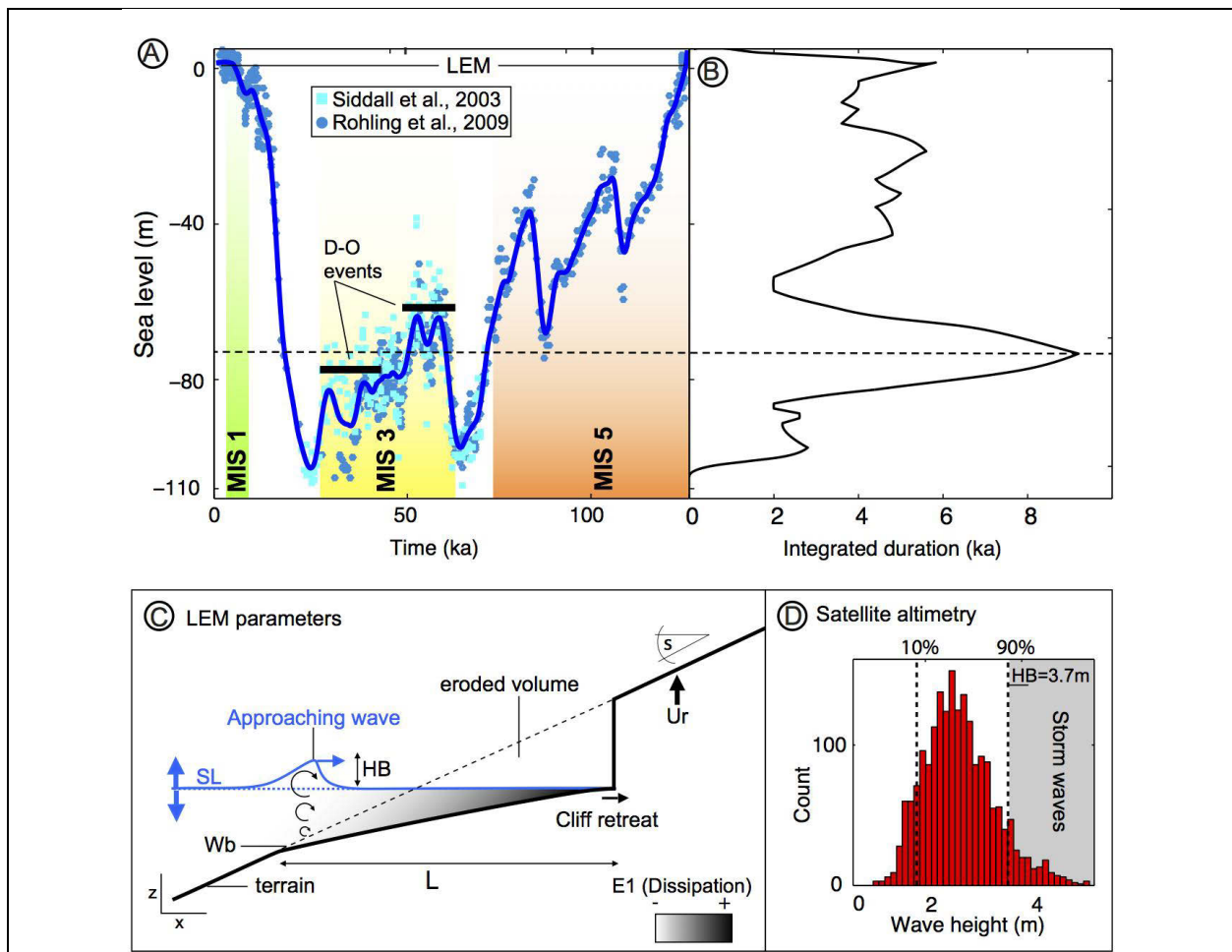


Figure 5.3: Sea-level variations since Marine Isotopic Stages (MIS) 5e and constraints of the Landscape Evolution Model (LEM). (A) Stack of sea-level curves based on Siddall (2003) and Rohling et al. (2009), see text for details. Dansgaard-Oeschger (D-O) events are indicated by black thick lines. B) Integrated sea-level using 100 yr time steps, note a prolonged integrated period lasting several thousand years with the sea level located at depths between 65 and 75 mbsl. C) Schematic representation of the LEM setup used to simulate the formation of drowned shorelines and its input parameters. The white-black gradient indicates the pattern of energy dissipation along the shore system (E1); HB: wave height; Wb: wave base, s: initial slope, L: Platform length, SL: Sea level, Ur: Uplift rate. D) Wave height histogram based on six years of satellite altimetry measurements used to define the value of HB (produced and distributed by the AVISO website of the French Spatial Agency (CNES) at www.aviso.com as part of the Ssalto/Duacs ground-processing segment.

Onshore, the elevation of marine terraces has been commonly used to estimate uplift rates using the shoreline angle, a point located at the intersection between the paleo-platform and paleo-cliff, representing the maximum elevation of sea level at the moment of terrace formation (Lajoie, 1986). Similar submarine features have been documented using high-resolution bathymetry in shallow marine areas, such as the Antilles and California, and were used to estimate past sea-level positions and uplift rates (e.g. Chaytor et al., 2008; Johnson et al., 2014; Leclerc et al., 2015).

5.3.2 Mapping drowned shorelines in the Arauco Bay area using high-resolution bathymetry

We applied different methods to map and estimate deformation rates from drowned shorelines imaged by multibeam bathymetry and submarine observations; we studied the setting of these features using geomorphology, sedimentology, paleontology, and numerical modeling of landscape evolution. In addition, we used the obtained deformation rates to infer the kinematics and slip rates of splay faults in the Arauco Bay area.

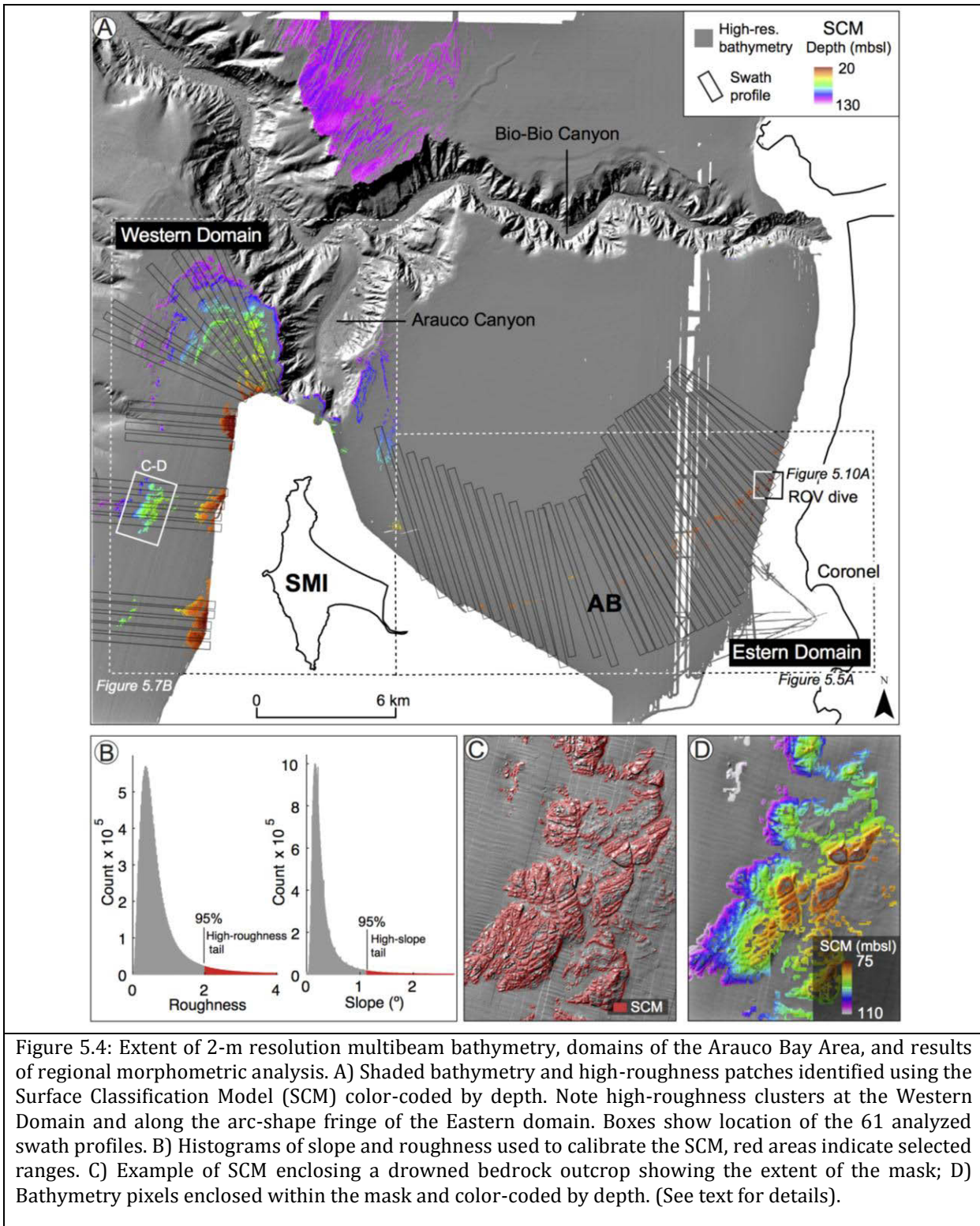
New generation echo sounders designed for shallow water depths allow mapping submarine geomorphic features with unprecedented detail (e.g. Beaman et al., 2011; Luján et al., 2011). In this study, we use ~1000 km² of high-resolution bathymetry (Fig. 5.4A) surveyed by the USS Pathfinder (NAVOCEANO and SHOA) using a hull-mounted Simrad EM710 echosounder operating between 70 and 100 kHz. The survey was made one year after the Maule earthquake, and processing was carried out by SHOA using the CARIS, HIPS, and SIPS 7.1 software packages (González-Acuña and Arroyo-Suarez, 2013). Point clouds were referred to a mean sea-level datum using GPS buoys, tide gauges and onshore topographic benchmarks, and gridded at 2 m for shallow regions and 5 m for the deeper parts. The areas immediately adjacent to the coast were not surveyed by the USS Pathfinder and were filled using a 20-m grid made from bathymetric soundings available from digital nautical charts (SHOA, 2004) and also from the surveys of Wesson et al. (2015).

5.3.3 Morphometric analysis

We define the bathymetric surface classification model (SCM) to semi-automatically map remnants of paleo-platforms and paleo-cliffs from the rest of the landscape; this method is based on Bowless and Cowgill (2012), but focuses on isolating rough and steep areas that may represent erosion features (Fig. 5.4C and 5.4D).

The model uses a combination of depth, slope, and roughness, the former defined as the standard deviation of the slope (Frankel and Dolan, 2007). The analysis was performed only for depths above 140 mbsl, where SCM is defined by linearly combining ranges of slope (SLP) and surface roughness as:

$$SCM = \left(\frac{SLP}{2} * 0.5 \right) + \left(\frac{std(SLP)}{1.2} * 0.5 \right)$$



We tested several ranges of roughness and slopes to isolate rough areas from the rest of the bathymetry (Fig. 5.4A) by analyzing frequency distributions and isolating the values above the 95th percentile of each distribution, equivalent to $>1.2^\circ$ for slope and $>2^\circ$ for roughness (Fig. 5.4B). Roughness and slope were then normalized and linearly combined (Eq. 1), and the isolated areas

were manually corrected by removing false-positive classifications such as shipwrecks and survey noise.

We studied 60 swath profiles of 300 m width oriented perpendicular to the trace of the high roughness patches identified by the SCM (Fig. 5.4A). In emerged marine terraces, the intersection between the paleo-cliff and paleo-platform defines the shoreline angle (e.g. Lajoie, 1986; Jara-Muñoz et al., 2015b); however, as described in Section 4.1 and Figure 5B, the morphology of submerged erosive features in the AB differs from the typical paleo-cliff morphology. To localize the shoreline angle on swath profiles, we first fitted linear and exponential regressions and then intersected extrapolated curved to find the location of the shoreline angle, and estimated the error by intersecting the 2σ confidence intervals of each regression (Fig. 5.5B).

5.3.4 Submarine imaging and sampling

To enhance the interpretations and mapping based on high-resolution bathymetry we selected a shallow area to perform in-situ observations and sampling. The area was located in the Eastern Domain of AB, 5 km from the coastline and 7 km north of Coronel (Location in Fig. 5.4A and 5.5A). We used a Remotely Operated Vehicle (ROV) to explore a ~70-m-long track along the edge of a drowned cliff obtaining video and still images, which we used to select a sediment sampling site. The sampling was carried by professional divers that collected cobbles from the base of a paleo-cliff and sand from the flat area adjacent to its base.

The textural and morphoscopic characteristics of sediments have been largely used to identify the mode of transport and energy of the depositional environment (e.g. Klován, 1966; Friedman, 1967; Folk, 1980; Kasper-Zubillaga and Dickinson, 2001; Jara-Muñoz and Melnick, 2015). We studied two sand samples collected at 46 mbsl. The main statistical parameters (mean, sorting, skewness, and kurtosis) of grain-size distributions were calculated using the method of moments in phi scale (ϕ) (Blott and Pye, 2001), and compared with 22 sand samples of active coastal environments from SMI (Jara-Muñoz and Melnick, 2015) to interpret their depositional environment.

The surface morphology of grains is shaped by the effects of mechanical and chemical processes; the former are intensified at the shallow portion of the shore profile in clastic coasts (Bradley, 1958; Allen et al., 2015), imprinting characteristic marks into clast surfaces that store information about the mode of transport and energy of the depositional environment (e.g. Bourke et al., 2007). In addition, bioerosion processes may also reshape the surface morphology of clasts and bedrock storing paleo-ecological information of past sea-level positions (e.g. Pleydell and Jones, 1988; Perry, 1996). Pebbles and cobbles recovered from the AB were morphoscopically studied through close range photogrammetry using series of 90 photographs taken from different angles and used to extract dense point clouds. The shape and surface morphology of the clasts was inspected using shaded relief models searching for impact features and bioerosion marks that may allow determining paleo-ecological and paleo-environmental conditions.

5.3.5 Estimating uplift rates from drowned shorelines using a Landscape Evolution Model

We used a Landscape Evolution Model (LEM) to simulate the development of wave-cut marine terraces and compared the results systematically with bathymetric swath profiles to estimate local uplift rates. At wave-dominated coastal systems LEMs have been used to study the development of marine landscapes under an oscillating sea-level and variable uplift, simulating various processes

responsible for generating and dismantling the geomorphic expression of marine terraces including coral growth, sediment transport and deposition, cliff retreat, cliff diffusion, and fluvial incision (e.g. Hanks et al., 1984; Anderson et al., 1999; Storms and Swift, 2003; Nakamura and Nakamori, 2007; Refice et al., 2012; Thébaudeau et al., 2013; Shikakura, 2014; Melnick, 2016).

The LEM developed in this study has been adapted from the wave erosion and dissipation model of Anderson et al. (1999), based on Sunamura (1992). The model simulates the formation of wave-cut terraces under an oscillating sea level and constant uplift rate (Fig. 5.3C). The model assumes wave erosion as a linear function of the rate of wave energy dissipation ($E1$) (Sunamura, 1992) that follows an exponential increase in relation to depth ($Sl-Z$) landwards:

$$E1 = \Sigma \exp\left(\frac{Sl - Z}{Wb}\right) \left(\frac{dz}{dt}\right),$$

where Wb is the wave base depth, Z is the local water depth and Sl the sea level position at time t ; dz/dt represents the vertical seabed erosion rate through time. Seawards, at depths below the wave base, water particle motions are too small to accomplish significant work on the sea floor and no erosion is assumed (e.g. Bradley, 1958; Sunamura, 1992). The breaking wave height (HB) is related to Wb by a dimensionless constant B :

$$Wb = \frac{HB}{B},$$

which has been the subject of numerous studies obtaining mean values of between 0.1 to 0.5 depending on sea-floor morphology (Hallermeier, 1978; Thornton and Guza, 1983; Kline et al., 2014). We used a value of $B=0.25$ appropriate for the relatively smooth bathymetry of the Arauco Bay Area. HB was estimated from six years of radar altimetry measurements (produced and distributed by the AVISO website of the French Spatial Agency (CNES) at www.avis.com as part of the Ssalto/Duacs ground-processing segment, extracted from the dataset: nrt-global-mswh). We assume that wave heights higher than the 90th percentile of the entire distribution (3.7 m) are highly erosive associated with mayor storm events (Fig. 5.3D), following (Young et al., 2011).

The wave energy declines with local depth following the trajectory of an approaching wave. Actually, the dissipation depends not only on the depth but also on the near-shore platform morphology that in some cases is inherited from previous sea-level positions (Bradley, 1958; Komar, 1998). In fact, wider shallow platforms likely attenuate the erosive power of waves more efficiently. We defined the efficiency of energy dissipation along the platform ($E2$):

$$E2 = \left(\frac{L}{X}\right) * 0.5 \left(\frac{dx}{dt}\right),$$

which is a function of platform width (L) and distance from the shore (X) at time (dt), in a ratio proportional to half the cliff erosion rate (dx/dt). The energy in the far field is assumed to be constant ($E0$), when the dissipation represented by $E1$ and $E2$ is lower than $E0$, the remaining energy in the system ($E3$) is capable to produce cliff retreat resulting in a widening of the wave-cut platform (Anderson et al., 1999).

$$E3 = E0 - E2 - E1$$

The main input parameter for the LEM is a sea-level history based on a stack of two curves spanning the past 125 ka. We tested several combinations of sea-level curves (See Appendix D.2), and selected those of Siddall (2003) and Rohling et al. (2009), because they have the highest resolution in the time of interest (MIS 5 to 1), and because both curves have been successfully used to estimate uplift rates from MIS 5-3 marine terraces in the region (Melnick et al., 2006; Jaramuñoz et al., 2015a). In order to generate marine terraces that can be compared with those observed in the AB, we chose a model time spanning the past 125 ka. This model time is based on: a) Emerged sea-level markers in the areas surrounding the Arauco Bay have been dated to between MIS 5 and 1 (See Section 2.2). b) Drowned marine terraces have been usually associated with lowstand periods, either during the LGM or the preceding interstadial stages (e.g. Webster et al., 2004; Chaytor et al., 2008; Johnson et al., 2014; Leclerc et al., 2015; Martinez-Martos et al., 2016). Furthermore, if we consider that the uplift rate of the AB should lie between that of SMI (~1.5 m/ka) and of Coronel (0.4 to 0.6 m/ka), shorelines of lowstands periods should be present below modern sea level. c) Marine terraces older than MIS 5 have a lower probability to be preserved underwater due to erosion from subsequent flooding episodes (Section 3.1). The stable sea-level period between 65 and 75 mbsl (Fig. 5.3B) started approximately at ~75 ka immediately after the MIS 4 and may be the best candidate for the formation of drowned marine terraces due prolonged wave action (e.g. Caputo, 2007). The stacked sea-level data was linearly interpolated at 50-years intervals and smoothed using a 150-yr moving mean to prevent the formation of artifacts in the LEM due to spikes and outliers in the sea-level curve.

The bathymetry of drowned shorelines was compared with the LEM results to determine local uplift rates. The initial model geometry consists of a linear slope calculated from the maximum and minimum depths along the length of each swath profile. In order to find the best-fitting model we scaled the pattern of modeled terraces using the shoreline angle determined from the swath profiles. The horizontal scale between the LEM and each swath profile was adjusted by collocating both shoreline angles at the LEM time of formation (T). The best fitting initial cliff erosion rate (E_0) and uplift rate (Ur) are obtained by minimizing the root mean square (RMS), where n is the number of elements, Z_{obs} is the observed bathymetry and Z_{LEM} the modeled depth profiles respectively.

$$RMS = \sqrt{\frac{\sum(Z_{LEM} - Z_{obs})^2}{n}}$$

The standard error Se is calculated using the following relation (Gallen et al., 2014):

$$Se = \sqrt{\left(\frac{\sigma H}{H}\right)^2 + \left(\frac{\sigma T}{T}\right)^2}$$

where σH is given by the sum of vertical errors,

$$\sigma H = \sqrt{Se^2 + Sle^2 + RMS^2}$$

and include the 5-m uncertainty in absolute sea level (sle) (Rohling et al., 2009), error estimates of the shoreline angle elevations (she), and the RMS from the LEM; we also propagate an arbitrary 5 ka as error of the estimates in sea-level correlations (σT).

5.4 Results

5.4.1 Submarine geomorphology of the Arauco Bay

The Arauco Bay area comprises two domains characterized by different morphology and depth distribution of shoreline angles and high-roughness areas identified by the SCM: an Eastern Domain centered at the Arauco Bay (AB) and to the coast off Coronel; and a Western Domain, centered on the Santa Maria Island (SMI) reaching the edge of the continental slope (Fig. 5.4A).

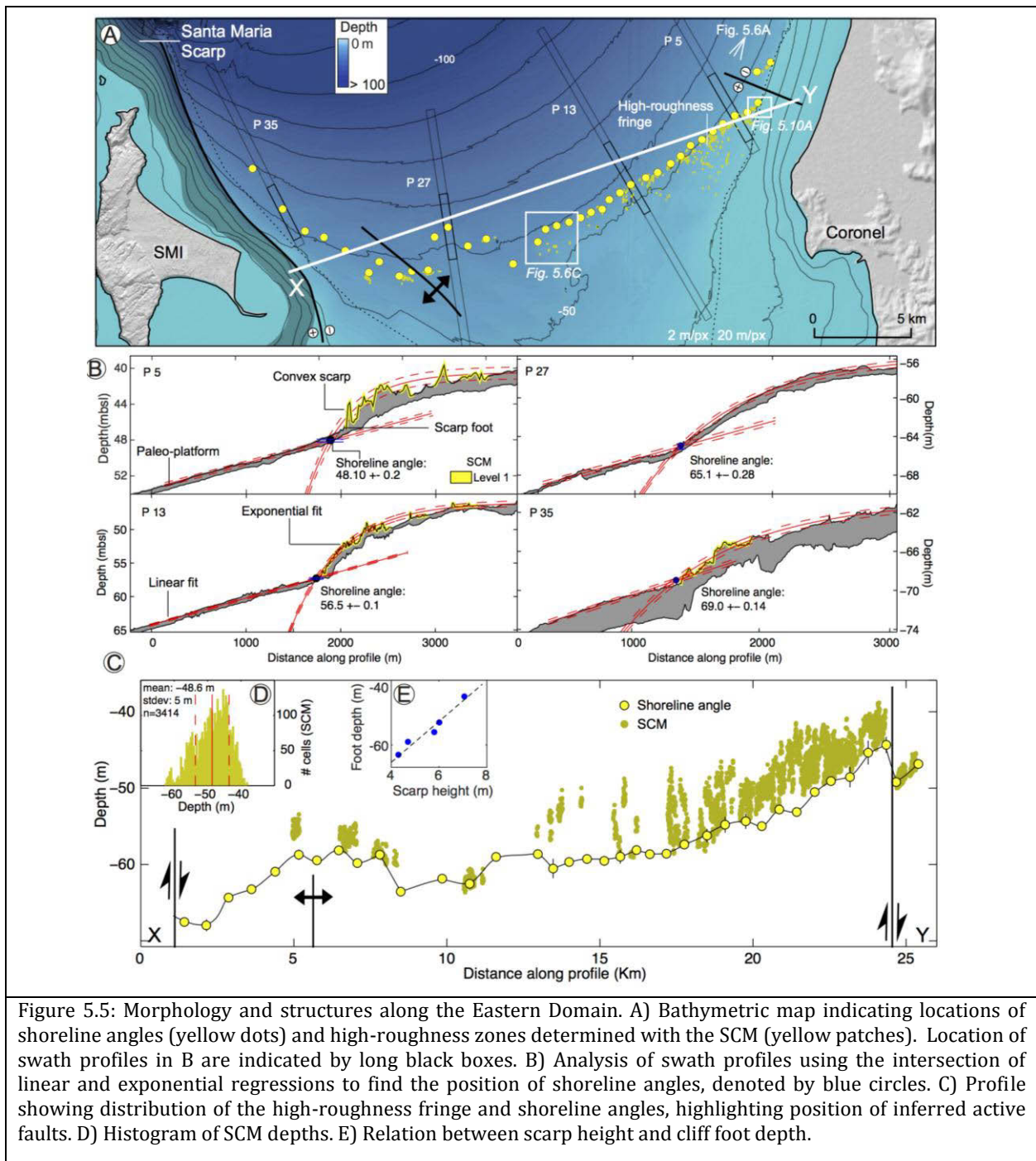


Figure 5.5: Morphology and structures along the Eastern Domain. A) Bathymetric map indicating locations of shoreline angles (yellow dots) and high-roughness zones determined with the SCM (yellow patches). Location of swath profiles in B are indicated by long black boxes. B) Analysis of swath profiles using the intersection of linear and exponential regressions to find the position of shoreline angles, denoted by blue circles. C) Profile showing distribution of the high-roughness fringe and shoreline angles, highlighting position of inferred active faults. D) Histogram of SCM depths. E) Relation between scarp height and cliff foot depth.

The smooth and northward-dipping surface of the Eastern Domain is disrupted by an E-W oriented, ~25-km-long arcuate fringe spanning the entire center of the bay between Coronel and SMI (Fig. 5.4A and 5.5A). In profile view, the fringe represents a submarine scarp that separates the bay into an area with a southward- ($\sim 0.25^\circ$) and a northward-inclined slope ($\sim 0.5^\circ$), respectively. The surface morphology of the fringe comprises clustered rough patches detected by the SCM and defined as Level 1; eastwards these patches enclose irregular positive bathymetric features of 8 to 15 m height bounded by small polygonal scarps forming isolated columnar features sculpted into hard substrate and resembling erosional structures developed on scarp faces (Figs. 5.6A and 5.6B). To the west the scarp trace is less irregular and its surface is smoother comprising scattered rocky outcrops (Fig. 5.6C). Depths of the Level 1 high-roughness patches follow a Gaussian distribution with a mean at 48.6 mbsl and standard deviation of 5 m (Fig. 5.5D), suggesting the presence of a distinct, single terrace level.

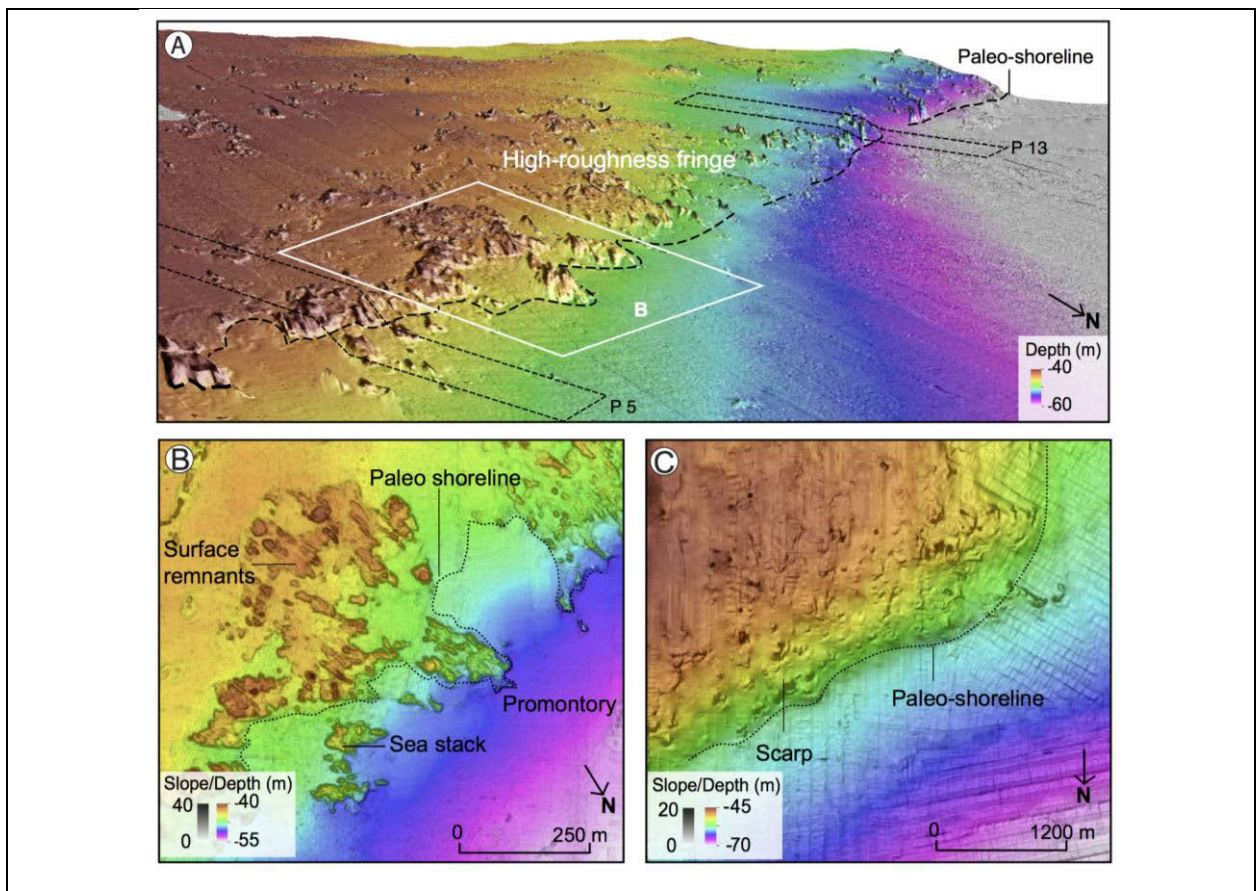


Figure 5.6: Examples of geomorphic features associated with drowned shorelines along the Eastern Domain. A) Perspective view of the arc-shaped scarp denoting the high-roughness fringe that traverses the Arauco Bay (location in Fig. 5.5A). Note the increase in depth of the cliff foot trace to the west. Dashed black rectangles indicate location of swath profiles in Fig. 5.5B. B) Shaded bathymetry near the mainland off Coronel, where the high-roughness fringe has a rather irregular scarp comprising stacks, promontories, and rocky outcrops. C) Shaded bathymetry near the center of the bay showing the notorious linear trace of the scarp and sharp character with smooth surface and scattered rocky outcrops.

A total of 38 swath profiles were analyzed along the high-roughness fringe obtaining shoreline angles between 43 and 69 mbsl; the maximum depths of all swath profiles display a convex scarp formed by several peaks that emerge from the smooth surface of AB. Here, shoreline angles are

generally located in close association with the surface, suggesting the absence of significant diffusion processes. Considering its morphology and continuous trace, the fringe resembles a partly eroded sea-cliff bounded by isolated bathymetric peaks resembling sea-stacks and promontories (Fig. 5.6B).

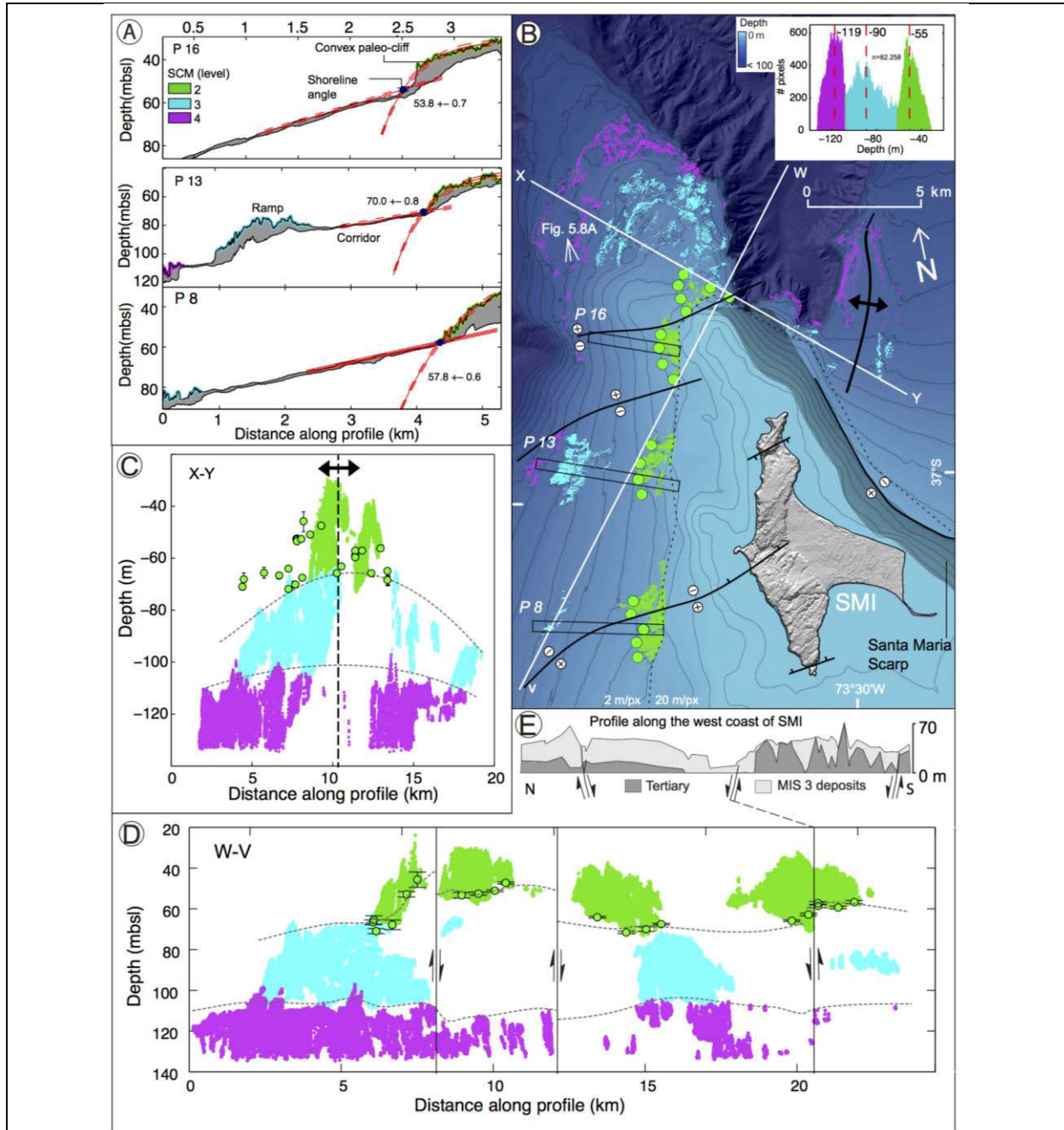


Figure 5.7: Morphology and structures along the Western Domain. A) Swath profiles located along the western coast of Santa Maria Island. High roughness areas define three distinct levels between 40 and 120 mbsl. B) Shaded bathymetry indicating location of drowned shorelines angles (green dots), high-roughness areas (color coded by depth), active structures. Inset shows depth distribution of high-roughness areas. Note the three peaks associated with distinct shoreline levels. C) NW-SE oriented profile showing depth of the high-roughness areas, shoreline angles, and the projected axis of the western anticline. D) NNE-SSW oriented profile showing distribution of high-roughness areas, shoreline angles, and inferred active faults. E) N-S geologic profile along the western coast of Santa Maria Island after Melnick et al. (2012).

The Santa Maria scarp is a well-developed feature that separates the deep and smooth bathymetry of AB from the shallow area that surrounds SMI (Fig. 5.9A). The scarp has a steep slope of $\sim 35^\circ$ and a linear trace, and its height increases progressively northward reaching 100 m north of SMI (Fig. 5.9B). We studied this scarp using 6 swath profiles, recognizing aligned rocky outcrops between 90 and 130 mbsl at the scarp foot, extending ~ 6 km northward of SMI towards the shelf edge. In this area, zones of high-roughness highlight the flanks of a north-plunging anticline whose hinge has been eroded. The core of the anticline likely exposed weaker strata that were subsequently removed by wave erosion.

The Western Domain, west of SMI, consists of a smooth and westward-inclined surface ($\sim 0.9^\circ$ slope) disrupted by rocky outcrops at different depths rising from the rather flat adjacent seafloor and partly covered by sediments towards the north (Fig. 5.8A). The rocky outcrops consist of deformed and densely fractured sedimentary units of inferred Tertiary age (based on their similarity with exposed platforms onshore), characterized by high surface roughness confidently classified by the SCM (Fig. 5.8b and 5.8C). The depth distribution of these outcrops is polymodal characterized by three sharp bands at 119, 90, and 55 mbsl (Fig. 5.7B), representing a staircase sequence of drowned shorelines defined as levels 4, 3, and 2, respectively.

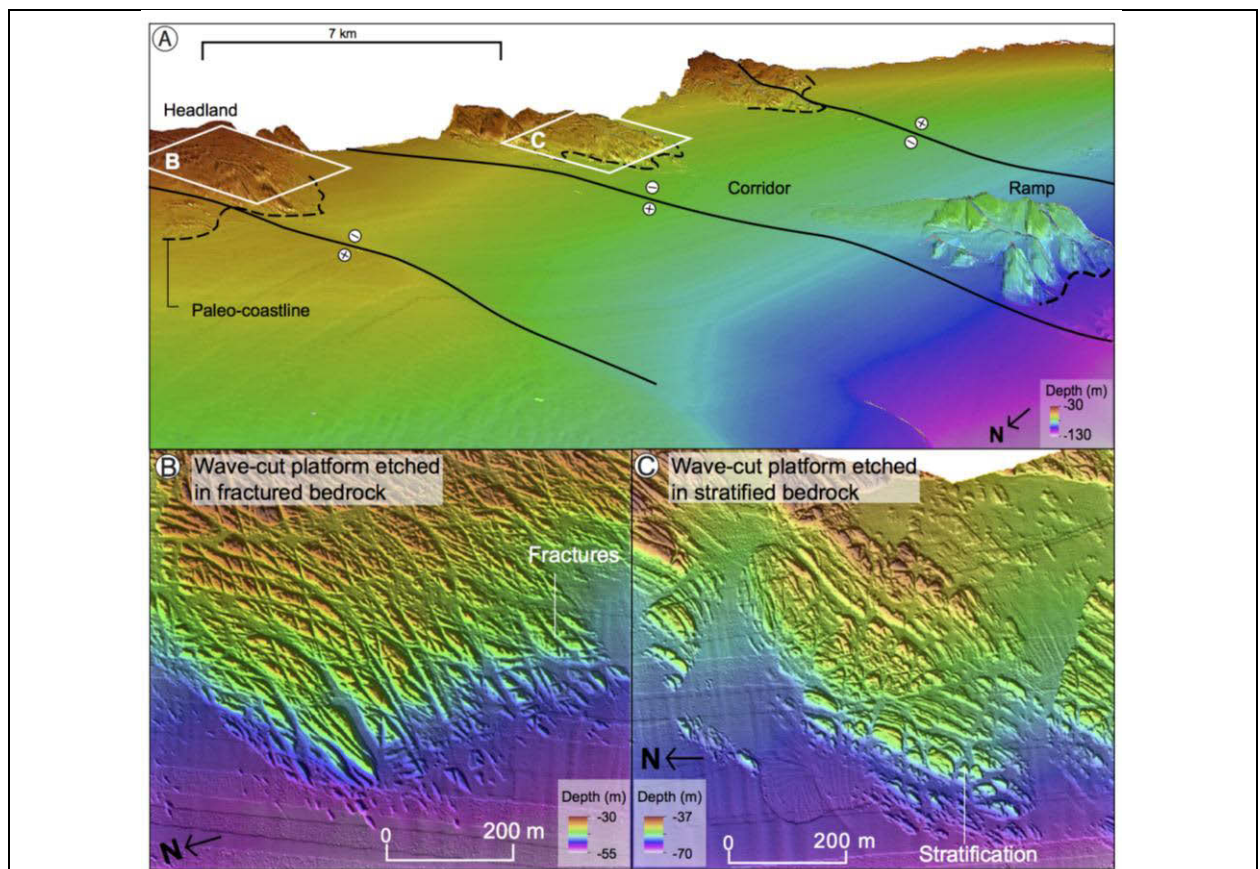
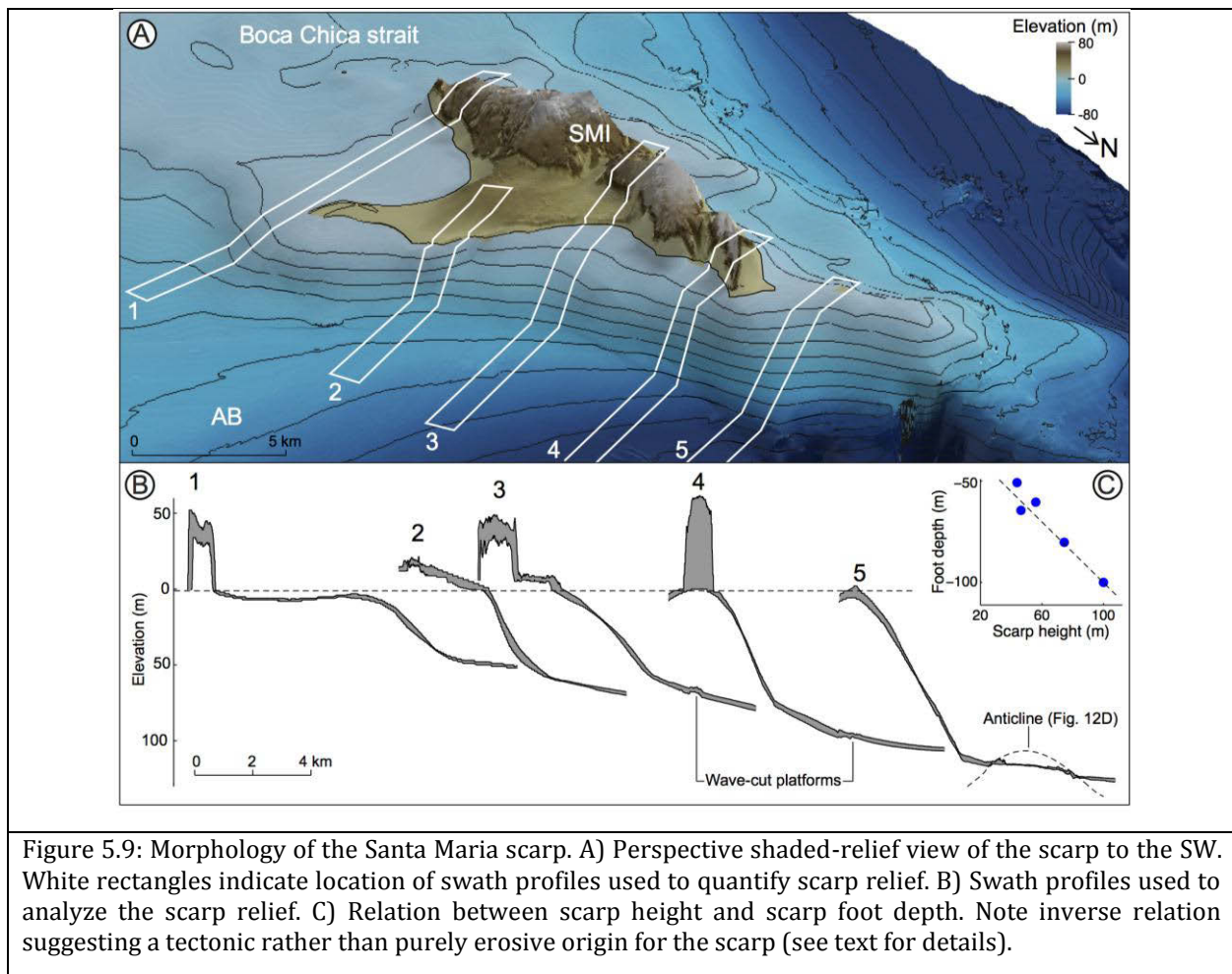


Figure 5.8: Examples of geomorphic features associated with drowned shorelines along the Western Domain. A) Perspective view of the three isolated promontories formed by outcrops of probable Tertiary bedrock depicting remnants of a drowned scarp. Black lines indicate positions of active faults (See text for details). B) and C) shaded-relief maps highlighting the morphology of abrasion platforms and scarps sculpted in deformed and pervasively fractured Tertiary sedimentary rocks. These drowned features resemble exposed platform along rocky coasts bordering the Arauco Bay Area.

We analyzed these levels with 22 swath profiles. The uppermost level 2 comprises high-roughness convex scarps distributed in three main N-S aligned rocky outcrops (Fig. 5.8A); the scarps intersect a smooth platform covered by sediments south of SMI with shoreline angles between 70 and 45 mbsl. The abrasion platform of Level 2 is disrupted by corridors and ramps (Figs. 5.7A and 5.8A), which are typical features of wave-cut platforms developed in high-energy coasts (e.g. Twidale et al., 2005). Level 3 comprises the central band of high roughness, a broad platform at ~90 mbsl extending northwest of SMI formed by rocky outcrops partly covered by weak sediments. Immediately west of SMI this level is represented by a pronounced cliff sculpted in the bedrock (Fig. 5.8A). The lower level 4 is formed by scattered patches of high roughness reaching ~120 mbsl, bounded by a small scarp and widening north of SMI. Differential erosion processes capable of truncating bedrock stratification are expected to occur only at shallower depths, associated with the effect of wave abrasion that generates wave-cut surfaces. The similarity of these drowned surfaces with active wave-cut platforms nearby (See Appendix D.1), suggests that these features were developed a few meters below sea-level.



5.4.2 In-situ observations at drowned shorelines

ROV imaging and sampling were performed along an elongated and pristine-looking sea-stack facing the seaward edge of the AB fringe (Fig. 5.10A). We started the ROV dive from the top of the structure at 38 mbsl, continuing downward toward its base at 44 mbsl (Fig. 5.10A).

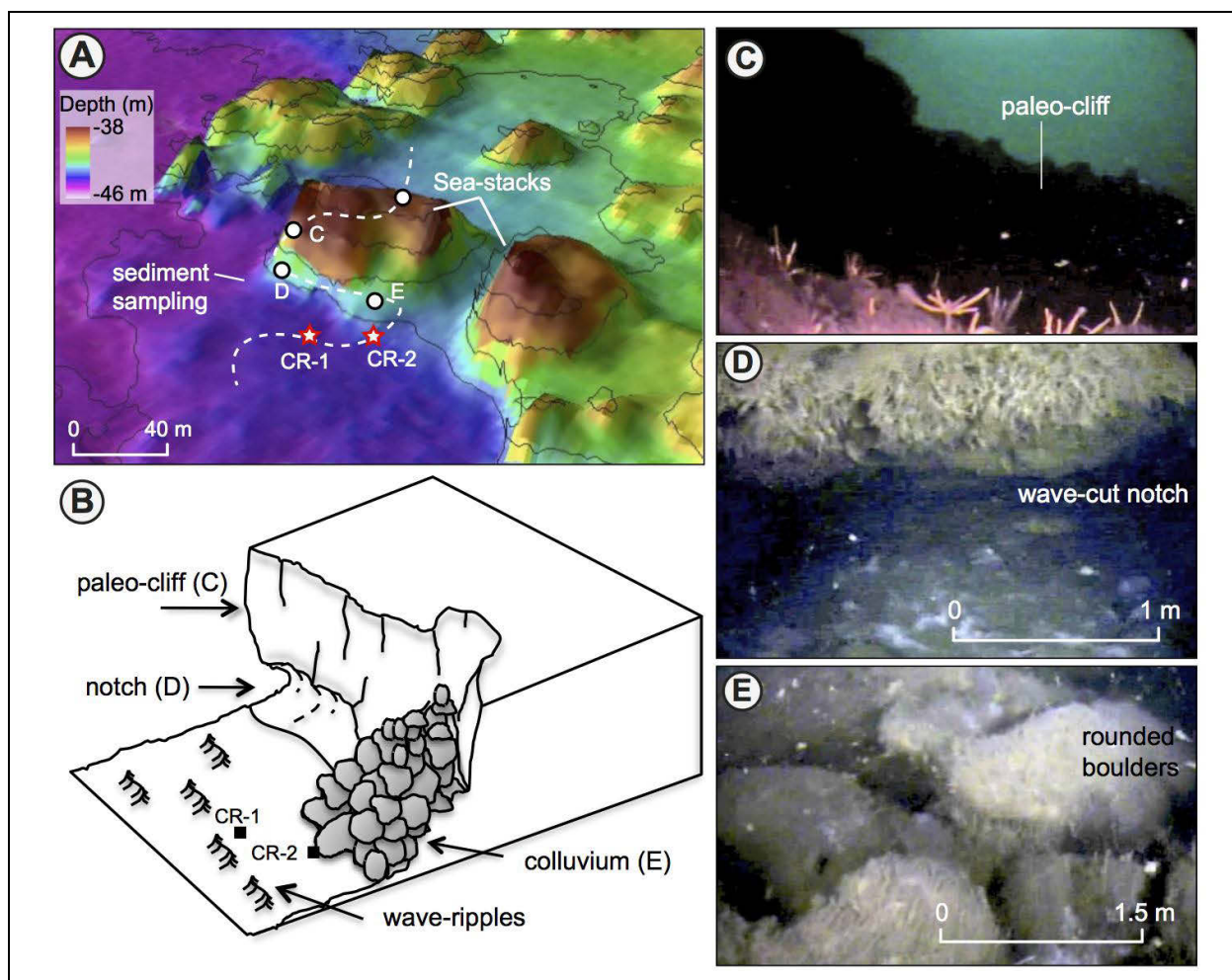


Figure 5.10: In-situ observations of a drowned shoreline features at a dive site in the Eastern Domain. A) Perspective shaded-relief map showing path and location of observations made with a Remotely Operated Vehicle (ROV), and sites CR-1 and CR-2 where professional divers collected samples of rocks and sediments. B) Schematic representation of the in-situ observations made with the ROV. C) Submarine photo made with the ROV of the drowned paleo-cliff looking upwards from the bottom. D) Submarine photo of a wave-cut notch at the base of the cliff. E) Photo of rounded boulders at the base of the cliff, likely deposited by partial localized collapse of the cliff.

The stack top is flat and covered by brown algae and bounded abruptly by a 7-m-high steep cliff with a $\sim 70^\circ$ slope (Fig. 5.10A and 5.10C) sculpted into poorly lithified black sandstone as suggested by fragments collected from the foot of the cliff (Figs. 5.11B and 5.11C). The foot of the cliff is covered by a chaotic deposit that includes rounded and angular boulders reaching a maximum diameter of 2 m that likely constitute colluvial wedge material (Figs. 5.10B and 5.10E). The sea floor adjacent to the foot of the cliff below 46 mbsl is covered by sand with decimetric-scale wave-ripples, which we sampled for granulometric analysis (Fig. 5.11A). At one location the cliff has apparently not yet collapsed and its internal part is exposed revealing a cavity sculpted at its base that we interpret as a wave-cut notch (Fig. 5.10B and 5.10D); the notch is a sharp, well expressed feature with ~ 50 cm height and ~ 70 cm length. The presence of a notch at the base of the cliff suggests that these drowned geomorphic features were formed by wave erosion associated with past sea-level positions.

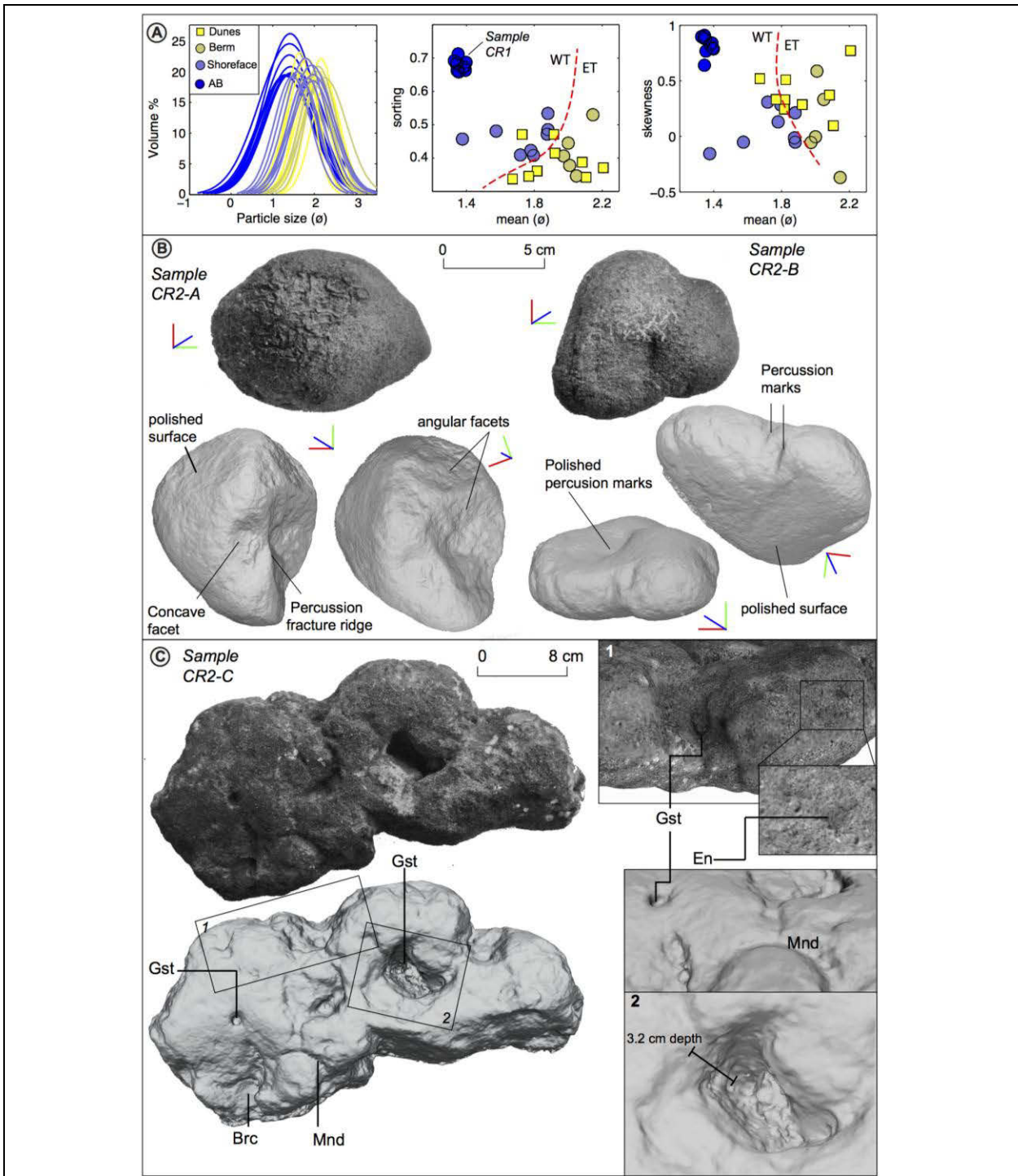


Figure 5.11: Sedimentological and morphoscopic analysis of submarine samples from the dive site. A) Cumulative distribution curves and scatter plot of statistical parameters of submarine sand samples from the dive site and from the active environments sampled at Santa Maria Island (from Jara-Muñoz and Melnick, 2015), which include berms, shorefaces, and active dunes. B) Photos and shaded-relief models constructed with structure-from-motion illustrating the surface morphology of small cobbles collected from dive site CR2. Note the multiple impact marks and polished surfaces. C) Photos and shaded-relief models illustrating the surface morphology of the largest recovered cobble from the dive site. Note marks interpreted as types of bioerosion, likely associated with different ichniospecies including *Meandropolydora* (Mnd), *Gastrachaenolites* (Gst), and *Entobia* (En). Brc: alive brachiopods. See text for details.

We compared the mineralogy and grain-size distribution of the samples collected from the AB with those of modern environments at SMI. The mineralogy of sample CR-1 obtained at 46 mbsl is identical to shoreface, berm, and backshore samples from active environments at SMI (Jara-Muñoz and Melnick, 2015). The AB samples comprise non-lithified black volcanic sands with a mean grain size of 1.35ϕ (Fig. 5.11A), containing ~2% of bioclastic content of barnacle fragments and small living brachiopods. Fig. 5.11A shows the relation between skewness and sorting with respect to the mean grain size. From these plots two distinct groups can be clearly differentiated and associated with eolian and water-transported sediments; the latter includes sediments deposited near or immediately below the shoreline driven by wave action, whereas the former comprise sediments from active dunes. In both cases, the AB samples are located within the water-transport group, but separated from the ISM samples due their overall coarser grain sizes (Fig. 5.11A). Although the grain-size distribution curves of all samples are well constrained to a relatively-sharp range between 0 and 3ϕ , the mean grain size of the AB samples is slightly coarser, probably because these sediments were either derived from a proximal source or they were associated with a higher energy depositional environment, such as at the shoreface.

Three cobbles and four pebbles were collected at 44 mbsl from the lower sector of the colluvial wedge (Fig. 5.10B and 5.10E). The fragments range in size between 6 and 30 cm; they have low sphericity, are sub-rounded to rounded, and have polished surfaces with impact marks (Fig. 5.11B). A 3D digital model of CR2-A sample shows the smooth surface intersected by a concave facet bounded by a muted percussion fracture ridge, which outlines a structure analogous to a partial Hertzian cone (e.g. Whittaker, 2010) generated by a strong impact against another fragment or bedrock. Sample CR2-B is a flattened cobble with a smooth surface disrupted by minor percussion marks (Fig. 5.11B), some partly polished indicating some degree of reworking after the impact. The coexistence of cobbles with rounded facets and surfaces is usually generated by mechanical attrition in relatively high-energy environments, such as along rocky shorelines frequently impacted by recurrent storms.

We searched for biological evidence of past sea-level positions at the surface of the biggest cobble collected at 44 mbsl. The 35-cm-diameter cobble is asymmetric with one side of concentrated borings that are typically formed by bioerosion. These cavities have a circular shape at the surface, becoming irregular at depths toward the main chamber. The diameter of these vertical borings varies from 1 to 3 cm, reaching 0.5 to 1.8 cm depth (Fig. 5.11C). The most notorious cavity is analogous to those generated by dwelling boring organisms such as *Gastrochaenolites* isp. (bivalves) (Leymerie, 1841) (Fig. 5.11C). Small borings of 2-3 mm diameter show chambers of rounded and irregular shape, tentatively correlated with borings of *Entobia* isp. (sponges) (Pleydell and Jones, 1988; Perry, 1996). Another structure related to boring organisms consists of cylindrical galleries parallel to the surface of the sample resembling marks produced by *Meandropolydora* isp. (polychaetes and barnacles) (Bromley and D'Alessandro, 1983) (Fig. 5.11C). Due to the poor preservation of borings and lack of shell remains, an accurate taxonomic identification at the level of species was not possible. However, modern *Gastrochaenolites* communities are distributed at depths above 10 mbsl according to Bromley (1994), and Bromley and D' Alessandro (1987) constrained the association of *Gastrochaenolites*, *Meandropolydora*, and *Entobia* to a depth range between 1 and 2 mbsl in limestone cliffs of the Mediterranean coasts. Together these observations strongly suggest that the drowned geomorphic features along the AB fringe were formed near a former sea-level position and represent a paleo-shoreline.

5.4.3 Distribution of uplift rates inferred from drowned shorelines

To estimate uplift rates from drowned shorelines we compared swath profiles with LEM results. We first calibrated the LEM with two sensitivity simulations to evaluate the factors that favor the preservation of drowned shorelines and their different levels (Fig. 5.12).

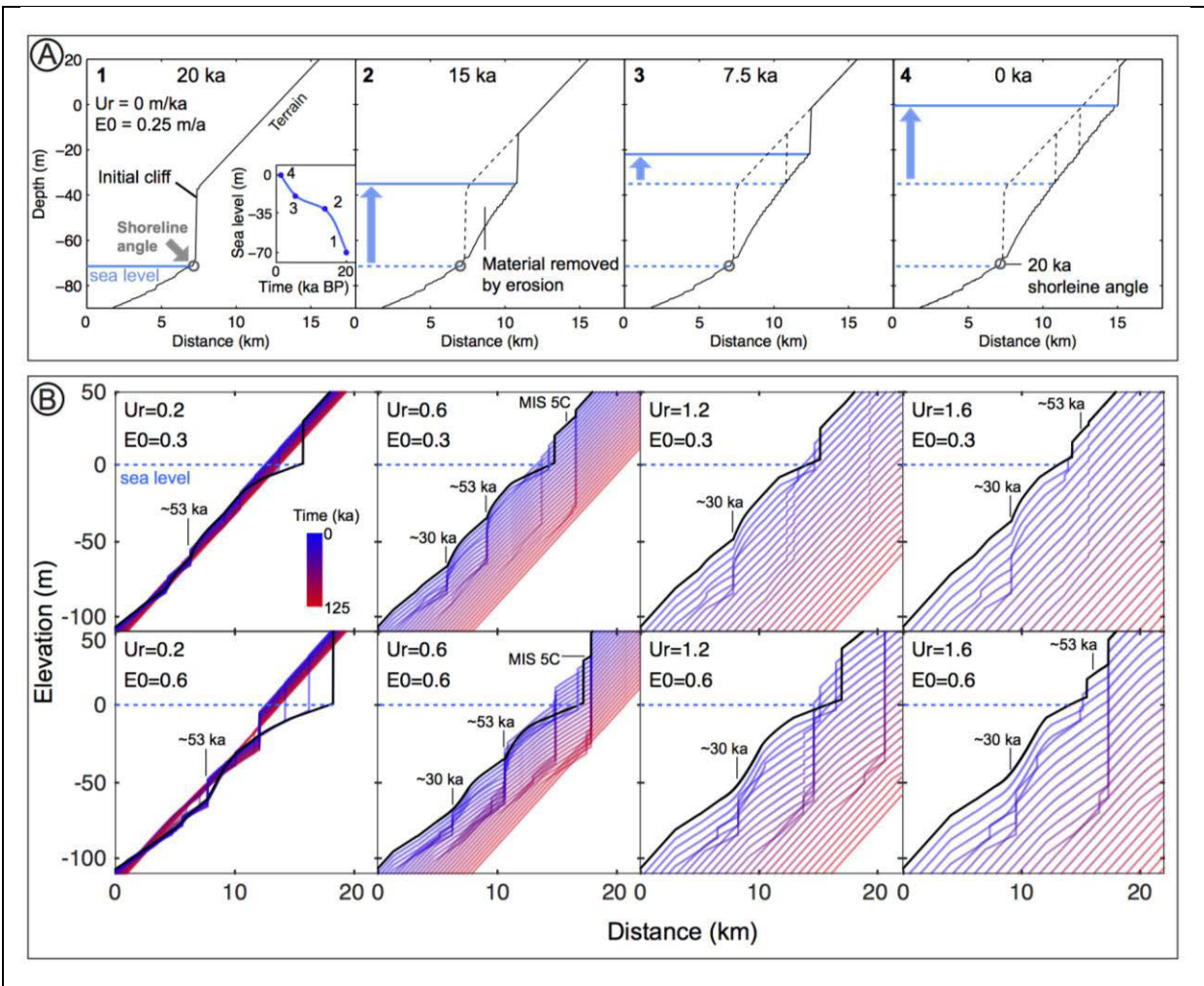


Figure 5.12: Landscape Evolution Model of wave erosion under oscillatory sea level and steady tectonic uplift. A) Synthetic simulation to evaluate the preservation potential of a drowned wave-cut cliff scarp after a flooding episode. Models start with an initial cliff at 20 ka etched in the terrain. Inset displays a synthetic trajectory of sea-level rise divided in 4 episodes, surface uplift is not considered. The circle indicates the location of the shoreline angle through each time step, preserved as a smoothed slope inflection after flooding. B) Sensitivity simulations of the model to variable uplift rate (U_r) and initial erosion rate (E_0), highlighting distinct levels with higher preservation potential. A sea-level history spanning the past 125 ka was compiled from Siddall (2003) and Rohling et al. (2012). Colored curves show evolving bathymetry with time. The age of modeled drowned shoreline levels in this study is indicated.

The first sensitivity simulation started at 20 ka with a synthetic terrace bounded by a 30-m-high sea cliff affected by rapid flooding under a simulated sea-level rise, with a low initial cliff erosion rate (0.25 m/a) and no tectonic uplift (Fig. 5.12A). The experiment shows that such a rapid flooding may produce sufficient erosion to smoothen the original cliff morphology generating a

convex profile analogous to those observed along the drowned shorelines at SMI and AB (Figs. 5.5B and 5.7A). Small changes in the rate of sea-level rise, as those simulated for the interval between 15 and 7.5 ka (Fig. 5.12A) results in negligible effects on the profile bathymetry. We recognize a slope inflection preserved at the intersection between the flat and the convex slopes, which marks the original location of the terrace shoreline angle before flooding and that may be thus correlated with a specific sea-level position.

The second calibration experiment focused on the temporal evolution of drowned shorelines using the two stacked sea-level curves (Section 3.3), exploring the contribution of initial erosion rate (E_0) and uplift rate (U_r) on surface morphology. Eight scenarios for the preservation of drowned marine terraces are shown in Fig. 5.12B. The initial geometry of the model comprises a 25-km-long plane with a slope of 0.5° and a wave base of 12 m, as estimated from satellite altimetry (Section 3.3). Our results show that two levels (~ 53 and ~ 30 ka) have the highest potential to be preserved, with different expression depending on the initial cliff erosion and uplift rates (Fig. 5.12B). A relatively high initial cliff erosion rate (0.5 m/a) results in more pronounced, wider terrace levels, whereas lower rates (0.25 m/a) result in smoothed levels located slightly farther inland. We compared the sensitivity to different uplift rates by increasing its value from 0.2 to 1.6 m/ka with 0.4 m/ka increments. At the lowest uplift rates only one sharp slope inflection is formed by reoccupation at 30 ka and 53 ka; as the uplift rate increases, two distinct levels form in normal arrangement with the youngest level located deeper than the oldest one. At the highest uplift rate, the 53 ka level rises above sea level and is preserved as an uplifted marine terrace. This is analogous to the setting at SMI characterized by rapid uplift at ~ 1.5 m/ka that results in exposure of the ~ 53 ka wave-cut platform at elevations between 0 and 30 masl.

At ISM, the deposits that cover the ~ 53 ka platform include a lower marine unit covered by eolian sediments deposited until ~ 30 ka, suggesting that the coastline was at lower position and distant from the island. Based on these field observations, we correlate the shallower drowned shoreline mapped off the western coast of SMI with the ~ 30 ka level reproduced by the LEM. On the other hand, the AB is characterized by a single distinct drowned shoreline level with the deepest shoreline angles, suggesting that it has experienced less uplift than SMI. Therefore, we correlate the drowned AB shoreline angles with the ~ 53 ka terrace level produced by the LEM simulations with lower uplift rates (0 – 0.4 m/ka).

The range in uplift and initial erosion rates obtained from the sensitivity models was used as an input parameter to estimate the best-fitting model that reproduced the minimum depth of each bathymetric swath profile. We compared 130,000 model runs for the total of 61 swath profiles. Figure 13A-D shows examples of model fits and their associated RMS; all profiles can be found in the Supplementary Materials (See SP2).

The best-fitting models have relatively low RMS values between 0.4 to 6.6 m, suggesting robust results for most, but 4 profiles from the Western Domain, which we considered outliers that were discarded due to their anomalously high RMS (Fig. 5.13E). The best-fitting initial cliff-erosion rate ranged between 0.1 and 0.6 m/a increasing towards the center of the AB, and with slightly higher, but more scattered values west of SMI. The resulting uplift rates follow a similar trend as the depth, ranging between -0.1 and 0.4 m/ka across the AB and between 0.3 and 1.3 m/ka around SMI (Fig. 5.16), with associated errors between 0.07 and 0.13 m/ka.

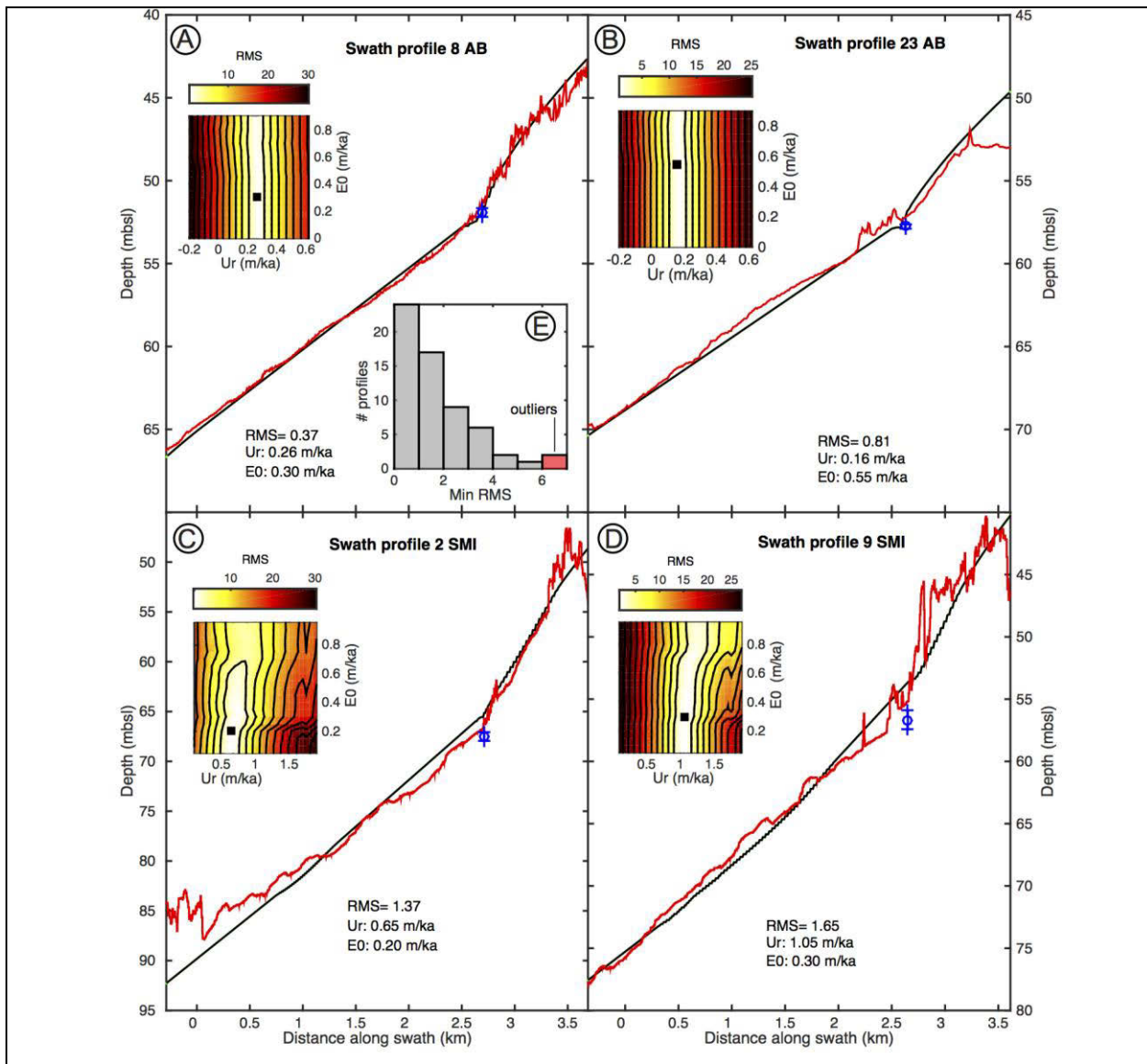


Figure 5.13: Examples of forward model results showing comparisons between bathymetric swath profiles extracted from the multibeam data and modeled with the Landscape Evolution Model. A) and B) show examples from the Eastern Domain. C) and D) are from the Western Domain. Inset shows Root Mean Square (RMS) space with 2.5 contour lines. Note lack of dependence on initial erosion rates and strong dependence on uplift rate.

5.4.4 Active structures in the Arauco Bay area mapped from multibeam bathymetry

To link the pattern of uplift rates inferred from the drowned shorelines with the mapped faults in the area, we projected the SCM and shoreline-angle depths along different profiles perpendicular to the structures mapped from the high-resolution bathymetry (Figs. 5.5C, 5.7C-D, and 5.14A).

Along the Eastern Domain both SCM and shoreline-angle depths increase progressively westward from 38 to 69 mbsl delineating a ~20-km-wide synform, which is locally disrupted by minor faults at the central and eastern parts of the bay (Fig. 5.5C). Immediately east of SMI the shoreline angles are locally warped about a ~10-m-high and ~7-km-wide anticline that slightly offsets the trace of the drowned shoreline. Towards the east along the coast off Coronel the depth of shoreline angles

decreases continuously and at the easternmost parts of the bay they are locally offset ~6 m by a NW-SE striking fault (Figs. 5.5A and 5.5C).

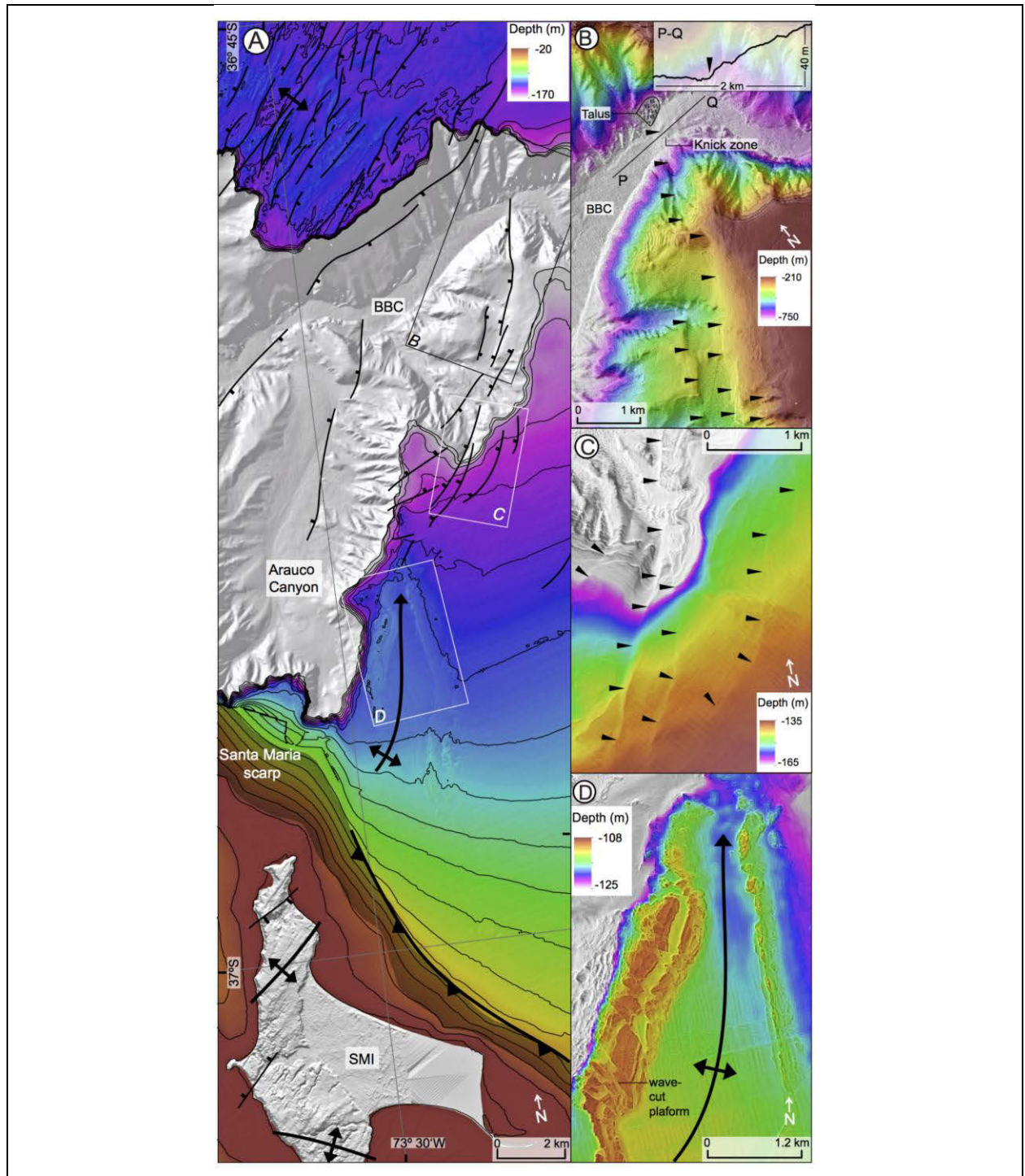


Figure 5.14: Active structures inferred from multibeam bathymetry north of Santa Maria Island (SMI) into the Bio-Bio Canyon (BBC). A) Shaded-relief map showing distribution of active structures. B) Detailed view of graben structures near the Bio-Bio Canyon. Inset shows talweg profile P-Q displaying a sharp knickzone associated with the intersection of normal faults with the canyon bottom. C) View of curved normal faults forming a transfer zone between the graben and anticline to the south. D) View of northward-plunging anticline outlined by deformed outcrops of Tertiary. The anticline axis merges southwards with the Santa Maria scarp.

At the Western Domain we projected shoreline angles and SCM depths along two profiles to assess warping patterns and to estimate vertical displacements by local faults (Fig. 5.7B). The WNW-ENE oriented profile (Fig. 5.7C) reveals a ~15-km-wide antiform delineated by all of the drowned shoreline levels; the hinge of this anticline is parallel to the NNE-SSW oriented tilt axis of the northern SMI (Melnick et al., 2006). Along the NNE-SSW oriented section, parallel to the axis of the anticline (Fig. 5.7D), the shoreline angles are displaced by three distinct faults. The southern fault offsets the shoreline angles by ~5 m as well as the SCM depths of the deeper levels. This structure may correspond to the offshore prolongation of a normal fault mapped at the center of SMI (Melnick et al., 2006). The two additional structures farther north offset the shoreline angles by 9 and 5 m, respectively, and may be similar to those mapped at the northern part of SMI (Fig. 5.7C).

The area located northeast of ISM including the eastern flank of the Arauco Canyon (Bernhardt et al., 2015) includes different deformed geomorphic features that we link with the surface expression of the main strands of the SMFS (Fig. 5.14A). Several NNE-SSW striking structures deform Tertiary bedrock platforms and the sea floor. A well-defined graben bounded by subparallel synthetic normal faults is found in the eastern part of the Arauco Canyon (Fig. 5.14B) at ~400 mbsl, with the east-bounding fault extending into the BBC where it controls the position of a prominent knickzone that offsets the canyon thalweg by 40 m, at 750 mbsl (Bernhardt et al., 2015). This structure is bounded to the south by a group of small curvilinear faults (Fig. 5.14C), which may constitute a transfer zone linking two anticlines that are separated by the Arauco and Bio-Bio canyons (Fig. 5.2 and 5.14A). These normal faults merge with the flank of a ~2-km-wide north-plunging anticline located immediately east of SMI (Fig. 5.14D). The anticline axis is oriented NNE-SSE and extends southward to the Santa Maria Scarp. Interestingly, the inverse relation between scarp height and cliff-foot depth along the Santa Maria Scarp (Fig. 5.9C) is opposite to the direct relation observed along the AB fringe (Fig. 5.5E). We explain the inverse relation with a continuous growth of the scarp by slip on the underlying SMFS (Fig. 5.9A and 5.14A), creating the observed relief.

5.5 Estimating fault-slip rates using dislocation models

5.5.1 Structural model setups

To link structural observations and estimate the millennial-scale slip rate of the SMFS, we used models based on dislocation theory in an elastic half-space (Okada, 1985). First we defined two contrasting structural scenarios: (1) deep-reaching reverse faults and shallow normal faults; and (2) deep-reaching normal faults. The first setup includes faults mapped in coal mines at Coronel (Wenzel et al., 1975), structures inferred from seismic reflection profiles in the AB and exposed at SMI (Gonzalez, 1990; Melnick et al., 2006; Melnick et al., 2012d), and inferred from displaced onshore marine terraces (Jara-Muñoz et al., 2015a). Although deep-reaching extensional splay faults have not been yet described in the Arauco Bay Area, Aron et al. (2013) proposed that long-term kinematics in the Maule segment is dominated by extensional structures that slip during megathrust earthquakes. Quaternary normal faults have indeed been described along the northern half of the Maule earthquake rupture (Jara-Muñoz et al., 2015a), including the Pichilemu normal fault that generated two M6.7 and M6.9 earthquakes 11 days after the Maule mainshock (Farías et al., 2011; Ryder et al., 2012). Allmendinger et al. (2013) questioned the interpretation of reverse slip along the SMFS during the 2010 event, and based on the model of Aron et al. (2013) propose

normal slip along the SMFS. In an attempt to test the hypothesis of Aron et al. (2013) for the long-term control of topography by repeated extensional faulting during megathrust earthquakes, we present a second model setup that includes exclusively normal faults.

5.5.1.1 Structural setup 1: Deep reverse faults and shallow normal faults

This model included the main NE-SW striking blind reverse fault (F1) associated with the $\sim 70^\circ$ -dipping plane of aligned crustal seismicity (Figs. 5.2 and 5.15A). F1 is formed by segments F1A and F1B that strike NNE-SSW and NNW-SSE, respectively (Fig. 5.15A), and for which we increased the dip between 55° and 80° (Table 5.1). We included two secondary reverse faults located at the rim of the AB: F3, a thrust that branches from F1 dipping between 30° and 40° to the west and linked with F1B at 5 km depth; and F4, a 30° north-dipping thrust located near Coronel and extending onshore associated at the surface with F10, a set of normal faults mapped in coal mines and that locally offset the drowned shorelines (Fig. 5.5C). We included five shallow normal faults, F5 to F9, located west of SMI following observations of shallow faulting in a seismic reflection profile parallel to the island and on outcrops along its western coast (Fig. 5.7E). We assigned dip angles of 80° to these structures and allowed for normal slip to reach the surface. Northwest of SMI a NNE-SSW oriented anticline interpreted from seismic profiles and observed in the high-resolution bathymetry (Melnick et al., 2012d; Bernhardt et al., 2015) has been included as F2 in the model with a dip of 85° and intersecting F1 at 7 km depth following the ramp-flat-ramp upper-crustal geometry (Fig. 5.1).

5.5.1.2 Structural setup 2: normal faults

We assumed that all structures of the setup 1 have extensional kinematics. We evaluated different scenarios by systematically varying the down-dip termination of the main fault to a depth between 12 and 23 km while always allowing slip to reach the surface; this configuration implies that the main splay fault is rooted in deeper parts of the plate interface than in the model setup 1. The secondary faults F2, F3, and F4 were modeled with dip angles of 80° , as the shallow normal faults in Model 1 (Table 1), but with down-dip depths reaching between 2 and 6 km. The updip extent of slip for faults F3 and F4 was limited to between 2 and 3 km, to better reproduce the deformation patterns in the central part of Arauco Bay.

Reverse and normal kinematics															
Scenario 1			Scenario 2			Scenario 3			Scenario 4						
ID	DDP	UPDP	SLR	DIP	RAKE	DDP	UPDP	SLR	DIP	RAKE	DDP	UPDP	SLR	DIP	RAKE
F1A	23	3	4.5	-80	90	12	3	4.5	-55	90	16	0	3.0	-80	90
F1B	23	3	5.5	-80	90	12	3	5.0	-55	90	16	0	3.7	-75	90
F2	6	2	3.0	-80	90	6	2	3.0	-80	90	6	2	3.2	-80	90
F3	5	2	1.2	-40	90	5	2	0.4	-30	90	5	2	1.2	-40	90
F4	8	3	1.0	-30	90	7	3	0.4	-30	90	8	3	0.4	-30	90
F5	2	0	1.2	80	-90	2	0	1.2	80	-90	2	0	1.2	80	-90
F6	2	0	0.7	80	90	2	0	0.7	80	90	2	0	0.7	80	90
F7	2	0	0.4	80	-90	2	0	0.4	80	-90	2	0	0.4	80	-90
F8	2	0	0.3	80	90	2	0	0.3	80	90	2	0	0.3	80	90
F9	2	0	0.5	80	-90	2	0	0.5	80	-90	2	0	0.5	80	-90
F10	2	0	0.3	-80	90	2	0	0.1	-80	90	2	0	0.1	-80	90

Normal fault kinematics															
Scenario 1			Scenario 2			Scenario 3			Scenario 4						
ID	DDP	UPDP	SLR	DIP	RAKE	DDP	UPDP	SLR	DIP	RAKE	DDP	UPDP	SLR	DIP	RAKE
F1A	23	3	2.0	80	-90	23	0	0.5	55	-90	16	0	2.0	80	-90
F1B	23	3	6.0	82	-90	23	0	0.5	55	-90	16	0	4.0	85	-90
F2	6	2	0.7	80	-90	6	2	0.7	80	-90	6	2	0.7	80	-90
F3	7	2	0.8	78	-90	6	2	0.8	75	-90	5	2	0.8	77	-90
F4	8	3	0.4	80	-90	8	3	0.4	80	-90	8	3	0.4	80	-90
F5	2	0	1.2	80	-90	2	0	0.8	80	-90	2	0	1.2	80	-90
F6	2	0	0.7	80	90	2	0	0.7	80	90	2	0	0.7	80	90
F7	2	0	0.4	80	-90	2	0	0.4	80	-90	2	0	0.4	80	-90
F8	2	0	0.1	-80	90	2	0	0.1	-80	90	2	0	0.1	-80	90
F9	2	0	0.5	80	-90	2	0	0.5	80	-90	2	0	0.5	80	-90
F10	2	0	0.3	80	90	2	0	0.3	80	90	2	0	0.3	80	90

DDP: Down dip (km) UPDP: Up dip (km) SLR: Slip rate (m/ka) DIP: (°) RAKE: (°) ID: Fault

Table 5.1: Parameters of elastic models.

5.5.2 Model results

We determined the model parameters that best reproduce deformation patterns revealed from uplift rates inferred at 57 sites from drowned and emerged shorelines by comparing the distributions of residual rates. Figure 5.15 shows the deformation patterns associated with three end-member scenarios to illustrate the effect of major changes in the input parameters as well as the preferred models for both structural setups. The results clearly show that the model setup 1, characterized by deep-reaching reverse faults and shallow normal faults, reproduces the observed deformation patterns better.

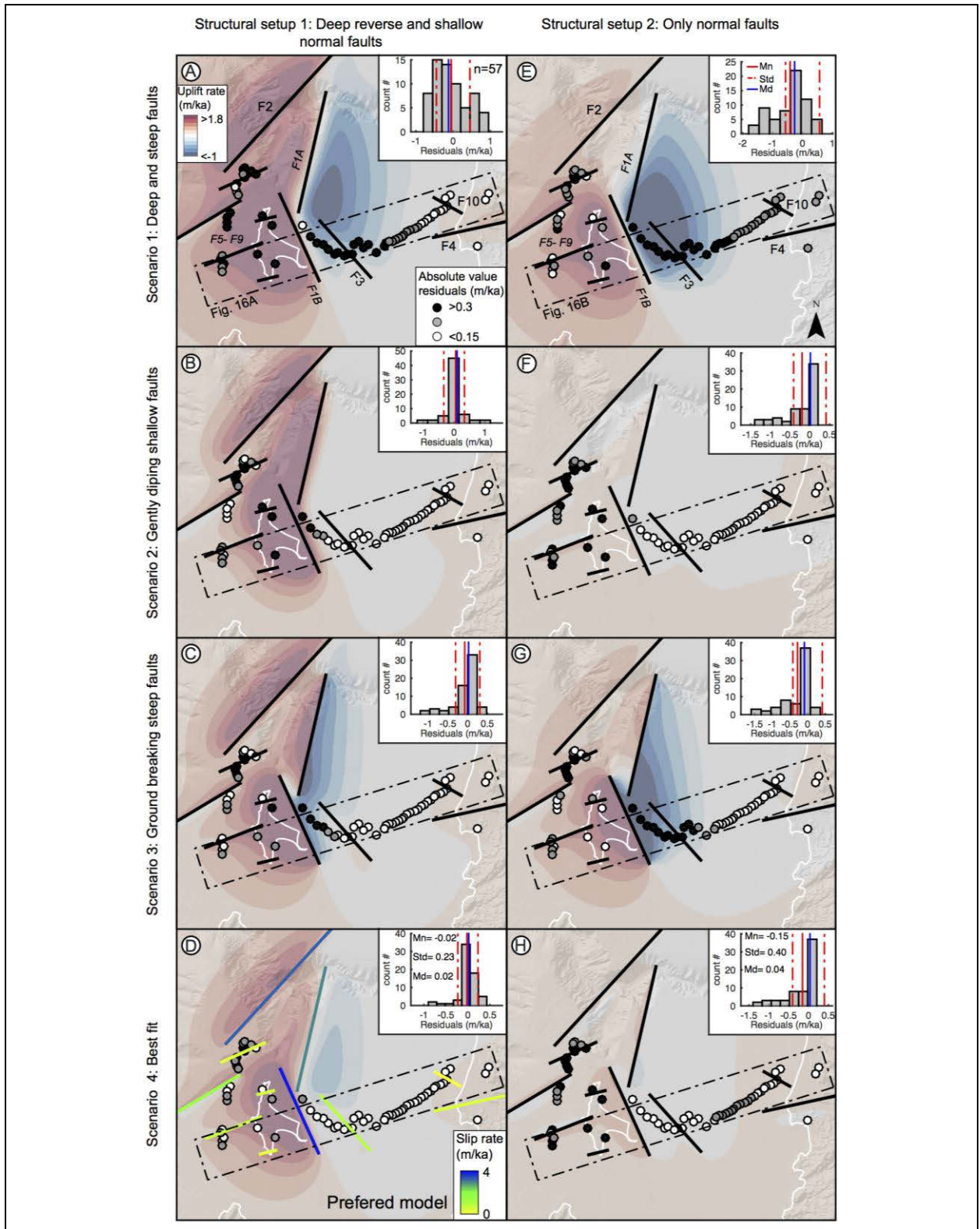


Figure 5.15: Uplift rates predicted by elastic dislocation modes. The two columns show model setups for deep reverse faults with shallow normal faults (left) and exclusively normal faults (right). Rows show different modeling scenarios for both setups. D) and H) are the preferred models for each setup. Black thick lines indicate the faults included in the model; Dots indicate drowned shorelines used to calculate residual uplift rates. Back dashed lines indicate the location of swath profiles in Fig. 5.16. Insets show histograms of residual uplift rates. Mn: Mean, Std: Standard deviation, Md: Median.

The first scenario shows deformation results produced by a steep (80° dip) and deep-reaching (23 km depth) F1 blind splay fault with a tip at 3 km. Both model setups fail to reproduce the wavelengths and overall deformation patterns across the AB (Figs. 5.15A and 5.15E). Anyway, such scenarios would require slip rates of 5 and 6 m/ka for each respective setup (Table 5.2). The second scenario includes a gently-dipping fault F1 (55° dip) with slip restricted to between 12 km and 3 km depth for setup 1, and to between 23 km and the surface for setup 2. Both setups reproduce moderately well the permanent deformation patterns across the AB requiring slip rates of 5 and 0.5 m/ka, respectively, but fail to reproduce the high uplift rate of SMI and the Western Domain (Figs. 5.15B and 5.15F). The third scenario includes a steeper (80°) and deeper (16 km) fault F1 with slip reaching the surface. These parameters provide a slightly better fit with the overall deformation patterns and uplift rates in both domains, requiring slip rates of 3.7 and 4.0 m/ka for reverse and normal kinematics, respectively. However, the wavelength of the synform across the AB is underestimated by both setups (Figs. 5.15C and 5.15G). Our preferred model includes a blind reverse splay fault dipping 80° that reaches the megathrust at 16 km depth and has a tip at 3 km depth, with a slip rate of 3.7 ± 0.2 m/ka. Secondary faults F3 and F4 require slip rates of 0.8 and 0.4 m/ka, respectively, to obtain residual uplift rates that are not significantly different from a normal distribution, with a standard deviation of 0.2 m/ka.

5.6 Discussion

5.6.1 Age and preservation of drowned shorelines in the Arauco Bay area

Vestiges of drowned Quaternary landscapes along the western coast of South America had been only described at Quintero, ~500 km north of AB, where archaeological remains recovered at 13 mbsl were dated to ~17 ka (Cartajena et al., 2013). Although these findings cannot be used to estimate a past sea-level position, their preservation suggests that the rapid sea-level rise episode after the LGM was fast enough to produce a minimum amount of erosion on the landscape as predicted by our LEM. However, other factors not accounted for by our simple 2D LEM may play a mayor role on the generation and preservation of drowned shorelines. For instance, it has been proposed that specific geomorphic scenarios such as bays, inlets, and island clusters may favor the preservation of submerged landscapes and paleo-shorelines (e.g. Faught and Gusick, 2011; Pedoja et al., 2014); a common paleo-geographic evolution corresponds to the emergence of an island, followed by its connection to the adjacent mainland (Pedoja et al., 2014). However, this progression would be the opposite for shorelines formed during lowstand periods such as those interpreted in the Arauco Bay area. The distribution of drowned shorelines north and south of SMI during MIS 3 outlines a N-S elongated peninsula that connected the island with the mainland extending toward Coronel. During MIS 2 most of the AB was emerged and the coastline was located ~34 km seaward of its current position (Bernhardt et al., 2015). Consequently, after MIS 2 the AB was flooded at a 1.8 m/yr mean horizontal rate of coastline migration. Therefore the 300- to 500-m-wide cliffs along the gentle slopes of the AB may have been drowned after only ~300 years of continuous sea-level rise allowing for the preservation of the observed geomorphic features. Considering the 0.1 to 0.3 m/yr mean cliff erosion rate obtained from the LEM (See Appendix D.3), the cliff would have eroded only between 30 and 90 m during the ~300-year-timespan. This relatively small amount of erosion, when compared to the width of the drowned cliff at AB, may have been crucial for the preservation of these drowned shorelines after the dramatic drowning episode that followed MIS 2.

5.6.2 Millennial-scale kinematics and slip rate of the SMFS

Two contrasting models have been proposed to link deformation during a single earthquake and integrated over several earthquake cycles at millennial timescales. Aron et al. (2013) proposed that faults favorably oriented to the distribution of coseismic slip might be reactivated as normal faults during megathrust earthquakes and may accumulate permanent upper-plate extension over several earthquake cycles. However, this model fails to explain the deformation patterns in the Arauco Bay area and the greater Arauco Peninsula, as deep-reaching active normal faults have not been yet described in this region. Along these lines, numerical experiments show that the upper-plate strain regime leading to reactivation of splay faults during megathrust earthquakes will mainly depend on the position of such faults with respect to the locus of plate-boundary slip (Melnick et al., 2013; Li et al., 2014). Because the SMFS is located at the seaward edge of the southern patch of slip during the 2010 Maule earthquake, it may well have been reactivated as a reverse fault. The similarity in tilt patterns observed in emerged Holocene beach ridges and measured during the 2010 earthquake may suggest that permanent deformation is accumulated during great megathrust earthquakes.

The elastic models developed in this study show that magnitudes of uplift rates derived from drowned shorelines may be reproduced with relatively low residual rates for both reverse and normal kinematics (Table 5.2); however, the choice of a preferred model based on residual rates is not straightforward when observations are not homogeneously distributed as in our study. Although residuals of model setups with normal kinematics are low on average, these models fail to reproduce the overall pattern of deformation (Fig. 5.16B), including both the high uplift rates at SMI and the syncline across the AB.

Table 5.2: Distribution of residual values of each elastic model

	Reverse and normal kinematics				Normal kinematics			
	Scenario 1	Scenario 2	Scenario 3	Scenario 4	Scenario 1	Scenario 2	Scenario 3	Scenario 4
Mean	-0.05	0.05	-0.07	-0.02	-0.42	-0.2	-0.29	-0.15
Median	-0.12	0.1	0.02	0.02	-0.26	0.02	-0.09	0.04
Standard deviation	0.45	0.34	0.31	0.2	0.57	0.41	0.42	0.4

Along the Eastern Domain, the synform delineated by drowned shorelines can be successfully reproduced in wavelength and uplift rates by our preferred reverse-fault model of setup 1 (Fig. 5.16A). In turn, the preferred normal-fault model adequately reproduces observations near the main fault (F1), but underestimates the wavelength of the syncline (Fig. 5.16B). Along the Western Domain the uplift patterns of both best-fit models are quite different. The reverse-fault model successfully reproduces the ~15-km-wavelength antiform in the Western Domain, whereas the normal-fault model fails to reproduce the high uplift rates at SMI.

We selected a preferred model of millennial-scale reverse kinematics that reproduces the magnitude of uplift rates with the lowest standard deviation of residual rates as well as the amplitudes and wavelengths of deformation patterns in both domains of the Arauco Bay area (Fig.

5.16A). This model suggests millennial-scale slip rates of 3.7 ± 0.2 m/ka and 3.0 ± 0.2 m/ka for the southern and northern branches of the SMFS respectively. The lineal dependence between fault-slip and surface uplift measured at SMI, suggests that both magnitudes can be directly compared (Fig. 5.17A), and represents an integrated mean value since MIS 3 when the drowned shorelines were abandoned.

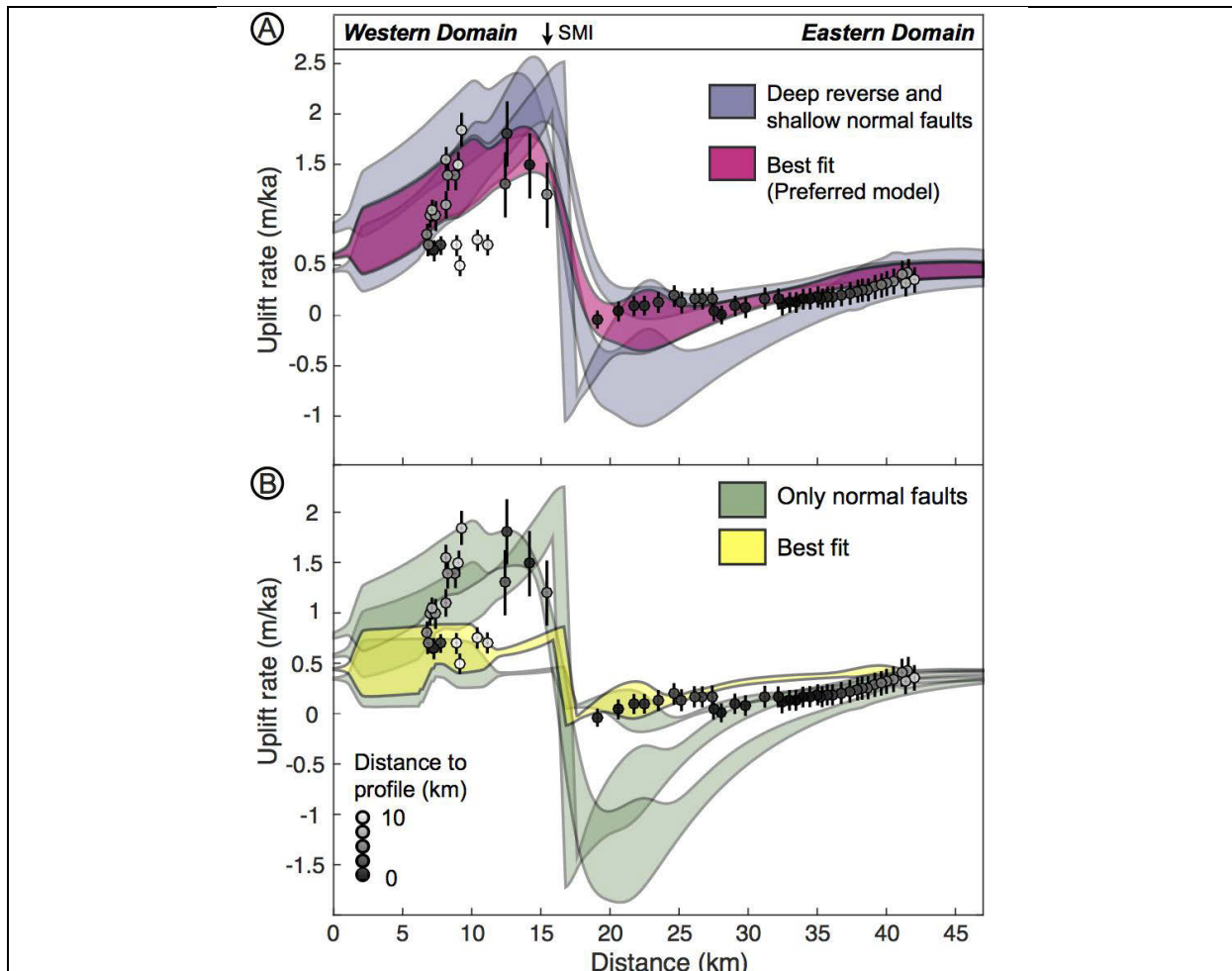


Figure 5.16: Stacked swath profiles of uplift rates from elastic dislocation model results in Fig. 5.15. Dots are uplift rates estimated from drowned shorelines. A) Reverse fault models. The preferred, best-fit model successfully reproduce observations at both domains. B) Normal fault models. Note that the best-fit model is unable to reproduce observations at the Western Domain and the overall warping pattern along the Arauco Bay Area.

5.6.3 Splay-fault slip during the megathrust seismic cycle

The pattern of permanent deformation across the Arauco Bay since MIS3 can be explained by slip along a system of high-angle reverse faults and secondary normal faults. Two $M \sim 4$ earthquakes were registered along the SMFS during the 3-month-long observation period of the ISSA network in the year 2000 (Fig. 5.1). However, no seismicity was recorded in this area by the TIPTEQ seismic network installed during one year in 2004-2005 (Haberland et al., 2005), highlighting the transient nature of the ISSA cluster. Therefore, part of the permanent deformation may be accrued during transient pulses of splay-fault slip driven by upper-plate contraction resulting from interplate interseismic locking. Moreno et al. (2008) used a limited number of campaign GPS measurements

to determine ~ 7 mm/yr of shortening across the SMFS during the interseismic period. However, the rate will depend on the fault geometry and the distribution of interplate locking, and these authors assumed unconstrained structures and uniform locking, which might introduce a significant bias.

The similarity between coseismic tilting during the Maule earthquake, tilt associated with emerged Holocene shorelines at SMI, and surface fault ruptures during the Maule earthquake, suggests that uplift of the island, and hence slip along the SMFS, occurs during megathrust earthquakes (Melnick et al., 2012d; Melnick et al., 2013). If we assume that slip along the SMFS occurs exclusively during such events, with a recurrence time of 150 to 200 years as determined from historical and geological observations (e.g. Lomnitz, 2004; Bookhagen et al., 2006), slip between 0.3 and 0.7 m per event would be required to account for the 3.7 m/ka millennial slip rate (Fig. 5.17B). However, if the SMFS slips only every ~ 1000 years, representing a few megathrust earthquakes, then a slip of ~ 3.5 m per event would be required to account for the long-term rate, which would be equivalent to a magnitude ~ 6.7 earthquake using the empirical relationships proposed by Wells and Coppersmith (1994). Such an event could constitute a secondary source for the tsunami resulting in shorter arrival times in the Arauco Bay area and higher local amplitudes.

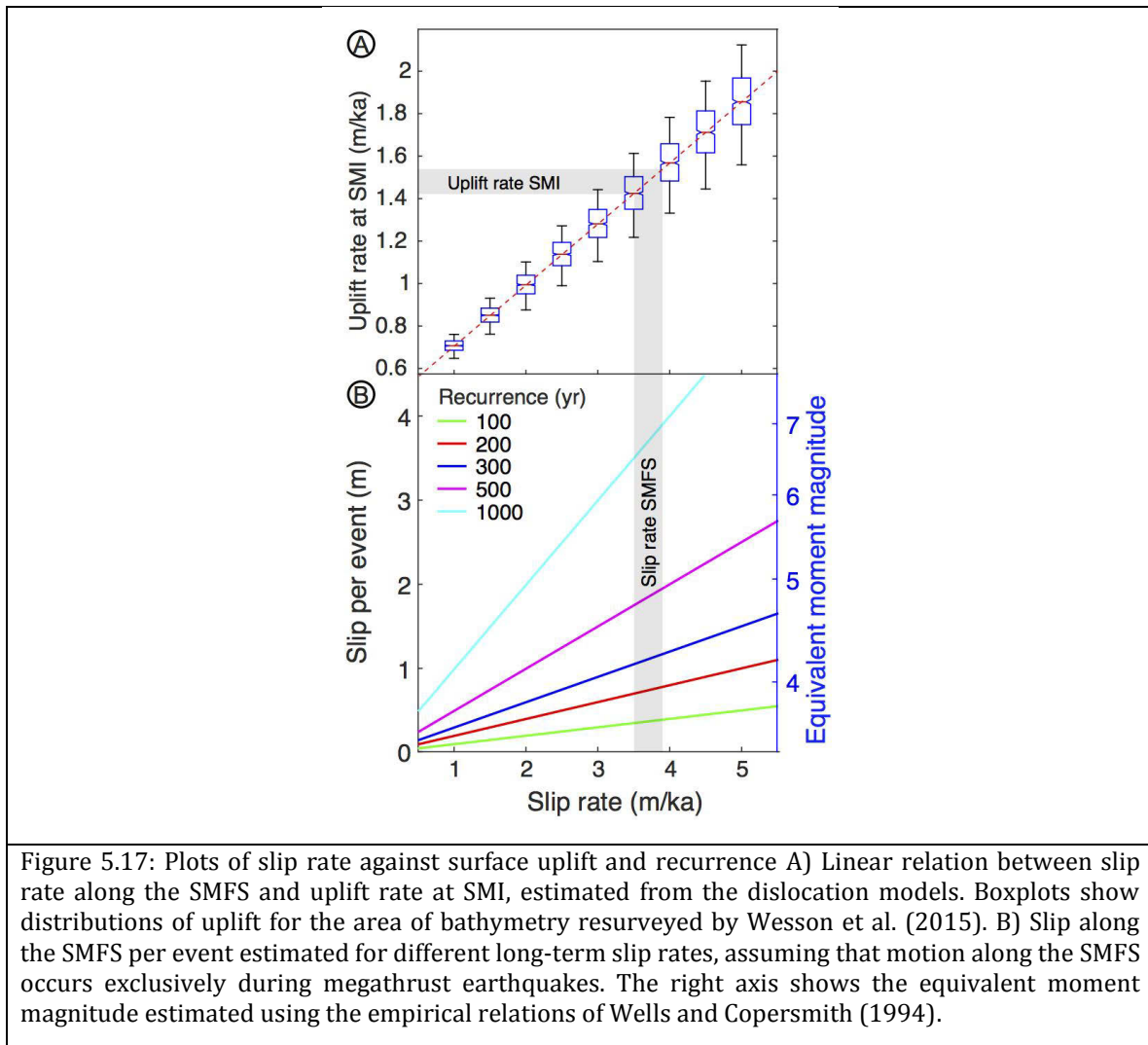


Figure 5.17: Plots of slip rate against surface uplift and recurrence A) Linear relation between slip rate along the SMFS and uplift rate at SMI, estimated from the dislocation models. Boxplots show distributions of uplift for the area of bathymetry resurveyed by Wesson et al. (2015). B) Slip along the SMFS per event estimated for different long-term slip rates, assuming that motion along the SMFS occurs exclusively during megathrust earthquakes. The right axis shows the equivalent moment magnitude estimated using the empirical relations of Wells and Copersmith (1994).

Our observations and interpretations of fault activity associated with megathrust earthquakes in the Arauco Bay area are compatible with observation from other regions subjected to similar earthquakes. The Yunodake fault that ruptured after the Tohoku earthquake, Japan, has a recurrence time of ~12-17 ka, as inferred from paleoseismic trenching (Toda and Tsutsumi, 2013). However, the Yunodake fault is a normal fault not rooted in the plate interface and located much farther inland than the SMFS, and might thus have a different behavior. Conversely, reverse splay faults in the Prince Williams Sound, Alaska, that are rooted in the plate interface have similarly fast slip rates reaching ~9 mm/yr in the Holocene, and an average slip of ~2 m per megathrust ($M > 9$) event has been estimated based on seismic-reflection data (Liberty et al., 2013). Using resurveyed bathymetry, these authors showed that many of the splay faults slipped together during the 1964 Alaska earthquake forming metric scarps on the seafloor and acted as a secondary source for the tsunami.

This study highlights the application of quantitative geomorphology with high-resolution bathymetry to estimate deformation rates in submarine settings. In addition, this study provides substantial evidence of active structures in the Arauco Bay area that may help improving current models of tsunami inundation and our understanding of forearc deformation processes in offshore areas. Some of the codes and the Landscape Evolution Model used in this work are available at <http://www.terracem.com>.

5.7 Conclusions

We studied the pattern of permanent deformation of a splay fault in a forearc setting – the Santa Maria Fault System – by means of hitherto unrecognized drowned shorelines in the Arauco Bay area of south-central Chile. We identified, mapped, and assessed uplift rates by combining morphometry, sedimentology, and the output of a landscape evolution model (LEM).

- The Arauco Bay area can be subdivided into an Eastern and a Western Domains, based on the geomorphic expression of drowned shorelines. A single arc-shaped fringe of bedrock outcrops representing remnants of a drowned paleo-cliff characterizes the Eastern Domain, whereas scattered drowned paleo-cliffs and wave-cut platforms forming a staircase sequence characterize the Western Domain. A sensitivity analysis of a tuned LEM, geomorphic observations, and the age of nearby onshore marine terraces suggest that these shorelines were formed during the MIS 3, when the SMI was connected with the continent. The preservation of these shorelines is likely a result of the gentle slopes that cause very rapid horizontal coastal flooding after the LGM.
- Uplift rates between -0.1 and 0.4 m/ka at the Eastern Domain and between 0.3 and 1.3 at the Western Domain may be estimated by fitting LEM-derived bathymetry to the minimum depth of swath profiles extracted from the multibeam data. We reproduced the spatial distribution of these uplift rates using elastic dislocation models in which the Santa Maria Fault System is an integral part of a deep-reaching, but blind high-angle reverse fault rooted in the plate interface and with a slip rate between 3 and 3.7 m/ka. Normal faults observed in the region appear to be secondary structures that only affect the shallow levels of the crust.

- Assuming that the millennial-scale slip rate of the SMFS is exclusively accounted for by triggered motion during each single great megathrust earthquakes allows estimating a slip per event of 0.3-0.7 m for the historical recurrence period of ~150-200 years, which would be equivalent to a $M_w \sim 4$ earthquake. In turn, if motion along the SMFS is triggered by earthquakes with a recurrence of ~1000 years, then a slip per event of ~3.5 m would be required to account for the long-term rate, equivalent to a $M_w \sim 6.5$ earthquake. Such an event could be a secondary source for the local tsunami resulting in higher amplitude waves with shorter arrival times around the Arauco Bay area.

6 Summary and discussion

This thesis was developed following the main foundations of the scientific method (Chang, 2014) that comprises: systematic observation, testing a hypothesis, acquiring new knowledge, or correcting and integrating previous knowledge. Along this thesis, I focused on map and analyze marine terraces systematically along the (2010) Maule earthquake rupture zone at different spatial scales. These observations were used to compare different hypothesis about the accumulation of permanent deformation through the cycle of mega-earthquakes in subduction zones. I integrated previous knowledge of marine terraces to developed new methods and programming tools for the assessment of permanent deformation in a systematic and repeatable manner.

Along the first part of this thesis I studied wave-built and wave-cut marine terraces in detail, developing new methodologies to assess uplift rates and associated error estimates:

- The stratigraphic architecture of wave-built terraces was studied to determine terrace reoccupation events.
- A novel method was developed to estimate uplift rates, iterating a relative sea level curves tied with the stratigraphic pattern of wave-built terraces. The best fit between submerged and emerged periods was obtained for an uplift rate of 1.5 m/ka.
- I propose that transgressive-regressive sedimentary cycles overlying a wave-cut platform may be used as distinctive criteria to define this type of terrace and to determine uplift rates.
- Series of functions were developed in Matlab® to determine shoreline angles in wave-cut terraces under different geomorphic scenarios, comprising staircase marine terraces, rough coasts, and sediment-covered marine terraces exposed along the Maule earthquake rupture zone and California. The elevation of the shoreline angle is estimated using lineal interpolations upon selected segments of swath profiles.
- These functions were incorporated inside a Graphic User Interface (GUI). This user-friendly tool named TerraceM allows mapping a bulk of shoreline angles systematically from aligned profiles; their distributions are studied using statistics and descriptive geometry, and can be exported to different software platforms.
- The repeatability of these methods was tested through an experiment involving 10 students in a classroom setting at the University of Potsdam, Germany.

Along the second part of this thesis, I validated and combined these methods to analyze different types of marine terraces along the (2010) Maule earthquake rupture zone. I compared permanent deformation rates with seismic cycle deformation patterns and historic earthquake ruptures to discuss about the mechanisms of upper plate deformation through several earthquake cycles at different spatial scales.

- Marine terraces were dated using 12 IRSL ages, and measured using the methods developed in Chapters 2 and 3, determining the pattern of permanent deformation accrued along the Maule earthquake rupture.
- Three areas of high permanent uplift were detected, comprising terrace warping, and sharp fault offsets. These areas correlate with high slip and/or low coupling and with the rupture extent of at least 8 historical megathrust earthquakes (M8-9.5).
- Zones of long-wavelength upwarping at the northern and southern boundaries of the Maule rupture reflect changes in frictional properties of the megathrust resulting in barriers to the propagation of great earthquakes.
- Permanent deformation may be accumulated during the coseismic face at the northern and southern rupture boundaries. In turn, in regions where the subducting slab is deeper and farther inland from the trench, such as the center of the Maule rupture, show inverse relationships between long-term uplift rate and interseismic coupling, suggesting they might rise permanently during the interseismic face.
- The last study of this thesis focus on determine permanent deformation rates in offshore areas. Hitherto unrecognized drowned shorelines at the Arauco Bay are used to estimate deformation rates. Their origin was studied using a multidisciplinary approach including morphometric analysis of high-resolution bathymetry, ROV and dive exploration, paleontology, sedimentology, and clasts morphoscopy.
- A landscape evolution model based in Anderson (1999) and adapted to submarine realms is used to estimate permanent deformation rates. By using an elastic model of a high angle reverse fault with a slip rate of 3.7 m/ka I successfully reproduced the uplift rates derived from drowned shorelines for relatively low residuals.
- Documented activity of the Santa Maria Fault System during the Maule earthquake suggest that permanent deformation may be accumulated during the coseismic face. However relocalized shallow seismic events, obtained ten years before the (2010) Maule earthquake, suggest transient pulses of slip during the interseismic face.

The study of marine terraces systematically using quantitative methods and continuous measurements has proved to be useful to determine patterns and magnitudes of permanent deformation along extended regions, with precision and accuracy. To date, several colleagues from seven universities and institutes are developing their research using the programmatic tool (TerraceM) developed in this thesis, including: the Institut de Physique du Globe de Paris, University of Istanbul, University of Boston, Iranian Institute for Oceanography, University of Grenoble, University of Normandy, Universidad Católica del Norte, and Universidad Austral, both in Chile.

The results of this thesis provided new knowledge about the patterns and magnitudes of permanent deformation accrued in the crust in the Maule earthquake region. Along this study I identified different patterns of permanent deformation that may be indicative of the processes

responsible for its accumulation. For instance, long-wavelength structures are associated to deeper sources of deformation, such as those that occur at the megathrust zone; instead short wavelength structures are associated to local shallow sources of deformation, such as active structures at the upper plate. Thus, the wavelength of the permanent deformation patterns may be useful criteria to differentiate the mechanisms of accumulation of permanent deformation and detect areas of active faulting in forearc region in subduction zones.

The magnitude of permanent deformation accrued along the Maule earthquake rupture is heterogeneous. However, areas of higher uplift rates roughly match with areas of high coseismic slip in the megathrust. Considering that the magnitude of permanent deformation accrued along the Maule rupture zone also correlates other factors, such as the distance to trench and the depth of the slab. The geometry of the subduction system may represent good criteria to distinguish if permanent deformation was accrued during the interseismic or coseismic phase. However, to test this relation further observations and comparisons with other subduction zones and using the same methods are necessary.

Finally, there are still open questions about the amount of permanent deformation accrued along the 2010 Maule earthquake region not answered in this study, for instance:

- Are permanent deformation rates constant through longer time scales?
- How stable are the seismotectonic boundaries in subduction zones?
- What is the role of super cycle mega-earthquakes ruptures in the accumulation of permanent deformation?
- Can we extrapolate the correlations between permanent deformation and megathrust geometry observed in the Maule area to other subduction zones?

Further investigations are necessary to answer these questions, in order to link different temporal and spatial scales of deformation, and. My personal desire is to continue investigating in these and other matters related with the activity of forearc regions in the future, beyond the development of this thesis.

7 References

- Alexander, C.S., 1953. The marine and stream terraces of the Capitola-Watsonville area. University of California Press.
- Allen, P.A., Armitage, J.J., Whittaker, A.C., Michael, N.A., Roda-Boluda, D., x, Arcy, M., 2015. Fragmentation Model of the Grain Size Mix of Sediment Supplied to Basins. *The Journal of Geology* 123, 405-427.
- Allmendinger, R.W., González, G., Cembrano, J., Aron, F., Yañez, G., 2013. Splay fault slip during the Mw 8.8 2010 Maule Chile earthquake: COMMENT. *Geology* 41, e309-e309.
- Anderson, R., Densmore, A., Ellis, M., 1999. The generation and degradation of marine terraces. *Basin Research* 11, 7-19.
- Anderson, R.S., Menking, K.M., 1994. The Quaternary marine terraces of Santa Cruz, California: Evidence for coseismic uplift on two faults. *Geological Society of America Bulletin* 106, 649-664.
- Ando, M., 1975. Source mechanisms and tectonic significance of historical earthquakes along the Nankai Trough, Japan. *Tectonophysics* 27, 119-140.
- Angermann, D., Klotz, J., Reigber, C., 1999. Space-geodetic estimation of the Nazca-South America Euler vector. *Earth and Planetary Science Letters* 171, 329-334.
- Araya-Vergara, J.F., 1976. Reconocimiento de tipos e individuos geomorfológicos regionales en la costa de Chile. *Información Geográfica (Chile)* 23, 9-30.
- Armijo, R., Meyer, B., King, G., Rigo, A., Papanastassiou, D., 1996. Quaternary evolution of the Corinth Rift and its implications for the Late Cenozoic evolution of the Aegean. *Geophysical Journal International* 126, 11-53.
- Arnott, R., 1995. The Parasequence Definition--Are Transgressive Deposits Inadequately Addressed? *Journal of Sedimentary Research* 65.
- Aron, F., Allmendinger, R.W., Cembrano, J., González, G., Yañez, G., 2013. Permanent fore-arc extension and seismic segmentation: Insights from the 2010 Maule earthquake, Chile. *Journal of Geophysical Research: Solid Earth* 118, 724-739.
- Arz, H.W., Lamy, F., Ganopolski, A., Nowaczyk, N., Patzold, J., 2007. Dominant Northern Hemisphere climate control over millennial-scale glacial sea-level variability. *Quaternary Science Reviews* 26, 312-321.
- Ashby, J.R., Ku, T., Minch, J.A., 1987. Uranium series ages of corals from the upper Pleistocene Mulege terrace, Baja California Sur, Mexico. *Geology* 15, 139-141.
- Aster, G., 2011. Validation Team, 2009. ASTER Global DEM.
- Athanassas, C., Fountoulis, I., 2013. Quaternary neotectonic configuration of the southwestern Peloponnese, Greece, based on luminescence ages of marine terraces. *Journal of Earth Science* 24, 410-427.

- Audin, L., Lacan, P., Tavera, H., Bondoux, F., 2008. Upper plate deformation and seismic barrier in front of Nazca subduction zone: the Chololo Fault System and active tectonics along the Coastal Cordillera, southern Peru. *Tectonophysics* 459, 174-185.
- Bailey, S., Bristow, C., 2004. Migration of parabolic dunes at Aberffraw, Anglesey, north Wales. *Geomorphology* 59, 165-174.
- Bangs, N.L., Cande, S.C., 1997. Episodic development of a convergent margin inferred from structures and processes along the southern Chile margin. *Tectonics* 16, 489-503.
- Bard, E., Hamelin, B., Arnold, M., Montaggioni, L., Cabioch, G., Faure, G., Rougerie, F., 1996. Deglacial sea-level record from Tahiti corals and the timing of global meltwater discharge. *Nature* 382, 241-244.
- Barnes, P.M., Nicol, A., Harrison, T., 2002. Late Cenozoic evolution and earthquake potential of an active listric thrust complex above the Hikurangi subduction zone, New Zealand. *Geological Society of America Bulletin* 114, 1379-1405.
- Barrientos, S., 1987. Is the Pichilemu-Talcahuano (Chile) a seismic gap. *Seismological Research Letters* 61, 43-48.
- Barrientos, S.E., 1988. Slip distribution of the 1985 Central Chile earthquake. *Tectonophysics* 145, 225-241.
- Beaman, R.J., O'Brien, P.E., Post, A.L., De Santis, L., 2011. A new high-resolution bathymetry model for the Terre Adélie and George V continental margin, East Antarctica. *Antarctic Science* 23, 95-103.
- Beck, S., Barrientos, S., Kausel, E., Reyes, M., 1998. Source characteristics of historic earthquakes along the central Chile subduction. *Journal of South American Earth Sciences* 11, 115-129.
- Bedford, J., Moreno, M., Baez, J.C., Lange, D., Tilmann, F., Rosenau, M., Heidbach, O., Oncken, O., Bartsch, M., Rietbrock, A., 2013. A high-resolution, time-variable afterslip model for the 2010 Maule Mw= 8.8, Chile megathrust earthquake. *Earth and Planetary Science Letters* 383, 26-36.
- Bernhardt, A., Melnick, D., Jara-Muñoz, J., Argandoña, B., González, J., Strecker, M.R., 2015. Controls on submarine canyon activity during sea-level highstands: The Biobio canyon system offshore Chile. *Geosphere* 11, 1226-1255.
- Berryman, K., 1993. Age, height, and deformation of Holocene marine terraces at Mahia Peninsula, Hikurangi subduction margin, New Zealand. *Tectonics* 12, 1347-1364.
- Berryman, K., Ota, Y., Hull, A., 1989. Holocene paleoseismicity in the fold and thrust belt of the Hikurangi subduction zone, eastern North Island, New Zealand. *Tectonophysics* 163, 185-195.
- Bianca, M., Catalano, S., De Guidi, G., Gueli, A., Monaco, C., Ristuccia, G., Stella, G., Tortorici, G., Tortorici, L., Troja, S., 2011. Luminescence chronology of Pleistocene marine terraces of Capo Vaticano peninsula (Calabria, southern Italy). *Quaternary International* 232, 114-121.
- Bilek, S.L., Schwartz, S.Y., DeShon, H.R., 2003. Control of seafloor roughness on earthquake rupture behavior. *Geology* 31, 455-458.
- Billauer, E., 2008. peakdet: Peak detection using MATLAB. Eli Billauer's home page.

- Bintanja, R., van de Wal, R.S., Oerlemans, J., 2005. Modelled atmospheric temperatures and global sea levels over the past million years. *Nature* 437, 125-128.
- Bird, E.C.F., Bird, E., 2000. Coastal geomorphology: an introduction. Wiley Online Library.
- Bishop, D., 1985. Inferred uplift rates from raised marine surfaces, southern Fiordland, New Zealand. *New Zealand journal of geology and geophysics* 28, 243-251.
- Bishop, P., Hoey, T.B., Jansen, J.D., Artza, I.L., 2005. Knickpoint recession rate and catchment area: the case of uplifted rivers in Eastern Scotland. *Earth Surface Processes and Landforms* 30, 767-778.
- Bland, J.M., Altman, D., 1986. Statistical methods for assessing agreement between two methods of clinical measurement. *The lancet* 327, 307-310.
- Bloom, A., Broecker, W., Chappell, J., Matthews, R., Mesoella, K., 1974. Quaternary sea level fluctuations on a tectonic coast: New ^{230}Th / ^{234}U dates from the Huon Peninsula, New Guinea. *Quaternary Research* 4, 185-205.
- Bloom, A.L., Yonekura, N., 1985. Coastal terraces generated by sea-level change and tectonic uplift, In: Woldenberg, M.J. (Ed.), *Models in geomorphology*. The Binghamton Symposia in Geomorphology, Binghamton, New York, pp. 139-154.
- Blott, S.J., Pye, K., 2001. GRADISTAT: a grain size distribution and statistics package for the analysis of unconsolidated sediments. *Earth Surface Processes and Landforms* 26, 1237-1248.
- Boggs, S.J., 1987. *Principles of Sedimentology and Stratigraphy*. Merrill Publishing Company, Columbus.
- Bohm, M., Lüth, S., Echtler, H., Asch, G., Bataille, K., Bruhn, C., Rietbrock, A., Wigger, P., 2002. The Southern Andes between 36° and 40°S latitude: seismicity and average seismic velocities. *Tectonophysics* 356, 275-289.
- Bonnardot, M.-A., Hassani, R., Tric, E., Ruellan, E., Régnier, M., 2008. Effect of margin curvature on plate deformation in a 3-D numerical model of subduction zones. *Geophysical Journal International* 173, 1084-1094.
- Bookhagen, B., Echtler, H.P., Melnick, D., Strecker, M.R., Spencer, J.Q.G., 2006. Using uplifted Holocene beach berms for paleoseismic analysis on the Santa María Island, south-central Chile. *Geophysical Research Letters* 33, L15302.
- Bourke, M.C., Brearley, J.A., Haas, R., Viles, H.A., 2007. A photographic atlas of rock breakdown features in geomorphic environments.
- Bowles, C.J., Cowgill, E., 2012. Discovering marine terraces using airborne LiDAR along the Mendocino-Sonoma coast, northern California. *Geosphere* 8, 386-402.
- Bowman, S., 1990. Radiocarbon dating. Univ of California Press.
- Bradley, W.C., 1957. Origin of marine-terrace deposits in the Santa Cruz area, California. *Geological Society of America Bulletin* 68, 421-444.
- Bradley, W.C., 1958. Submarine abrasion and wave-cut platforms. *Geological Society of America Bulletin* 69, 967-974.

- Bradley, W.C., Addicott, W.O., 1968. Age of first marine terrace near Santa Cruz, California. *Geological Society of America Bulletin* 79, 1203-1210.
- Bradley, W.C., Griggs, G., 1976. Form, genesis, and deformation of central California wave-cut platforms. *Geological Society of America Bulletin* 87, 433-449.
- Briggs, R.W., Engelhart, S.E., Nelson, A.R., Dura, T., Kemp, A.C., Haeussler, P.J., Corbett, D.R., Angster, S.J., Bradley, L.Ä., 2014. Uplift and subsidence reveal a nonpersistent megathrust rupture boundary (Sitkinak Island, Alaska). *Geophysical Research Letters* 41, 2289-2296.
- Briggs, R.W., Sieh, K., Amidon, W.H., Galetzka, J., Prayudi, D., Suprihanto, I., Sastra, N., Suwargadi, B., Natawidjaja, D., Farr, T.G., 2008. Persistent elastic behavior above a megathrust rupture patch: Nias island, West Sumatra. *Journal of Geophysical Research: Solid Earth* 113, B12406.
- Bromley, G.R., 1994. *The palaeoecology of bioerosion, Palaeobiology of Trace Fossils*. Wiley.
- Bromley, R.G., D'Alessandro, A., 1983. Bioerosion in the Pleistocene of southern Italy: ichnogenera *Caulostrepis* and *Maeandropolydora*. *Rivista Italiana di Paleontologia e Stratigrafia* 89, 283-309.
- Bromley, R.G., D'Alessandro, A., 1987. Bioerosion of the Plio-Pleistocene transgression of southern Italy. *Rivista Italiana di Paleontologia e Stratigrafia*.
- Brooke, B., Olley, J., Pietsch, T., Playford, P., Haines, P., Murray-Wallace, C., Woodroffe, C., 2014. Chronology of Quaternary coastal aeolianite deposition and the drowned shorelines of southwestern Western Australia: a reappraisal. *Quaternary Science Reviews* 93, 106-124.
- Brooks, B.A., Bevis, M., Smalley, R., Kendrick, E., Manceda, R., Lauria, E., Maturana, R., Araujo, M., 2003. Crustal motion in the Southern Andes (26-36 S): Do the Andes behave like a microplate? *Geochemistry, Geophysics, Geosystems* 4.
- Bruhn, C., 2003. *Momententensoren hochfrequenter Ereignisse in Südchile*. University of Potsdam.
- Burbank, D.W., Anderson, R.S., 2011. *Tectonic geomorphology*. John Wiley & Sons.
- Cabioch, G., Ayliffe, L.K., 2001. Raised coral terraces at Malakula, Vanuatu, Southwest Pacific, indicate high sea level during marine isotope stage 3. *Quaternary Research* 56, 357-365.
- Campos, J., Hatzfeld, D., Madariaga, R., Lopez, G., Kausel, E., Zollo, A., Iannaccone, G., Fromm, R., Barrientos, S., Lyon-Caen, H., 2002. A seismological study of the 1835 seismic gap in south-central Chile. *Physics of the Earth and Planetary Interiors* 132, 177-195.
- Cantalamesa, G., Di Celma, C., 2004. Origin and chronology of Pleistocene marine terraces of Isla de la Plata and of flat, gently dipping surfaces of the southern coast of Cabo San Lorenzo (Manabi, Ecuador). *Journal of South American Earth Sciences* 16, 633-648.
- Caputo, R., 2007. Sea-level curves: perplexities of an end-user in morphotectonic applications. *Global and Planetary Change* 57, 417-423.
- Carr, A.S., Thomas, D.S., Bateman, M.D., 2006. Climatic and sea level controls on Late Quaternary eolian activity on the Agulhas Plain, South Africa. *Quaternary Research* 65, 252-263.
- Cartajena, I., López, P., Carabias, D., Morales, C., Vargas, G., Ortega, C., 2013. First evidence of an underwater Final Pleistocene terrestrial extinct faunal bone assemblage from Central Chile (South America): Taxonomic and taphonomic analyses. *Quaternary International* 305, 45-55.

- Cawthra, H.C., Bateman, M.D., Carr, A.S., Compton, J.S., Holmes, P.J., 2014. Understanding Late Quaternary change at the land-ocean interface: a synthesis of the evolution of the Wilderness coastline, South Africa. *Quaternary Science Reviews* 99, 210-223.
- Cecioni, G., 1983. Chanco Formation, a potential Cretaceous reservoir, central Chile. *Journal of Petroleum Geology* 6, 89-93.
- Challinor, J., 1949. A principle in coastal geomorphology. *Geography*, 212-215.
- Chang, M., 2014. *Principles of Scientific Methods*. Chapman and Hall Massachusetts.
- Chapman, J.B., Elliott, J., Doser, D.I., Pavlis, T.L., 2014. Slip on the Suckling Hills splay fault during the 1964 Alaska earthquake. *Tectonophysics* 637, 191-197.
- Chappell, J., 1974. Geology of coral terraces, Huon Peninsula, New Guinea: A study of Quaternary tectonic movements and sea-level changes. *Geological Society of America Bulletin* 85, 553-570.
- Chappell, J., Omura, A., Esat, T., McCulloch, M., Pandolfi, J., Ota, Y., Pillans, B., 1996. Reconciliation of late Quaternary sea levels derived from coral terraces at Huon Peninsula with deep sea oxygen isotope records. *Earth and Planetary Science Letters* 141, 227-236.
- Chaytor, J.D., Goldfinger, C., Meiner, M.A., Huftile, G.J., Romsos, C.G., Legg, M.R., 2008. Measuring vertical tectonic motion at the intersection of the Santa Cruz, Catalina Ridge and Northern Channel Islands platform, California Continental Borderland, using submerged paleoshorelines. *Geological Society of America Bulletin* 120, 1053-1071.
- Chen, M.-C., Frohlich, C., Taylor, F.W., Burr, G., Van Ufford, A.Q., 2011. Arc segmentation and seismicity in the Solomon Islands arc, SW Pacific. *Tectonophysics* 507, 47-69.
- Chlieh, M., Avouac, J.-P., Hjorleifsdottir, V., Song, T.-R.A., Ji, C., Sieh, K., Sladen, A., Hebert, H., Prawirodirdjo, L., Bock, Y., 2007. Coseismic slip and afterslip of the great Mw 9.15 Sumatra-Andaman earthquake of 2004. *Bulletin of the Seismological Society of America* 97, S152-S173.
- Cifuentes, I.L., 1989. The 1960 Chilean earthquakes. *Journal of Geophysical Research: Solid Earth* 94, 665-680.
- Cisternas, M., Ely, L., Wesson, R., Pilarczic, J., Gorigoitia, N., Dura, T., Melnick, D., Carvajal, M., 2014. The 1730 and 1751 Chilean earthquakes: Two Major Contributors to the Seismically Prolific 18th Century along the Pacific Coast of the Americas., SSA Annual Meeting, Anchorage, Alaska.
- Cisternas, M., Melnick, D., Ely, L., Wesson, R., Norambuena, R., 2010. Similarities between the great Chilean earthquakes of 1835 and 2010, Chapman Conference on Giant earthquakes and their Tsunamis, AGU.
- Collot, J.-Y., Agudelo, W., Ribodetti, A., Marcaillou, B., 2008. Origin of a crustal splay fault and its relation to the seismogenic zone and underplating at the erosional north Ecuador-south Colombia oceanic margin. *Journal of Geophysical Research: Solid Earth* 113.
- Collot, J.-Y., Marcaillou, B., Sage, F., Michaud, F., Agudelo, W., Charvis, P., Graindorge, D., Gutscher, M.-A., Spence, G., 2004. Are rupture zone limits of great subduction earthquakes controlled by upper plate structures? Evidence from multichannel seismic reflection data acquired across the northern Ecuador-southwest Colombia margin. *Journal of Geophysical Research: Solid Earth* (1978-2012) 109.

- Cornée, J.J., Moissette, P., Joannin, S., Suc, J.P., Quiellévéré, F., Krijgsman, W., Hilgen, F., Koskridou, E., Münch, P., Lécuyer, C., Desvignes, P., 2006. Tectonic and climatic controls on coastal sedimentation: The Late Pliocene - Middle Pleistocene of northeastern Rhodes, Greece. *Sedimentary Geology* 187, 159-181.
- Crosby, B.T., Whipple, K.X., 2006. Knickpoint initiation and distribution within fluvial networks: 236 waterfalls in the Waipaoa River, North Island, New Zealand. *Geomorphology* 82, 16-38.
- Cunningham, D., Grebby, S., Tansey, K., Gosar, A., Kastelic, V., 2006. Application of airborne LiDAR to mapping seismogenic faults in forested mountainous terrain, southeastern Alps, Slovenia. *Geophysical Research Letters* 33.
- Dahlen, F., Suppe, J., Davis, D., 1984. Mechanics of fold-and-thrust belts and accretionary wedges: Cohesive Coulomb theory. *Journal of Geophysical Research: Solid Earth* 89, 10087-10101.
- Darwin, C., 1851. *Geological observations of South America*. Smith, Elder, London.
- Delouis, B., Nocquet, J.-M., Vallée, M., 2010. Slip distribution of the February 27, 2010 Mw = 8.8 Maule Earthquake, central Chile, from static and high-rate GPS, InSAR, and broadband teleseismic data. *Geophysical Research Letters* 37, L17305.
- Dickinson, W.R., 2013. Control of paleoshorelines by trench forebulge uplift, Loyalty Islands. *Quaternary Research* 80, 125-137.
- Dietrich, R., Ivins, E., Casassa, G., Lange, H., Wendt, J., Fritsche, M., 2010. Rapid crustal uplift in Patagonia due to enhanced ice loss. *Earth and Planetary Science Letters* 289, 22-29.
- Dietz, R.S., 1963. Wave-base, marine profile of equilibrium, and wave-built terraces: a critical appraisal. *Geological Society of America Bulletin* 74, 971-990.
- Dumas, B., Hoang, C.T., Raffy, J., 2006. Record of MIS 5 sea-level highstands based on U/Th dated coral terraces of Haiti. *Quaternary International* 145, 106-118.
- Dupré, W.R., 1984. Reconstruction of paleo-wave conditions during the late Pleistocene from marine terrace deposits, Monterey Bay, California. *Developments in Sedimentology* 39, 435-454.
- Emery, K., 1958. Shallow submerged marine terraces of southern California. *Geological Society of America Bulletin* 69, 39-60.
- Encinas, A., Herve, F., Villa-Martinez, R., Nielsen, S.N., Finger, K.L., Peterson, D.E., 2006a. Finding of a Holocene marine layer in Algarrobo (33° 22 ' S), central Chile. Implications for coastal uplift. *Revista Geologica De Chile* 33, 339-345.
- Encinas, A., Le Roux, J.P., Buatois, L.A., Nielsen, S.N., Finger, K.L., Fourtanier, E., Lavenu, A., 2006b. Nuevo esquema estratigrafico para los depositos marinos mio-pliocenos del area de Navidad (33 - 34 30'S), Chile central. *Revista geologica de Chile* 33, 221-246.
- Fairbanks, R.G., 1989. A 17, 000-year glacio-eustatic sea level record: influence of glacial melting rates on the Younger Dryas event and deep-ocean circulation. *Nature* 342, 637-642.
- Fairbanks, R.G., Matthews, R., 1978. The marine oxygen isotope record in Pleistocene coral, Barbados, West Indies. *Quaternary Research* 10, 181-196.

- Farías, M., Charrier, R., Carretier, S., Martinod, J., Fock, A., Campbell, D., Cáceres, J., Comte, D., 2008. Late Miocene high and rapid surface uplift and its erosional response in the Andes of central Chile (33-35 S). *Tectonics* 27.
- Farias, M., Comte, D., Charrier, R., Martinod, J., David, C., Tassara, A., Tapia, F., Fock, A., 2010a. Crustal, escale structural architecture in central Chile based on seismicity and surface geology: Implications for Andean mountain building. *Tectonics* 29.
- Farías, M., Comte, D., Roecker, S., Carrizo, D., Pardo, M., 2011. Crustal extensional faulting triggered by the 2010 Chilean earthquake: The Pichilemu Seismic Sequence. *Tectonics* 30, TC6010.
- Farias, M., Vargas, G., Tassara, A., Carretier, S., Baize, S., Melnick, D., Bataille, K., 2010b. Land-level changes produced by the Mw 8.8 2010 Chilean earthquake. *Science* 329, 916-916.
- Faught, M., Gusick, A., 2011. Submerged prehistory in the Americas. *Submerged prehistory*, 145-157.
- Finger, K.L., Nielsen, S.N., Devries, T.J., Encinas, A., Peterson, D.E., 2007. Paleontologic evidence for sedimentary displacement in Neogene forearc basins of central Chile. *Palaios* 22, 3-16.
- FitzRoy, R., King, P.P., Darwin, C., 1839. *Narrative of the Surveying Voyages of His Majesty's Ships Adventure and Beagle Between the Years 1826 and 1836: Describing Their Examination of the Southern Shores of South America, and the Beagle's Circumnavigation of the Globe*. H. Colburn.
- Folk, R.L., 1980. *Petrology of Sedimentary Rocks*, Austin, Texas.
- Fraccascia, S., Chiocci, F., Scrocca, D., Falese, F., 2013. Very high-resolution seismic stratigraphy of Pleistocene eustatic minima markers as a tool to reconstruct the tectonic evolution of the northern Latium shelf (Tyrrhenian Sea, Italy). *Geology* 41, 375-378.
- Frankel, K.L., Dolan, J.F., 2007. Characterizing arid region alluvial fan surface roughness with airborne laser swath mapping digital topographic data. *Journal of Geophysical Research: Earth Surface* (2003-2012) 112.
- Friedman, G.M., 1967. Dynamic processes and statistical parameters compared for size frequency distribution of beach and river sands. *Journal of Sedimentary Petrology* 37, 327-356.
- Fritz, H.M., Phillips, D.A., Okayasu, A., Shimozono, T., Liu, H., Mohammed, F., Skanavis, V., Synolakis, C.E., Takahashi, T., 2012. The 2011 Japan tsunami current velocity measurements from survivor videos at Kesenuma Bay using LiDAR. *Geophysical Research Letters* 39.
- Fukao, Y., 1979. Tsunami earthquakes and subduction processes near deep-sea trenches. *Journal of Geophysical Research: Solid Earth* 84, 2303-2314.
- Galbraith, R.F., Roberts, R.G., Laslett, G., Yoshida, H., Olley, J.M., 1999. Optical dating of single and multiple grains of quartz from jinnium rock shelter, northern australia: part i, experimental design and statistical models*. *Archaeometry* 41, 339-364.
- Gallen, S., Wegmann, K., Bohnenstiehl, D., Pazzaglia, F., Brandon, M., Fassoulas, C., 2014. Active simultaneous uplift and margin-normal extension in a forearc high, Crete, Greece. *Earth and Planetary Science Letters* 398, 11-24.

- Garcin, Y., Melnick, D., Strecker, M.R., Olago, D., Tiercelin, J.-J., 2012. East African mid-Holocene wet-dry transition recorded in palaeo-shorelines of Lake Turkana, northern Kenya Rift. *Earth and Planetary Science Letters* 331, 322-334.
- Geersen, J., Behrmann, J.H., Völker, D., Krastel, S., Ranero, C.R., Diaz-Naveas, J., Weinrebe, W., 2011. Active tectonics of the South Chilean marine fore arc (35°S–40°S). *Tectonics* 30, TC3006.
- Gesch, D., Oimoen, M., Greenlee, S., Nelson, C., Steuck, M., Tyler, D., 2002. The national elevation dataset. *Photogrammetric engineering and remote sensing* 68, 5-32.
- Gilbert, G.K., 1890. Lake Bonneville. United States Geological Survey.
- Glodny, J., Echtler, H., Collao, S., Ardiles, M., Burón, P., Figueroa, O., 2008. Differential Late Paleozoic active margin evolution in South-Central Chile (37°S-40°S) -The Lanalhue Fault Zone. *Journal of South American Earth Sciences* 26, 397-411.
- Glodny, J., Lohrmann, J., Echtler, H., Gräfe, K., Seifert, W., Collao, S., Figueroa, O., 2005. Internal dynamics of a paleoaccretionary wedge: insights from combined isotope tectonochronology and sandbox modelling of the South-Central Chilean forearc. *Earth and Planetary Science Letters* 231, 23-39.
- Gonzalez, E., 1990. Hydrocarbon resources in the coastal zone of Chile.
- González, G., Salazar, P., Loveless, J.P., Allmendinger, R.W., Aron, F., Shrivastava, M., 2015. Upper plate reverse fault reactivation and the unclamping of the megathrust during the 2014 northern Chile earthquake sequence. *Geology* 43, 671-674.
- González-Acuña, J., Arroyo-Suarez, E., 2013. Comparative Methodologies for Sounding Reduction Applied to a Bathymetric Survey Referred to the WGS-84 Ellipsoid, Executed in Concepcion Bay and Gulf of Arauco, VIII Region, Chile., U.S. Hydro 2013, New Orleans, Louisiana USA.
- Guilcher, A., Bodere, J.-C., Coude, A., Hansom, J.D., Moign, A., Peullvast, J., 1986. Le problème des strandflats en cinq pays de hautes latitudes. *Revue de Géologie dynamique et de Géographie physique* 27, 47-79.
- Gurrola, L.D., Keller, E.A., Chen, J.H., Owen, L.A., Spencer, J.Q., 2014. Tectonic geomorphology of marine terraces: Santa Barbara fold belt, California. *Geological Society of America Bulletin* 126, 219-233.
- Haberland, C., Rietbrock, A., Lange, D., Bataille, K., Dahm, T., 2009. Structure of the seismogenic zone of the southcentral Chilean margin revealed by local earthquake traveltimes tomography. *Journal of Geophysical Research: Solid Earth* (1978-2012) 114.
- Haberland, C., Rietbrock, A., Lange, D., Bataille, K., Hofmann, S., Dahm, T., Scherbaum, F., Tilman, F., Hermosilla, G., 2005. The TIPTEQ seismological network in Southern Chile-Studying the Seismogenic Coupling Zone, AGU Fall Meeting Abstracts.
- Hallermeier, R.J., 1978. Uses for a calculated limit depth to beach erosion. *Coastal Engineering Proceedings* 1.
- Hanebuth, T., Stattegger, K., Grootes, P.M., 2000. Rapid flooding of the Sunda Shelf: a late-glacial sea-level record. *Science* 288, 1033-1035.

- Hanks, T.C., Bucknam, R.C., Lajoie, K.R., Wallace, R.E., 1984. Modification of wave-cut and faulting-controlled landforms. *Journal of Geophysical Research: Solid Earth* (1978-2012) 89, 5771-5790.
- Hearty, P.J., Hollin, J.T., Neumann, A.C., O'Leary, M.J., McCulloch, M., 2007. Global sea-level fluctuations during the Last Interglaciation (MIS 5e). *Quaternary Science Reviews* 26, 2090-2112.
- Hetland, E., Simons, M., 2010. Post-seismic and interseismic fault creep II: transient creep and interseismic stress shadows on megathrusts. *Geophysical Journal International* 181, 99-112.
- Hicks, S.P., Rietbrock, A., Haberland, C.A., Ryder, I.M.A., Simons, M., Tassara, A., 2012. The 2010 Mw 8.8 Maule, Chile earthquake: Nucleation and rupture propagation controlled by a subducted topographic high. *Geophysical Research Letters* 39, L19308.
- Hogg, A.G., Hua, Q., Blackwell, P.G., Niu, M., Buck, C.E., Guilderson, T.P., Heaton, T.J., Palmer, J.G., Reimer, P.J., Reimer, R.W., 2013. SHCal13 Southern Hemisphere calibration, 0, 50,000 years cal BP. *Radiocarbon*.
- Hsu, J.T., 1992. Quaternary uplift of the Peruvian coast related to the subduction of the Nazca Ridge: 13.5 to 15.6 degrees south latitude. *Quaternary International* 15, 87-97.
- Huntley, D., Baril, M., 1997. The K content of the K-feldspars being measured in optical dating or in thermoluminescence dating. *Ancient TL* 15, 11-13.
- Hyndman, R., Wang, K., 1995. The rupture zone of Cascadia great earthquakes from current deformation and the thermal regime. *Journal of Geophysical Research: Solid Earth* 100, 22133-22154.
- Imbrie, J., Boyle, E., Clemens, S., Duffy, A., Howard, W., Kukla, G., Kutzbach, J., Martinson, D., McIntyre, A., Mix, A., 1992. On the structure and origin of major glaciation cycles 1. Linear responses to Milankovitch forcing. *Paleoceanography* 7, 701-738.
- Imbrie, J., Hays, J., Martinson, D., McIntyre, A., A. C. M., Morley, J., Pisias, N., Prell, W., NJ, S., 1984. The orbital theory of Pleistocene climate: Support from a revised chronology of the marine $\delta^{18}O$ record. *Milankovitch and Climate*. D. Reidel, Norwell, Mass, 269-305.
- Isla, F.I., Flory, J.Q., Martínez, C., Fernández, A., Jaque, E., 2012. The Evolution of the Bio Bio Delta and the Coastal Plains of the Arauco Gulf, Bio Bio Region: the Holocene Sea-Level Curve of Chile. *Journal of Coastal Research* 28, 102-111.
- Jackson, J.A., Mehl, J.P., Neuendorf, K.K., 2005. *Glossary of geology*. Springer.
- Jara-Muñoz, J., Melnick, D., 2015. Unraveling sea-level variations and tectonic uplift in wave-built marine terraces, Santa María Island, Chile. *Quaternary Research* 83, 216-228.
- Jara-Muñoz, J., Melnick, D., Brill, D., Strecker, M.R., 2015a. Segmentation of the 2010 Maule Chile earthquake rupture from a joint analysis of uplifted marine terraces and seismic-cycle deformation patterns. *Quaternary Science Reviews* 113, 171-192.
- Jara-Muñoz, J., Melnick, D., Strecker, M.R., 2015b. TerraceM: A MATLAB(R) tool to analyze marine and lacustrine terraces using high-resolution topography. *Geosphere* 12, 20.
- Jaramillo, E., Dugan, J.E., Hubbard, D.M., Melnick, D., Manzano, M., Duarte, C., Campos, C., Sanchez, R., 2012. Ecological implications of extreme events: footprints of the 2010 earthquake along the Chilean coast. *PloS one* 7, e35348.

- Johnson, S.Y., Hartwell, S.R., Dartnell, P., 2014. Offset of Latest Pleistocene Shoreface Reveals Slip Rate on the Hosgri Strike-Slip Fault, Offshore Central California. *Bulletin of the Seismological Society of America* 104, 1650-1662.
- Kaizuka, S., Matsuda, T., Nogami, M., Yonekura, N., 1973. Quaternary tectonic and recent seismic crustal movements in the arauco peninsula and its environs, central chile. *Geographical reports of Tokyo Metropolitan University* 8, 1-49.
- Kaneko, Y., Avouac, J.-P., Lapusta, N., 2010. Towards inferring earthquake patterns from geodetic observations of interseismic coupling. *Nature Geoscience* 3, 363-369.
- Kasper-Zubillaga, J.J., Dickinson, W.W., 2001. Discriminating depositional environments of sands from modern source terranes using modal analysis. *Sedimentary Geology* 143, 149-167.
- Kato, T.T., 1985. Pre-Andean orogenesis in the Coast Ranges of central Chile. *Geological Society of America Bulletin* 96, 918-924.
- Kelsey, H.M., Bockheim, J.G., 1994. Coastal landscape evolution as a function of eustasy and surface uplift rate, Cascadia margin, Southern Oregon. *GSA Bulletin* 106, 840-854.
- Kendrick, E., Bevis, M., Smalley, R., Brooks, B., 2001. An integrated crustal velocity field for the central Andes. *Geochemistry, Geophysics, Geosystems* 2.
- Keskin, S., Pedoja, K., Bektas, O., 2011. Coastal uplift along the eastern Black Sea coast: new marine terrace data from Eastern Pontides, Trabzon (Turkey) and a Review. *Journal of Coastal Research* 27, 63-73.
- Khazaradze, G., Klotz, J., 2003. Short-and long-term effects of GPS measured crustal deformation rates along the south central Andes. *Journal of Geophysical Research: Solid Earth (1978-2012)* 108.
- Kiser, E., Ishii, M., 2011. The 2010 Mw 8.8 Chile earthquake: Triggering on multiple segments and frequency-dependent rupture behavior. *Geophysical Research Letters* 38, L07301.
- Kitamura, A., Koyama, M., Itasaka, K., Miyairi, Y., Mori, H., 2014. Abrupt Late Holocene uplifts of the southern Izu Peninsula, central Japan: Evidence from emerged marine sessile assemblages. *Island Arc* 23, 51-61.
- Kliem, P., Buylaert, J.-P., Hahn, A., Mayr, C., Murray, A., Ohlendorf, C., Veres, D., Wastegård, S., Zolitschka, B., 2013. Magnitude, geomorphologic response and climate links of lake level oscillations at Laguna Potrok Aike, Patagonian steppe (Argentina). *Quaternary Science Reviews* 71, 131-146.
- Kline, S.W., Adams, P.N., Limber, P.W., 2014. The unsteady nature of sea cliff retreat due to mechanical abrasion, failure and comminution feedbacks. *Geomorphology* 219, 53-67.
- Klotz, J., Khazaradze, G., Angermann, D., Reigber, C., Perdomo, R., Cifuentes, O., 2001. Earthquake cycle dominates contemporary crustal deformation in Central and Southern Andes. *Earth and Planetary Science Letters* 193, 437-446.
- Klovan, J.E., 1966. The Use of Factor Analysis in Determining Depositional Environments from Grain-Size Distributions. *Journal of Sedimentary Petrology* 36, 115-125.

- Kodaira, S., No, T., Nakamura, Y., Fujiwara, T., Kaiho, Y., Miura, S., Takahashi, N., Kaneda, Y., Taira, A., 2012. Coseismic fault rupture at the trench axis during the 2011 Tohoku-oki earthquake. *Nature Geoscience* 5, 646-650.
- Koestler, A., 1964. *The act of creation* (London, Hutchinson and Co.).
- Kölbl-Ebert, M., 1999. Observing orogeny e Maria Graham's account of the earthquake in Chile in 1822. *Geologische Staatssammlung München, München, Germany*.
- Komar, P.D., 1998. *Beach processes and sedimentation*. Prentice-Hall.
- Komar, P.D., Allan, J.C., 2008. Increasing hurricane-generated wave heights along the US east coast and their climate controls. *Journal of Coastal Research*, 479-488.
- Kondo, H., Toda, S., Okumura, K., Takada, K., Chiba, T., 2008. A fault scarp in an urban area identified by LiDAR survey: a case study on the Itoigawa-Shizuoka Tectonic Line, central Japan. *Geomorphology* 101, 731-739.
- Krumbein, W.C., Pettijohn, F.J., 1938. *Manual of Sedimentary Petrology*. Appleton Century and Crofts, New York.
- Kukla, G.J., Bender, M.L., de Beaulieu, J.-L., Bond, G., Broecker, W.S., Cleveringa, P., Gavin, J.E., Herbert, T.D., Imbrie, J., Jouzel, J., 2002. Last interglacial climates. *Quaternary Research* 58, 2-13.
- Lajoie, K.R., 1986. Coastal tectonics. *Active Tectonics*, 95-124.
- Lambeck, K., Yokoyama, Y., Purcell, T., 2002. Into and out of the Last Glacial Maximum: sea-level change during Oxygen Isotope Stages 3 and 2. *Quaternary Science Reviews* 21, 343-360.
- Lange, D., Tilmann, F., Barrientos, S.E., Contreras-Reyes, E., Methe, P., Moreno, M., Heit, B., Agurto, H., Bernard, P., Vilotte, J.-P., Beck, S., 2012. Aftershock seismicity of the 27 February 2010 Mw 8.8 Maule earthquake rupture zone. *Earth and Planetary Science Letters* 317-318, 413-425.
- Lavenu, A., Cembrano, J., 1999. Compressional-and transpressional-stress pattern for Pliocene and Quaternary brittle deformation in fore arc and intra-arc zones (Andes of Central and Southern Chile). *Journal of Structural Geology* 21, 1669-1691.
- Le Roux, J., Elgueta, S., 2000. Sedimentologic development of a late Oligocene, Miocene forearc embayment, Valdivia Basin Complex, southern Chile. *Sedimentary Geology* 130, 27-44.
- Leclerc, F., Feuillet, N., Perret, M., Cabioch, G., Bazin, S., Lebrun, J.-F., Saurel, J., 2015. The reef platform of Martinique: Interplay between eustasy, tectonic subsidence and volcanism since Late Pleistocene. *Marine Geology* 369, 34-51.
- Leymerie, A., 1841. *Suite du mémoire sur le terrain crétacé du département de l'Aube*. Langlois et Leclercq.
- Li, S., Moreno, M., Rosenau, M., Melnick, D., Oncken, O., 2014. Splay fault triggering by great subduction earthquakes inferred from finite element models. *Geophysical Research Letters* 41, 385-391.
- Liberty, L.M., Finn, S.P., Haeussler, P.J., Pratt, T.L., Peterson, A., 2013. Megathrust splay faults at the focus of the Prince William Sound asperity, Alaska. *Journal of Geophysical Research: Solid Earth* 118, 5428-5441.

- Lieser, K., Grevemeyer, I., Lange, D., Flueh, E., Tilmann, F., Contreras-Reyes, E., 2014. Splay fault activity revealed by aftershocks of the 2010 Mw 8.8 Maule earthquake, central Chile. *Geology* 42, 823-826.
- Limber, P.W., Murray, A.B., 2011. Beach and sea-cliff dynamics as a driver of long-term rocky coastline evolution and stability. *Geology* 39, 1147-1150.
- Lin, Y.-n.N., Sladen, A., Ortega-Culaciati, F., Simons, M., Avouac, J.-P., Fielding, E.J., Brooks, B.A., Bevis, M., Genrich, J., Rietbrock, A., 2013. Coseismic and postseismic slip associated with the 2010 Maule Earthquake, Chile: Characterizing the Arauco Peninsula barrier effect. *Journal of Geophysical Research: Solid Earth* 118, 3142-3159.
- Loget, N., Van Den Driessche, J., 2009. Wave train model for knickpoint migration. *Geomorphology* 106, 376-382.
- Lomnitz, C., 2004. Major Earthquakes of Chile: A Historical Survey, 1535-1960. *Seismological Research Letters* 75, 368-378.
- Lorito, S., Romano, F., Atzori, S., Tong, X., Avallone, A., McCloskey, J., Cocco, M., Boschi, E., Piatanesi, A., 2011. Limited overlap between the seismic gap and coseismic slip of the great 2010 Chile earthquake. *Nature Geoscience* 4, 173-177.
- Loveless, J.P., Allmendinger, R.W., Pritchard, M.E., González, G., 2010. Normal and reverse faulting driven by the subduction zone earthquake cycle in the northern Chilean fore arc. *Tectonics* 29.
- Loveless, J.P., Meade, B.J., 2011. Spatial correlation of interseismic coupling and coseismic rupture extent of the 2011 MW= 9.0 Tohoku-oki earthquake. *Geophysical Research Letters* 38.
- Luján, M., Crespo-Blanc, A., Comas, M., 2011. Morphology and structure of the Camarinal Sill from high-resolution bathymetry: evidence of fault zones in the Gibraltar Strait. *Geo-Marine Letters* 31, 163-174.
- Lyell, C., 1832. *Principles of Geology: Being an Attempt to Explain the Former Changes of the Earth's Surface, by Reference to Causes Now in Operation.* J. Murray.
- Macharé, J., Ortlieb, L., 1992. Plio-Quaternary vertical motions and the subduction of the Nazca Ridge, central coast of Peru. *Tectonophysics* 205, 97-108.
- Mardones, M., Jaque, E., 1991. *Geomorfología del Valle del Río Laja, Extensos de Ponencias y Seminarios.* Servicio Geografico Militar, Santiago, Chile, p. 6.
- Marquardt, C., Lavenu, A., Ortlieb, L., Godoy, E., Comte, D., 2004. Coastal neotectonics in Southern Central Andes: uplift and deformation of marine terraces in Northern Chile (27 S). *Tectonophysics* 394, 193-219.
- Martinez-Martos, M., Galindo-Zaldivar, J., Lobo, F.J., Pedrera, A., Ruano, P., Lopez-Chicano, M., Ortega-Sánchez, M., 2016. Buried marine-cut terraces and submerged marine-built terraces: The Carchuna-Calahonda coastal area (southeast Iberian Peninsula). *Geomorphology* 264, 29-40.
- Masselink, G., Hughes, M., Knight, J., 2014. *Introduction to coastal processes and geomorphology.* Routledge.

- Matsu'ura, T., Kimura, H., Komatsubara, J., Goto, N., Yanagida, M., Ichikawa, K., Furusawa, A., 2014. Late Quaternary uplift rate inferred from marine terraces, Shimokita Peninsula, northeastern Japan: A preliminary investigation of the buried shoreline angle. *Geomorphology* 209, 1-17.
- Matsuda, T., Ota, Y., Ando, M., Yonekura, N., 1978. Fault mechanism and recurrence time of major earthquakes in southern Kanto district, Japan, as deduced from coastal terrace data. *Geological Society of America Bulletin* 89, 1610-1618.
- Maune, D.F., 2007. Digital elevation model technologies and applications: the DEM users manual. Asprs Publications.
- Mauz, B., 1999. Late Pleistocene records of littoral processes at the Tyrrhenian Coast (Central Italy): depositional environments and luminescence chronology. *Quaternary Science Reviews* 18, 1173-1184.
- McCalpin, J.P., 2009. *Paleoseismology*. Academic press.
- Meigs, A., 2013. Active tectonics and the LiDAR revolution. *Lithosphere* 5, 226-229.
- Melnick, D., 2016. Rise of the central Andean coast by earthquakes straddling the Moho. *Nature Geosci* 9, 401-407.
- Melnick, D., Moreno, M., Motagh, M., Cisternas, M., Wesson, R.L., 2013. Splay fault slip during the Mw 8.8 2010 Maule Chile earthquake: REPLY. *Geology* 41, e310-e310.
- Melnick, D., Cisternas, M., Moreno, M., Norambuena, R., 2012a. Estimating coseismic coastal uplift with an intertidal mussel: calibration for the 2010 Maule Chile earthquake (Mw = 8.8). *Quaternary Science Reviews* 42, 29-42.
- Melnick, D., Garcin, Y., Quinteros, J., Strecker, M.R., Olago, D., Tiercelin, J.-J., 2012b. Steady rifting in northern Kenya inferred from deformed Holocene lake shorelines of the Suguta and Turkana basins. *Earth and Planetary Science Letters* 331, 335-346.
- Melnick, D., Moreno, M., Cisternas, M., Tassara, A., 2012c. Darwin seismic gap closed by the 2010 Maule earthquake. *Andean Geology* 39, 558-563.
- Melnick, D., Moreno, M., Motagh, M., Cisternas, M., Wesson, R.L., 2012d. Splay fault slip during the Mw 8.8 2010 Maule Chile earthquake. *Geology* 40, 251-254.
- Melnick, D., Bookhagen, B., Strecker, M.R., Echtler, H.P., 2009. Segmentation of megathrust rupture zones from fore-arc deformation patterns over hundreds to millions of years, Arauco peninsula, Chile. *Journal of Geophysical Research: Solid Earth* (1978-2012) 114.
- Melnick, D., Bookhagen, B., Echtler, H., Strecker, M., 2006. Coastal deformation and great subduction earthquakes, Isla Santa María, Chile (37°S). *Geological Society of America Bulletin* 118, 1463-1480.
- Melnick, D., Echtler, H.P., 2006. Inversion of forearc basins in south-central Chile caused by rapid glacial age trench fill. *Geology* 34, 709-712.
- Melnick, D., Echtler, H., Pineda, V., Bohm, M., Manzanares, A., Vietor, T., 2003. Active faulting and northward growing of the Arauco Peninsula, Southern Chile (37° 30'S), X Congreso Geológico Chileno, Concepcion, Chile.

- Melosh, H., Raefsky, A., 1980. The dynamical origin of subduction zone topography. *Geophysical Journal of the Royal Astronomical Society* 60, 333-354.
- Merritts, D., Bull, W.B., 1989. Interpreting Quaternary uplift rates at the Mendocino triple junction, northern California, from uplifted marine terraces. *Geology* 17, 1020-1024.
- Merritts, D., Chadwick, O., Hendricks, D., 1991. Rates and processes of soil evolution on uplifted marine terraces, northern California. *Geoderma* 51, 241-275.
- Metois, M., Socquet, A., Vigny, C., 2012. Interseismic coupling, segmentation and mechanical behavior of the central Chile subduction zone. *Journal of Geophysical Research: Solid Earth* (1978-2012) 117.
- Mitrovica, J.X., Davis, J.L., 1995. Present-day post-glacial sea level change far from the Late Pleistocene ice sheets: Implications for recent analyses of tide gauge records. *Geophysical Research Letters* 22, 2529-2532.
- Moore, G., Bangs, N., Taira, A., Kuramoto, S., Pangborn, E., Tobin, H., 2007. Three-dimensional splay fault geometry and implications for tsunami generation. *Science* 318, 1128-1131.
- Moore, J.C., 1979. Variation in strain and strain rate during underthrusting of trench deposits. *Geology* 7, 185-188.
- Mordojovich, C., 1981. Sedimentary basins of Chilean Pacific Offshore, In: Halbouty, M.T. (Ed.), *Energy Resources of the Pacific Region*. AAPG Studies in Geology, pp. 63-82.
- Morell, K.D., Fisher, D.M., Gardner, T.W., La Femina, P., Davison, D., Teletzke, A., 2011. Quaternary outer fore - arc deformation and uplift inboard of the Panama Triple Junction, Burica Peninsula. *Journal of Geophysical Research* 116.
- Moreno, M., Melnick, D., Rosenau, M., Baez, J., Klotz, J., Oncken, O., Tassara, A., Chen, J., Bataille, K., Bevis, M., Socquet, A., Bolte, J., Vigny, C., Brooks, B., Ryder, I., Grund, V., Smalley, B., Carrizo, D., Bartsch, M., Hase, H., 2012. Toward understanding tectonic control on the Mw 8.8 2010 Maule Chile earthquake. *Earth and Planetary Science Letters* 321-322, 152-165.
- Moreno, M., Rosenau, M., Oncken, O., 2010. 2010 Maule earthquake slip correlates with pre-seismic locking of Andean subduction zone. *Nature* 467, 198-202.
- Moreno, M.S., Bolte, J., Klotz, J., Melnick, D., 2009. Impact of megathrust geometry on inversion of coseismic slip from geodetic data: Application to the 1960 Chile earthquake. *Geophysical Research Letters* 36.
- Moreno, M.S., Klotz, J., Melnick, D., Echtler, H., Bataille, K., 2008. Active faulting and heterogeneous deformation across a megathrust segment boundary from GPS data, south central Chile (36–39°S). *Geochemistry, Geophysics, Geosystems* 9, Q12024.
- Morris, A., Ferrill, D.A., Henderson, D.B., 1996. Slip-tendency analysis and fault reactivation. *Geology* 24, 275-278.
- Muhs, D.R., 2002. Evidence for the timing and duration of the last interglacial period from high-precision uranium-series ages of corals on tectonically stable coastlines. *Quaternary Research* 58, 36-40.

- Muhs, D.R., Kelsey, H.M., Miller, G.H., Kennedy, G.L., Whelan, J.F., McInelly, G.W., 1990. Age estimates and uplift rates for Late Pleistocene marine terraces: southern Oregon portion of the Cascadia Forearc. *Journal of Geophysical Research* 95, 6685-6698.
- Muhs, D.R., Simmons, K.R., Schumann, R.R., Groves, L.T., DeVogel, S.B., Minor, S.A., Laurel, D., 2014. Coastal tectonics on the eastern margin of the Pacific Rim: late Quaternary sea-level history and uplift rates, Channel Islands National Park, California, USA. *Quaternary Science Reviews* 105, 209-238.
- Mukoyoshi, H., Sakaguchi, A., Otsuki, K., Hirono, T., Soh, W., 2006. Coseismic frictional melting along an out-of-sequence thrust in the Shimanto accretionary complex. Implications on the tsunamigenic potential of splay faults in modern subduction zones. *Earth and Planetary Science Letters* 245, 330-343.
- Munhoven, G., 2002. Glacial-interglacial changes of continental weathering: estimates of the related CO₂ and HCO₃⁻ flux variations and their uncertainties. *Global and Planetary Change* 33, 155-176.
- Muñoz, P., Lange, C., Gutiérrez, D., Hebbeln, D., Salamanca, M., Dezileau, L., Reyss, J., Benninger, L., 2004. Recent sedimentation and mass accumulation rates based on ²¹⁰Pb along the Peru - Chile continental margin. *Deep Sea Research Part II: Topical Studies in Oceanography* 51, 2523-2541.
- Naish, T.R., Kamp, P.J.J., 1997. Sequence stratigraphy of sixth-order (41 k.y.) Pliocene- Pleistocene cyclothems, Wanganui basin, New Zealand: a case for the regressive systems tract. *Geological Society of America Bulletin* 109, 978-999.
- Nakamura, T., Nakamori, T., 2007. A geochemical model for coral reef formation. *Coral Reefs* 26, 741-755.
- Nanayama, F., Satake, K., Furukawa, R., Shimokawa, K., Atwater, B.F., Shigeno, K., Yamaki, S., 2003. Unusually large earthquakes inferred from tsunami deposits along the Kuril trench. *Nature* 424, 660-663.
- Nelson, A.R., Manley, W.F., 1992. Holocene coseismic and aseismic uplift of Isla Mocha, south-central Chile. *Quaternary International* 15-16, 61-76.
- Okada, Y., 1985. Surface deformation due to shear and tensile faults in a half-space. *Bulletin of the Seismological Society of America* 75, 1135-1154.
- Oka, E.A., 2005. A re-evaluation of the great Aleutian and Chilean earthquakes of 1906 August 17. *Geophysical Journal International* 161, 268-282.
- Ota, Y., Hull, A.G., Berryman, K.R., 1991. Coseismic uplift of Holocene marine terraces in the Pakarae River area, eastern North Island, New Zealand. *Quaternary Research* 35, 331-346.
- Ota, Y., Yamaguchi, M., 2004. Holocene coastal uplift in the western Pacific Rim in the context of late Quaternary uplift. *Quaternary International* 120, 105-117.
- Ozawa, S., Nishimura, T., Suito, H., Kobayashi, T., Tobita, M., Imakiire, T., 2011. Coseismic and postseismic slip of the 2011 magnitude-9 Tohoku-Oki earthquake. *Nature* 475, 373-376.
- Palamara, D.R., Dickson, M.E., Kennedy, D.M., 2007. Defining shore platform boundaries using airborne laser scan data: a preliminary investigation. *Earth Surface Processes and Landforms* 32, 945-953.

- Park, J.-O., Tsuru, T., Kodaira, S., Cummins, P.R., Kaneda, Y., 2002. Splay fault branching along the Nankai subduction zone. *Science* 297, 1157-1160.
- Paskoff, R.P., 1977. Quaternary of Chile: the state of research. *Quaternary Research* 8, 2-31.
- Pearson, D.L., 1988. Biology of Tiger Beetles. *Annual Review of Entomology* 33, 123-147.
- Pedoja, K., Husson, L., Johnson, M.E., Melnick, D., Witt, C., Pochat, S., Nexer, M.I., Delcaillau, B., Pinegina, T., Poprawski, Y., 2014. Coastal staircase sequences reflecting sea-level oscillations and tectonic uplift during the Quaternary and Neogene. *Earth-Science Reviews* 132, 13-38.
- Pedoja, K., Husson, L., Regard, V., Cobbold, P.R., Ostanciaux, E., Johnson, M.E., Kershaw, S., Saillard, M., Martinod, J., Furgerot, L., 2011. Relative sea-level fall since the last interglacial stage: Are coasts uplifting worldwide? *Earth-Science Reviews* 108, 1-15.
- Pedoja, K., Shen, J.-W., Kershaw, S., Tang, C., 2008. Coastal Quaternary morphologies on the northern coast of the South China Sea, China, and their implications for current tectonic models: A review and preliminary study. *Marine Geology* 255, 103-117.
- Pérez-Gussinyé, M., Lowry, A., Phipps Morgan, J., Tassara, A., 2008. Effective elastic thickness variations along the Andean margin and their relationship to subduction geometry. *Geochemistry, Geophysics, Geosystems* 9.
- Perfettini, H., Avouac, J.-P., Tavera, H., Kositsky, A., Nocquet, J.-M., Bondoux, F., Chlieh, M., Sladen, A., Audin, L., Farber, D.L., 2010. Seismic and aseismic slip on the central Peru megathrust. *Nature* 465, 78-81.
- Perry, C.T., 1996. Distribution and abundance of macroborers in an upper Miocene reef system, Mallorca, Spain: implications for reef development and framework destruction. *Palaios*, 40-56.
- Plafker, G., Rubin, M., 1978. Uplift history and earthquake recurrence as deduced from marine terraces on Middleton Island, Alaska. *US Geol. Surv. Open File Rep.*, 78 943, 687-721.
- Plafker, G., Savage, J., 1970. Mechanism of the Chilean earthquakes of May 21 and 22, 1960. *Geological Society of America Bulletin* 81, 1001-1030.
- Pleydell, S., Jones, B., 1988. Boring of various faunal elements in the Oligocene-Miocene Bluff Formation of Grand Cayman, British West Indies. *Journal of Paleontology* 62, 348-367.
- Pollitz, F.F., Brooks, B., Tong, X., Bevis, M.G., Foster, J.H., Bürgmann, R., Smalley, R., Vigny, C., Socquet, A., Ruegg, J.-C., 2011. Coseismic slip distribution of the February 27, 2010 Mw 8.8 Maule, Chile earthquake. *Geophysical Research Letters* 38.
- Potter, E.-K., Lambeck, K., 2004. Reconciliation of sea-level observations in the Western North Atlantic during the last glacial cycle. *Earth and Planetary Science Letters* 217, 171-181.
- Prescott, J., Hutton, J.T., 1994. Cosmic ray contributions to dose rates for luminescence and ESR dating: large depths and long-term time variations. *Radiation measurements* 23, 497-500.
- Pulido, N., Yagi, Y., Kumagai, H., Nishimura, N., 2011. Rupture process and coseismic deformations of the 27 February 2010 Maule earthquake, Chile. *Earth Planets and Space* 63, 955-959.
- Rabassa, J., Clapperton, C.M., 1990. Quaternary glaciations of the southern Andes. *Quaternary Science Reviews* 9, 153-174.

- Raitzsch, M., Völker, D., Heubeck, C., 2007. Neogene sedimentary and mass-wasting processes on the continental margin off south-central Chile inferred from dredge samples. *Marine Geology* 244, 166-183.
- Ramsey, C.B., 1994. Analysis of chronological information and radiocarbon calibration: the program OxCal. *Archaeological Computing Newsletter* 41, e16.
- Ramsey, C.B., Staff, R.A., Bryant, C.L., Brock, F., Kitagawa, H., Van Der Plicht, J., Schlolaut, G., Marshall, M.H., Brauer, A., Lamb, H.F., 2012. A complete terrestrial radiocarbon record for 11.2 to 52.8 kyr BP. *Science* 338, 370-374.
- Refice, A., Giachetta, E., Capolongo, D., 2012. SIGNUM: A Matlab, TIN-based landscape evolution model. *Computers & Geosciences* 45, 293-303.
- Regard, V., Saillard, M., Martinod, J., Audin, L., Carretier, S., Pedoja, K., Riquelme, R., Paredes, P., Hérail, G., 2010. Renewed uplift of the Central Andes Forearc revealed by coastal evolution during the Quaternary. *Earth and Planetary Science Letters* 297, 199-210.
- Rehak, K., Strecker, M.R., Echtler, H.P., 2008. Morphotectonic segmentation of an active forearc, 37-41° S, Chile. *Geomorphology* 94, 98-116.
- Reuter, M., Piller, W., Harzhauser, M., Berning, B., Kroh, A., 2009. Sedimentary evolution of a late Pleistocene wetland indicating extreme coastal uplift in southern Tanzania. *Quaternary Research* 73, 136-142.
- Roberts, G., Meschis, M., Houghton, S., Underwood, C., Briant, R.M., 2013. The implications of revised Quaternary palaeoshoreline chronologies for the rates of active extension and uplift in the upper plate of subduction zones. *Quaternary Science Reviews* 78, 169-187.
- Rohling, E., Grant, K., Bolshaw, M., Roberts, A., Siddall, M., Hemleben, C., Kucera, M., 2009. Antarctic temperature and global sea level closely coupled over the past five glacial cycles. *Nature Geoscience* 2, 500-504.
- Rosenbloom, N.A., Anderson, R.S., 1994. Hillslope and channel evolution in a marine terraced landscape, Santa Cruz, California. *Journal of Geophysical Research: Solid Earth* (1978-2012) 99, 14013-14029.
- Ruegg, J.C., Rudloff, A., Vigny, C., Madariaga, R., de Chabaliér, J.B., Campos, J., Kausel, E., Barrientos, S., Dimitrov, D., 2009. Interseismic strain accumulation measured by GPS in the seismic gap between Constitución and Concepción in Chile. *Physics of the Earth and Planetary Interiors* 175, 78-85.
- Ruiz, S., Grandin, R., Dionicio, V., Satriano, C., Fuenzalida, A., Vigny, C., Kiraly, E., Meyer, C., Baez, J.C., Riquelme, S., 2013. The Constitución earthquake of 25 March 2012: A large aftershock of the Maule earthquake near the bottom of the seismogenic zone. *Earth and Planetary Science Letters* 377, 347-357.
- Ruz, M.-H., Meur-Ferec, C., 2004. Influence of high water levels on aeolian sand transport: upper beach/dune evolution on a macrotidal coast, Wissant Bay, northern France. *Geomorphology* 60, 73-87.
- Ryder, I., Rietbrock, A., Kelson, K., Bürgmann, R., Floyd, M., Socquet, A., Vigny, C., Carrizo, D., 2012. Large extensional aftershocks in the continental forearc triggered by the 2010 Maule earthquake, Chile. *Geophysical Journal International* 188, 879-890.

- Saillard, M., Hall, S., Audin, L., Farber, D., Hérail, G., Martinod, J., Regard, V., Finkel, R., Bondoux, F., 2009. Non-steady long-term uplift rates and Pleistocene marine terrace development along the Andean margin of Chile (31 S) inferred from ¹⁰Be dating. *Earth and Planetary Science Letters* 277, 50-63.
- Saillard, M., Hall, S., Audin, L., Farber, D., Regard, V., Hérail, G., 2011. Andean coastal uplift and active tectonics in southern Peru: ¹⁰Be surface exposure dating of differentially uplifted marine terrace sequences (San Juan de Marcona, ~ 15.4 S). *Geomorphology* 128, 178-190.
- Sasaki, K., Omura, A., Murakami, K., Sagawa, N., Nakamori, T., 2004. Interstadial coral reef terraces and relative sea-level changes during marine oxygen isotope stages 3 - 4, Kikai Island, central Ryukyus, Japan. *Quaternary International* 120, 51-64.
- Satake, K., Fujii, Y., Harada, T., Namegaya, Y., 2013. Time and space distribution of coseismic slip of the 2011 Tohoku earthquake as inferred from tsunami waveform data. *Bulletin of the Seismological Society of America* 103, 1473-1492.
- Savage, J., 1983. A dislocation model of strain accumulation and release at a subduction zone. *Journal of Geophysical Research: Solid Earth* 88, 4984-4996.
- Schurr, B., Asch, G.n., Hainzl, S., Bedford, J., Hoechner, A., Palo, M., Wang, R., Moreno, M., Bartsch, M., Zhang, Y., 2014. Gradual unlocking of plate boundary controlled initiation of the 2014 Iquique earthquake. *Nature* 512, 299-302.
- Scott, A.T., Pinter, N., 2003. Extraction of coastal terraces and shoreline-angle elevations from digital terrain models, Santa Cruz and Anacapa Islands, California. *Physical Geography* 24, 271-294.
- Shackleton, N.J., 2000. The 100,000-year ice-age cycle identified and found to lag temperature, carbon dioxide, and orbital eccentricity. *Science* 289, 1897-1902.
- Shackleton, N.J., Imbrie, J., Hall, M., 1983. Oxygen and carbon isotope record of East Pacific core V19-30: implications for the formation of deep water in the late Pleistocene North Atlantic. *Earth and Planetary Science Letters* 65, 233-244.
- Shackleton, N.J., Sanchez-Goni, M.F., Pailler, D., Lancelot, Y., 2003. Marine isotope substage 5e and the Eemian interglacial. *Global and Planetary Change* 36, 151-155.
- Shao, G., Li, X., Liu, Q., Zhao, X., Yano, T., Li, C., 2010. A Slip model of the Feb 27, 2010 Mw 8.9 Maule, Chile Earthquake, EGU General Assembly Conference Abstracts, p. 15704.
- Shennan, I., Bruhn, R., Plafker, G., 2009. Multi-segment earthquakes and tsunami potential of the Aleutian megathrust. *Quaternary Science Reviews* 28, 7-13.
- Shepherd, A., Wingham, D., 2007. Recent sea-level contributions of the Antarctic and Greenland ice sheets. *Science* 315, 1529-1532.
- Sherman, C., Fletcher, C., Rubin, K., 1999. Marine and meteoric diagenesis of Pleistocene carbonates from a nearshore submarine terrace, Oahu, Hawaii. *Journal of Sedimentary Research* 69.
- Sherrod, B., Gomberg, J., 2014. Crustal earthquake triggering by pre-historic great earthquakes on subduction zone thrusts. *Journal of Geophysical Research: Solid Earth* 119, 1273-1294.

- Shikakura, Y., 2014. Marine terraces caused by fast steady uplift and small coseismic uplift and the time-predictable model: Case of Kikai Island, Ryukyu Islands, Japan. *Earth and Planetary Science Letters* 404, 232-237.
- SHOA, 2004. Golfo de Arauco In: 6120 (Ed.), *Cartas nauticas Digitales*. Servicio Hidrografico y Oceanografico de la Armada de Chile, Santiago.
- Sibson, R.H., 1985. A note on fault reactivation. *Journal of Structural Geology* 7, 751-754.
- Siddall, M., Rohling, E., Thompson, W.G., Waelbroeck, C., 2008. Marine isotope stage 3 sea level fluctuations: data synthesis and new outlook. *Reviews of Geophysics* 46.
- Siddall, M., Rohling, E.J., Almogi-Labin, A., Hemleben, C., Meischner, D., Schmelzer, I., Smeed, D., 2003. Sea-level fluctuations during the last glacial cycle. *Nature* 423, 853-858.
- Singh, S., Hananto, N., Chauhan, A., 2011. Enhanced reflectivity of backthrusts in the recent great Sumatran earthquake rupture zones. *Geophysical Research Letters* 38.
- Sommerfield, C.K., Lee, H.J., 2004. Across-shelf sediment transport since the Last Glacial Maximum, southern California margin. *Geology* 32, 345-348.
- Stanford, J.D., Hemingway, R., Rohling, E.J., Challenor, P.G., Medina-Elizalde, M., Lester, A.J., 2011. Sea-level probability for the last deglaciation: A statistical analysis of far-field records. *Global and Planetary Change* 79, 193-203.
- Stofer, S., Moernaut, J., Melnick, D., Echtler, H.P., Arz, H.W., Lamy, F., De Batist, M., Oncken, O., Haug, G.H., 2010. Forearc uplift rates deduced from sediment cores of two coastal lakes in south-central Chile. *Tectonophysics* 495, 129-143.
- Steffen, D., Preusser, F., Schlunegger, F., 2009. OSL quartz age underestimation due to unstable signal components. *Quaternary Geochronology* 4, 353-362.
- Stewart, I.S., Sauber, J., Rose, J., 2000. Glacio-seismotectonics: ice sheets, crustal deformation and seismicity. *Quaternary Science Reviews* 19, 1367-1389.
- Storms, J.E., Swift, D.J.P., 2003. Shallow-marine sequences as the building blocks of stratigraphy: insights from numerical modelling. *Basin Research* 15, 287-303.
- Strecker, M., Bloom, A., Gilpin, L., Taylor, F., 1986. Karst morphology of uplifted Quaternary coral limestone terraces: Santo Island. Vanuatu: *Zeitschrift für Geomorphologie* 30, 387-405.
- Subarya, C., Chlieh, M., Prawirodirdjo, L., Avouac, J.-P., Bock, Y., Sieh, K., Meltzner, A.J., Natawidjaja, D.H., McCaffrey, R., 2006. Plate-boundary deformation associated with the great Sumatra-Andaman earthquake. *Nature* 440, 46-51.
- Suito, H., Freymueller, J.T., 2009. A viscoelastic and afterslip postseismic deformation model for the 1964 Alaska earthquake. *Journal of Geophysical Research: Solid Earth* (1978-2012) 114.
- Sunamura, T., 1983. Processes of sea cliff and platform erosion. *CRC Handbook of Coastal Processes and Erosion*, CRC Press, Boca Raton Florida, 233-265.
- Sunamura, T., 1992. *Geomorphology of rocky coasts*. John Wiley & Son Ltd.

- Swann, G.E., Mackay, A.W., Leng, M.J., Demory, F., 2005. Climatic change in Central Asia during MIS 3/2: a case study using biological responses from Lake Baikal. *Global and Planetary Change* 46, 235-253.
- Talling, P.J., 1998. How and where do incised valleys form if sea level remains above the shelf edge? *Geology* 26, 87-90.
- Tassara, A., Götze, H.J., Schmidt, S., Hackney, R., 2006. Three-dimensional density model of the Nazca plate and the Andean continental margin. *Journal of Geophysical Research: Solid Earth* (1978-2012) 111.
- Taylor, F.W., Briggs, R.W., Frohlich, C., Brown, A., Hornbach, M., Papabatu, A.K., Meltzner, A.J., Billy, D., 2008. Rupture across arc segment and plate boundaries in the 1 April 2007 Solomons earthquake. *Nature geoscience* 1, 253-257.
- Taylor, F.W., Frohlich, C., Lecolle, J., Strecker, M., 1987. Analysis of partially emerged corals and reef terraces in the central Vanuatu arc: Comparison of contemporary coseismic and nonseismic with Quaternary vertical movements. *Journal of Geophysical Research: Solid Earth* (1978-2012) 92, 4905-4933.
- Tebbens, S.F., Cande, S.C., 1997. Southeast Pacific tectonic evolution from Early Oligocene to Present. *Journal of Geophysical Research: Solid Earth* 102, 12061-12084.
- Thatcher, W., 1984. The earthquake deformation cycle, recurrence, and the time predictable model. *Journal of Geophysical Research: Solid Earth* 89, 5674-5680.
- Thébaudeau, B., Trenhaile, A.S., Edwards, R.J., 2013. Modelling the development of rocky shoreline profiles along the northern coast of Ireland. *Geomorphology* 203, 66-78.
- Thornburg, T.M., Kulm, L.D., 1987a. Sedimentation in the Chile Trench: Depositional morphologies, lithofacies, and stratigraphy. *Geological Society of America Bulletin* 98, 33-52.
- Thornburg, T.M., Kulm, L.D., 1987b. Sedimentation in the Chile Trench: petrofacies and provenance. *Journal of Sedimentary Research* 57.
- Thornton, E.B., Guza, R., 1983. Transformation of wave height distribution. *J. Geophys. Res* 88, 5925-5938.
- Toda, S., Tsutsumi, H., 2013. Simultaneous Reactivation of Two, Subparallel, Inland Normal Faults during the Mw 6.6 11 April 2011 Iwaki Earthquake Triggered by the Mw 9.0 Tohoku, Earthquake. *Bulletin of the Seismological Society of America* 103, 1584-1602.
- Tong, X., Sandwell, D., Luttrell, K., Brooks, B., Bevis, M., Shimada, M., Foster, J., Smalley, R., Parra, H., Báez Soto, J.C., Blanco, M., Kendrick, E., Genrich, J., Caccamise, D.J., 2010. The 2010 Maule, Chile earthquake: Downdip rupture limit revealed by space geodesy. *Geophysical Research Letters* 37, L24311.
- Trenhaile, A., 2000. Modeling the development of wave-cut shore platforms. *Marine Geology* 166, 163-178.
- Trenhaile, A., 2001. Modelling the Quaternary evolution of shore platforms and erosional continental shelves. *Earth Surface Processes and Landforms* 26, 1103-1128.

- Trenhaile, A., Pepper, D., Trenhaile, R., Dalimonte, M., 1998. Stacks and notches at Hopewell Rocks, New Brunswick, Canada. *Earth Surface Processes and Landforms* 23, 975-988.
- Trenhaile, A.S., 2002a. Modeling the development of marine terraces on tectonically mobile rock coasts. *Marine Geology*, 341-361.
- Trenhaile, A.S., 2002b. Rock coasts, with particular emphasis on shore platforms. *Geomorphology* 48, 7-22.
- Turcotte, D., Schubert, G., 1982. *Geodynamics: Applications of continuum physics to geological problems*, 450 pp. John Wiley, New York.
- Twidale, C., Bourne, J., Romani, J.V., 2005. Beach etching and shore platforms. *Geomorphology* 67, 47-61.
- Udías, A., Madariaga, R., Buforn, E., Muñoz, D., Ros, M., 2012. The Large Chilean Historical Earthquakes of 1647, 1657, 1730, and 1751 from Contemporary Documents. *Bulletin of the Seismological Society of America* 102, 1639-1653.
- Valensise, G., Pantosti, D., 1992. A 125 Kyr -long geological record of seismic source repeatability: the Messina Straits (southern Italy) and the 1908 earthquake (Ms 7.1/2). *Terra Nova* 4, 472-483.
- Valle-Levinson, A., Atkinson, L.P., Figueroa, D., Castro, L., 2003. Flow induced by upwelling winds in an equatorward facing bay: Gulf of Arauco, Chile. *Journal of Geophysical Research: Oceans* (1978-2012) 108.
- Van Andel, T., Perissoratis, C., 2006. Late Quaternary depositional history of the North Evvoikos Gulf, Aegean Sea, Greece. *Marine Geology* 232, 157-172.
- Vargas, G., Farias, M., Carretier, S., Tassara, A., Baize, S., Melnick, D., 2011. Coastal uplift and tsunami effects associated to the 2010 M(w)8.8 Maule earthquake in Central Chile. *Andean geology* 38, 219-238.
- Vargas, I., 2005. Análisis morfoestructural, sedimentológico y geoquímico del margen continental chileno entre los 36° y 37°S, Departamento de Ciencias de la Tierra. Universidad de Concepcion, Concepcion, p. 117.
- Victor, P., Sobiesiak, M., Glodny, J., Nielsen, S., Oncken, O., 2011. Long-term persistence of subduction earthquake segment boundaries: Evidence from Mejillones Peninsula, northern Chile. *Journal of Geophysical Research: Solid Earth* (1978-2012) 116.
- Vigny, C., Rudloff, A., Ruegg, J.-C., Madariaga, R., Campos, J., Alvarez, M., 2009. Upper plate deformation measured by GPS in the Coquimbo Gap, Chile. *Physics of the Earth and Planetary Interiors* 175, 86-95.
- Vigny, C., Socquet, A., Peyrat, S., Ruegg, J.-C., Métois, M., Madariaga, R., Morvan, S., Lancieri, M., Lacassin, R., Campos, J., Carrizo, D., Bejar-Pizarro, M., Barrientos, S., Armijo, R., Aranda, C., Valderas-Bermejo, M.-C., Ortega, I., Bondoux, F., Baize, S., Lyon-Caen, H., Pavez, A., Vilotte, J.P., Bevis, M., Brooks, B., Smalley, R., Parra, H., Baez, J.-C., Blanco, M., Cimbaro, S., Kendrick, E., 2011. The 2010 Mw 8.8 Maule Megathrust Earthquake of Central Chile, Monitored by GPS. *Science* 332, 1417-1421.
- Völker, D., Geersen, J., Contreras-Reyes, E., Sellanes, J., Pantoja, S., Rabbell, W., Thorwart, M., Reichert, C., Block, M., Weinrebe, W.R., 2014. Morphology and geology of the continental shelf and

- upper slope of southern Central Chile (33 S-43 S). *International Journal of Earth Sciences* 103, 1765-1787.
- Waldhauser, F., Schaff, D.P., Diehl, T., Engdahl, E.R., 2012. Splay faults imaged by fluid-driven aftershocks of the 2004 Mw 9.2 Sumatra-Andaman earthquake. *Geology* 40, 243-246.
- Wang, K., 2007. Elastic and viscoelastic models of crustal deformation in subduction earthquake cycles. *The seismogenic zone of subduction thrust faults*, 540-575.
- Wang, K., Hu, Y., 2006. Accretionary prisms in subduction earthquake cycles: The theory of dynamic Coulomb wedge. *Journal of Geophysical Research: Solid Earth* (1978-2012) 111.
- Watts, A., Daly, S., 1981. Long wavelength gravity and topography anomalies. *Annual Review of Earth and Planetary Sciences* 9, 415-448.
- Weber, G.E., 1990. Late Pleistocene slip rates on the San Gregorio fault zone at Point Ano Nuevo, San Mateo County, California.
- Webster, J.M., Wallace, L., Silver, E., Applegate, B., Potts, D., Braga, J.C., Riker, A., Coleman, K., Gallup, C., 2004. Drowned carbonate platforms in the Huon Gulf, Papua New Guinea. *Geochemistry, Geophysics, Geosystems* 5.
- Wells, D.L., Coppersmith, K.J., 1994. New empirical relationships among magnitude, rupture length, rupture width, rupture area, and surface displacement. *Bulletin of the Seismological Society of America* 84, 974-1002.
- Wells, R.E., Blakely, R.J., Sugiyama, Y., Scholl, D.W., Dinterman, P.A., 2003. Basin-centered asperities in great subduction zone earthquakes: A link between slip, subsidence, and subduction erosion? *Journal of Geophysical Research: Solid Earth* 108.
- Wendt, J., Oglesby, D.D., Geist, E.L., 2009. Tsunamis and splay fault dynamics. *Geophysical Research Letters* 36.
- Wenzel, G., Wathelet, J., Slighta, G., Vigneras, O., 1975. Mapas de minas de carbon de la octava region. ENACAR, Concepcion, p. 7.
- Wesson, R.L., Melnick, D., Cisternas, M., Moreno, M., Ely, L.L., 2015. Vertical deformation through a complete seismic cycle at Isla Santa Maria, Chile. *Nature Geoscience* 8, 547-551.
- Whittaker, J.C., 2010. *Flintknapping: making and understanding stone tools*. University of Texas Press.
- Yildirim, C., Melnick, D., Ballato, P., Schildgen, T.F., Echtler, H., Erginal, A.E., Kfayak, N.G.n., Strecker, M.R., 2013. Differential uplift along the northern margin of the Central Anatolian Plateau: inferences from marine terraces. *Quaternary Science Reviews* 81, 12-28.
- Young, I., Zieger, S., Babanin, A.V., 2011. Global trends in wind speed and wave height. *Science* 332, 451-455.
- Yue, H., Lay, T., Rivera, L., An, C., Vigny, C., Tong, X., Báez Soto, J.C., 2014. Localized fault slip to the trench in the 2010 Maule, Chile Mw= 8.8 earthquake from joint inversion of high-rate GPS, teleseismic body waves, InSAR, campaign GPS, and tsunami observations. *Journal of Geophysical Research: Solid Earth*.

Zazo, C., Goy, J.L., Dabrio, C.J., Bardají, T., Hillaire-Marcel, C., Ghaleb, B., González-Delgado, J.-Á., Soler, V., 2003. Pleistocene raised marine terraces of the Spanish Mediterranean and Atlantic coasts: records of coastal uplift, sea-level highstands and climate changes. *Marine Geology* 194, 103-133.

Zecchin, M., Civile, D., Caffau, M., Roda, C., 2009. Facies and cycle architecture of a Pleistocene marine terrace (Crotone, southern Italy): A sedimentary response to late Quaternary, high-frequency glacio-eustatic changes. *Sedimentary Geology* 216, 138-157.

Zielke, O., Arrowsmith, J.R., 2012. LaDiCaoz and LiDARimager, MATLAB GUIs for LiDAR data handling and lateral displacement measurement. *Geosphere* 8, 206-221.

Zielke, O., Arrowsmith, J.R., Ludwig, L.G., Akciz, S.O., 2010. Slip in the 1857 and earlier large earthquakes along the Carrizo Plain, San Andreas Fault. *Science* 327, 1119-1122.

Zielke, O., Klinger, Y., Arrowsmith, J.R., 2015. Fault slip and earthquake recurrence along strike-slip faults. *Contributions of high-resolution geomorphic data. Tectonophysics* 638, 43-62.

Appendix A: Sedimentology and dating of the Santa Maria Formation

A.1 Mineralogy of the Santa María Formation (SMF) and sediment source

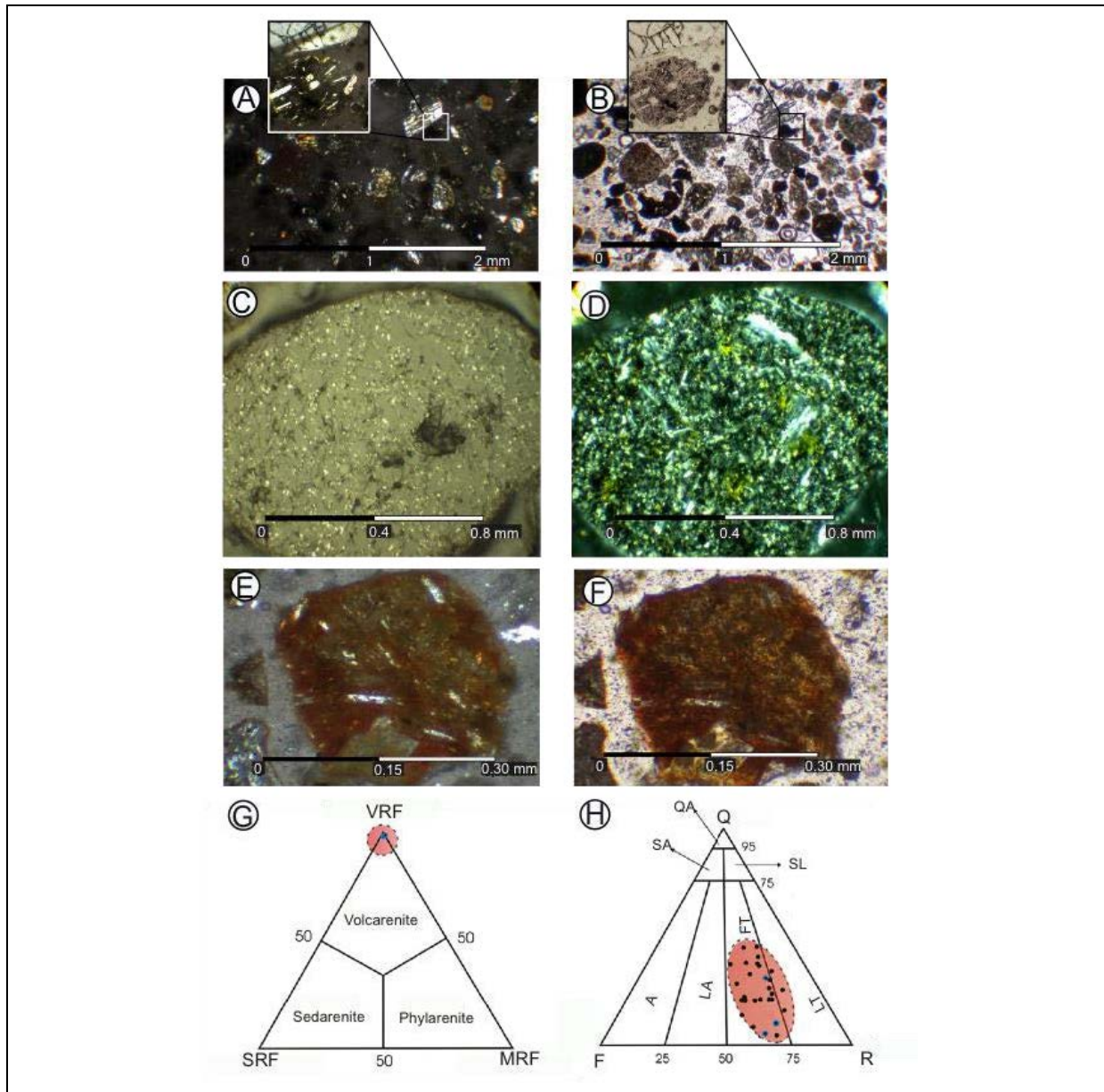


Figure A1: Mineralogy of the SMF. A and B: Cross- and plane-polarized light views of the mineralogy of *Fl* facies in SMF, notice the abundance of andesitic volcanic fragments (~80%). C and D: Cross- and plane-polarized light view of volcanic grains, with an andesitic composition and porphyritic texture. E and F: Cross- and plane-polarized light views of the weathering effects in volcanic fragments, the fine-grained matrix has been replaced with iron hydroxides (goethite) and clays. G and H: The SMF black sand consists of volcarenites and feldspathic litharenites (Folk, 1980). The axes for Figure G are: VRF: Volcanic rock fragments; SRF: Sedimentary rocks fragments; MRF: Metamorphic rock fragments. Axes for Figure H are: Q: Quartz; F: Feldspar; R: Rock fragments. Classifications if Figure H are: LT: Litharenite; FT: Feldspathic litharenite; LA: Lithic arcose; A: Arcose; SA: Subarcose; SL: Sublitharenite; QA: Quartzarenite.

The SMF is composed by black sandstone, transported from the Andean volcanic arc to the coastal region by the Bio-Bio River. Sediments consist of volcanic and feldspathic litharenites, based on the classification of Folk (1980) (Figure A1G and A1H). *Fls*, *Fl* and *Msc* facies contain 80 to 85% of andesitic fragments (Figure A1A – A1B) and only 2% of terrigenous material; quartz and feldspars are scarce not exceeding 15%. These facies have no effects of pedogenesis or iron oxides precipitation.

Terrestrial sediments, characterized by *Sxs* and *Sm* facies, consist of moderately to highly weathered feldspathic litharenites (Figure A1E and A1F). Metallic minerals are altered to limonite and clay cement resulting from the effects of weathering and pedogenesis. The sand fraction is dominated by andesitic grains (50-65%) and feldspars (20-25%). Modern environments (section A.3) are characterized by less altered black sand, identical in composition to those of the SMF (Figure A1C and A1D). Andesitic clasts preserve their metallic minerals with less oxidation. The same andesitic composition was also observed in the uplifted Holocene beach ridges and dunes.

The effect of pedogenesis in the SMF is predominantly restricted to the terrestrial facies and the position along the section. The upper levels of the SMF are those affected by minor weathering. Iron oxide colloids often precipitates at a maximum depth of ~3 m below the surface. The upper contacts of *Ps* loamy facies are often cemented by iron oxide colloids (goethite), this occurs as a result of the porosity contrast between facies, controlling the position of the phreatic level. Shallow marine facies at lower positions within the sections are less altered and cemented preserving the original texture of grains.

A.2 Modern and Holocene depositional environments

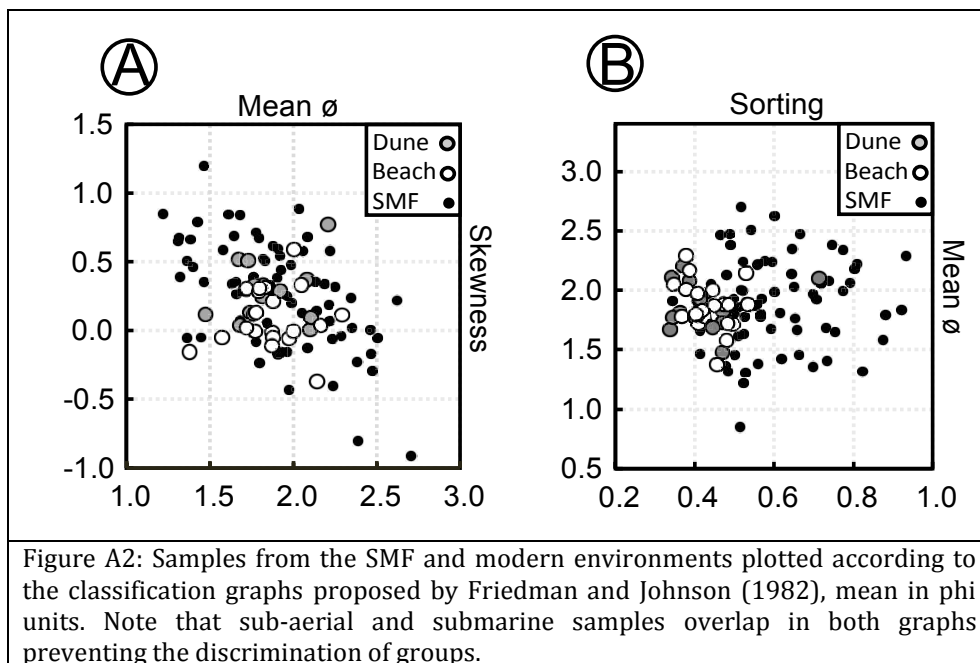
During the Quaternary the Bio-Bio River has supplied a large quantity of volcanic material to this area, derived from ancient lahar deposits of the Antuco Volcano in the high Andes (Pineda, 1986, 1999; Scholl et al., 1970; Galli, 1967; Brüggén, 1941). These predominantly black sands have been transported by the littoral drift along the coastal areas of the Arauco Bay and to SMI. The modern depositional environments are developed at the eastern part of the SMI and comprise active shorelines, dune fields, and swamps within the Holocene lowlands. Fossil strandlines in the form of raised beach ridges are widely distributed in this area and have been interpreted to be a result of coseismic uplift during great subduction earthquakes (Bookhagen et al., 2006). Dunes are widely distributed within the lowlands, forming series of barchans and blowouts, as well as large dune fields that partially cover the sequence of raised beach ridges. The morphology of the dunes suggests that prevailing southwesterly Pacific winds mainly controls them. All these modern depositional environments were sampled to perform grain-size comparison with the deposits of SMF, these includes (Modern berm, swash-zone, and active dunes).

A.3 Grain size distributions

All samples were sorted according to their degree of consolidation and percentage of fine fraction. Non-consolidated sand was sieved directly following the methodology proposed by Pettijohn et al. (1987); consolidated and semi-consolidated sediments were soaked in hydrogen peroxide, isolating the sand fraction by humid sieving.

The SMF sediments are characterized by distinctive statistical distributions reflected in their granulometric parameters and in the general fining-upwards trend in grain size (Figure 11). Grain size distributions are unimodal and bimodal comprising mud (silt and clay) and sand fraction. Bimodal populations are associated with *Ps*, *Bs*, *Sm* and *Sxs* facies, although they are characterized by more than 40% of fine fraction (Figure 9E). The presence of clay and silt in the *Ss* and *Ms* facies is interpreted as a result of weathering and pedogenesis. In turn, the different amounts of silt associated with *Fl* and *Fls* facies are probably resulting from different deposition depths along the shore.

The granulometric parameters from both samples of the SMF and of the modern environments were graphically represented according to the method proposed by Friedman and Johnson (1982) (Figures A2A and A2B), in order to test a preliminary classification of depositional environments. In these graphs the area is divided in zones that separate different depositional environments. The results are not consistent at all with the discrimination methods proposed by Friedman and Johnson (1982), as modern beach and dune deposits are not distributed according their defined environment.



A.4 Granulometric model of depositional environments

A.4.1 Factor analysis

Statistical tests are used to detect hidden relationships between samples by considering their granulometric characteristics; we study the grain populations by a R-mode factor analysis, following the methodology proposed by Pino and Navarro (2005) focused on unraveling the transport mechanism. To evaluate if the dataset is suitable for a factor analysis, a correlation matrix test was performed. The determinant coefficient for the correlation matrix (Table A1)

(Det=0.307) is different from zero and relatively low, indicating that the sample population is highly correlated and the matrix is not singular and appropriate for a factor analysis.

Table A1. Correlation matrix

	Mean	Sorting	Skewness	Kurtosis
Mean	1	0.058	-0.615	-0.288
Sorting		1	0.217	-0.532
Skewness			1	0.277
Kurtosis				1

The factor loads show that the granulometric parameters are independent in the plane generated by the selected factors indicating a priori associations:

Factor I explains 46.13% of the total variance, where the mean and skewness represent the main factor loads but with opposite sign. This relation can be interpreted in terms of their transport characteristics, considering for example the sand dunes that are mainly composed of fine to medium sand and characterized by positive skewness due the wind transport. The contrary case can be observed in the swash zone or the upper shore-face, characterized usually by medium to coarse fractions with negative skewness.

Factor II explains 35.81% of the total variance, where the sorting shows positive loads and kurtosis negative. This relation is not completely clear and could be related to beach-dune sediment interactions; usually beach sediments are characterized by mesocurtic distributions whereas dune sands are characterized by good sorting. The opposite relation between both parameters could be interpreted as a result of continuous recycling processes between platicurtic to mesocurtic beach sediments and well sorted wind transported sand as commonly occurs in the foreshore to backshore environment.

A second factor analysis of 28 samples collected from present-day depositional environments, and 14 samples from the SMF was carried out. The obtained factor loadings for the sample population evince a clear separation in two different groups. The first group is composed by beach sands that includes samples from the swash zone, shore face and berm sub-environments. The second group consists of samples of active and inactive dunes and some spurious samples of beach environments from SMF that were probably misinterpreted or may share granulometric similarities with sub-aerial sediments. A small overlapping zone is placed between both groups, which include two samples of shore-face and two samples of active dunes (Figure A3).

The factor analysis results showed that two factor groups were sufficient to explain 81.9% of the total variance of the samples. This suggests that two different environments were responsible for most of the grain-size variability. Similarly, the granulometric parameters (mean, skewness, sorting and kurtosis) show a high communality suggesting that only two factors are appropriate to describe the whole population of samples. The factor loadings for each granulometric parameter and for the entire sample population have been rotated according to the Varimax method (Kaiser, 1958) (Figure A4A and A4B).

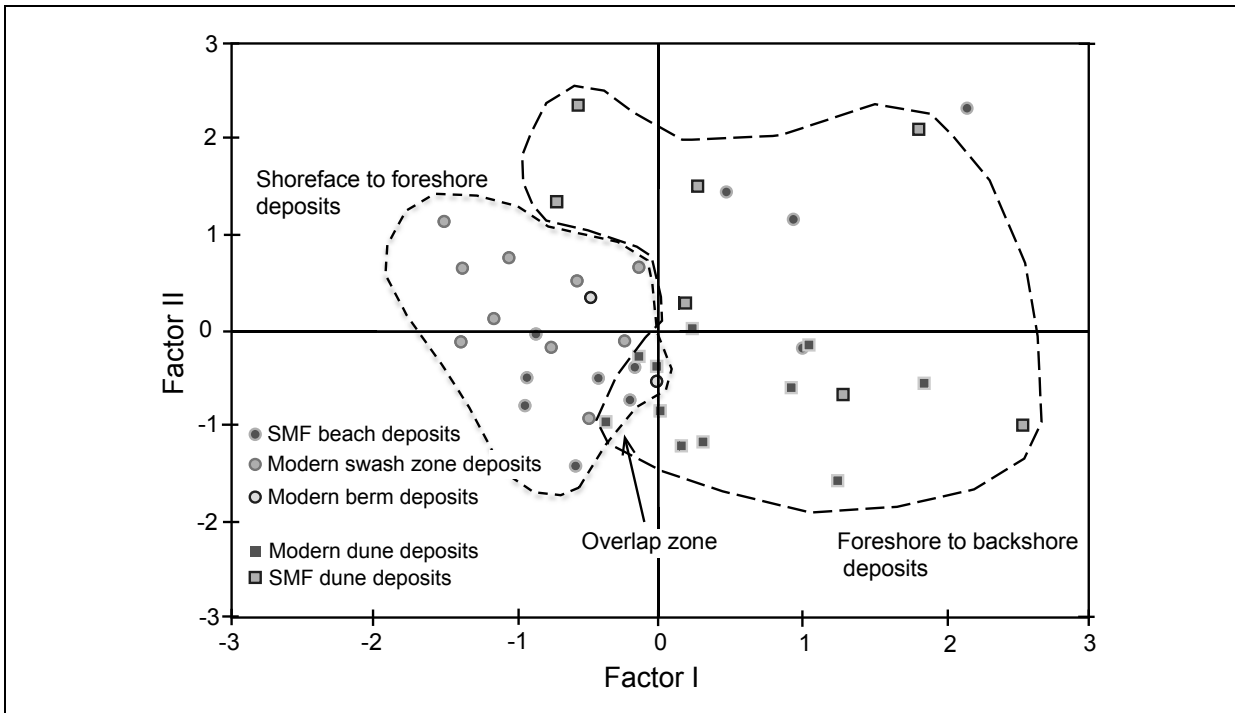


Figure A3: Factor scores for KES (known depositional environment samples), two groups are clearly separated, consisting of beach and eolian sand. A small overlapping zone is placed between both groups, which include three samples of shore-face and three samples of active dunes.

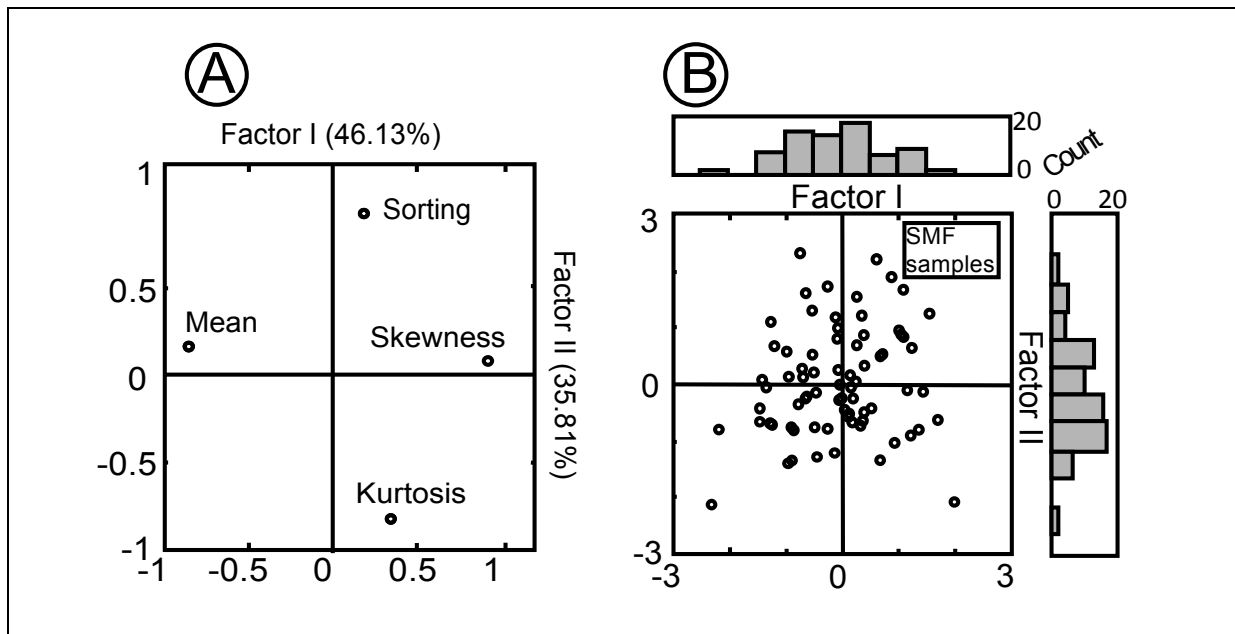


Figure A4: (A) Factor loadings for each granulometric parameter in the SMF samples, and (B) factor scores for the entire SMF sample population. The random distribution of the scores prevents the discrimination of separated groups.

The plot of the factor scores (77 SMF samples) in the bi-dimensional space generated by factors 1 and 2 exhibits a random arrangement (Figure A4B), preventing the discrimination of separated groups. However, since two factors can explain the variability between samples a discriminant analysis can be carried out. On the basis of the resulting groupings we divided the samples collected from the various present-day environments into two classes, using “d” (dune) for

samples of eolian or sub-aerial sediments and “p” (playa) for samples from beach or sub-aquatic environments.

A.4.2 Discriminant analysis

A discriminant analysis was carried out using the modern environments samples and 14 of the SMF samples, whose depositional environment was appointed by facies. The mean, skewness, kurtosis, and sorting were used as environment predictors. Discriminant analyses are used to find linear combinations of features that characterize or separate two or more classes. This method is used to distinguish groups on the basis of their hidden relationships or differences; it is commonly used in sedimentology to distinguish between two or more predefined groups of sediments and their depositional environments on the basis of multiple variables such as mean, skewness, kurtosis, and sorting (e.g., Kasper-Zubillaga and Carranza-Edwards, 2005; Guerzoni et al., 2004; Kasper-Zubillaga and Dickinson, 2001; Stapor and Tanner, 1975). Once the rate of success for discriminating between variables has been calculated, the resulting function is capable of identifying the depositional environment of each sample. The computation method has been described in detail by Nie et al. (1975).

The discriminant analysis method starts by testing the Quadratic Mahalanobis distance, which in this case was 8.886, indicating that categories are well separated with a high discrimination capability. The next step in discriminant analysis is to define the inputs, in this case we define the KES (Known depositional Environment Samples), which consist of 28 samples collected from recent depositional environments and 14 samples from the SMF whose depositional environment has been inferred by their facies. Subsequently, we proceed to define the environmental categories, the environment from which modern samples have been collected. In this case we assign “d” for sub-aerial deposited sediments, and “b” for beach or sub-aquatic environment, both categories were used to classify the KES. The obtained classification matrix shows a 100% of accuracy in the KES environment classification respect to their original acquainted environment. The obtained coefficients for the lineal classification functions (Table A2a) are divided in two equations (Table A2b), by replacing the values of mean, skewness, sorting and kurtosis on each equation we determine the depositional environment of each sample. These equations were then used in the SMF samples in order to determine the depositional environments for each sample (Table A3).

Table A2a. Coefficients for lineal classification functions (Discriminant analysis)

Variables	p	d
Mean (M)	1.791554	-1.34367
Sorting (S)	-1.23634	0.927255
Skewness (Sk)	1.863395	-1.39755
Kurtosis (K)	0.365637	-0.27423
Constant	-2.22914	-1.3369

Table A2b. Classification functions

$$SP = -1.337 - 1.344 * M + 0.927 * S - 1.397 * SK - 0.2742 * K \text{ (shallow marine environment)}$$

$$SD = -2.229 + 1.791 * M - 1.23634 * S + 1.863 * SK + 0.365 * K \text{ (backshore environment)}$$

Table A3. Classification of unknown environment samples of SMF using the classification functions (Granulometric Model). The highest value of SD or SP defines the classification of each sample.

Sample	SD	SP	Classification	Sample	SD	SP	Classification
A1	-0.419	-2.694	d	4, 3	1.350	-4.022	d
A2	-1.876	-1.602	b	6, 3	-3.128	-0.662	p
A4	-1.909	-1.577	b	8, 3	2.452	-4.847	d
A5	-1.558	-1.839	d	10, 3	-2.511	-1.124	p
1, 4	1.267	-3.959	d	13, 3	-1.960	-1.539	p
2, 4	0.635	-3.485	d	14, 3	-4.890	0.660	p
3, 4	-1.032	-2.235	d	14, 3a	-5.244	0.925	p
4, 4	-2.300	-1.284	p	16, 3	-1.751	-1.699	p
6, 4	-4.026	0.010	p	17, 3	-3.630	-0.288	p
7, 4	-5.579	1.176	p	U2	-3.287	-0.544	p
8, 4	-5.387	1.033	p	U3	-0.910	-2.327	d
9, 4	-5.118	0.831	p	U4	-2.476	-1.152	p
10, 4	-2.294	-1.287	p	U5	-2.437	-1.181	p
11, 4b	-2.748	-0.946	p	1, 2	0.665	-3.508	d
11, 4t	-2.116	-1.420	p	2, 2	0.581	-3.445	d
14, 4	-2.366	-1.235	p	3, 2	-0.332	-2.761	d
15, 4	-2.964	-0.786	p	5, 2	-2.198	-1.361	p
16, 4	-2.140	-1.404	p	6, 2	-2.958	-0.791	p
17, 4	-2.986	-0.769	p	7, 2	-1.005	-2.255	d
18, 4	-3.271	-0.554	p	9, 2	-2.067	-1.459	p
19, 4	-5.076	0.799	p	9, 2a	-2.541	-1.103	p
20, 4	-5.426	1.062	p	11, 2	-3.988	-0.017	p
21, 4	-5.162	0.863	p	12, 2	-4.472	0.346	p
3, 3	-2.268	-1.308	p	13, 2	-2.042	-1.477	p
5, 1	-2.029	-1.487	p	14, 2	0.571	-3.437	d
6, 1	-2.422	-1.192	p	1, 1	-4.351	0.255	p
7, 1	-0.885	-2.345	d	2, 1	-0.342	-2.753	d
8, 1	-1.014	-2.248	d	3, 1 (H)	-0.291	-2.791	d
12, 1	-3.762	-0.188	p	4, 1 H	-0.460	-2.665	d
13, 1	-2.630	-1.036	p	15, 1	-2.528	-1.113	p

The results of the discriminant analysis are in agreement with those from the factor analysis (Figure A4A) in showing that the mean and skewness are the variables that best discriminate between dune (d) and beach (b) environments. Furthermore, the resultant classification matrix showed 100% accuracy in the classification of the modern samples into to their original environment. The coefficients obtained for the lineal classification functions, which are shown in Table A2a and A2b, were used to classify all the SMF samples as deriving from either “b” or “d” environments.

A.5 Radiocarbon samples

Six new radiocarbon ages were obtained in this study, five from charcoal and wood fragments and one from bulk sediment dating. Wood and charcoal fragments were obtained from within paleosol levels (*Bs* and *Ps* facies). Wood remains, such as those shown on Figure A5, were founded in the upper contact of gley type paleosols. The material consists of weak dark-brown partly carbonified fragments, which preserve their vegetal structure. The size of the wood pieces range between 0.5 cm and 50 cm (Figure A7C and D).

Charcoal fragments like indicated in figure A6B, A6C and A7C are abundant in loamy paleosol levels (*Ps* facies), disseminated between the clay layers of the *Ps* facies. In most cases charcoal fragments were partially replaced by iron oxides and manganese in the rims. The charcoal fragments reproduce the original shape of the parental vegetal material, like in Figure A6C, or forming small rounded concretions coated by iron oxides. The size of charcoal fragments ranges from 0.2 to 2 cm.

Charcoal concretions and wood fragments were studied using Energy Dispersive spectrometry (SEM) in order to analyze the morphology and composition of the dated material. Wood remains preserve their original structure even in carbonified fragments with no evidences of mineral replacement or crystallization in the cavities. Charcoal fragments and charcoal concretions are rich in iron, essentially cubes of pyrite (Figure A8B) that encapsulates the organic fragments destroying the original vegetal structure. Mud, pyrite and silica compose the coating of charcoal concretions, where most of the charcoal is preserved in the lower concretionary layers and in the core of the concretions. This condition is often problematic when picking the samples for ^{14}C dating because a major amount of material is required.

The presence of pyrite suggests a highly reductive environment; however, we cannot explain when and what processes controls the crystallization of pyrite, and why seems to affect only some charcoal fragments. The coexistence of pyrite and limonites suggest that leaching processes have affected this facies after their deposition.

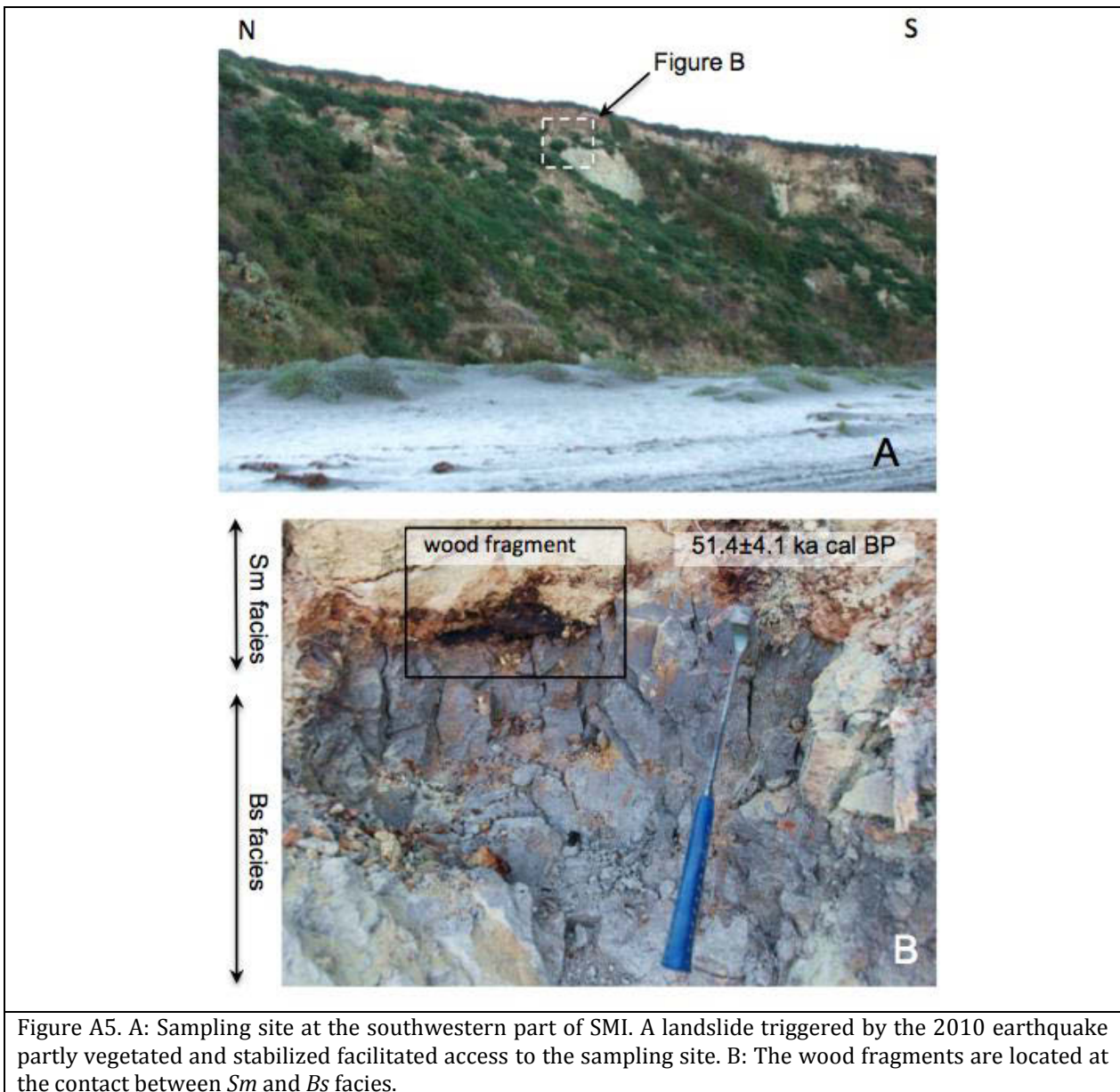


Figure A5. A: Sampling site at the southwestern part of SMI. A landslide triggered by the 2010 earthquake partly vegetated and stabilized facilitated access to the sampling site. B: The wood fragments are located at the contact between *Sm* and *Bs* facies.



Figure A6. A: View of a sampling site in the northwestern part of SMI. A landslide triggered by the 2010 earthquake facilitated access to the sea cliff. B: Angular charcoal fragments disseminated within *Ps* facies suggest no transport and in-situ conditions.

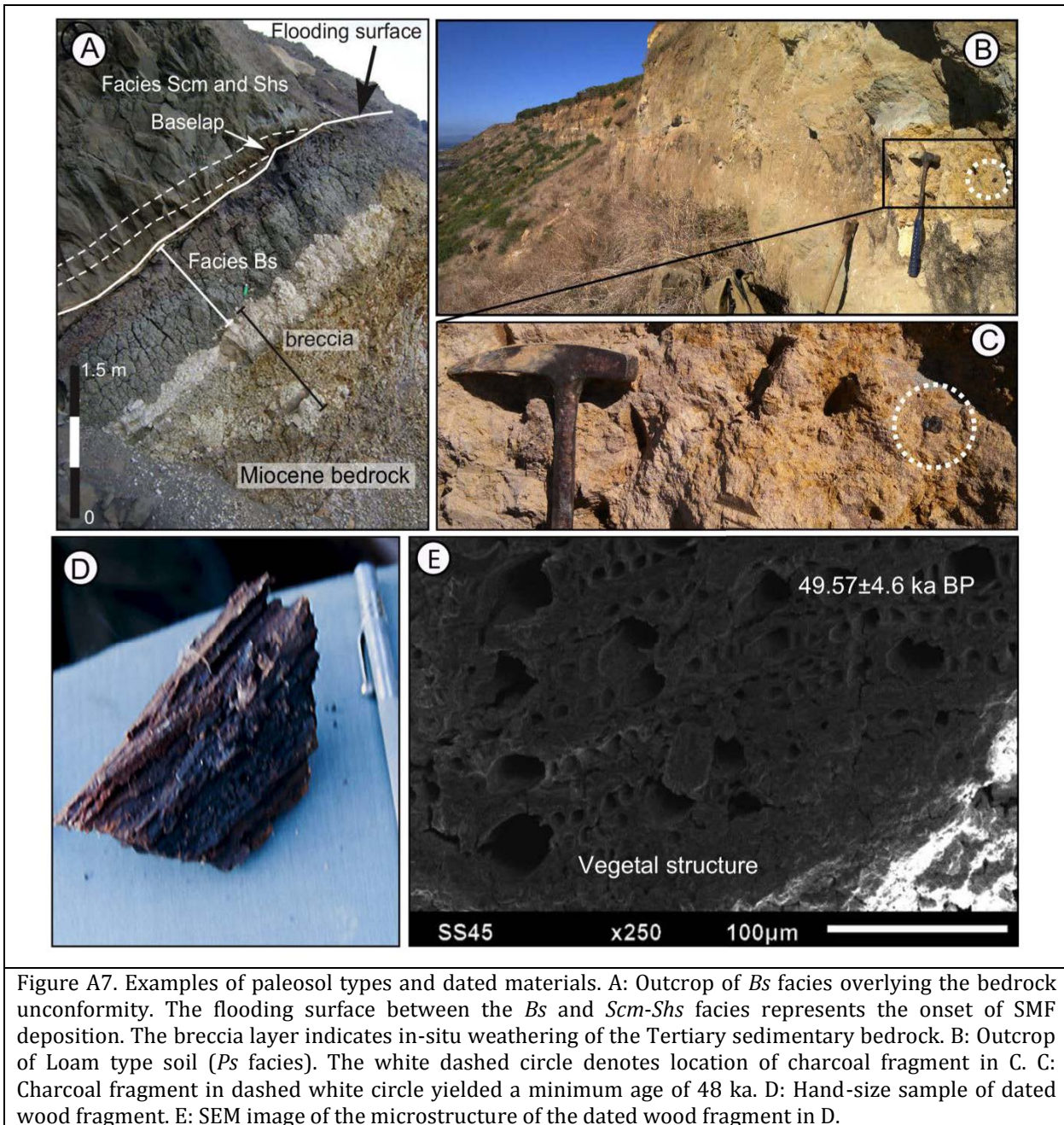


Figure A7. Examples of paleosol types and dated materials. A: Outcrop of *Bs* facies overlying the bedrock unconformity. The flooding surface between the *Bs* and *Scm-Shs* facies represents the onset of SMF deposition. The breccia layer indicates in-situ weathering of the Tertiary sedimentary bedrock. B: Outcrop of Loam type soil (*Ps* facies). The white dashed circle denotes location of charcoal fragment in C. C: Charcoal fragment in dashed white circle yielded a minimum age of 48 ka. D: Hand-size sample of dated wood fragment. E: SEM image of the microstructure of the dated wood fragment in D.

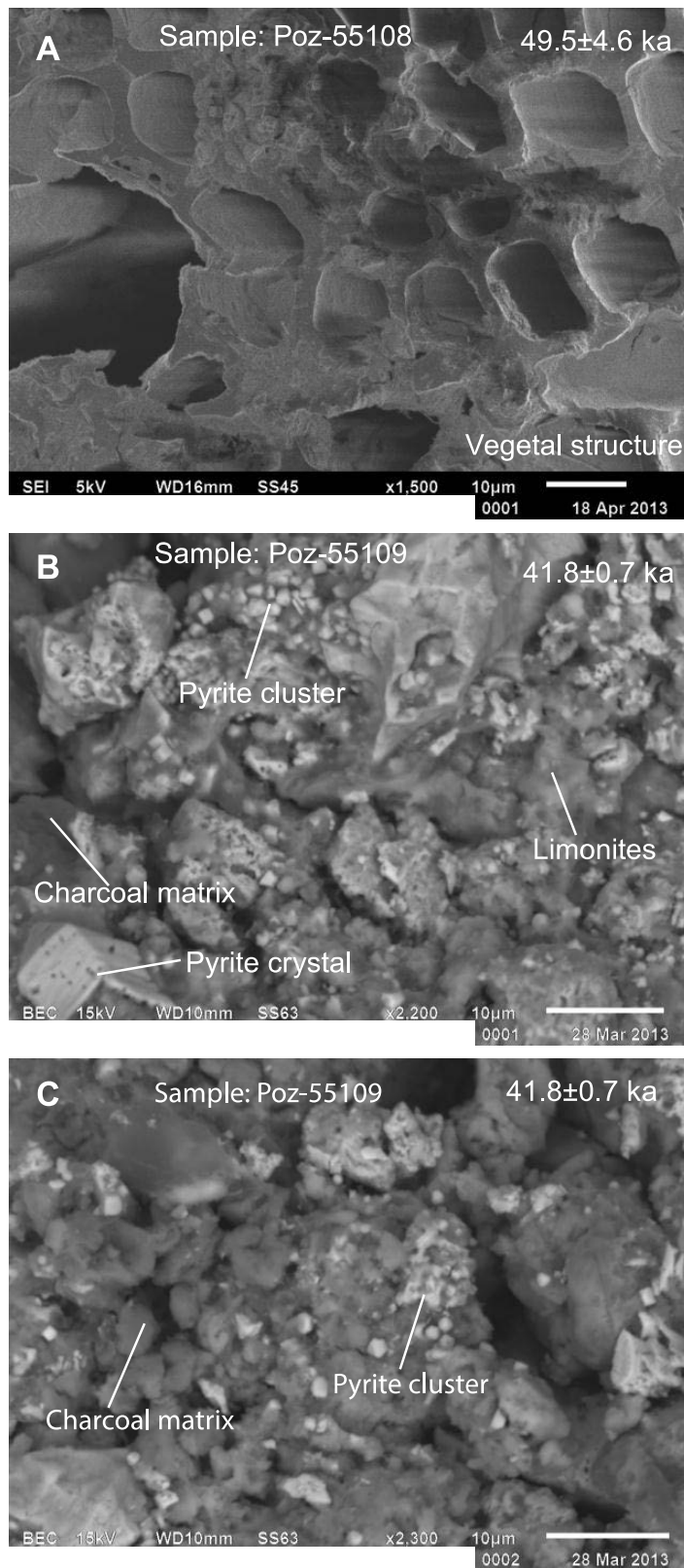


Figure A8. SEM images of dated material. A: Vegetal structure preserved in wood fragments obtained from *Bs* facies. B: Charcoal concretions are coated by pyrite, mud, iron oxides and amorphous silica, preserving charcoal only in the lower concretionary layers. C: Most of the pyrite is arranged in clusters in the external layers of concretions.

A.6 References of appendix A

- Bookhagen, B., Echtler, H.P., Melnick, D., Strecker, M.R., Spencer, J.Q.G., 2006. Using uplifted Holocene beach berms for paleoseismic analysis on the Santa María Island, south-central Chile. *Geophysical Research Letters* 33, L15302.
- Brüggen, J., 1941. El volcán Antuco y la geología glacial del valle del Laja. *Revista Chilena de Historia y Geografía* 91, 356-385.
- Folk, R.L., 1980. *Petrology of Sedimentary Rocks*, Austin, Texas.
- Friedman, G.M., Johnson, K.G., 1982. *Exercises in Sedimentology*. Wiley, New York.
- Galli, C., 1967. *Geología Urbana y suelo de fundación de Concepción y Talcahuano*. Universidad de Concepcion, Concepcion.
- Guerzoni, S., Portaro, R., Trincardi, F., Molinaroli, E., Langone, L., Correggiari, A., Vigliotti, L., Pistolato, M., Falco, G.D., Boccini, V., 2004. Statistical analyses of grain-size, geochemical and mineralogical data in core CM92-43, Central Adriatic basin. *Mem. Ist. ital. Idrobiol* 55, 231-245.
- Pineda, V., 1986. Evolución paleográfica de la cuenca sedimentaria Cretácico-Terciaria de Arauco, in: Frutos, J., Oyarzún, R., Pincheira, M. (Eds.), *Geología y Recursos Minerales de Chile*. Universidad de Concepción, Concepción, pp. 375-390.
- Pino, M., Navarro, R.X., 2005. Geoarqueología del sitio arcaico Chan-Chan 18, costa de Valdivia: Discriminación de ambientes de ocupación humana y su relación con la transgresión marina del Holoceno Medio. *Revista Geológica de Chile* 32, 59-75.
- Scholl, D.W., Christensen, M.N., Von Huene, R., Marlow, M.S., 1970. Peru-Chile Trench sediments and sea-floor spreading. *Geol. Soc. Am. Bull.* 81, 564-568.
- Kasper-Zubillaga, J.J., Carranza-Edwards, A., 2005. Grain size discrimination between sands of desert and coastal dunes from northwestern Mexico. *Revista Mexicana de Ciencias Geológicas* 22, 383-390.
- Kasper-Zubillaga, J.J., Dickinson, W.W., 2001. Discriminating depositional environments of sands from modern source terranes using modal analysis. *Sedimentary Geology* 143, 149-167.
- Nie, H.H., Hull, C.H., Jenkins, J.G., Steinbrenner, K., Bent, D.H., 1975. *SPSS: Statistical package for the social sciences*. McGraw-Hill New York.
- Pettijohn, F.J., Potter, P.E., Siever, R., 1987. *Sand and Sandstone*. Springer, New York.
- Stapor, F.W., Tanner, W.F., 1975. Hydrodynamic Implications of Beach, Beach Ridge and Dune Grain Size Studies. *Journal of Sedimentary Petrology* 45, 926-931.

Appendix B: TerraceM, detailed description and operation

Since over half a Century, marine terraces have been used as long baseline geodetic markers of tectonic deformation in coastal areas providing information about past sea-level variations and surface uplift. On the other hand, the study of marine terraces has benefited enormously from the recent advances in high-resolution topography led by Light Detection and Ranging (LiDAR). By mixing the longstanding concepts of marine terrace analysis, statistical methods, and high-resolution topography, we have developed TerraceM, a MATLAB® graphical user interface (GUI) to analyze wave-cut terraces in several geomorphic scenarios, here we present an intuitive guide to use all the capabilities of TerraceM conducting the user through the different options available for obtaining and processing of marine terrace data.

B.1 TerraceM functions

TerraceM is programmed in Matlab® GUIDE and contain several functions and interfaces stored together in a single folder named Terracem. The main code (Terracem_gui.m) consists of grouped nested functions:

a) **Interface functions:** are associated with the behavior of TerraceM GUI and graphic settings. (e.g. Opening function, plots settings, help buttons, parameters boxes, Information display, directories management, UTM zone and visualization options)

b) **Processing and analysis functions:** include functions to extract and analyze swath profiles, visualize and post-processing the results and export them in different formats. (Extract Swaths, Staircase analysis, Cliff analysis, Stack analysis, Scarp diffusion, Table and swath viewers, Project and Filter shorelines, Display statistics, and export)

c) **Utility functions:** Set of open source Matlab® functions available at Mathworks.com, created by other authors and used in TerraceM (Table 1).

Function	Author	Release	Version	Copyright
LatLon.m	Rafael Palacios	2006	1	Free
vline.m	Brandon Kuczenski	2001	1	Free
plot_google_map.m	Zohar Bar-Yehuda	2013	1.3	Free
acii2xyz.m	Andrew Stevens	2008	1	Free
d1mcell.m	Roland Pfister	2010	1	© Roland Pfister
errorbar_tick.m	Arnaud Laurent	2009	1	Free
peakdet.m	Eli Billauer	2005	1	Free
dem.m	François Beauducel	2014	10	© François Beauducel
ginputc.m	Jiro Doke	2012	1	© Jiro Doke

Table 1: Open source functions nested in TerraceM.

Functions work altogether to display the GUI interface (Fig. 1) and process swath profiles interactively.

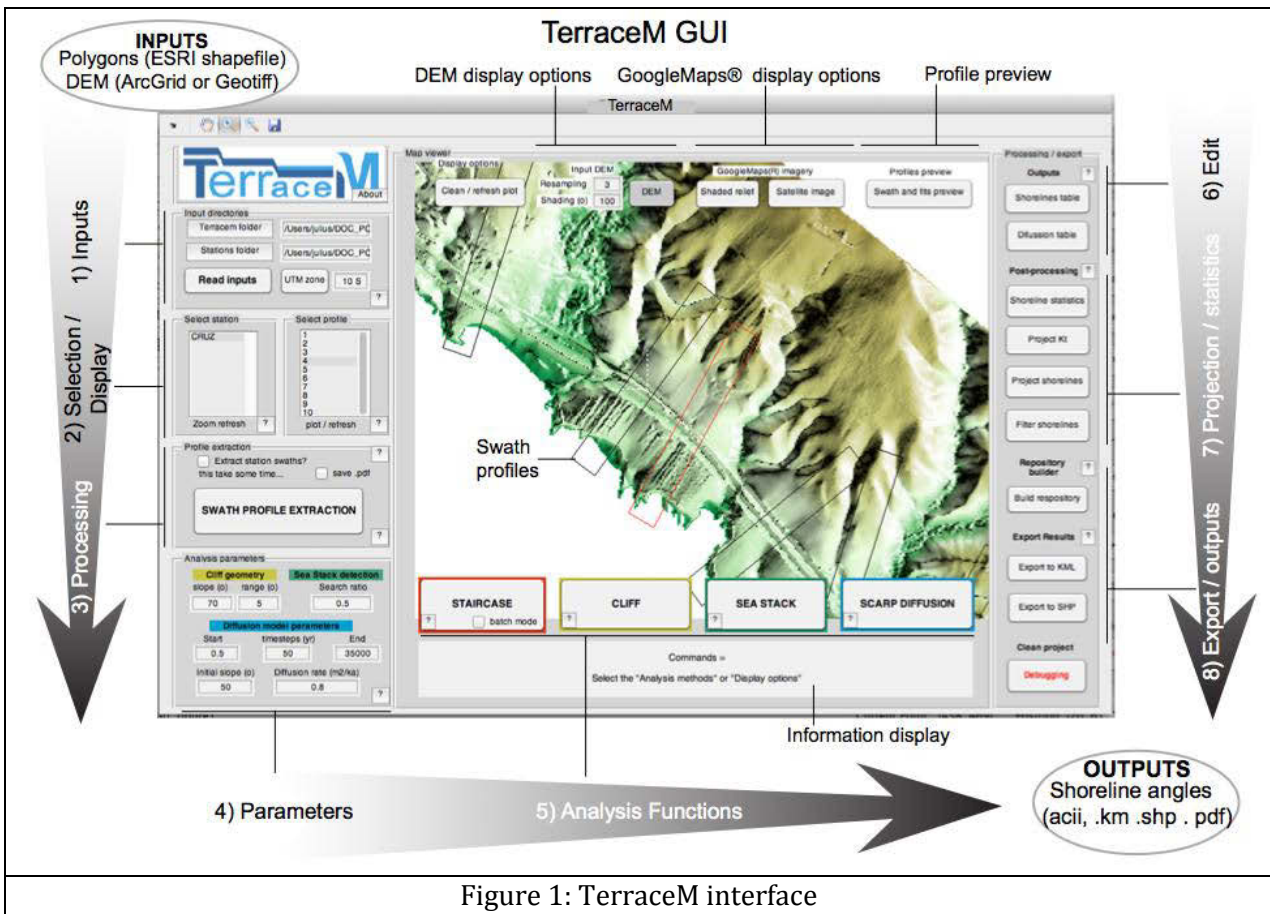


Figure 1: TerraceM interface

B.2 TerraceM workspace

TerraceM is designed to process and analyze a bulk of profiles in a systematic manner, organized in a tree structure of subfolders (Fig. 2A). Stations (or sites) are arranged in independent folders that contain the inputs and outputs of TerraceM. We recommend defining a four-letter station code for each site (e.g. AAAA), which will be also the name of the station folder. Each input file must be named according to the corresponding station, for instance the DEM for station AAAA should be named 'AAAA_dem.tif' and the associated Shapefile with polygons for swath profiles 'AAAA_clip.shp'. This Shapefile should have all the desired polygons, and should be in the standard 2D format.

B.3 TerraceM workflow

The TerraceM workflow (Fig. 2B) consists of several steps that should be executed sequentially in order to analyze a set of profiles. Inputs, Display, Processing and Analysis tools allow obtaining raw shoreline angles, which can be filtered, exported and projected along profiles in the following steps (Editing, Projecting and Export). While TerraceM is running, information messages are prompted inside the command bar, guiding the users through the steps to calculate shoreline angles.

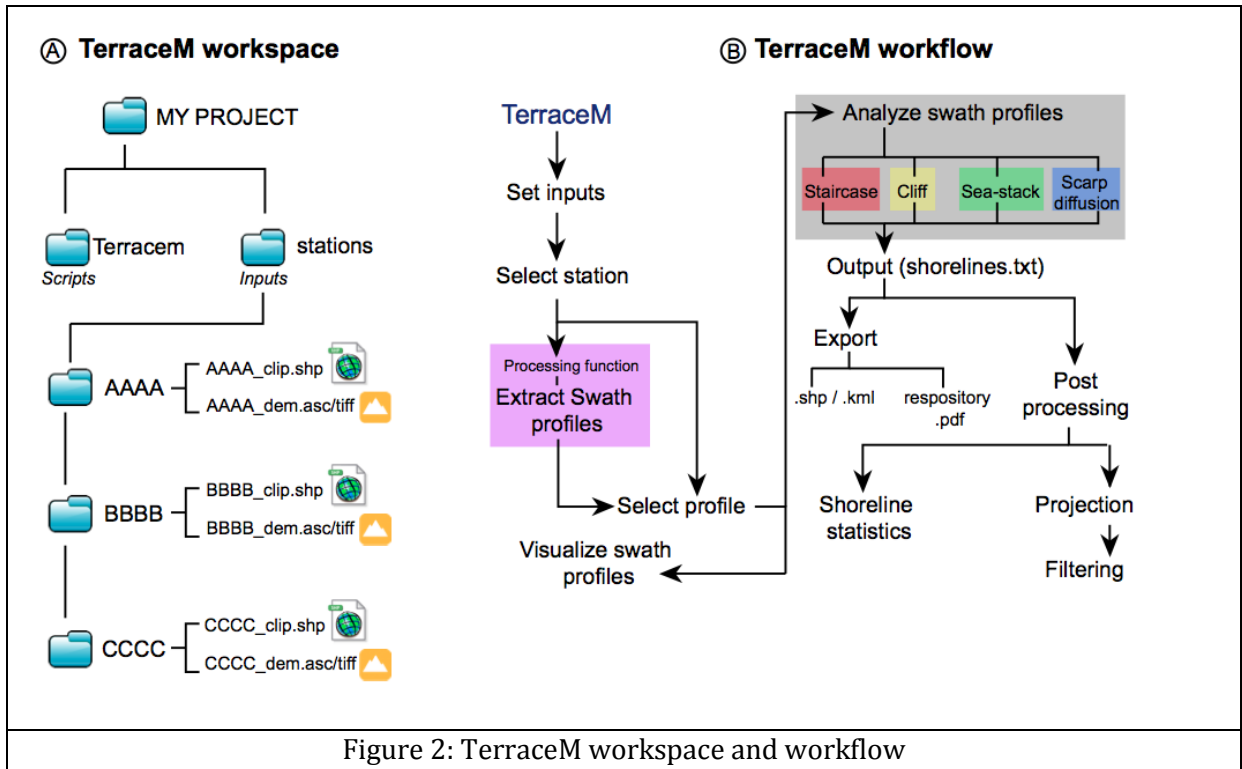


Figure 2: TerraceM workspace and workflow

TerraceM uses two inputs: a) a raster topography in Arcasci or Geotiff formats and b) boxes in shapefile format. The topography, in UTM projection, should be interpolated in order to fill small gaps in data; non-data values used (-32.767 or -99999) are the typical for most of GIS platforms such as Global Mapper® or ArcGIS®. The boxes must be regular polygons that may be created in ArcGIS® using the rectangle tool.

To start TerraceM the user set the “Current Folder” path to the project folder or the TerraceM folder. Then type “Terracem_gui” in the command window (Fig. 3).

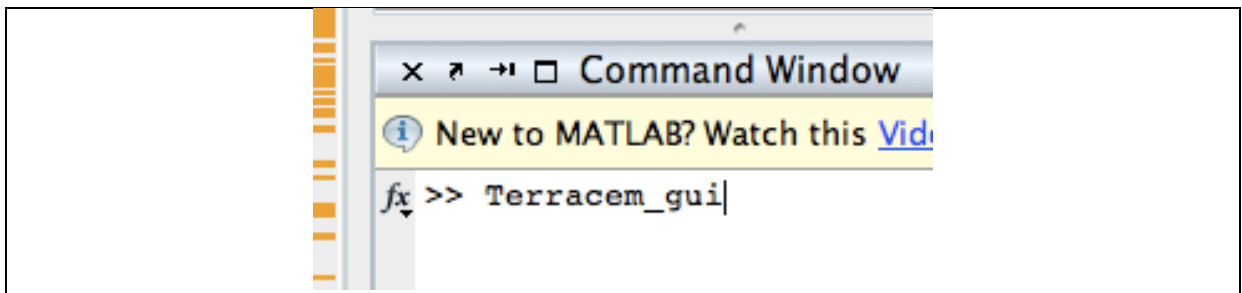


Figure 3: Call to TerraceM in Matlab®

B.3.1 Inputs interface

The next step is to set the directories. Inputs interface contains two pairs of buttons and text boxes used to explore the directories and a third UTM button to locate the UTM zone of the datasets (Fig. 4). Directories include: a) TerraceM folder, where the TerraceM scripts are stored, and b) the stations folder where your inputs (raster and shapefile) are stored. (Fig. 2A). Once the inputs are set, push the “Read inputs” to load the data.

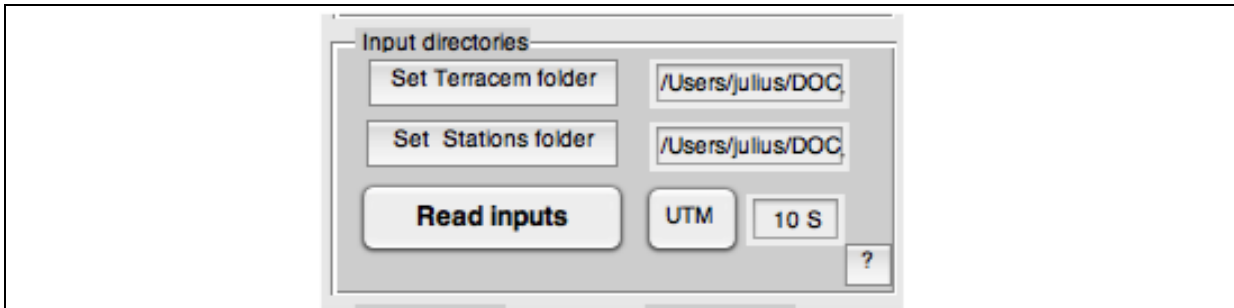


Figure 4: Directories interface

After this step the stations list will be populated with the names of each station. If swath profiles were extracted before, the profile list will be also populated (Fig. 6).

B.3.2 Profile extraction interface

Profile extraction interface contains one big button and two checkboxes, the first checkbox confirm the execution of the swath profiles after pressing “Swath Profile Extraction” (Fig. 5). This efficiency of this routine depends of the size and number of swath profiles and the resolution of the topography and can take several minutes in slow computers. We strongly recommend reduce the ram memory consumption closing other programs while Profile extraction is executed. The second checkbox confirm the creation of a graphic file (.pdf) containing the swath profiles that can be used to check the profiles.

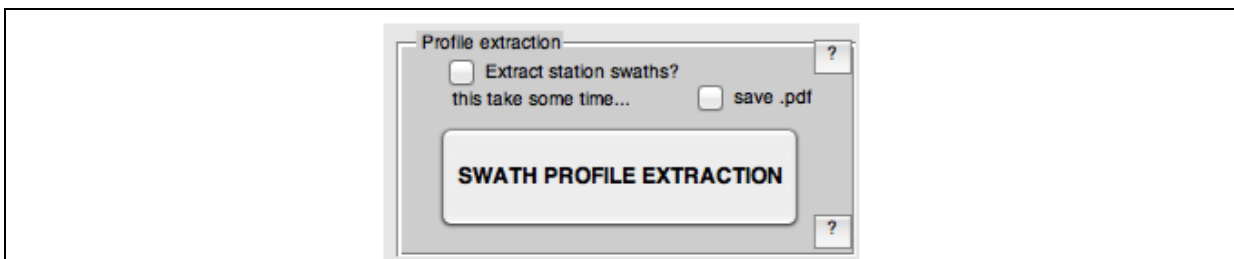


Figure 5: Swath profile extraction interface

Each time the profiles are edited inside a GIS platform (e.g. ArcGIS®) this function shall be used to update the swath profiles. After running swath profile extraction, the profile list will be displayed (Fig. 6).

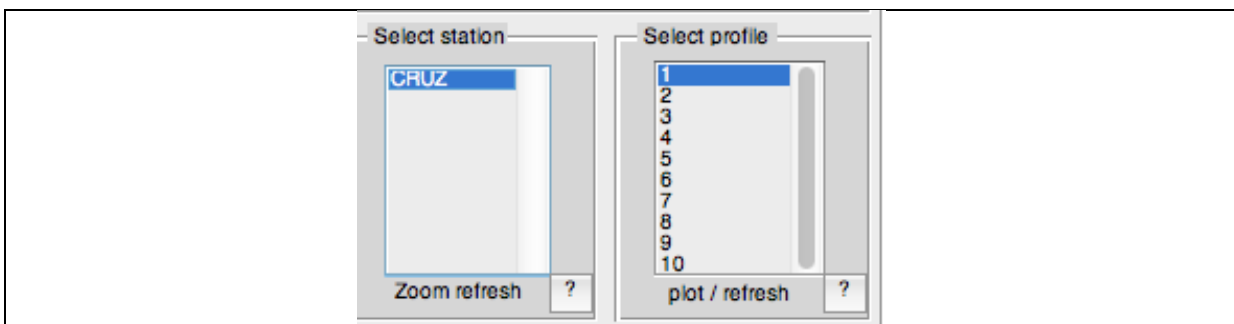


Figure 6: Station and profile selection interface

Click on any profile of the list to identify it location in the main plot, you can change the plot background by modifying the “display Interface”.

B.3.3 Display Interface

The display can be controlled from a rectangular panel at the top of the GUI (Fig. 7). The Display options panel consists of several buttons and two text boxes. The DEM button displays the DEM file used for the analysis, the text boxes are used to control the shaded direction and resolution, the Clean /Refresh button must be used to update the view each time the display options are modified.

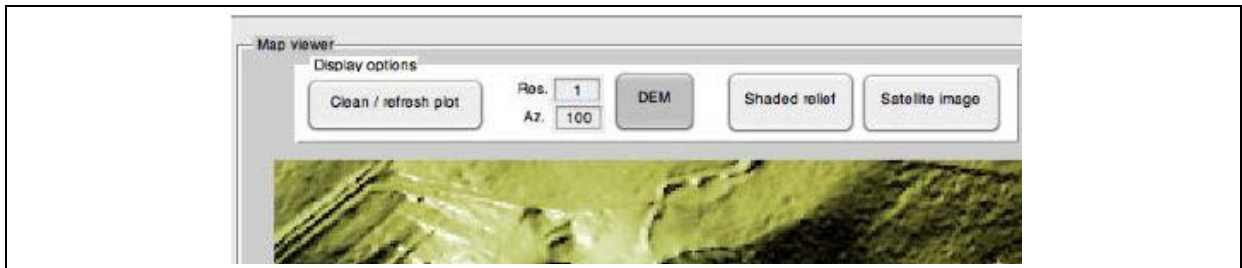


Figure 7: Display options

Shaded relief and satellite image are GoogleMaps® online imagery downloaded using an API, can be displayed after selecting any profile and pushing DEM, in a first view the DEM will be pixelated, to improve the display change resolution (e.g. 5m), however increase resolution will make the interface more slow, for working with profiles is better use white screen or the GoogleMaps® API display. Use Clear/Refresh each time you change between display options and to show a white screen.

B.3.4 Swath profile preview

The user is able to visualize the swaths profiles by using the “Profile preview interface”.

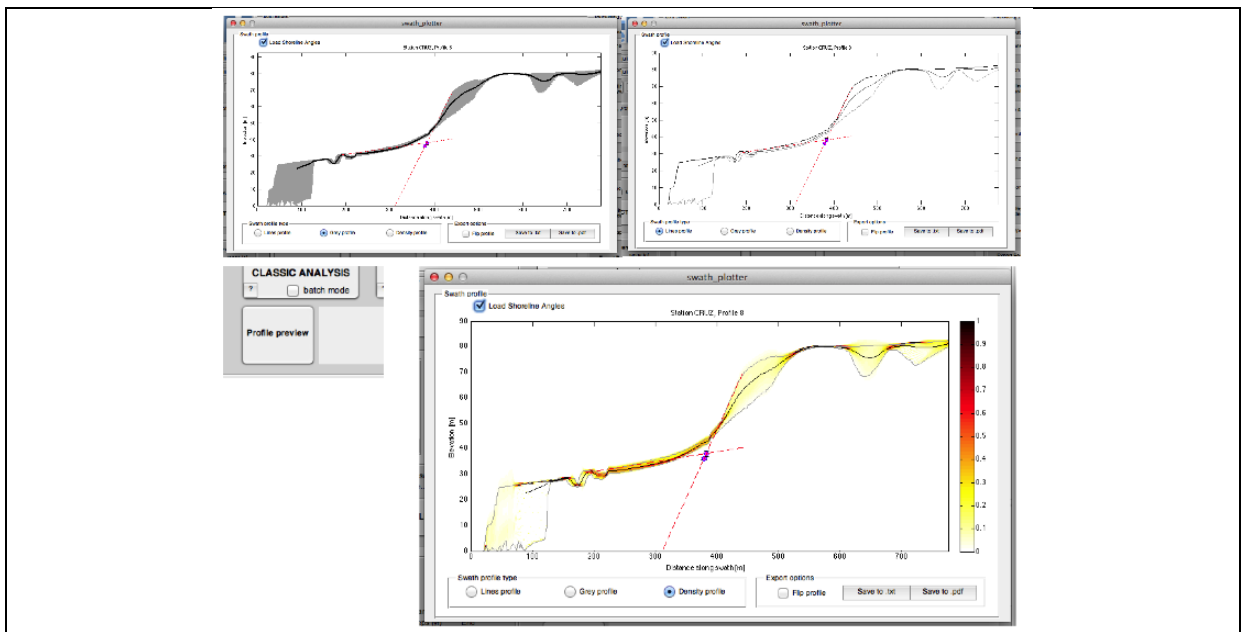


Figure 8: Swath profile viewer

This is a GUI subroutine that plots a selected profile by grey scale lines or patches or by normalized min-max topography spacing, a dimensionless value that represent the degree of incision, darker values indicates lesser incision that might highlight paleo surfaces. Shorelines-angles, if calculated, can be displayed together with their corresponding linear fits of paleo-platform and paleo-cliff. To change between different profiles the user must close the display each time.

B.3.5 Analytical functions

The analysis functions consist of four buttons defined by different colors, and named Staircase, Cliff, Stack and Scarp diffusion.

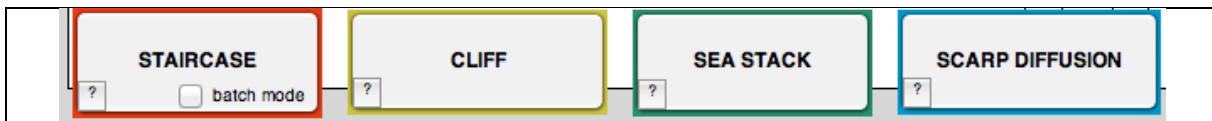


Figure 9: Analysis buttons

Each function use the same mapping display (Fig. 10), however with different ways to trace the terrace elements (Fig. 11). The mapping interface displays the swath profiles, the slope, and two GUI button in the lower part that allow selecting minimum or maximum relief for fitting. By default the display is set to maximum relief, however this use might vary for each case.

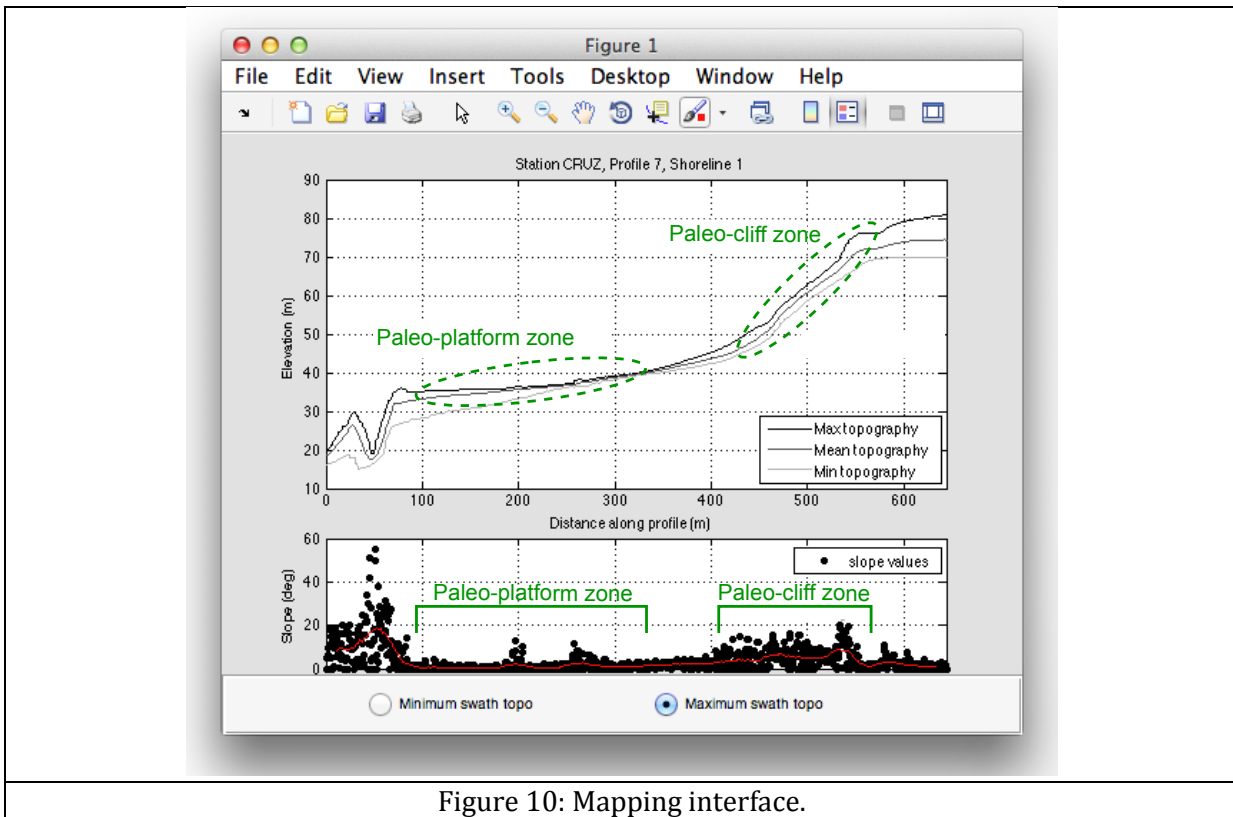


Figure 10: Mapping interface.

The user defines points on the profiles, enclosing the paleo-cliff and paleo-platform from right-to-left. The type and number of points vary between functions and are described next (Fig. 11):

Staircase: Staircase marine terraces are analyzed based on the concept of shoreline angle defined by Lajoie (1986). This function is useful when working with well-preserved paleo-platform and paleo-cliff morphologies. The identification of the shoreline angle can be performed using the maximum or minimum topographic distribution obtained from swath profiles. The maximum distribution of elevation in swath profiles allows observing the pre-incision topography; however, the maximum topography may be biased locally by climbing dunes. In this particular case the minimum elevations can be used to isolate the base of the dune field that should represent a maximum estimate of the original paleo-platform surface.

This function allows analyzing swath profiles interactively calculating the shoreline angle by clicking directly above the swath plots. Two user-defined points along the steepest part of the profile defines the paleo-cliff, and two further points delineate the extent of the paleo-platform (Fig. 11). Lineal regressions are then calculated upon the enclosed segments on the profile and extrapolated to find the intersection that marks the position of the shoreline angle. Vertical errors of shoreline angles are based on the extrapolation of the 2s ranges in the linear regressions.

Cliff: The Free-face analysis function allows locating the shoreline angle by using the slope distribution of modern cliffs as input angle to extrapolate the slope of a paleo-cliff below the colluvial wedge to find the shoreline angle. The concept of free-face refers to the exposed part of fault scarps above the colluvium (e.g. McCalpin, 2009), here extended to a wave-cut scarp. This analysis is recommended for terraces with well-defined colluvial wedges below exposed cliffs with restricted heights but formed on resistant bedrock, or for smoothed paleo-cliffs with marked transitions at the top of the colluvium. This method is also recommended for terraces covered by calcrete or beach-rock, where low diffusion rates are favourable for preserving the free-face morphology over longer periods of time.

The Free-face analysis is analogous to the Staircase analysis, but the slope of the cliff is not estimated by linear regression but defined by the user and incorporated by graphically selecting a single point on the topographic profile. This point should be defined at the lower limit of the free-face or at the contact between the colluvium and exposed bedrock. Two further points enclosing the paleo-platform are defined beyond the wash slope to find the shoreline angle and its associated 2s error (Fig. 11).

Stack: The Stack Analysis function allows estimating shoreline-angle elevations in rough coasts. Sea stacks and stumps form where portions of a retreating coast become isolated through erosion and dissection of the cliff base; these features are detached from the cliff forming isolated promontories, columns, stack-arcs and caves, which represent fragments of partly eroded terrace levels.

The maximum elevation of swath profiles highlights stack morphology and the location of peaks that delineate the dismantled terrace platform. By using a peak-detection algorithm, individual stack positions and their maximum elevations are extracted along the profile. Peaks are grouped in classes and linearly interpolated to reconstruct the paleo-topography of the platform.

The user start defining the area for peak detection defining two points from right-to-left (Fig. 11). Then an interactive window ask for the number of groups of peaks to isolate, usually is only one,

but can be a maximum of three groups. Finally an interactive window asks if you want to mark any remnant of inner edge or slope inflection at the paleo-cliff, this point must be located below the upper limit of a fringe (dashed line) and at the cliff.

Scarp Diffusion: The geomorphic age of a terrace paleo-cliff (Kt) may be estimated from the linear diffusion equation (see Hanks et al., 1984). The first step of Scarp Diffusion analysis is to define the temporal resolution of the model by specifying the range of iterations and the geometry of the profile. The user marks one point at the upper inflection of paleo-cliff, which represents a change in slope between the paleo-cliff and the extent of the platform above the cliff. Then, two points define the paleo-platform, finally the center of the profile is defined by one point, the center of profile is used to adjust the profile geometry usually is the center of topography distributions and marked by a dashed line, so the point is located at the intersection of the dashed line with the maximum topography, however in asymmetric profiles the location of center of profile might vary. We recommend adjust the zoom of the plot defining the area for fit and try several times the position of profile center in order to obtain low RMS values.

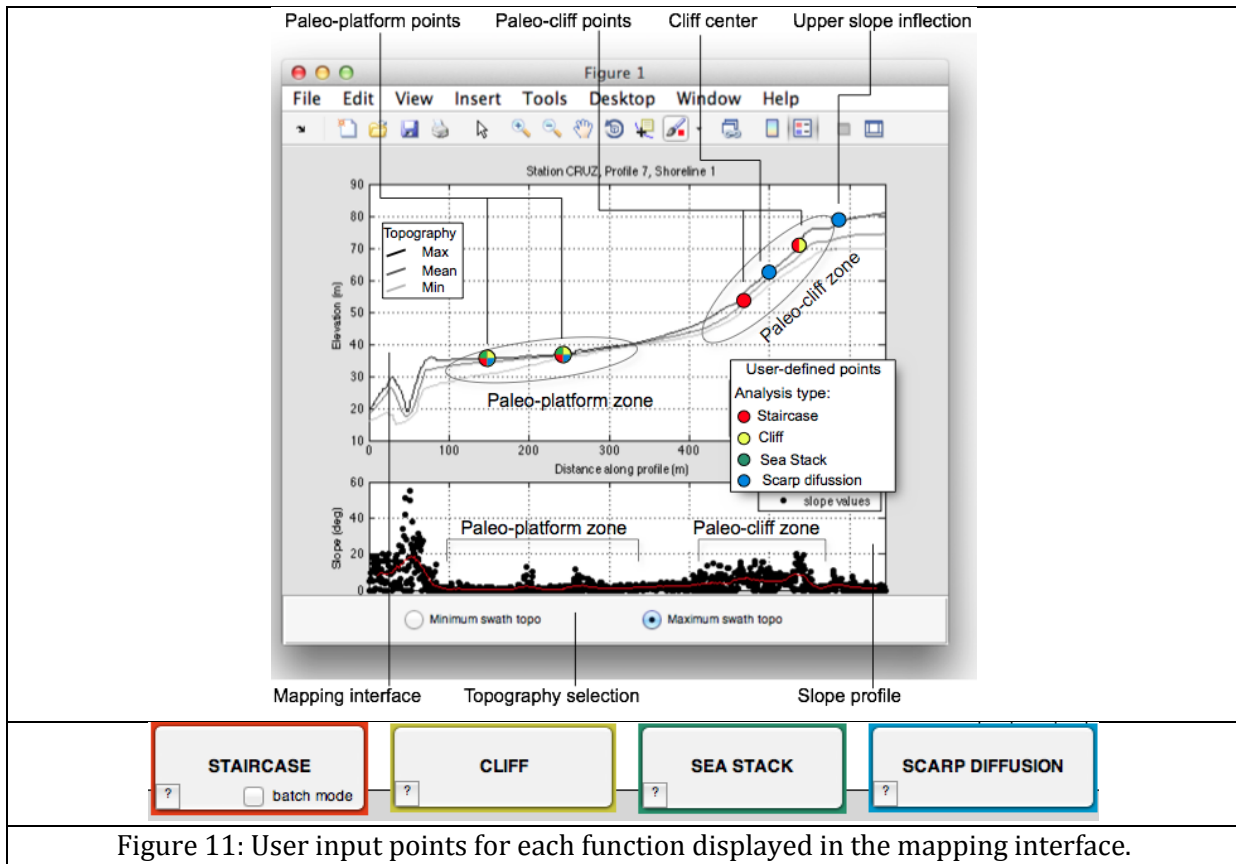


Figure 11: User input points for each function displayed in the mapping interface.

The type of user-defined points for each of the functions are different, in order to facilitate the understanding of shoreline angle mapping for each function we developed a video tutorial. Likewise, the criterion for correct mapping is explained through examples described in the TerraceM publication (see Geosphere paper).

B.3.6 Analysis parameters

Depending of each function the user selects she might need to modify its parameters in order to obtain adequate results. The “Analysis Parameters interface” is formed by groups of text boxes associated with each function by color (Fig. 12).

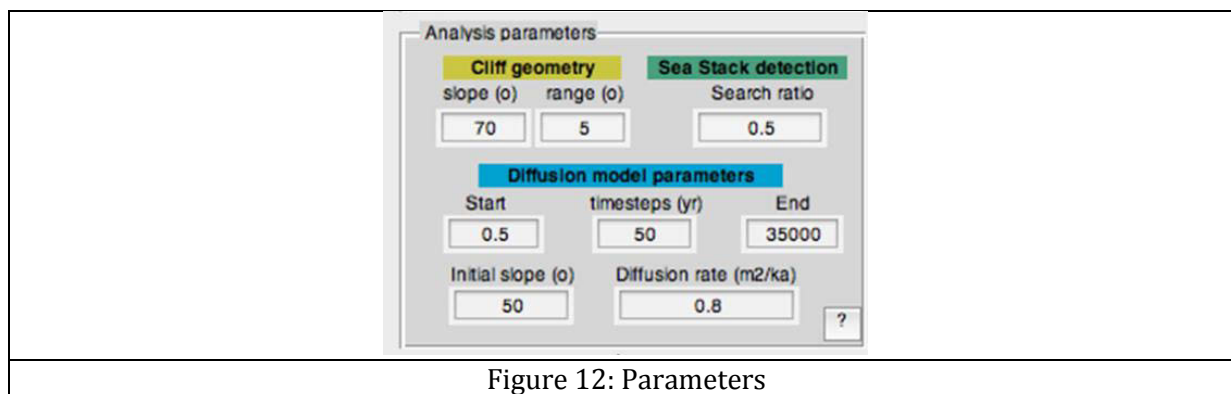


Figure 12: Parameters

When opening TerraceM these boxes are automatically filled with defaults parameters that might be adjusted according each case (See examples in the TerraceM paper in Geosphere). The parameters are:

Cliff: Slope and range are usually estimated from field measurements of cliff face slopes or by studying active cliffs slopes.

Stack: A point is considered a maximum peak if it has the maximal value, and was preceded by a value lower by search ratio. This value is usually the same as cell-size of your input raster, but can be modified to increase the sensitivity of peaks recognition.

Scarp Diffusion: The diffusion model parameters consist in two rows of textboxes (Fig. 12), the upper ones defines the time-steps and range of iterations. Initial slope calibrate the $t=0$ of the model, likewise, the diffusion rates is used to determine the best Kt fit (see Hanks et al., 1984).

B.3.7 Outputs

Outputs are stored inside the stations folder and inside each station, the outputs consist of graphic .pdf and, asccii and Matlab® tables (.txt and .mat), which are updated continuously by TerraceM and can be edited by the user. As an example we use the station name “CRUZ” in Table 2.

Main output tables:	
difussion.txt	ASCII table containing the shoreline angles and associated spatial data
shorelines.txt	ASCII table containing the KT values for Scarp Diffusion analysis and associated spatial data.
Secondary output tables:	
sh_projected.txt	ASCII table containing the shoreline angles projected along a user-defined line
Outliers_level_1.txt	ASCII table containing the shoreline angles classified as outliers
Interpolation_level_1.txt	ASCII table containing the linear interpolations between shoreline angles
Graphic outputs:	
Data-Repository_CRUZ_1.pdf	Output of Repository builder
CRUZ_1_stack.pdf	Graphic output of stack function
CRUZ_prof_1_shoreline_1_diff.pdf	Graphic output of diffusion function
Swaths_CRUZ_page_1.pdf	Graphic output of swath profiles
Temporal Matlab® outputs	
CRUZ_swaths.mat	Swath profiles of the station
CRUZ_Clicks.mat	History of fits defined by the user
CRUZ_fits.mat	Plots of fits saved as Matlab® structures
DEM_CRUZ.mat	DEM matrix input for the dem.m function.
CRUZ_diffusion.mat	Temporal table of scarp diffusion analysis

Table 2: Outputs of TerraceM

B.3.8 Table viewer interface

The two buttons at the upper right corner of TerraceM interface (Fig. 13) may be used to look up the main output tables (Table 2).

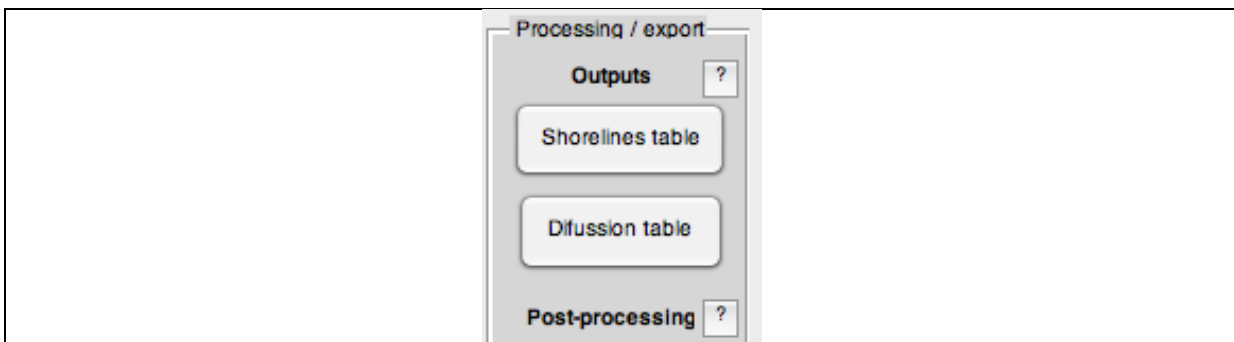


Figure 13: Outputs display

Stations, profiles and spatial data are within these tables as well as the time of analysis that can be transformed to date nomenclature using the date function in MATLAB®. Table viewer allows editing the table by selecting and deleting rows (Fig. 14).

Station	Profile_number	shoreline_number	east	north	distance_along_swath	shoreline_elevation	error	analysis_type	time
CRUZ	1	1	571196	4097054	653.9500	34.4600	2.4300	classic	7.3603e+05
CRUZ	2	1	571802	4096572	381.0900	34.6100	1.4600	classic	7.3603e+05
CRUZ	3	1	572220	4096167	445.1800	32.9800	0.5500	classic	7.3603e+05
CRUZ	4	1	572436	4096091	537.9700	37.4100	1.2500	classic	7.3603e+05
CRUZ	5	1	572756	4095676	499.6500	34.0100	0.6800	classic	7.3603e+05
CRUZ	6	1	572963	4095498	387.4100	38.5700	0.9000	classic	7.3603e+05
CRUZ	6	1	572945	4095442	327.9200	28.8500	0.9100	classic	7.3603e+05
CRUZ	7	1	573277	4095131	327.9600	34.3900	0.9600	classic	7.3603e+05
CRUZ	8	1	573467	4095022	362.7700	38.2300	1.1500	classic	7.3603e+05
CRUZ	9	1	573698	4094911	456.9700	39.4400	2.2500	classic	7.3603e+05
CRUZ	10	1	573906	4094778	399.2000	32.9700	1.1700	classic	7.3603e+05
CRUZ	2	2	571663	4096762	581.0600	60.9200	0.3300	classic	7.3604e+05
CRUZ	1	1	571218	4097075	724.3900	35.1100	1.4700	diffusion	7.3604e+05
CRUZ	2	1	571610	4096595	405.4400	35.5200	1.0100	diffusion	7.3604e+05
CRUZ	3	1	572290	4096208	495.3400	33.7400	0.2200	diffusion	7.3604e+05
ROTO	1	1	716515	6033414	249.6200	62.1900	0.8100	fxcliff	7.3604e+05
ROTO	2	1	717640	6033131	219.9600	60.2400	0.3300	fxcliff	7.3604e+05
ROTO	3	1	717437	6033065	222.5600	58.8500	-0.0700	fxcliff	7.3604e+05
ROTO	4	1	717918	6033374	182	71.2100	0.3600	fxcliff	7.3604e+05
ROTO	5	1	717797	6033192	213.0700	72.0200	0.3700	fxcliff	7.3604e+05
ROTO	6	1	718222	6033186	328.5700	74.7500	1.4800	fxcliff	7.3604e+05
ROTO	6	1	718222	6033187	327.4200	72.7900	1.8200	fxcliff	7.3604e+05
ROTO	6	1	718212	6033134	381.3500	186.1400	6.2500	fxcliff	7.3604e+05
ROTO	6	1	718222	6033188	325.9600	70.2300	2.0800	fxcliff	7.3604e+05
ROTO	1	1	718496	6033445	213.1600	61.1000	0.6400	fxcliff	7.3604e+05
ROTO	1	1	718500	6033438	220.6100	65.8000	4.7700	fxcliff	7.3604e+05
ROTO	1	1	718492	6033450	206.2300	60.2200	1.4400	fxcliff	7.3604e+05
ROTO	2	1	717640	6033128	222.3600	59.9200	1.0900	fxcliff	7.3604e+05
ROTO	2	1	717641	6033125	226.3900	59.3900	0.8300	fxcliff	7.3604e+05
ROTO	2	1	717641	6033128	223.0900	61.0300	1.2300	fxcliff	7.3604e+05
ROTO	2	1	717651	6033051	301.0900	60.9500	1.1100	fxcliff	7.3604e+05

Figure 14: Table viewer

B.3.9 Shoreline projection interface

Shoreline angles can be projected interactively through the Project Shorelines button at the right side of the TerraceM interface. Before start projection and/or the filtering routines, we recommend revise the main output table (shorelines.txt) and removing repeated measurements of shoreline angles or nan values.

The button opens a GUI subroutine (Fig. 15) that allows loading a shapefile line of two nodes. The profile can be set manually to test various projections. The buttons allows plot the projected shorelines, save and clear the interface to repeat the manual projection.

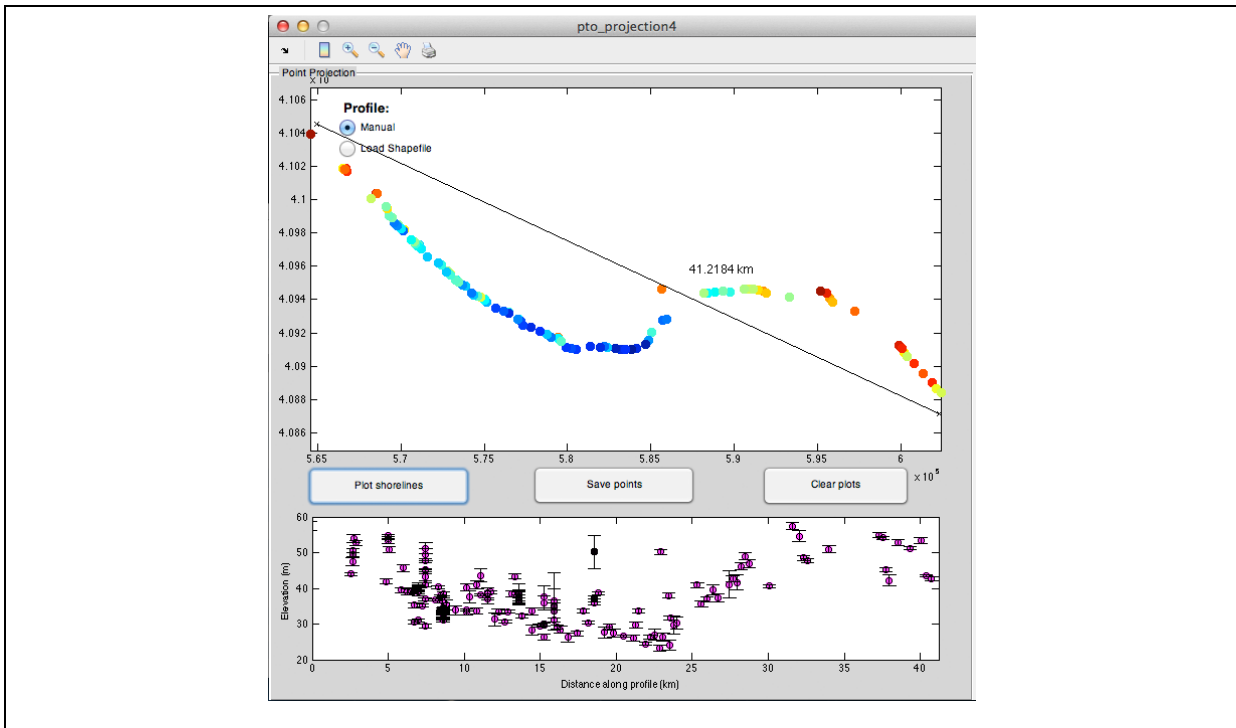


Figure 15: Shoreline projection interface

The points may be saved and stored as an ascii table and are used as input for the “Shoreline filtering interface”.

B.3.10 Shoreline filtering interface

Shoreline interface is used to filter outliers and improve the interpolations of shoreline angles previously projected along profiles using the “Shoreline projection interface”. The X-bin size defines the resolution in x of the interpolation. Y-range is usually defined by the standard deviation of elevations and marks the boundary where shorelines are considered outliers. We suggest that the number of outliers must not higher than the 20% of the population, this proportion can be visually checked in the bar plot (Fig. 16).

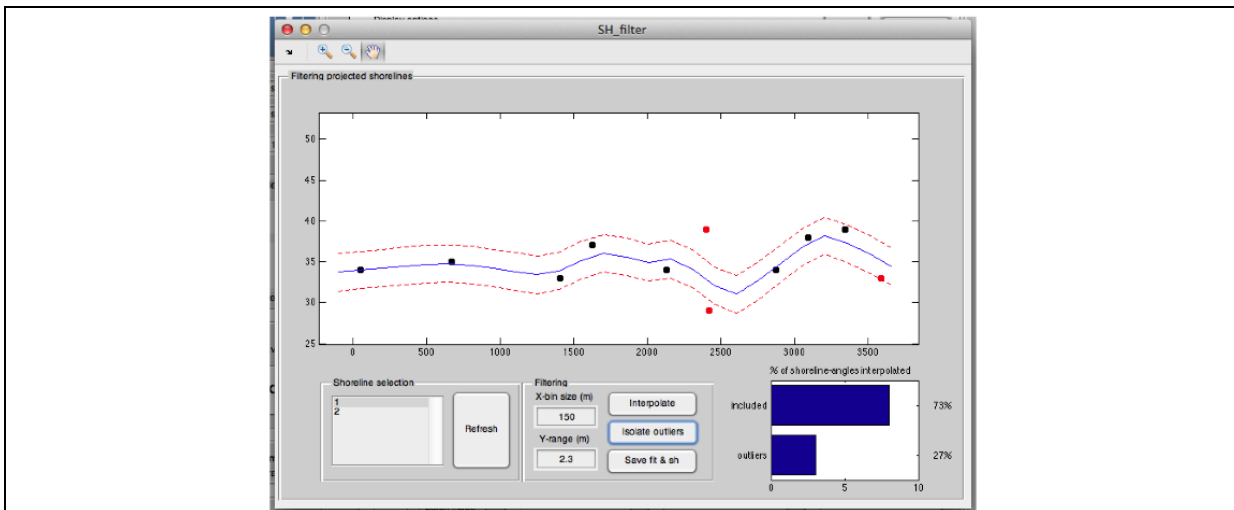


Figure 16: Shorelines filtering interface

B.3.11 Export functions

Export functions allows export the shoreline outputs (data in table shorelines.txt) in Google Earth® or ESRI® shapefile formats (Fig. 17); the outputs are stored inside the stations folder.

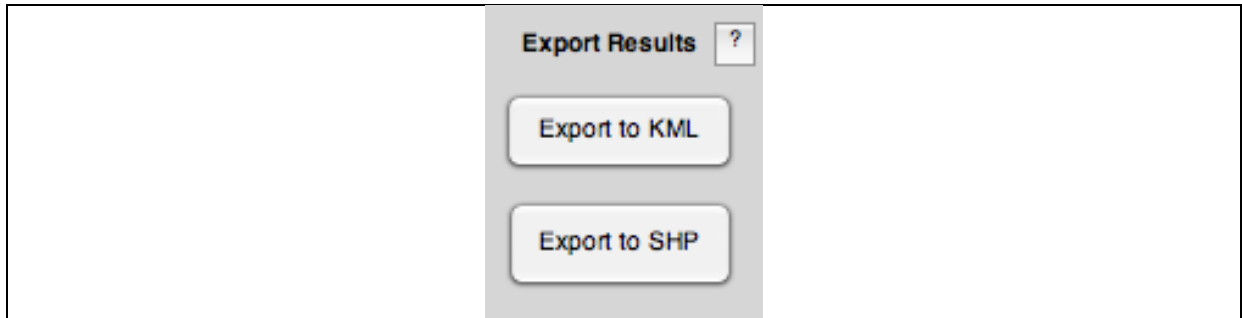


Figure 17: Export options

B.3.12 Debugging

TerraceM creates a path file (path.mat) allowing quickly access to the last edited project, however this might produce problems when the projects are moved to different directories or computers. Debugging (Fig. 18) deletes these path files from all folders in the project forcing redefine the paths the next time TerraceM is run.

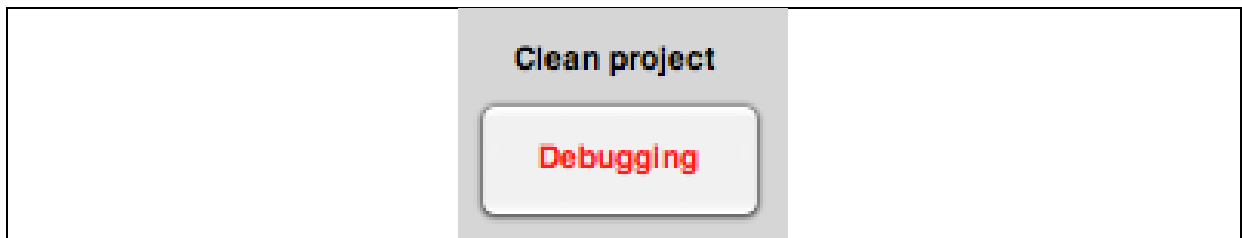


Figure 18: Debugging

B.4 Known issues

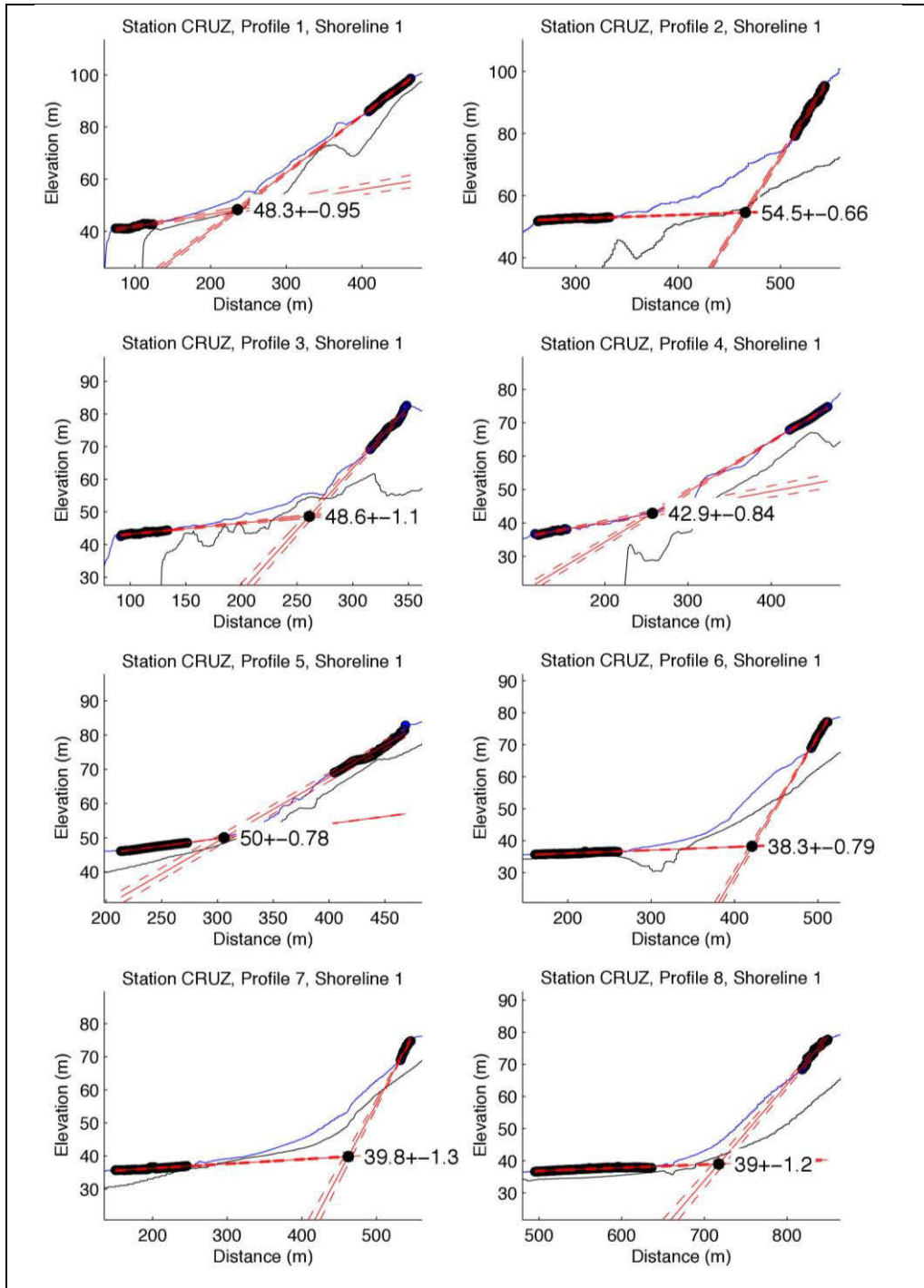
After testing TerraceM with multiple users we detected some issues that might produce errors or unexpected behavior. The most common issues are:

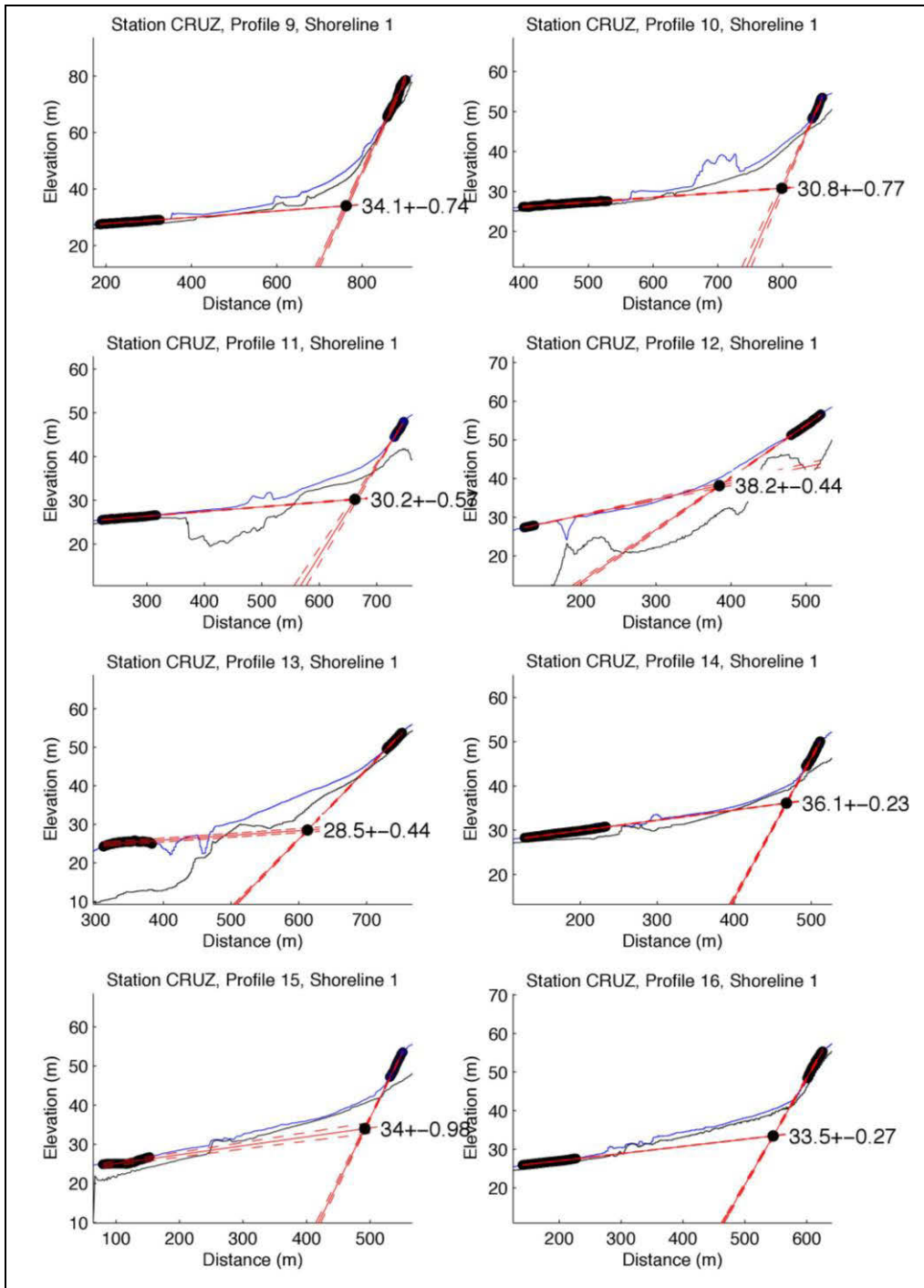
- 1) Shape of swath profiles: Non-rectangular or trapezoidal polygons are not recognized and generate errors during swath profile extraction.
- 2) Size of swath profiles: If the polygon is too narrow or does not enclose enough raster cells, an error will be displayed during the swath profile extraction.
- 3) The raster characteristics: Raster datasets containing voids or gaps in data may produce an error during the swath profile extraction. The topography should be interpolated to fill small gaps in data.

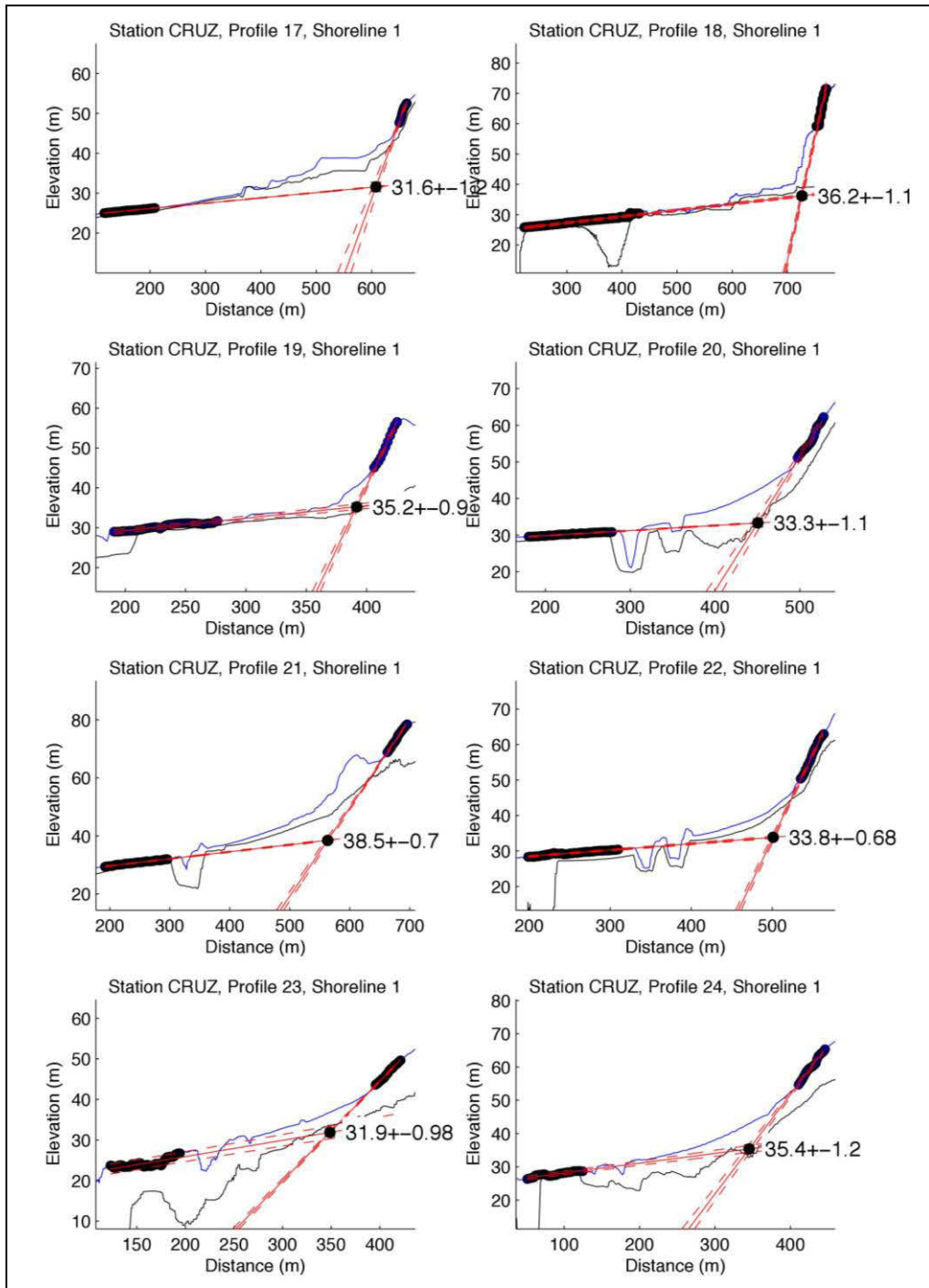
4) Path file: Incorrect path files may produce unexpected behavior, this could happen when the project is moved to other directory without previous debugging. Deleting the path.mat files from all folders or using the debugging routine may solve this problem.

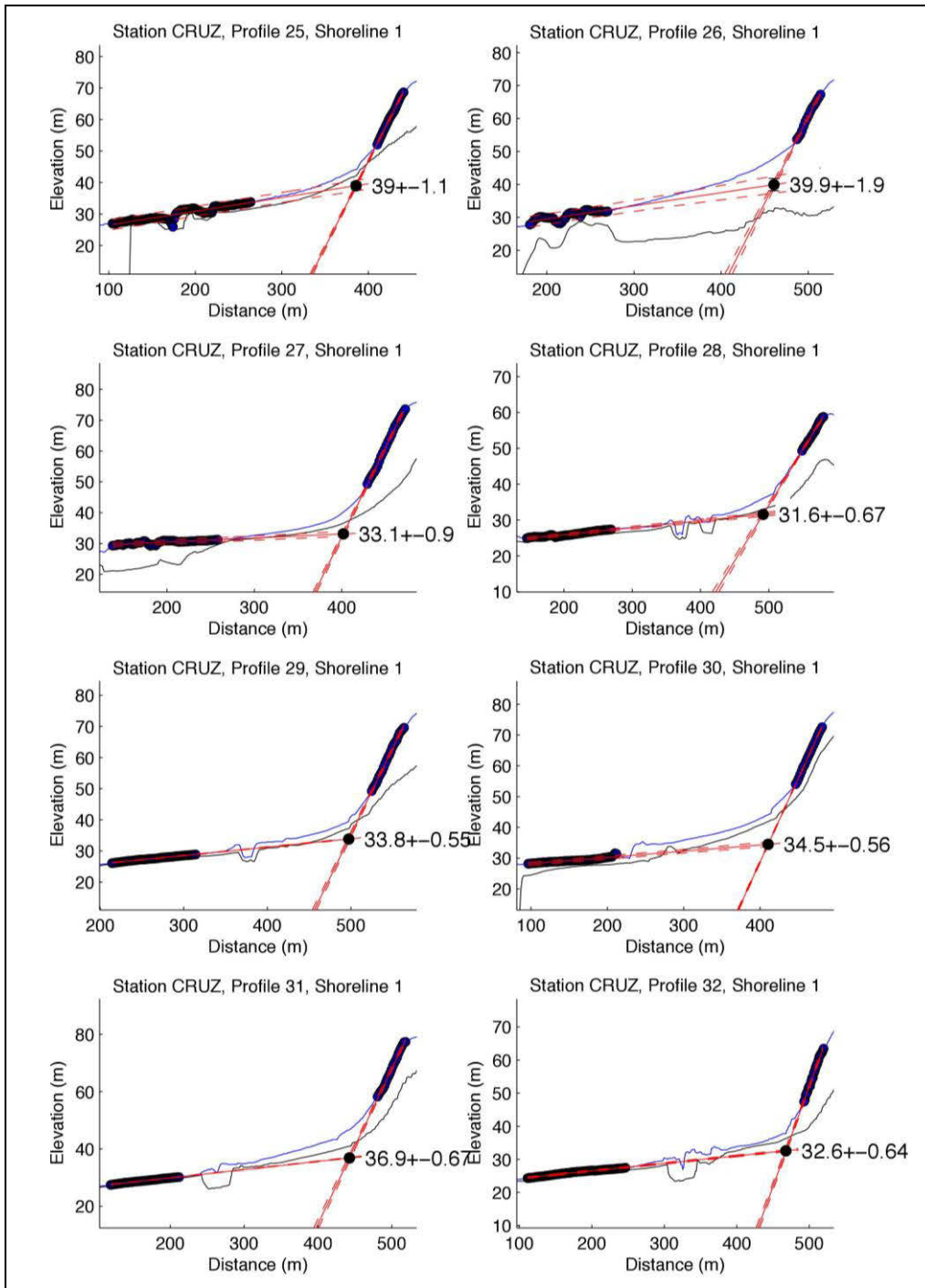
5) Filtering routine: Interpolations in the filtering routine cannot be accomplished if repeated values exist in X or Y-axes (Distance along profile or Elevation), or if elevation values are not a number (nan). The problem is fixed by removing these shoreline records from the main output table (shorelines.txt).

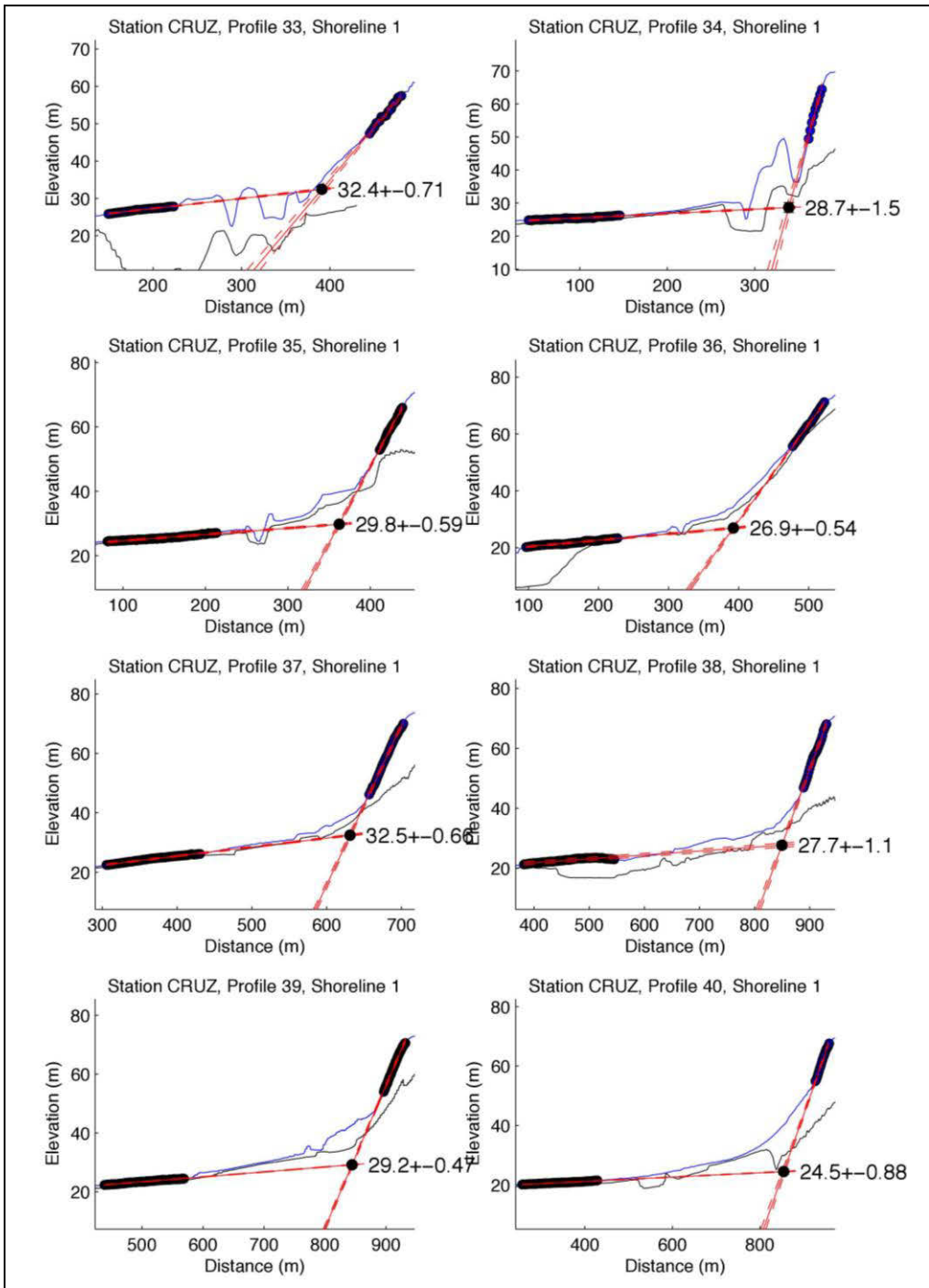
B.5 TerraceM fits at Santa Cruz

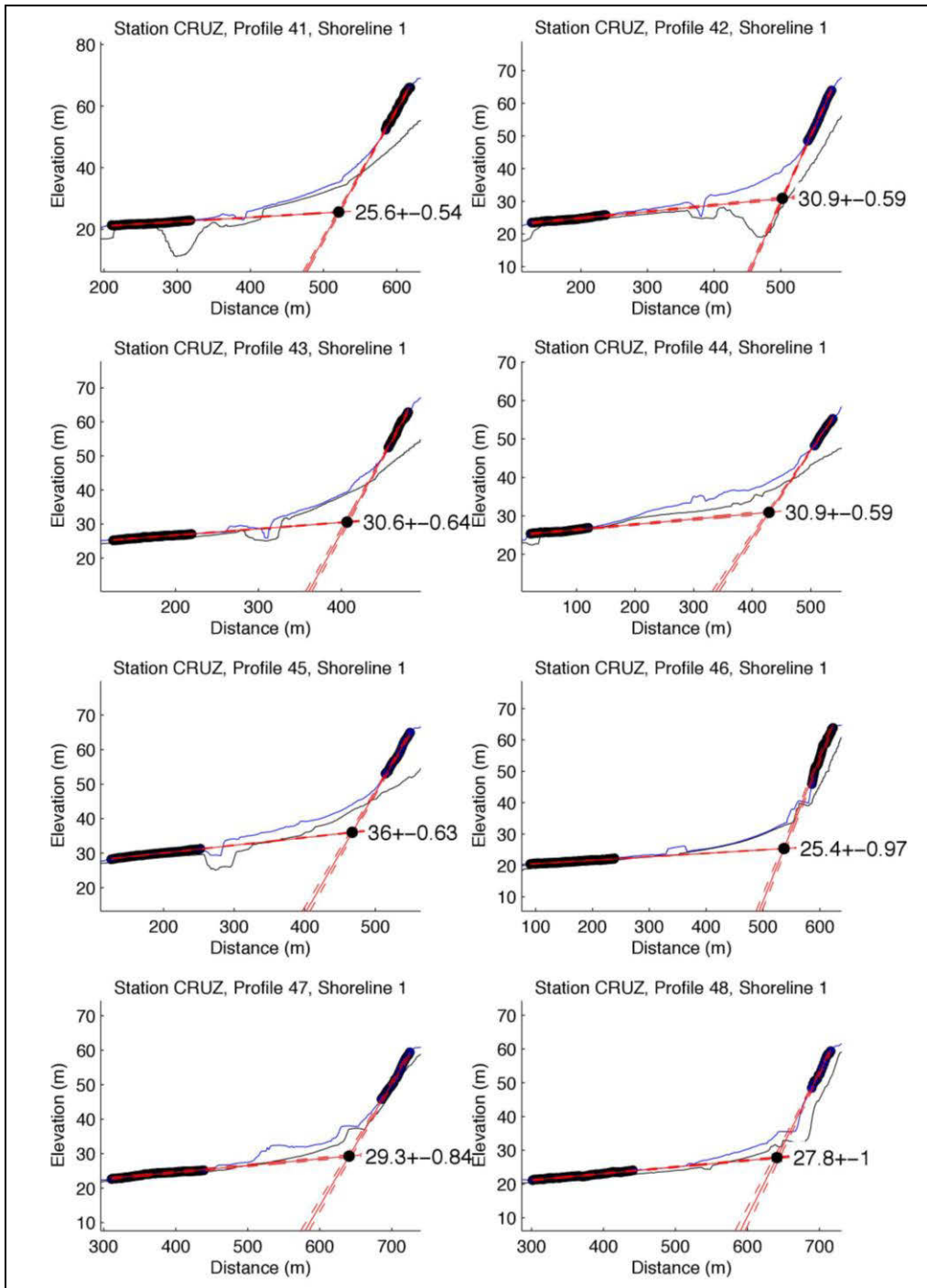


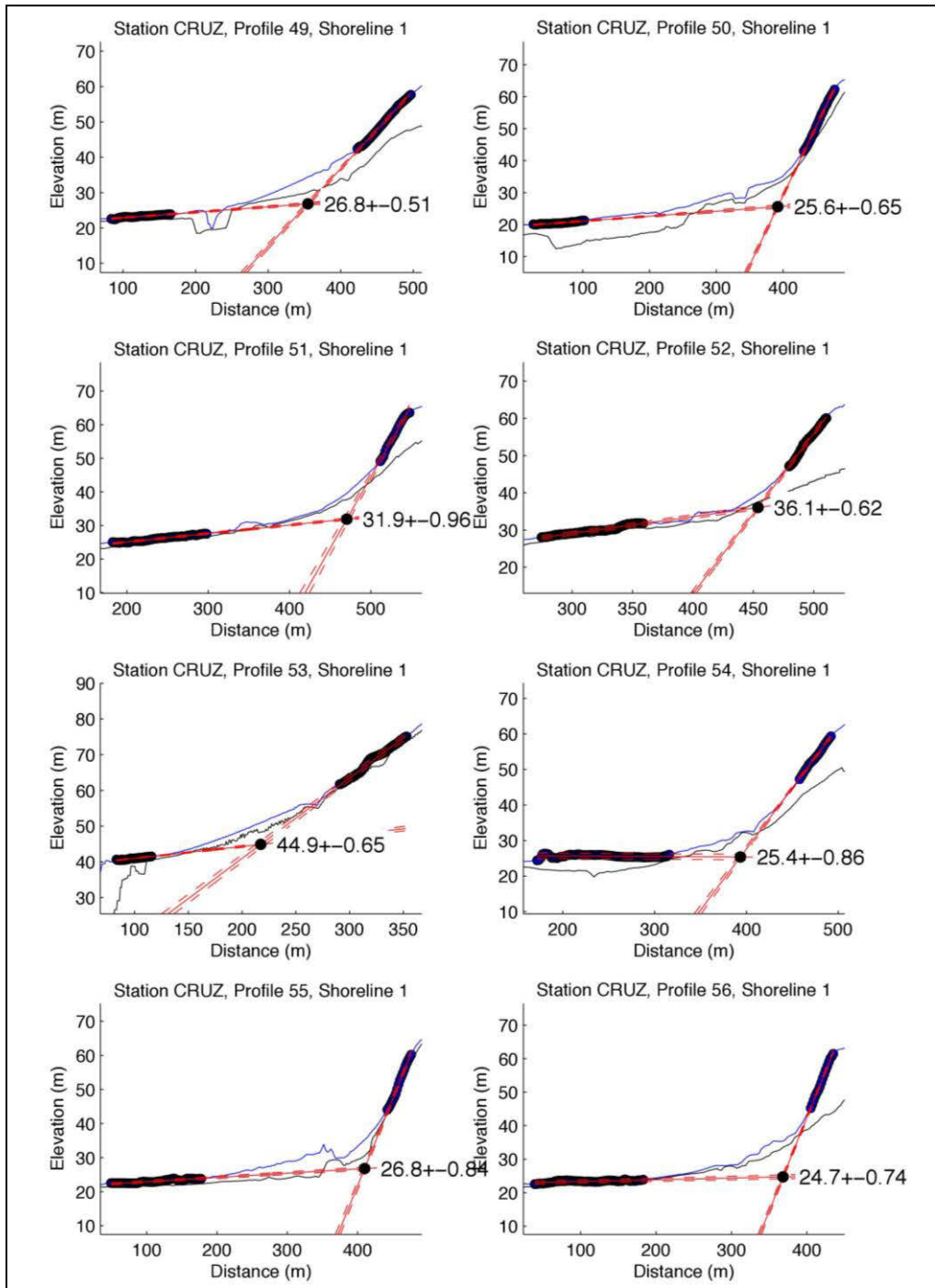


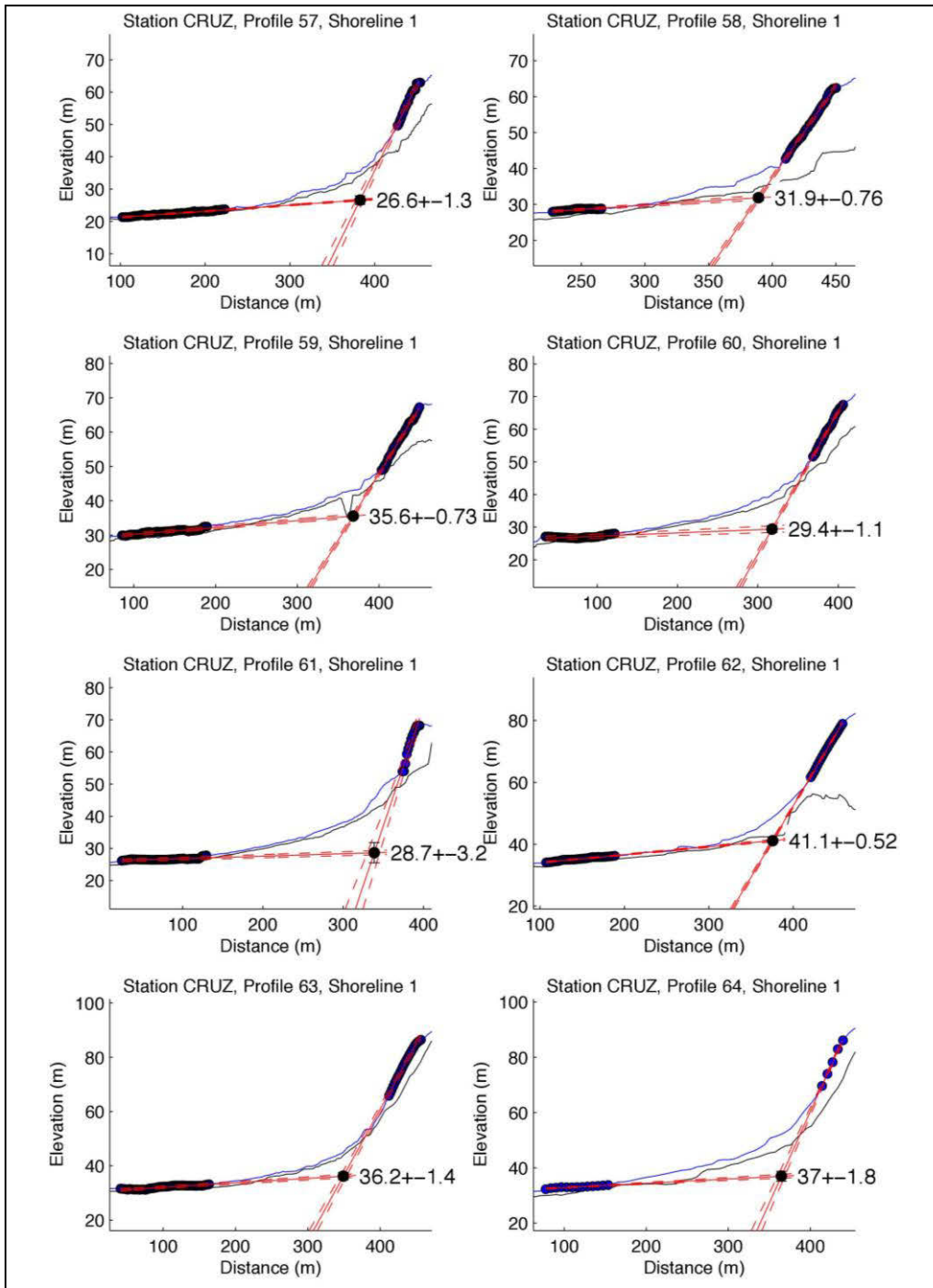


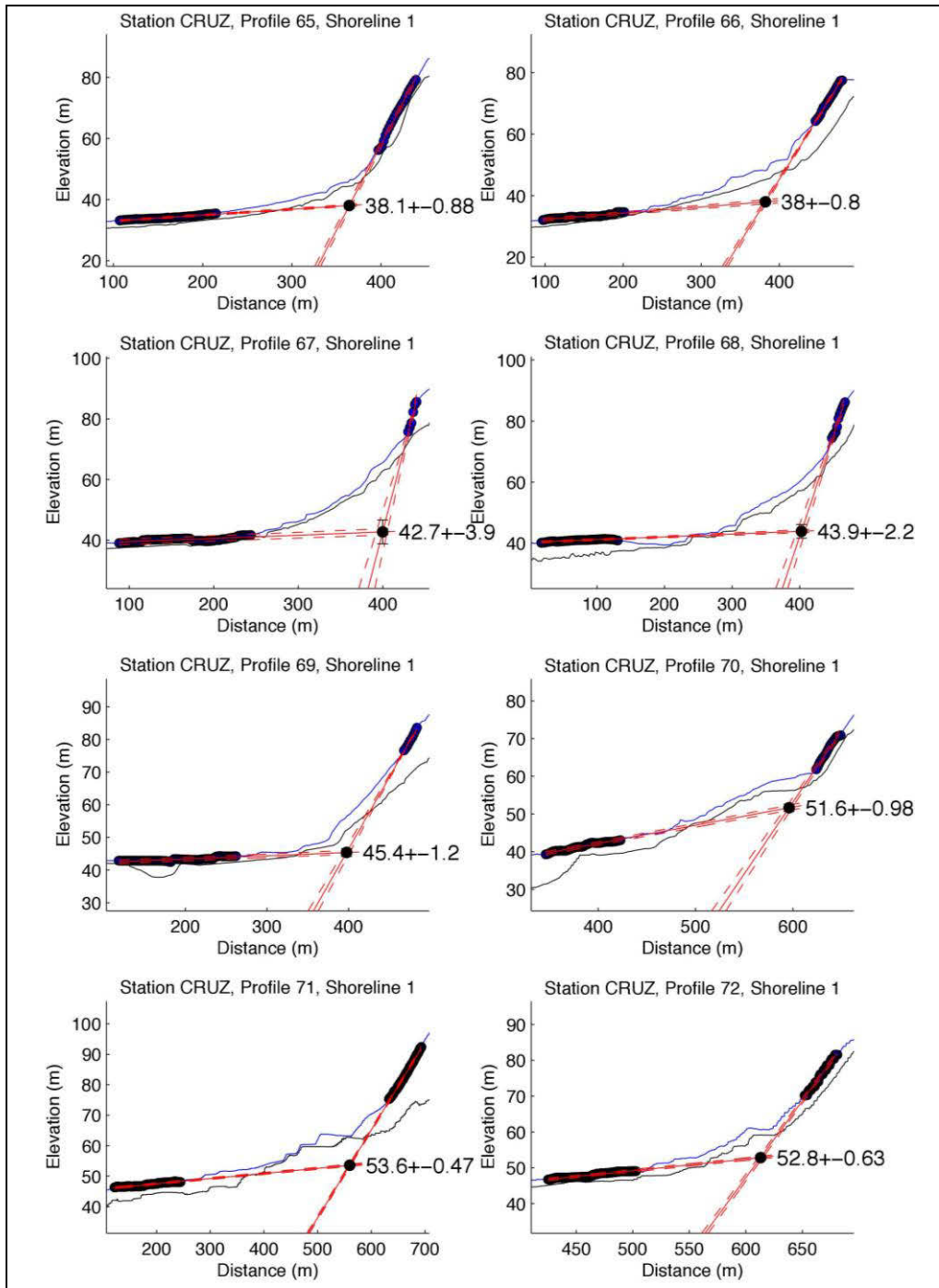


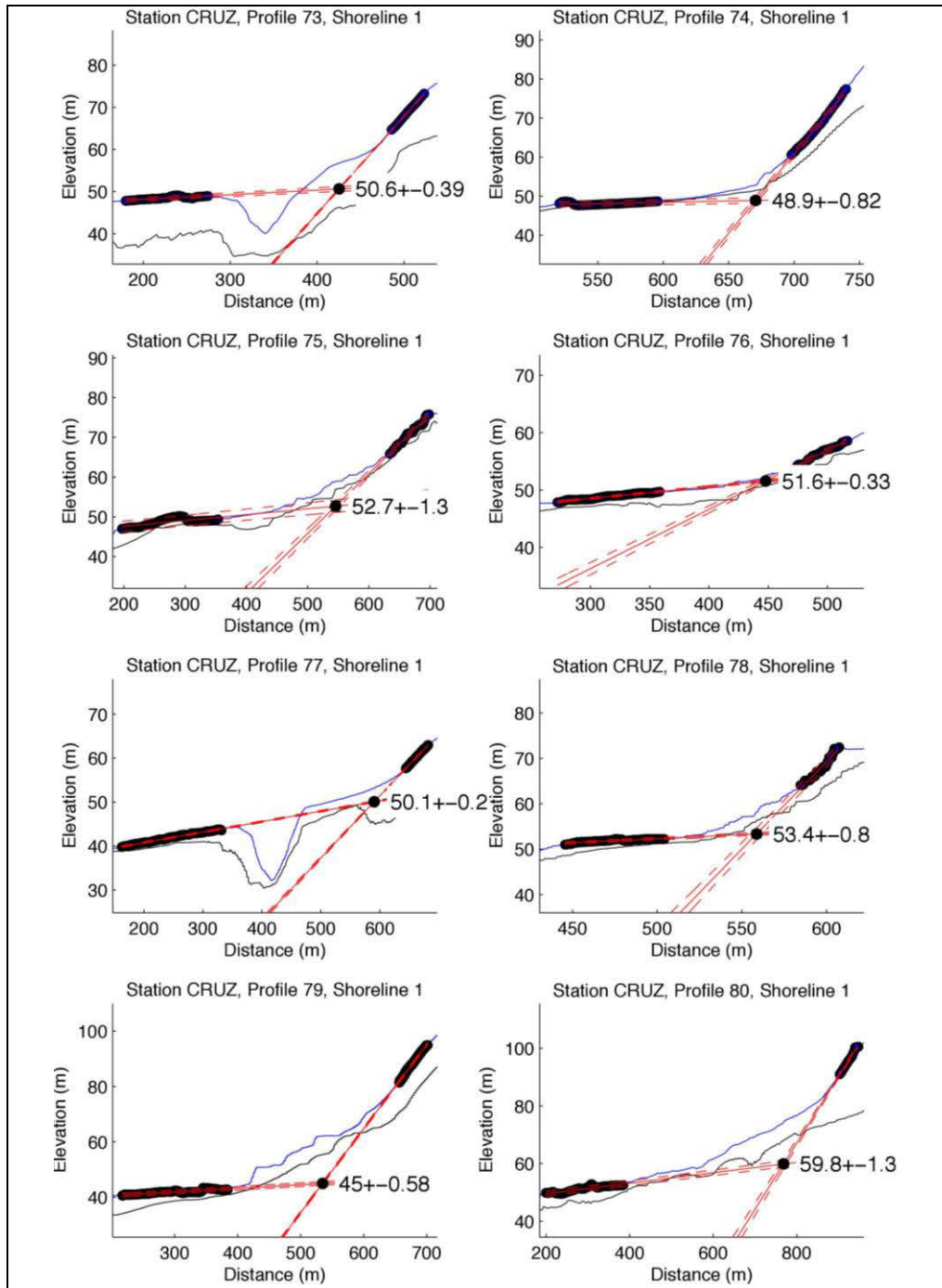


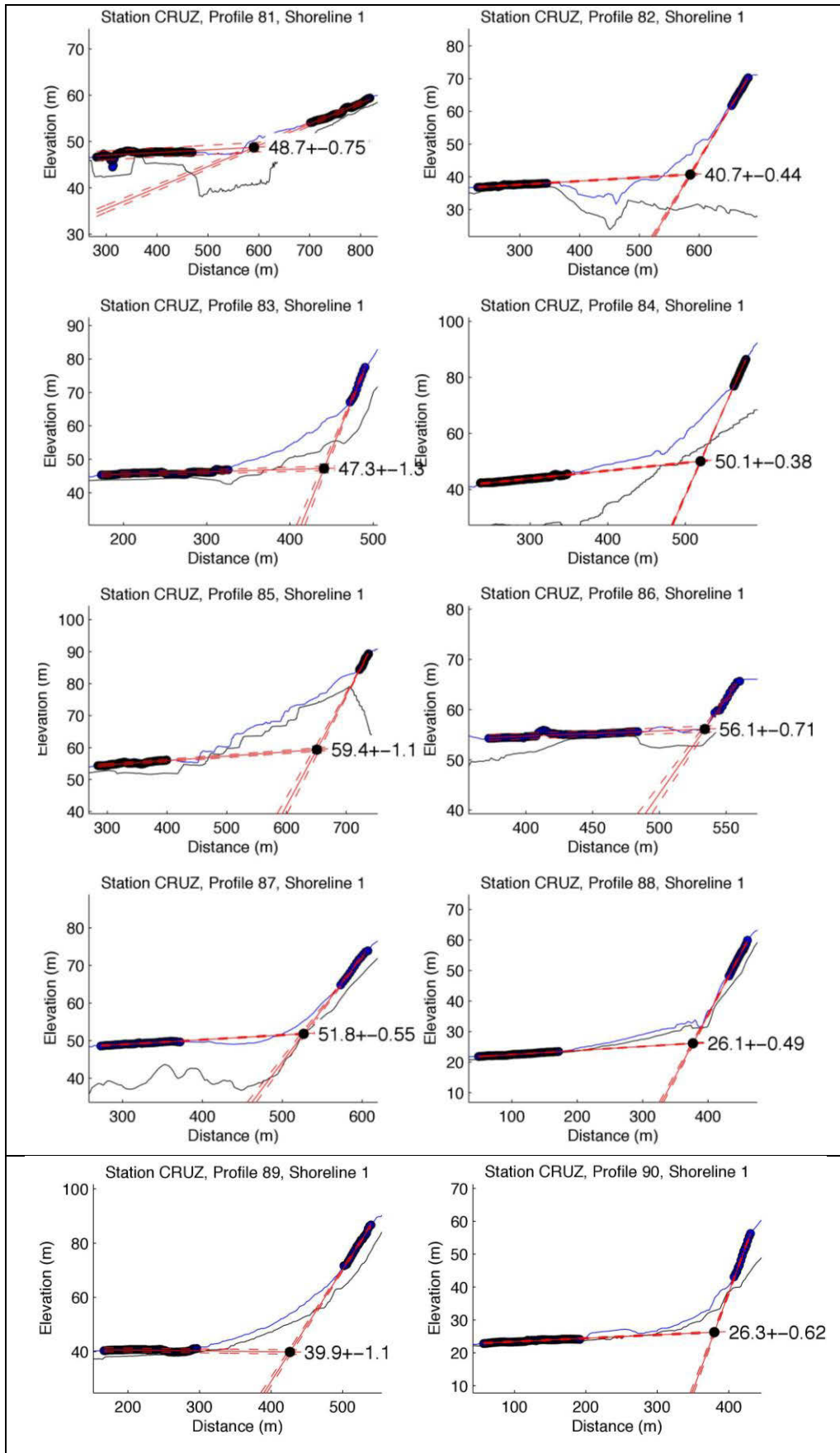












B.6 References of appendix B

Hanks, T. C., Bucknam, R. C., Lajoie, K. R., and Wallace, R. E., 1984, Modification of wave-cut and faulting-controlled landforms: *Journal of Geophysical Research: Solid Earth* (1978-2012), v. 89, no. B7, p. 5771-5790.

Lajoie, K. R., 1986, Coastal tectonics: *Active Tectonics*, p. 95-124.

McCalpin, J. P., 2009, *Paleoseismology*, Academic press.

Appendix C: Topography, IRSL dating, and geological maps along the 2010 Maule earthquake rupture.

C.1 Topographic datasets

Four different types of topographic datasets were used to analyze the morphology of marine terraces: digital terrain models (DTM) from LiDAR point clouds, DTMs from interpolated contour maps, and a regional 30-m DEM (Fig. C1).

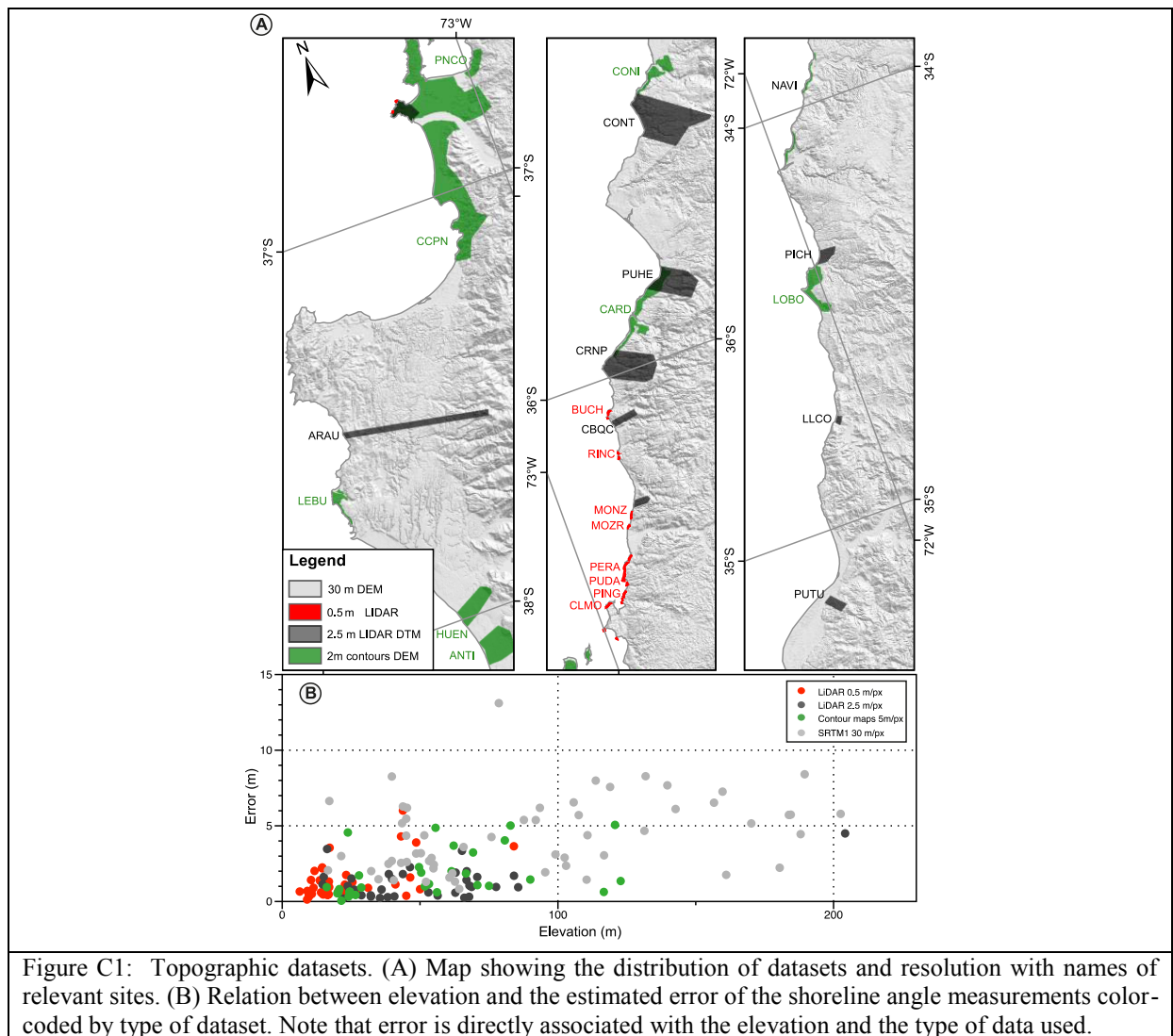
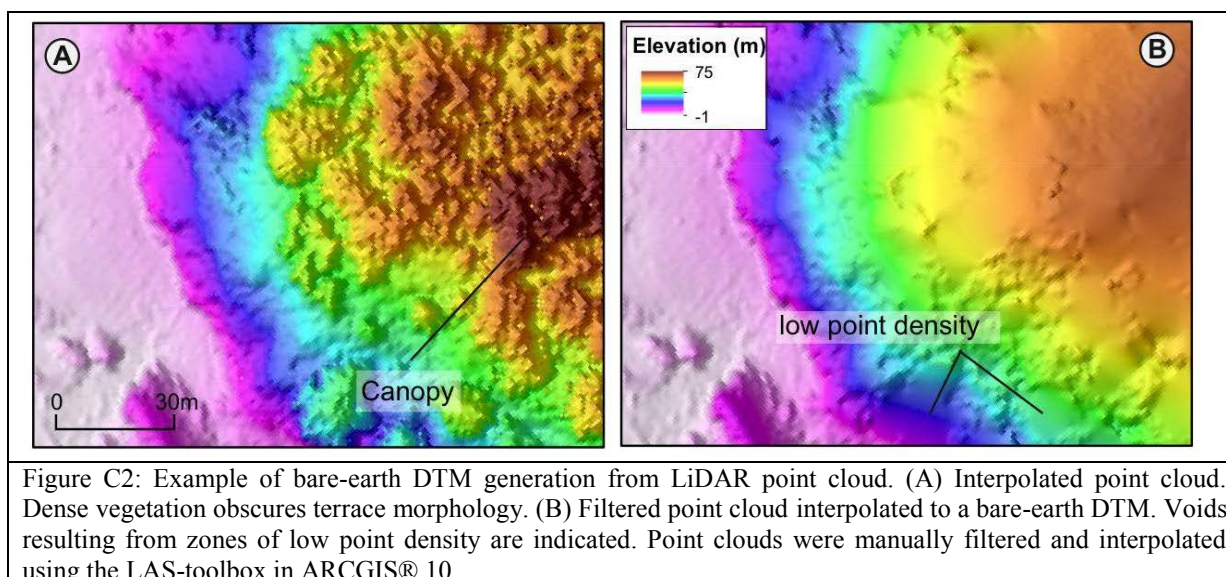


Figure C1: Topographic datasets. (A) Map showing the distribution of datasets and resolution with names of relevant sites. (B) Relation between elevation and the estimated error of the shoreline angle measurements color-coded by type of dataset. Note that error is directly associated with the elevation and the type of data used.



C.2 Luminescence dating

C.2.1 Sample preparation

Twelve sediment samples from coastal terraces along the Maule rupture zone were dated using the post-IR IRSL signal of K-feldspar. The sediment fraction for dating consisted of k-feldspar and quartz, using grain sizes between 100 and 250 μm . To feldspar the post-IR-IR measurement protocol of Thiel et al. (2011) with IR-diode stimulation at temperatures of 290 $^{\circ}\text{C}$ (pIRIR_{290}) was applied. The suitability of feldspar for luminescence dating was checked by means of dose recovery tests with laboratory doses of approximately the natural D_e . Bleaching experiments with signal resetting by IR diodes and in a solar simulator were performed to study the sensitivity to sunlight exposure.

Coarse grain K-feldspar (100-250 μm) was measured for all five samples using the pIRIR_{290} SAR protocol. Thomsen et al. (2008), Buylaert et al., (2012) and Thiel et al. (2011) showed that the post-IR IRSL signal using elevated stimulation temperatures has significant potential to derive a dating result that is far more independent from fading-correction than the conventional IRSL_{50} -signal. Thus, for the “old” samples analyzed here, the protocol suggested by Thiel et al. (2011) was selected, using a stimulation temperature of 290 $^{\circ}\text{C}$ after preheating at 320 $^{\circ}\text{C}$ and an IR bleach at 50 $^{\circ}\text{C}$.

The suitability of the protocol for the samples was tested by means of dose recovery tests on 8 mm aliquots (three aliquots per sample). While signal resetting with IR diodes (two times for 2000 seconds at room temperature, separated by a break of 10,000 seconds) resulted in acceptable ratios between measured and laboratory dose (0.9-1.1) for all samples except of PICH1 (1.17), after signal resetting in a Höhnle solar simulator for 12 hours the recovery of laboratory doses was of acceptable accuracy for all samples.

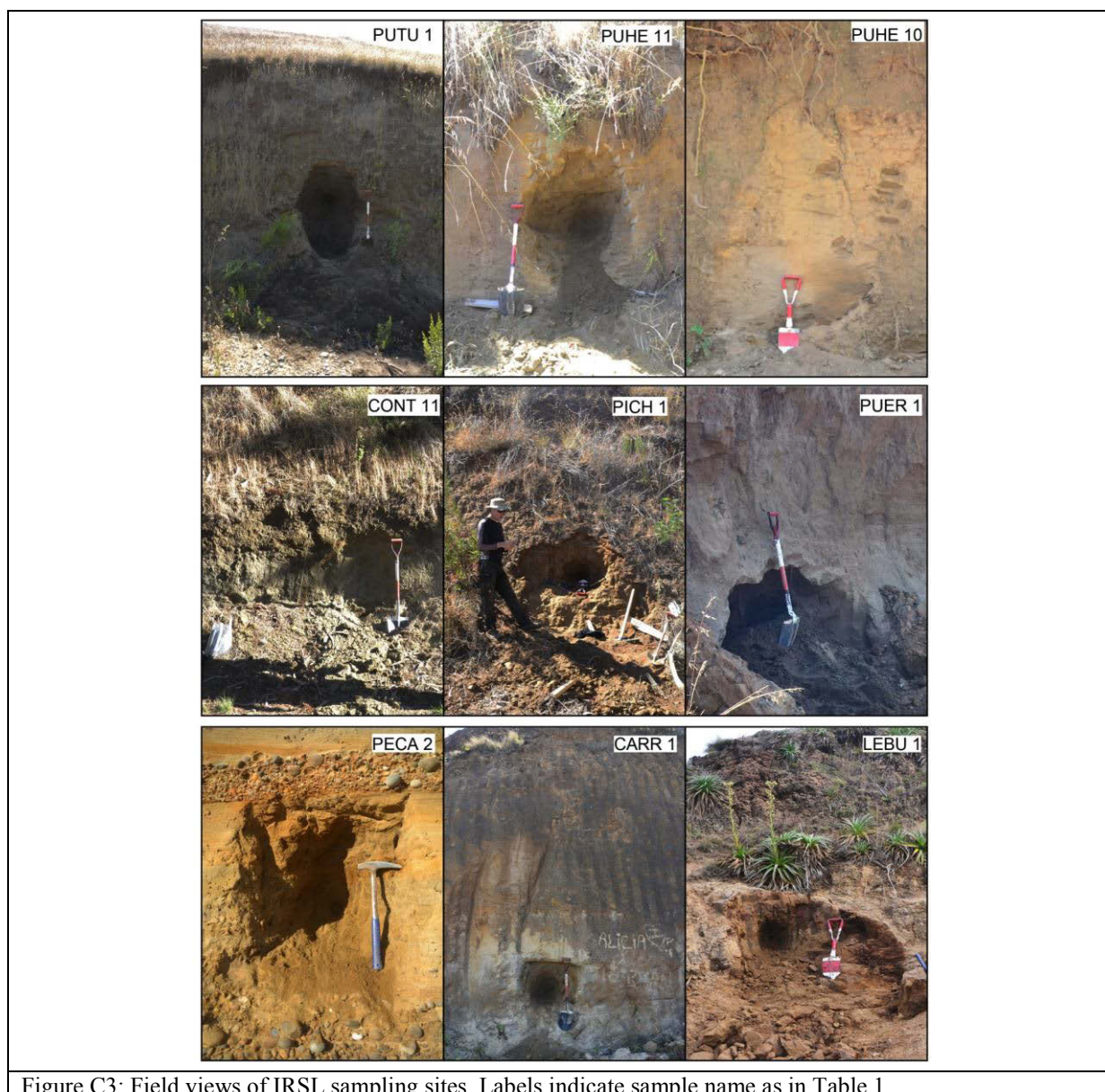


Figure C3: Field views of IRSL sampling sites. Labels indicate sample name as in Table 1.

C.2.2 Experiments: OSL measurements on quartz

To check the measurement protocol for quartz and to characterise the bleaching sensitivity of its luminescence signal, we performed combined dose-recovery-preheat tests and linear modulated OSL (LM-OSL) measurements (Bulur et al., 2000). After chemical pre-treatment with concentrated HF, a sufficient amount of quartz grains was left only for sample CONT11. The 100-250 μm coarse-grain fraction of CONT11 was measured using a standard SAR protocol with a preheat temperature of 240 $^{\circ}\text{C}$ (determined by a combined dose-recovery-preheat-plateau test based on 3 aliquots per temperature interval, Fig. C4), a cut-heat of 220 $^{\circ}\text{C}$, and test doses of ~ 18 Gy. Higher preheat temperatures were connected with problems to recover a known laboratory dose (ratios of measured/given dose of 0.89 and 1.16). Measurements at lower temperatures revealed severe influence of feldspar contamination (depletion ratios of 0.52-0.79). Out of 24 measured 2 mm aliquots, only 18 aliquots (75%) passed the SAR acceptance criteria. The adjacent D_e distribution showed relatively normal distribution and an

overdispersion of 22%. Based on the central age model (CAM) a burial dose of 79.05 ± 5.78 Gy was calculated, resulting in a respective age of 66.4 ± 6.6 ka.

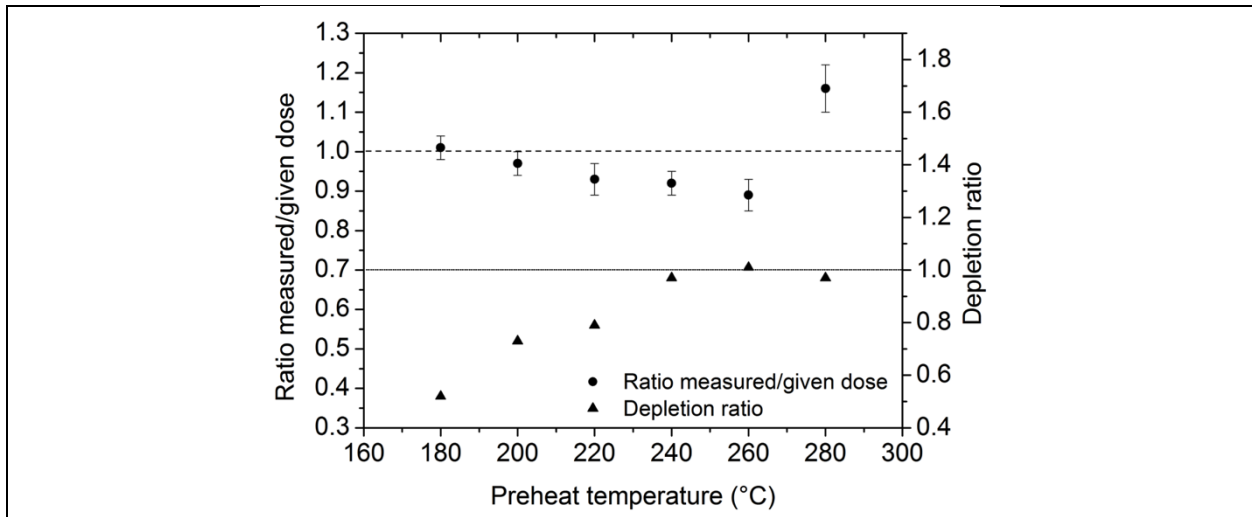


Figure C4: Dose-recovery-preheat test for the 100-250 μm quartz fraction of sample CONT11. The laboratory dose of ~ 78 Gy was recovered best using a preheat temperature of 240 $^{\circ}\text{C}$ (measured/given dose ratio = 0.92 ± 0.03 , depletion ratio = 0.97).

However, from the literature it is known that quartz from Chile is often affected by an instable medium component and therefore unsuitable for luminescence dating (e.g. Steffen et al., 2009). Therefore, further tests were performed, although the quartz of CONT11 seemed to perform well with the SAR protocol. (1) $D_e(t)$ plots document the relation between equivalent dose and illumination time (Bailey, 2003). Decreasing equivalent doses with increasing illumination time, as observed for sample CONT 11 (Fig. C5), are an indicator of thermally instable signal components within the quartz luminescence signal (Steffen et al. 2009). (2) LM-OSL measurements show dominance of the easily bleachable fast component in natural signals but increasing influence of the medium component in regenerated doses (Fig. C6), which might indicate instability of the medium component, as well (Steffen et al., 2009). Considering both indicators, we conclude that the quartz signal of CONT11 is thermally unstable and, thus, the calculated values for palaeodose and age are unreliable.

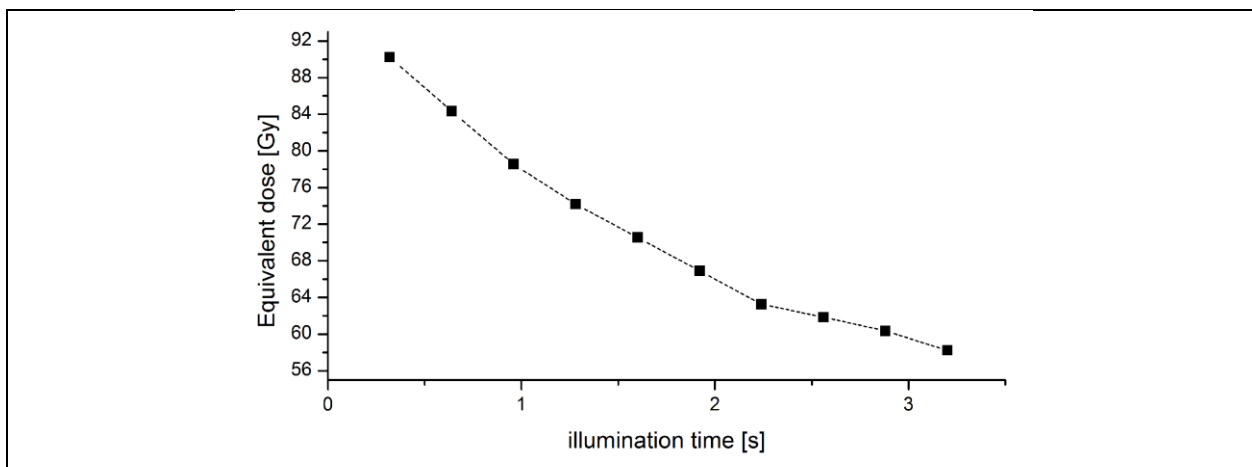


Figure C5: $D_e(t)$ plot for a 2 mm coarse-grain quartz aliquot of sample CONT11. The Equivalent dose is decreasing significantly with increasing illumination time.

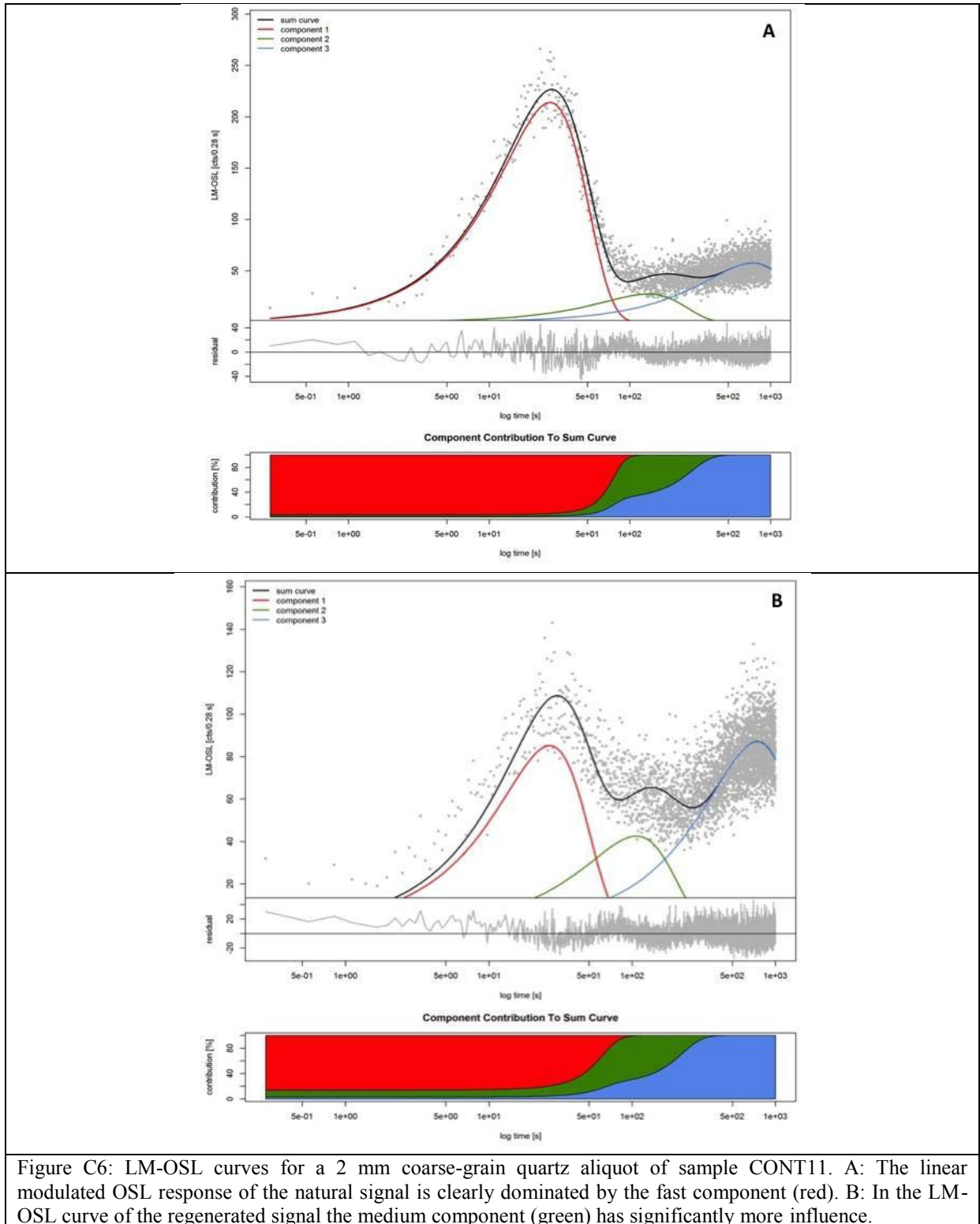


Figure C6: LM-OSL curves for a 2 mm coarse-grain quartz aliquot of sample CONT11. A: The linear modulated OSL response of the natural signal is clearly dominated by the fast component (red). B: In the LM-OSL curve of the regenerated signal the medium component (green) has significantly more influence.

C.2.3 IRSL equivalent dose

Equivalent doses were measured on 8 mm aliquots for feldspar. For the calculation of burial doses, only aliquots that passed the following SAR acceptance criteria were considered:

- (1) OSL signal 3x above background,
- (2) Test dose error < 10 %,
- (3) Recuperation < 5 % of the sensitivity-corrected natural OSL signal,
- (4) Recycling ratio between 0.9-1.1,
- (5) Depletion ratios between 0.9 and 1.1 (for quartz), and
- (6) OSL signal not in saturation (Jacobs et al., 2006).

Excluding all inadequate aliquots, between 11 and 18 D_e values were gathered to calculate a mean burial dose. Therefore, based on the decision tree procedure of Bailey and Arnold (2006), mean values for each D_e distribution (i.e. burial doses) were calculated by means of the central age model (CAM) of Galbraith et al. (1999).

Radionuclide analysis (uranium, thorium and potassium) was carried out using high-resolution gamma-spectrometry in order to estimate the dose rate. Attenuation of radiation by pore water was considered by using measured water contents (at the time of sampling) between 5 ± 5 weight-% and 16 ± 5 weight-%. Sampling depth, geographical position and altitude above sea level were used to calculate the contribution of cosmic radiation (Prescott and Hutton, 1994). For estimation of internal dose rates, a potassium content of $12.5\pm 0.5\%$ was adopted from Buylaert et al. (2012). Based on the decision tree procedure of Bailey & Arnold (2006), mean values for each D_e distribution (i.e. burial doses) were calculated by means of the central age model (CAM) of (Galbraith et al., 1999).

For palaeodose determination 11-13 aliquots were measured for each sample. All measured aliquots passed SAR acceptance criteria. The adjacent D_e distributions show low values of overdispersion (2-15%) and a more or less symmetric shape (normal distribution). Calculation of mean equivalent doses by means of CAM resulted in burial doses.

C.3 Geology and stratigraphy of marine terraces

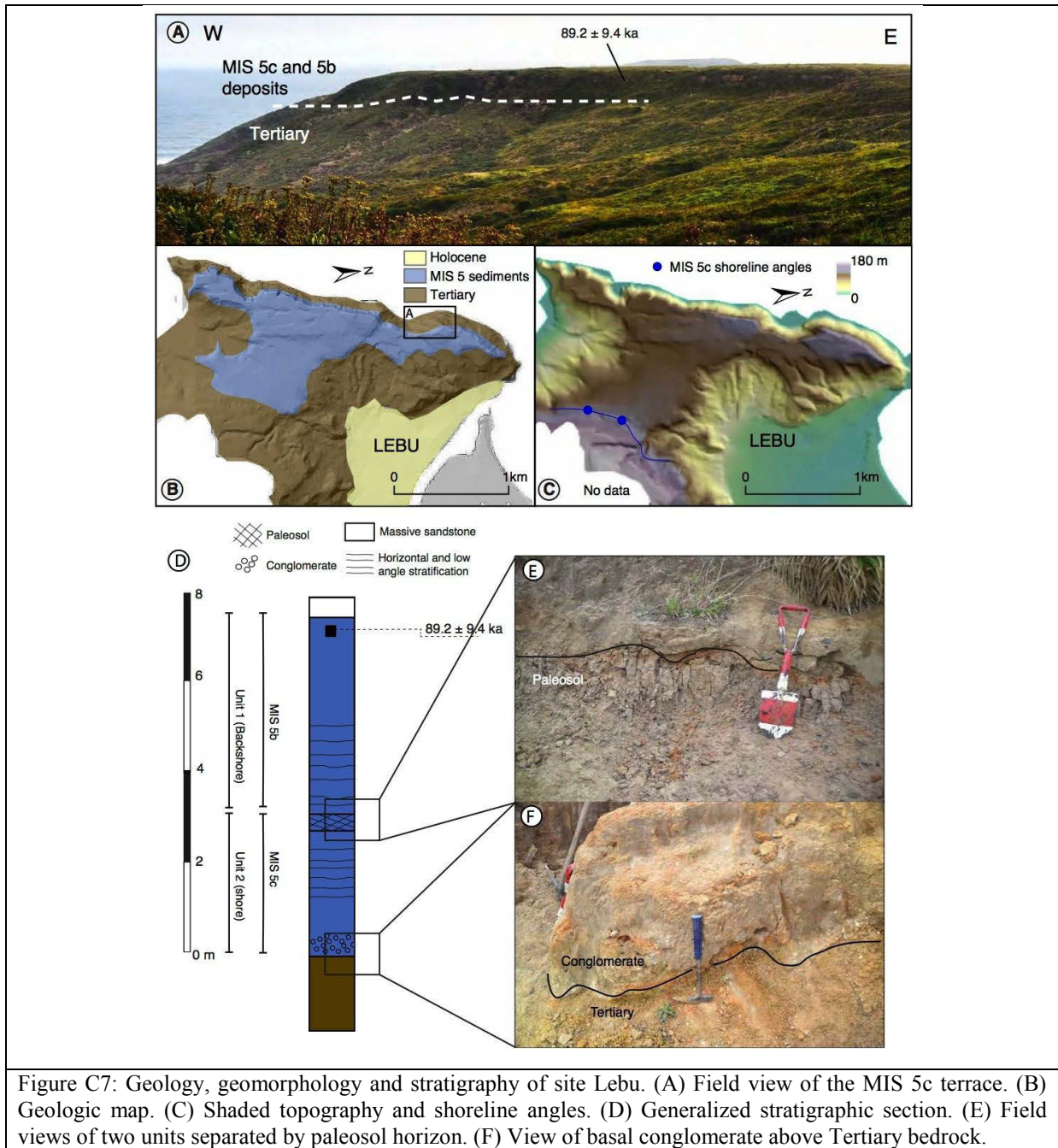


Figure C7: Geology, geomorphology and stratigraphy of site Lebu. (A) Field view of the MIS 5c terrace. (B) Geologic map. (C) Shaded topography and shoreline angles. (D) Generalized stratigraphic section. (E) Field views of two units separated by paleosol horizon. (F) View of basal conglomerate above Tertiary bedrock.

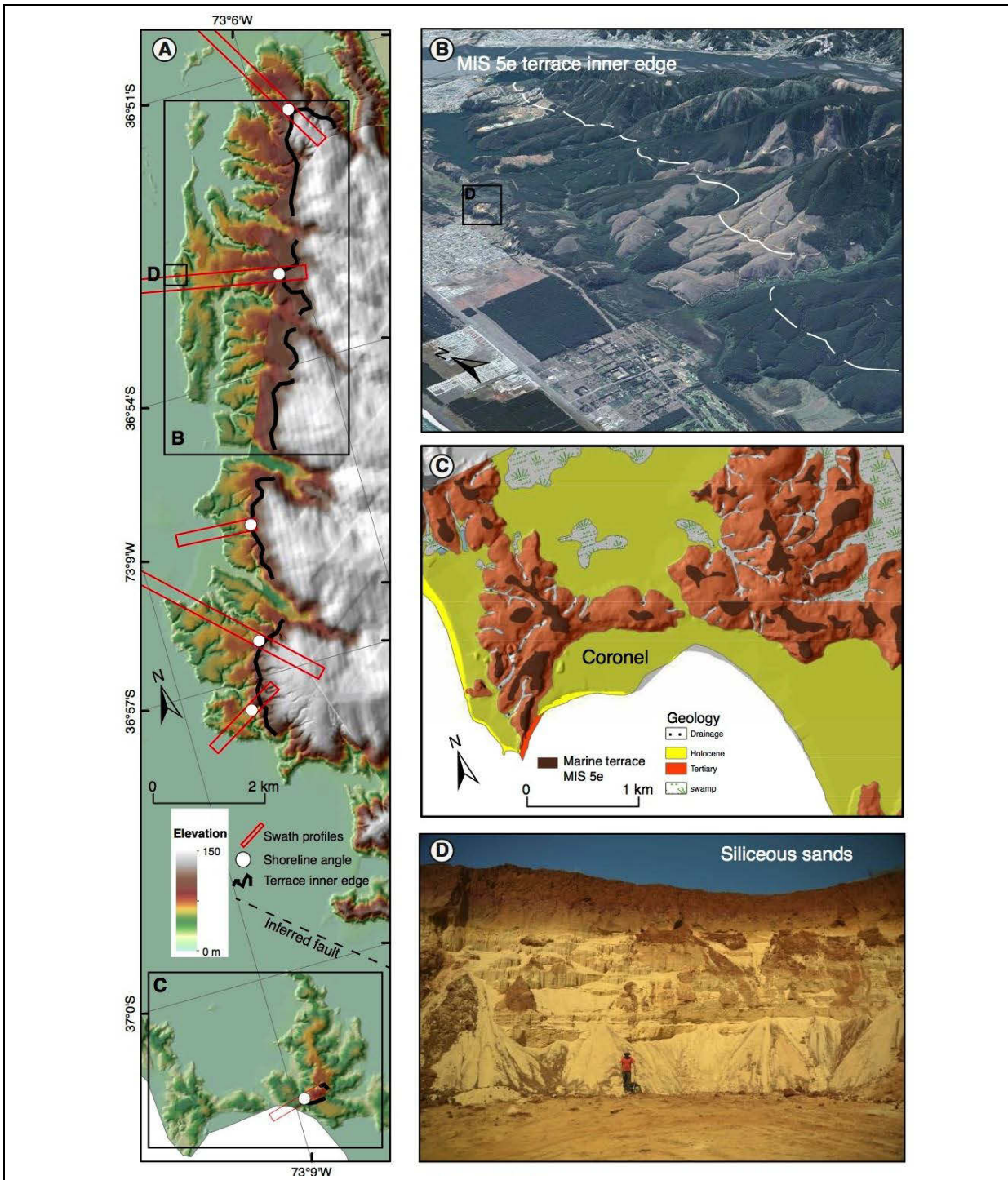


Figure C8: Geology and geomorphology between Coronel and Concepción. (A) Shaded-relief map showing the sharp and continuous MIS 5e terrace level with shoreline angles at elevation between 80 and 60 m. (B) Perspective Google Earth view of the MIS 5e terrace level. (C) Geologic map of Coronel with the MIS 5e terrace exposures. (D) Outcrop at quarry of siliceous sandstone north of Coronel.

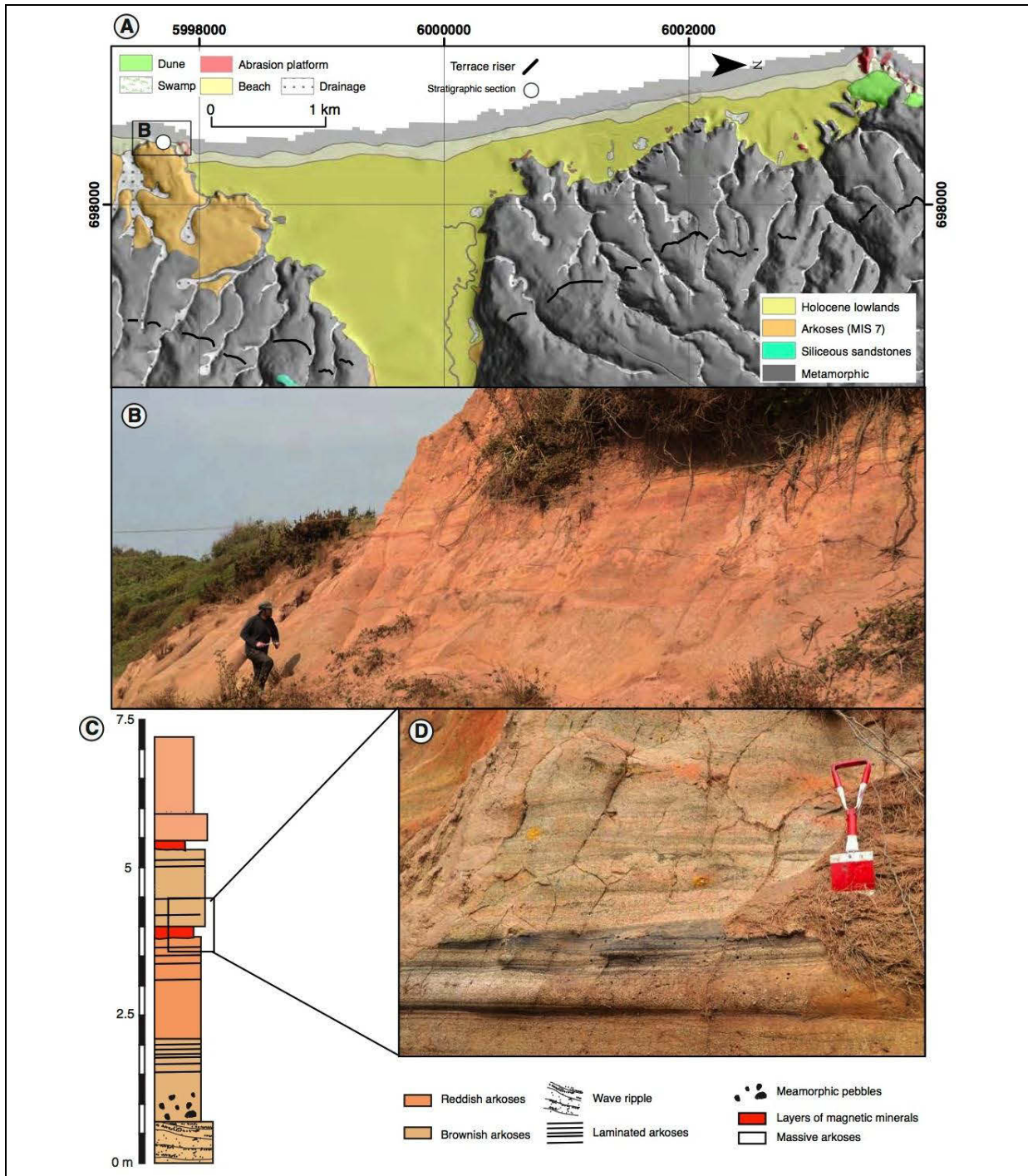


Figure C9: Geology and stratigraphy at Cobquecura (CBQC). (A) Geologic map. Note that no black volcanic sandstone (guide lithology of MIS5 levels) could be found at this site. (B) Field view of the arkosic units. The orange to reddish color of the sequences is related with the content of magnetic minerals. (C) The arkosic sequence is tentatively correlated with the MIS 7. (D) Detailed view of the base of the arkosic unit, where metamorphic pebbles occur probably associated with the flooding surface.

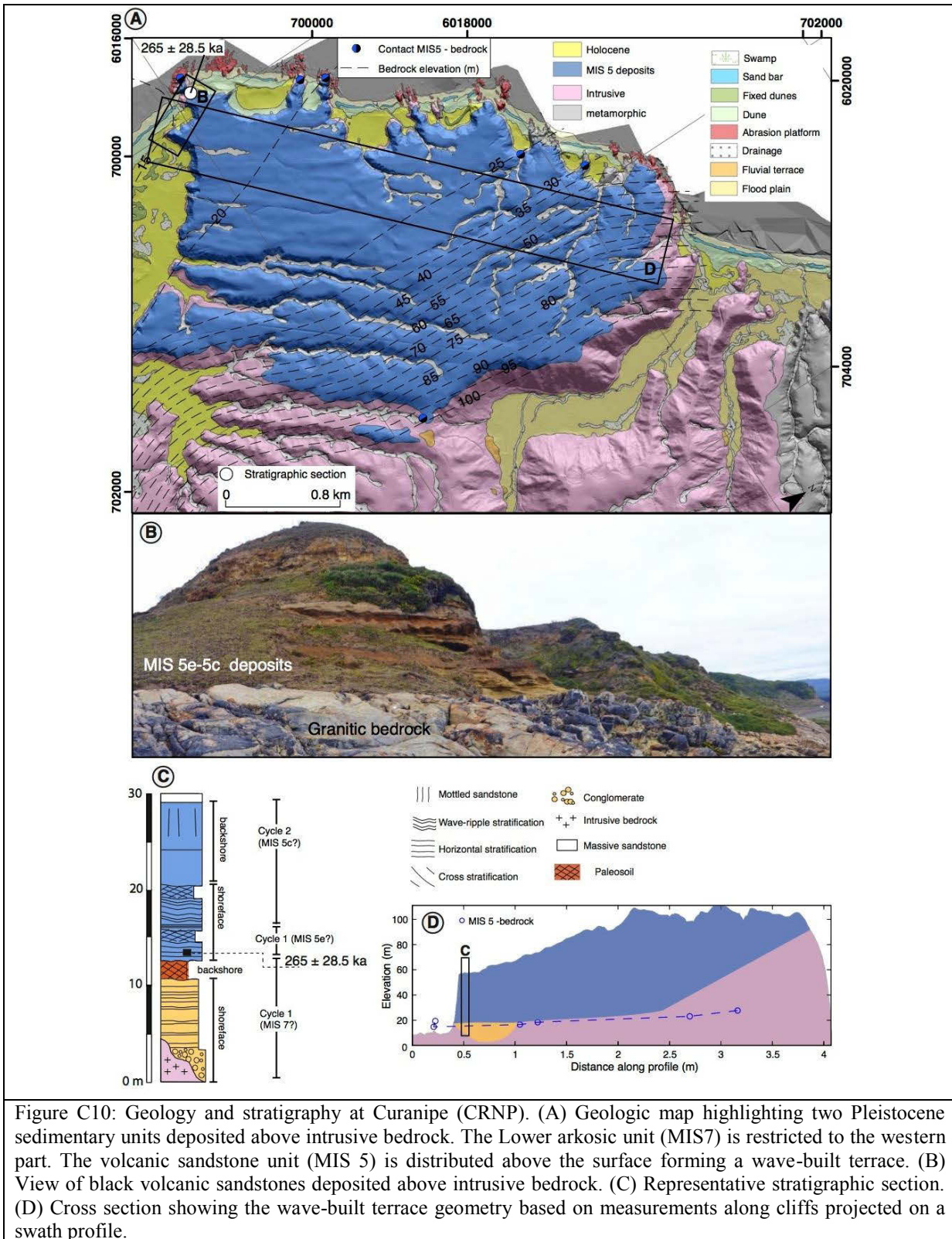


Figure C10: Geology and stratigraphy at Curanipe (CRNP). (A) Geologic map highlighting two Pleistocene sedimentary units deposited above intrusive bedrock. The Lower arkosic unit (MIS7) is restricted to the western part. The volcanic sandstone unit (MIS 5) is distributed above the surface forming a wave-built terrace. (B) View of black volcanic sandstones deposited above intrusive bedrock. (C) Representative stratigraphic section. (D) Cross section showing the wave-built terrace geometry based on measurements along cliffs projected on a swath profile.

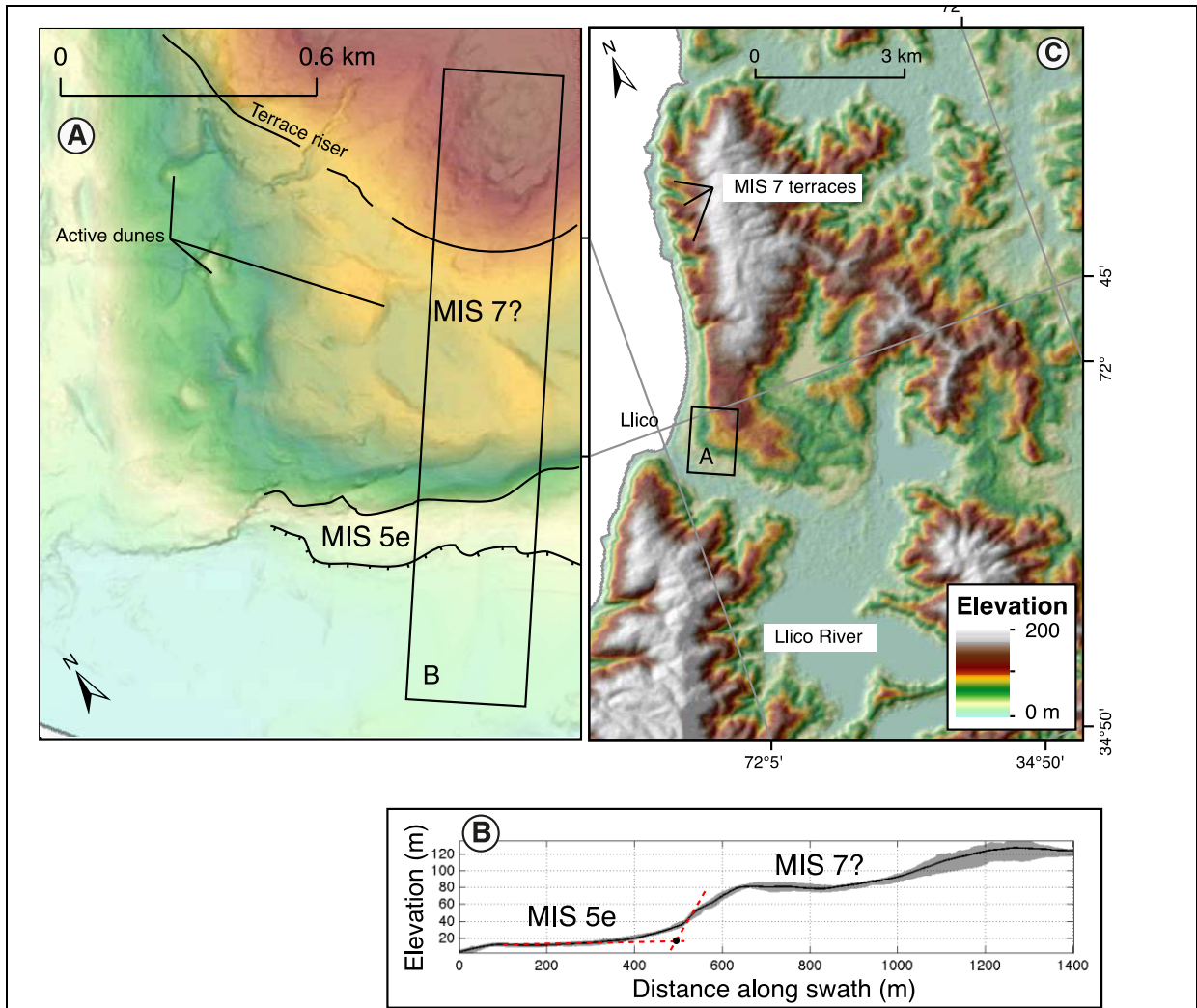


Figure C12: Geomorphology of Llico. (A) LiDAR shaded-relief map of MIS 5 terrace. The terrace tread is partly covered by active dunes. (B) Swath profile of the area indicated in (A), showing interpreted terrace levels. (C) The geomorphology of the northern part of Sector 6 is characterized by extensive MIS 7 and older terraces.

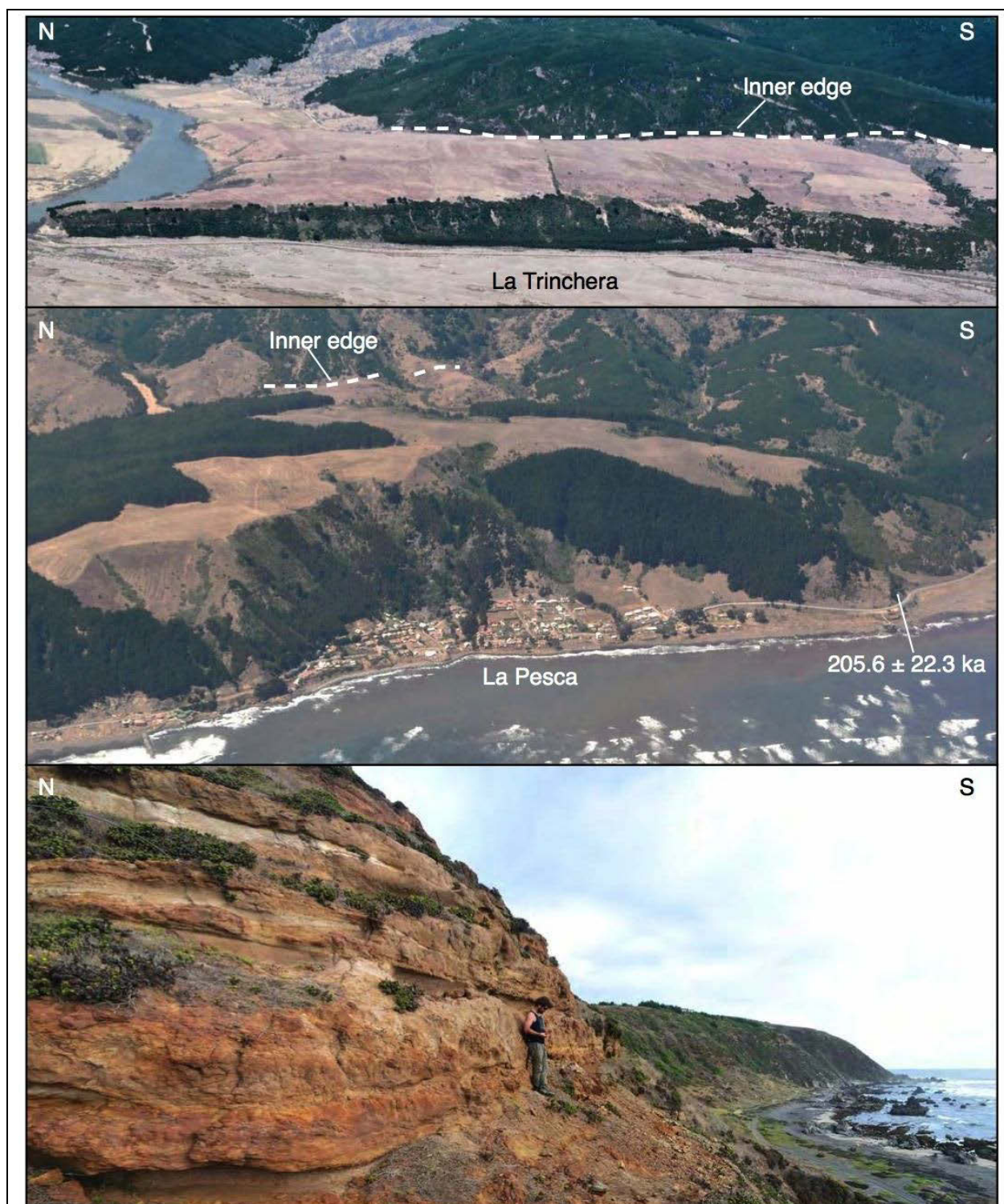


Figure C13: Terraces older than MIS 5 in Sector 6. (A) La Trinchera terrace at the southern part of Sector 6 (B) La Pesca, at the central part of Sector 6 (C) View of the shallow marine sedimentary sequences tentatively correlated with MIS 7 north of Llico.

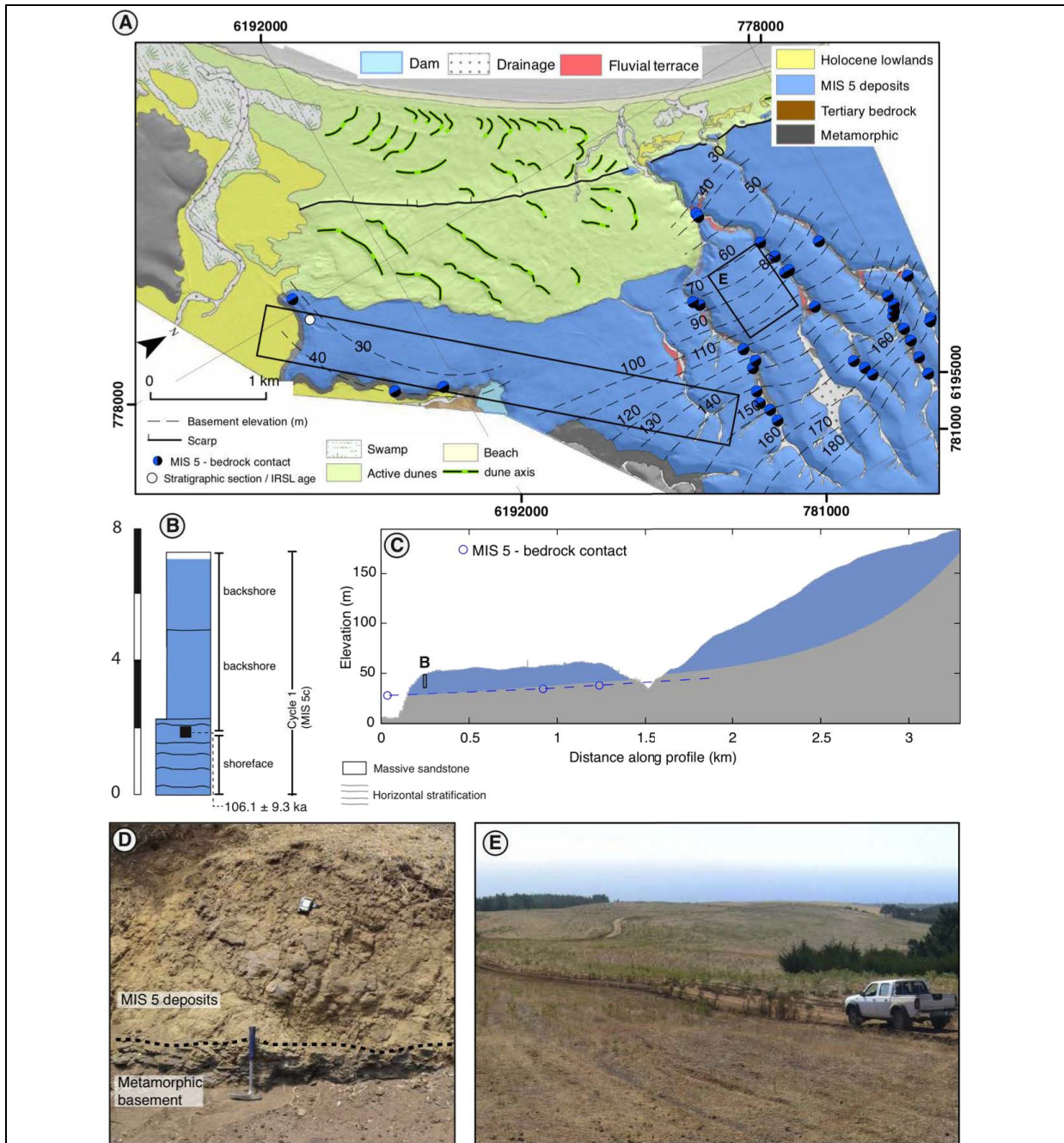


Figure C14: Geology and stratigraphy of the Pichilemu (PICH) site. (A) The geology consists of a sequence of black volcanic sandstones deposited above the metamorphic bedrock. This sequence is partly covered seawards by active dunes obscuring in part the terrace morphology. (B) The stratigraphy of the MIS 5c black volcanic sandstones consist of a succession of horizontally stratified sandstones, that represents shoreface deposits, overlaid by massive fine sandstones representing back-shore environment, forming altogether one sedimentary cycle. (C) The geometry of the sedimentary body, covering an old wave-cut platform, suggests a reoccupation of the terrace. (D) The sedimentary unit overlay the metamorphic basement. (E) The surface morphology of the deposits is smooth and no evident paleo-cliffs were observed.

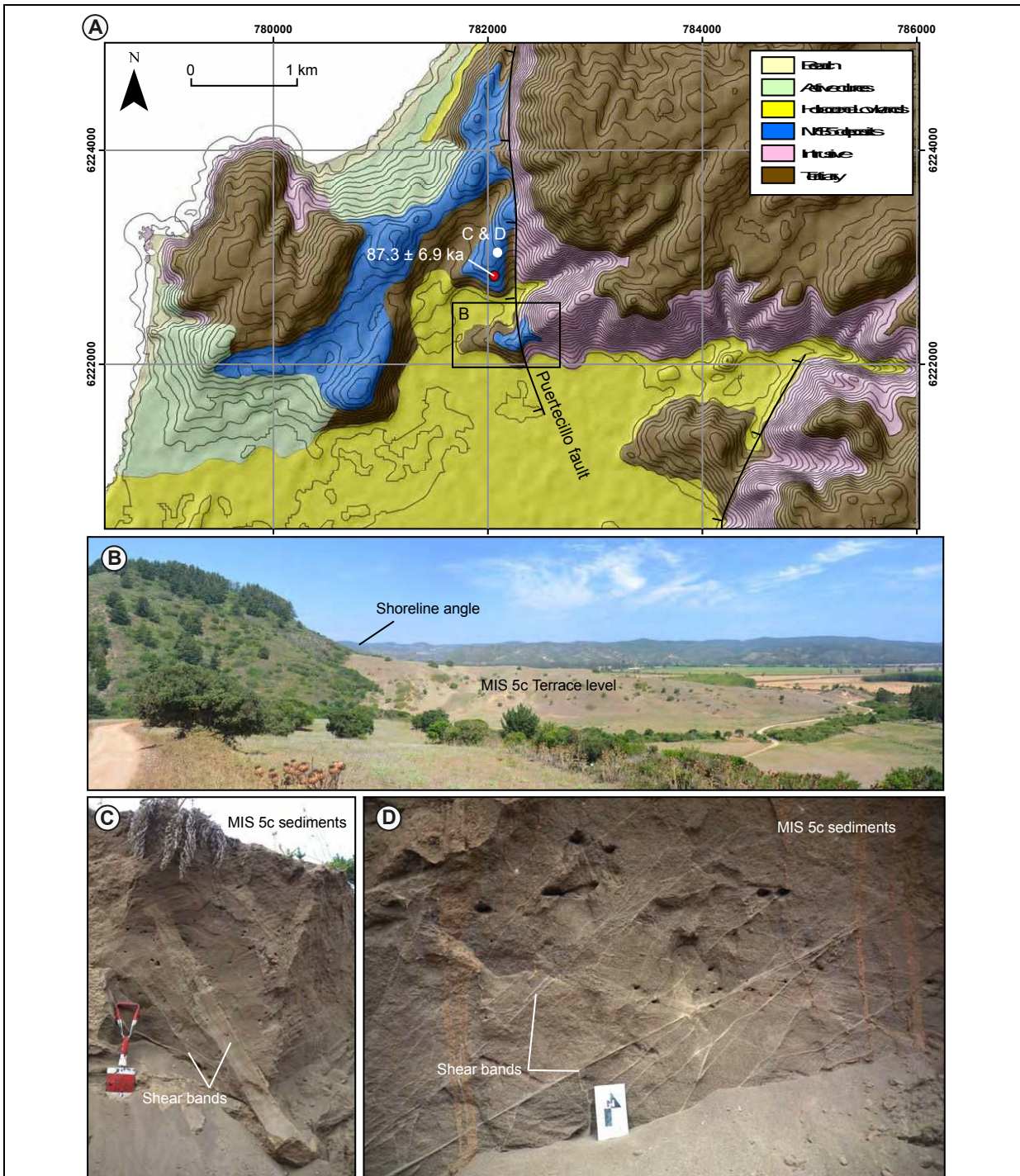


Figure C15: Geology and geomorphology at Puertecillo. (A) The Geology of Puertecillo consists of black volcanic sandstones deposited above the intrusive and Tertiary bedrock. The sequence is partly covered seaward by active dunes. The terraces paleo-cliff coincides with the trace of the Puertecillo Fault that offset the contact between Tertiary and intrusive. (B) The terraces have a sharp expression and have been correlated with the MIS 5c. (C and D) Terrace deposits near the trace of the Puertecillo Fault are deformed; shear bands and sand injections were observed within the MIS 5c sediments.

C.4 Estimates of shoreline angle elevations

We used TerraceM, our Matlab GUI, to calculate the elevation of shoreline angles by analyzing the maximum elevation extracted from topographic swaths profiles. This allows removing the cover of colluvial sediments. The minimum distribution is also analyzed when eolian processes dominate, as it allows estimating the base level of the eolian coerture, that might represent the approximate elevation of the wave cut platform.

Each of the topographic covertures represents a site, the next table resume the sites and their corresponding sector defined in Section 4.4.1.

Site	Data	Sector	Nº shorelines	Site	Data	Sector	Nº shorelines
ARAU	2	1	1	ANTI	3	1	1
CONT	2	5	12	CARD	3	4	9
CRNP	2	3	2	CCPN	3	2	7
LLCO	2	6	1	CONI	3	5	2
PICH	2	7	6	HUEN	3	1	1
PUHE	2	4	13	LEBU	3	1	3
ARCO	1	3	4	LOBO	3	7	7
BUCA	1	3	7	NAVI	3	7	2
BUCH	1	3	2	PNCO	3	2	2
RITA	1	3	1	PUTO	3	7	1
CLMO	1	3	5	ARAC	4	1	15
CUEV	1	3	1	CARN	4	5	18
MAQI	1	3	1	CARS	4	5	14
MELA	1	3	3	NAVD	4	7	1
MERQ	1	3	2	PUER	4	7	2
MONZ	1	3	2	PING	1	3	1
MORO	1	3	1	PNGE	1	3	1
MOZR	1	3	2	PUDA	1	3	2
PERA	1	3	4	RINC	1	3	1
PNGR	1	3	2	TOPO	4	7	7

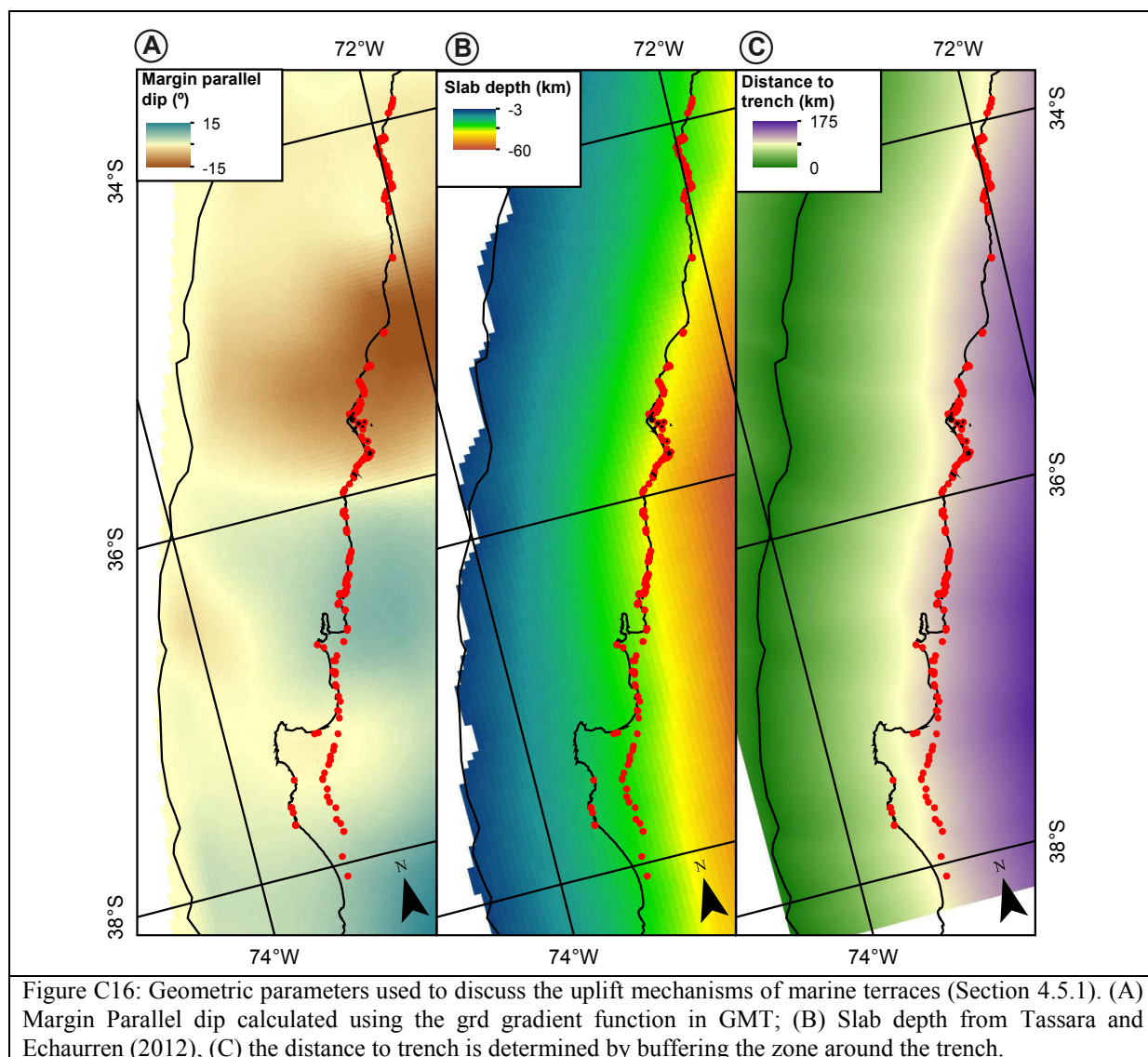
Table C1: Types of topographic dataset and number of shoreline angles estimated at each site. Data column: 1=0.5 m DTM; 2=2.5 m DTM; 3=5m DEM; 4=30m DEM (see Appendix C1 for further information).

Correlated MIS	Shoreline code
MIS 5e	1
MIS 5c	4

Table C2: Codes used to identify correlated terraces

Codes, sites and the number of profile are used to identify each of the shoreline angles mapped, indicated at the title of each one of the analyzed profiles included in this Appendix.

C.5 Geometric parameters of the Margin



C.6 References of appendix C

Bailey, R., 2003. Paper I: the use of measurement-time dependent single-aliquot equivalent-dose estimates from quartz in the identification of incomplete signal resetting. *Radiation Measurements* 37, 673-683.

Bailey, R., Arnold, L., 2006. Statistical modelling of single grain quartz De distributions and an assessment of procedures for estimating burial dose. *Quaternary Science Reviews* 25, 2475-2502.

Bulur, E., Botter-Jensen, L., Murray, A., 2000. Optically stimulated luminescence from quartz measured using the linear modulation technique. *Radiation Measurements* 32, 407-411.

Buylaert, J.-P., Jain, M., Murray, A.S., Thomsen, K.J., Thiel, C., Sohbaty, R., 2012. A robust feldspar luminescence dating method for Middle and Late Pleistocene sediments. *Boreas* 41, 435-451.

- Galbraith, R.F., Roberts, R.G., Laslett, G., Yoshida, H., Olley, J.M., 1999. Optical dating of single and multiple grains of quartz from jinnium rock shelter, northern australia: part i, experimental design and statistical models*. *Archaeometry* 41, 339-364.
- Jacobs, Z., Duller, G.A., Wintle, A.G., 2006. Interpretation of single grain De distributions and calculation of De. *Radiation Measurements* 41, 264-277.
- Prescott, J., Hutton, J.T., 1994. Cosmic ray contributions to dose rates for luminescence and ESR dating: large depths and long-term time variations. *Radiation measurements* 23, 497-500.
- Steffen, D., Preusser, F., Schlunegger, F., 2009. OSL quartz age underestimation due to unstable signal components. *Quaternary Geochronology* 4, 353-362.
- Tassara, A., Echaurren, A., 2012. Anatomy of the Andean subduction zone: three-dimensional density model upgraded and compared against global-scale models. *Geophysical Journal International* 189, 161-168.
- Thiel, C., Buylaert, J.-P., Murray, A., Terhorst, B., Hofer, I., Tsukamoto, S., Frechen, M., 2011. Luminescence dating of the Stratzing loess profile (Austria), -Testing the potential of an elevated temperature post-IR IRSL protocol. *Quaternary International* 234, 23-31.
- Thomsen, K.J., Murray, A., Jain, M., Botter-Jensen, L., 2008. Laboratory fading rates of various luminescence signals from feldspar-rich sediment extracts. *Radiation Measurements* 43, 1474-1486.

Appendix D: Quantifying offshore deformation using Pleistocene drowned shorelines, Arauco Bay, Chile.

D.1 Comparison of surface texture of drowned and active wave-cut platforms

I compared the morphology of wave-cut platforms recently uplifted during the (2010) Maule Earthquake at Santa Maria Island (SMI) and the Arauco Peninsula with drowned shorelines recognized in the Arauco Bay. Active wave-cut platforms at Punta Mourhuilla and the northern tip of SMI are both etched in tertiary rocks displaying similar morphologic features as those observed in their drowned counterparts at the Arauco Bay area.

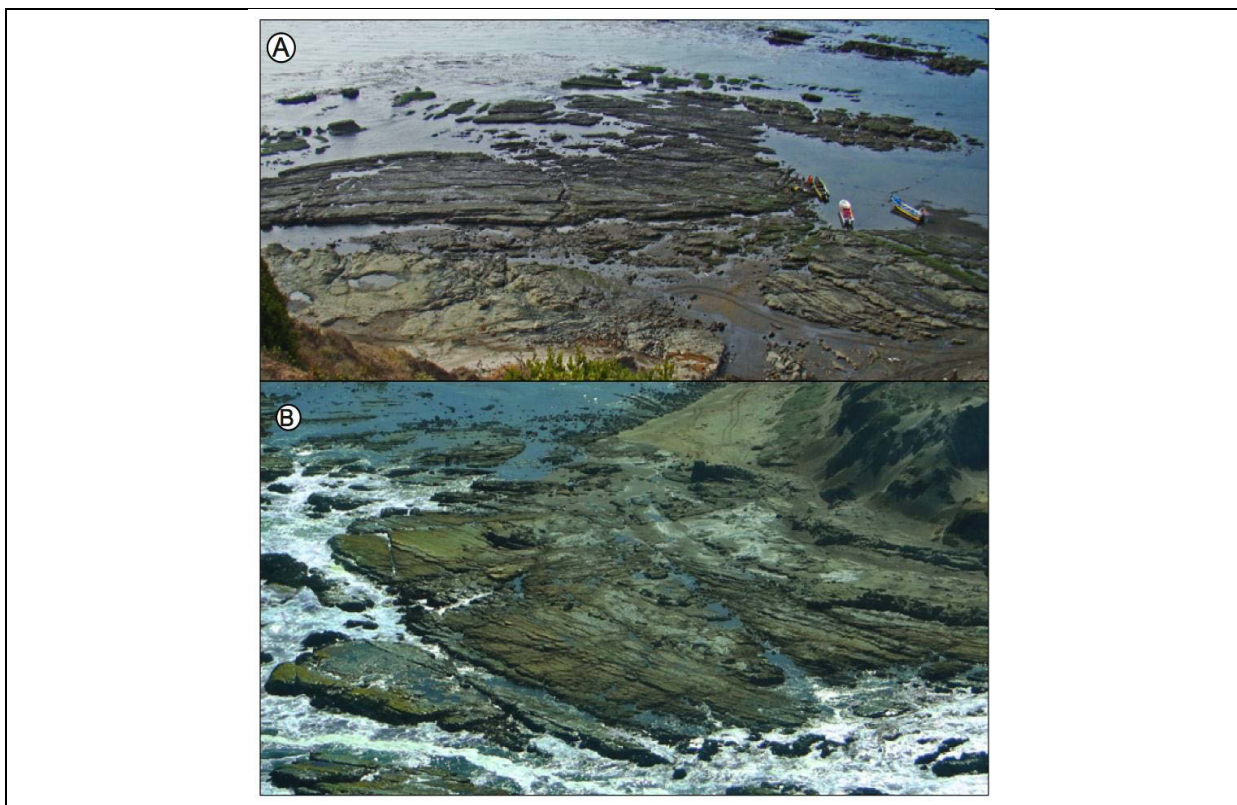


Figure D1: Wave-cut platforms uplifted ~ 1.6 m during the (2010) Maule Earthquake at the northern tip of SMI. A) View of the platform from the cliff. Notice the bedrock stratification truncated by the wave-cut surface and a corridor spanning the center of the platform. B) Aerial perspective of the same platform in A, bedrock erosion is intensified along fractures and stratification surfaces, dismembering the platform and generating characteristic surface textures and high-surface roughness. (Photo by Eduardo Jaramillo, 2012)

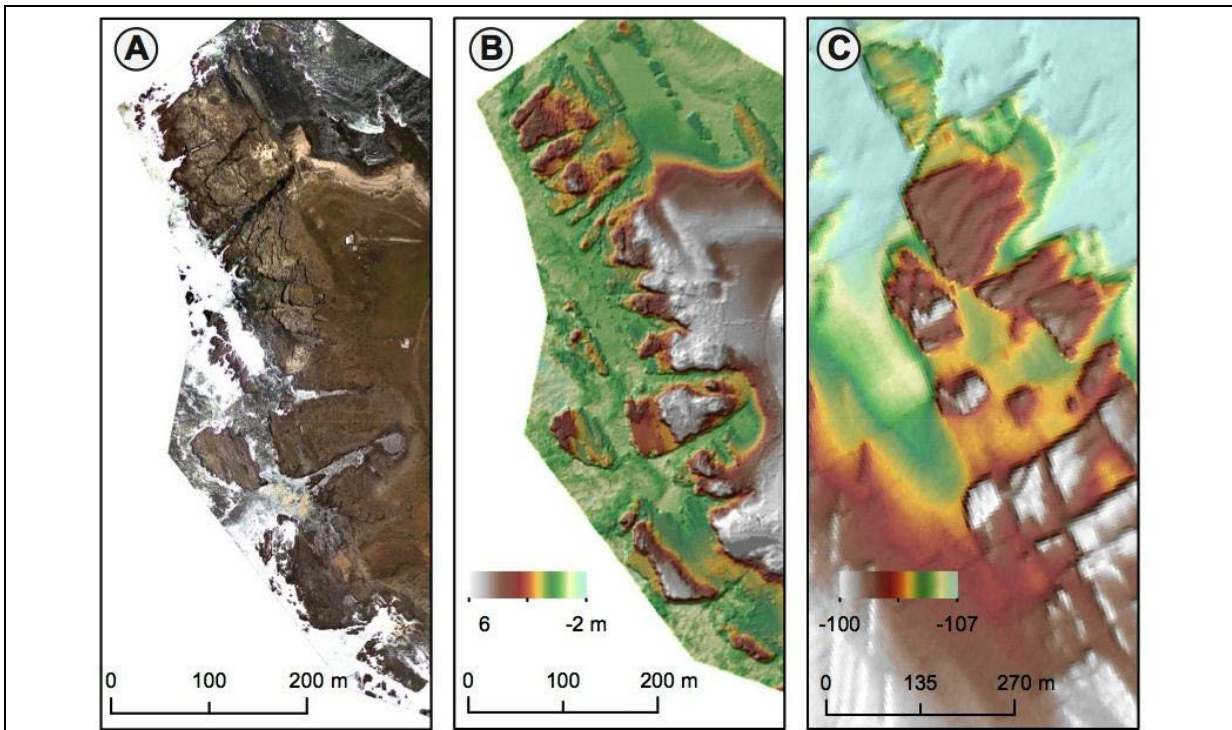


Figure D2: Comparison between active and drowned wave-cut platforms using high-resolution topography and bathymetry. A and B) 0.5 m-resolution IKonos Imagery and 2 m-resolution LiDAR topography of an active wave-cut platform in Punta Morhuilla, at the Southern part of the Arauco Peninsula. C) High resolution bathymetry east of SMI depicting a drowned wave-cut platform of similar rough surface morphology as B. Notice that in both examples the platforms are dismembered seawards and fractures appears at the surface, and widened due abrasion. These fractures isolate small blocks, representing stacks and stumps located at the edge of the platform.

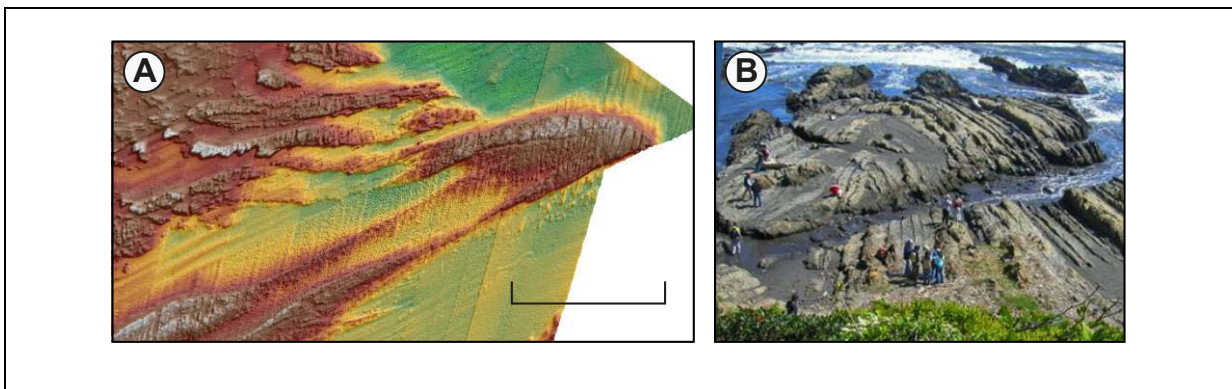


Figure D3: Comparison between geological structures outcropping at the surface wave-cut platforms using field observation and high-resolution bathymetry. A) Anticline structure observed with 2-m resolution bathymetry north of the Bio-Bio Canyon. B) Anticline structure excavated by a wave-cut platform north of Concepcion. Differential erosion is observed in platforms located at the intertidal zone, where erosion affects strata of different hardness producing outstanding outcrops. This can be used a distinctive morphologic characteristic to distinguish intertidal wave-cut platforms.

D.2 Testing the Landscape Evolution model with other sea-level proxies

We compared three different stacks of sea-level curves to evaluate the levels with better potential to be preserved and their surface expression. However only the combination of Siddall et al. (2007) and Rholing et al. (2009) was capable to generate sharp and well-defined levels of drowned shorelines. In figure D4 we illustrate the results obtained from other combinations of sea-level

curves for different uplift and erosion rates, notice that different ages of drowned shorelines are formed.

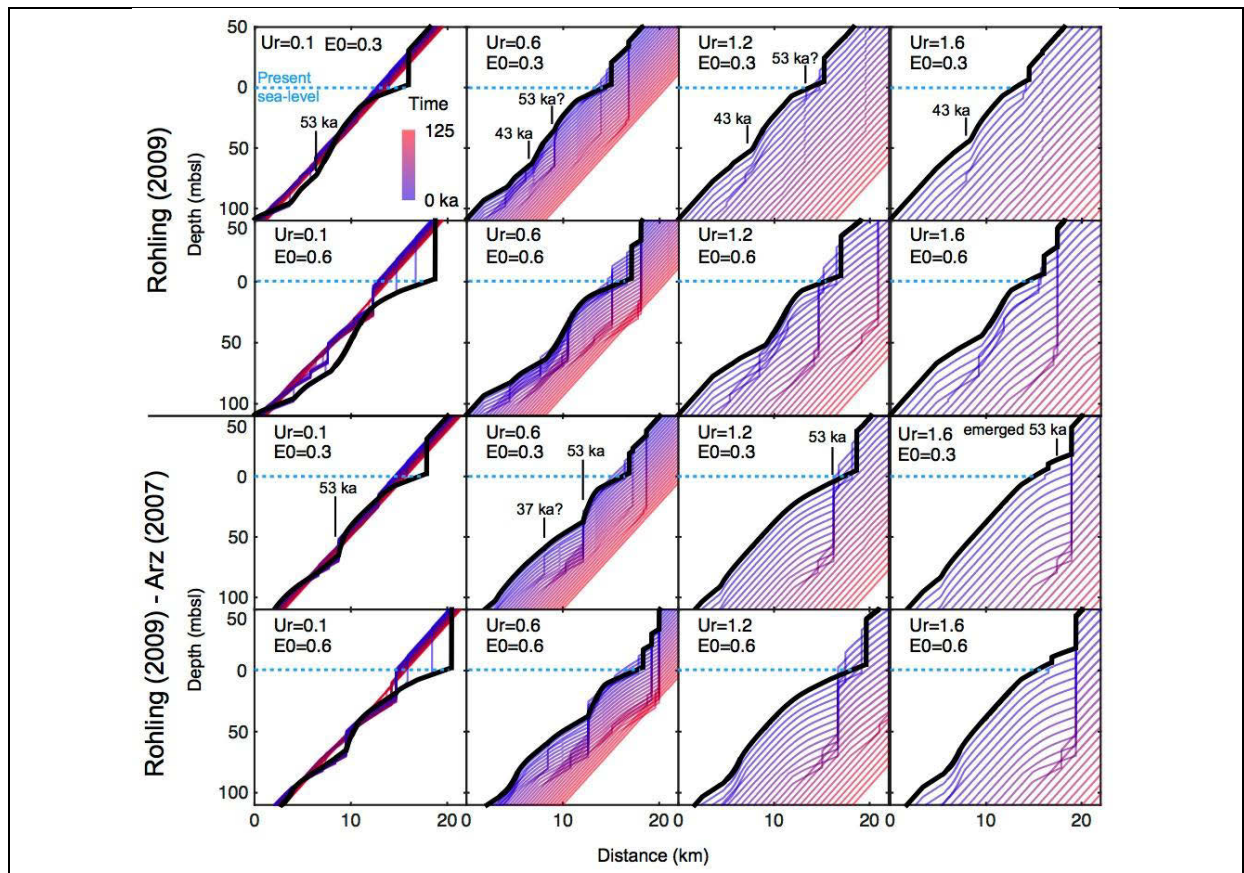


Figure D4 Sensitivity simulations to determine the levels with higher potential to be preserved, using the sea-level curve of Rhohling et al. (2009) and a combination of Rhohling et al., (2009) and Arz et al. (2007) spanning 125 ka. Each plot is a model run using different uplift (U_r) and initial erosion rates (E_0). The age of modeled drowned shoreline levels is indicated and vary due differences between the location of sea-level peaks of each curve. Notice that for Rhohling et al. (2009) the model is unable to generate a drowned terrace at ~ 55 ka, instead for Rhohling et al., (2009) and Arz et al. (2007) the ~ 55 ka terrace is sharper, however, the model cannot reproduce younger shoreline levels such as ~ 30 ka recognized using Siddall et al. (2007) and Rhohling et al. (2009).

D.3 Cliff erosion rates

Initial cliff erosion rate (E_0) and cliff erosion rate (E) are different lements in the LEM that may produce some confussion. The E_0 represent the initial energy in the system that may be dissipated along the platform and against the bottom. E represents the remaining amount of energy responsible to drive cliff retreat.

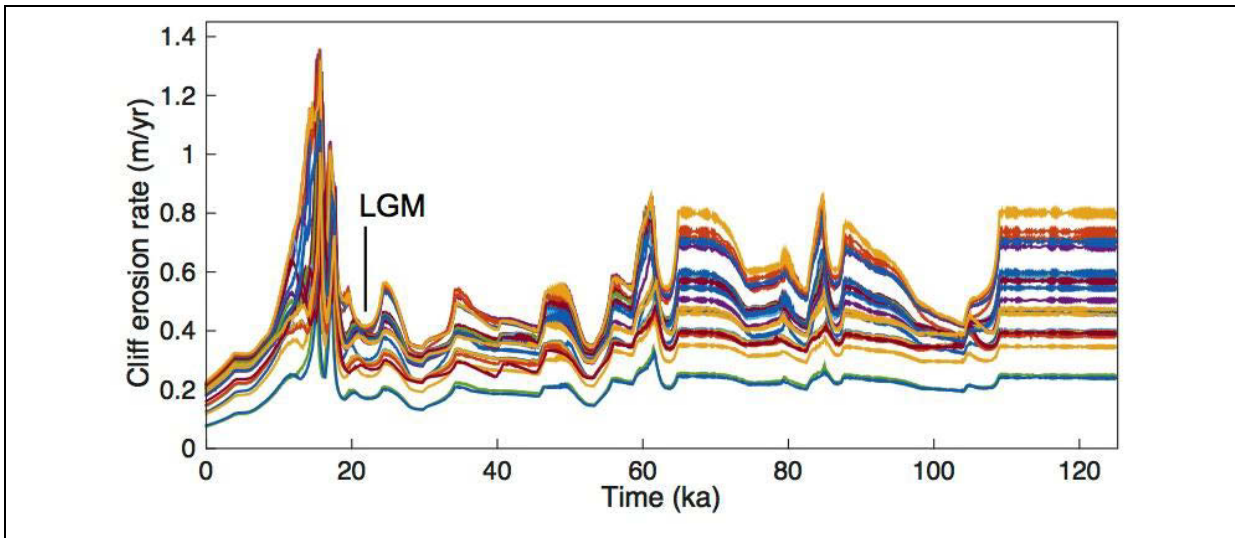


Figure D5: Plot of cliff erosion rates of drowned shorelines modeled at the Arauco Bay. These color lines represent the amount of erosion at the coastline for each forward Landscape Evolution Model (Chapter 5.3.5). Notice the highest peak of cliff erosion after 20 ka, representing rapid sea-level rise following the Last Glacial Maximum (LGM). The coastline was affected by a peak of erosion that lasted ~7 ka, we discuss this amount of erosion and the potential for preservation of drowned shorelines in Section 5.6.1.

Appendix E: Online Material

Curriculum Vitae:	https://www.dropbox.com/s/zz1pir4736dcplt/JARA_CURRICULUM_VITAE_updated.doc?dl=0
TerraceM Web:	http://www.terracem.com
List of publications:	https://www.researchgate.net/profile/Julius_Jara-Munoz
Publications (.zip):	https://www.dropbox.com/s/2e12ts9lo75xzpi/Publications.zip?dl=0
Presentations in congress (.zip):	https://www.dropbox.com/s/qoefv3583ynw49e/Presentations.zip?dl=0
Various Matlab® scripts (.zip):	https://www.dropbox.com/s/4wbq0a2hiom719f/Scripts.zip?dl=0